Relating the chemical reactivity of supramolecular hydrogelators and the physical properties of their gels

Jamie S. Foster

Submitted for the degree of Doctor of Philosophy

Heriot-Watt University

School of Engineering and Physical Sciences

Institute of Chemical Sciences

December 2016

ABSTRACT

This thesis reports a number of studies that examines low molecular weight hydrogelators forming through in situ chemical reactions and gel the water in which this reaction occurs. This in situ gelation process has allowed a number of chemical and physical reactions and assembly processes to be investigated.

Pathway complexity, an exciting concept within chemical systems has been explored with a multi-reactive hydrazone based gelation system that allows different gels to be formed from a single starting point through navigation of the systems' energy landscape. This work inspired the development of a large family of imine based gelators that would undergo an effectively irreversible tautomerisation. This allowed exploration and characterisation of the systems' ability to self-sort and co-assemble, at both the molecular and macroscopic level.

One particular imine inspired gelator featured a much slower in situ reaction. This allowed characterisation of its reaction kinetics and demonstrated its autocatalytic behaviour.

This thesis highlights the link between the chemical reactions that form the individual gelator molecules and the supramolecular assembly process. By using one to control the other, an in-depth understanding of the presented systems has been developed, allowing for the accurate targeting of desired physical properties.

Acknowledgements

I would like to thank my supervisor Dr Gareth Lloyd, from you I have learnt so much. It is a shame we did not get to finish chemistry but I think we made a fair dent.

To my mum and dad, you have gone above and beyond what I deserve. You have always supported me no matter what and given me a life with no regrets or complaints. You have made everything I have done and everything I have achieved possible.

To my brother, Calum. You never fail to amuse me which is a mission in itself. You are the guy everyone wants to be but I do not mind because you are a top boy.

To Claire, you are amazing. From the moment I met you I knew you were the one for me. You are always there when I need you and you will have my love forever and for always, moine Claire.

"To every man upon this earth
Death cometh soon or late.
And how can man die better
Than facing fearful odds,
For the ashes of his fathers,
And the temples of his gods"

- Thomas Babington Macaulay,
Lays of Ancient Rome

ACADEMIC REGISTRY
Research Thesis Submission

Name*:*	Jamie S. Foster		
School:	Engineering and Physical Sciences, Institute of Chemical Sciences		
Version: *(i.e. First, Resubmission, Final)*	Final	Degree Sought:	PhD Chemistry

Declaration

In accordance with the appropriate regulations I hereby submit my thesis and I declare that:

1) the thesis embodies the results of my own work and has been composed by myself
2) where appropriate, I have made acknowledgement of the work of others and have made reference to work carried out in collaboration with other persons
3) the thesis is the correct version of the thesis for submission and is the same version as any electronic versions submitted*.
4) my thesis for the award referred to, deposited in the Heriot-Watt University Library, should be made available for loan or photocopying and be available via the Institutional Repository, subject to such conditions as the Librarian may require
5) I understand that as a student of the University I am required to abide by the Regulations of the University and to conform to its discipline.
6) I confirm that the thesis has been verified against plagiarism via an approved plagiarism detection application e.g. Turnitin.

* *Please note that it is the responsibility of the candidate to ensure that the correct version of the thesis is submitted.*

Signature of Candidate*:*		Date:	

Submission

Submitted By *(name in capitals):*	Jamie S. Foster
Signature of Individual Submitting:	
Date Submitted:	

For Completion in the Student Service Centre (SSC)

Received in the SSC by *(name in capitals):*			
Method of Submission *(Handed in to SSC; posted through internal/external mail):*			
E-thesis Submitted (mandatory for final theses)			
Signature:		Date:	

Table of Contents

List of abbreviations

1D	One-dimensional
2D	Two-dimensional
3D	Three-dimensional
A	Absorbance
AFM	Atomic Force Microscopy
ALS	Aromatic linker steroid
BTA	Benzene triamide
CDC	Constitutional dynamic chemistry
CGC	Critical Gelation Concentration
cm	centimeter
conc	Concentration
DCC	Dynamic combinatorial chemistry
DCvC	Dynamic covalent chemistry
DMF	Dimethylformamide
DMSO	Dimethyl sulfoxide
EtOH	Ethanol
F	Phenylalanine
Fmoc	Fluorenylmethyloxycarbonyl
FTIR	Fourier transform infrared spectroscopy
G′	Storage or elastic shear modulus
G″	Loss or viscous modulus
HFIP	Hexafluoroisopropanol
Hz	Hertz
IR	InfraRed
LMW	Low Molecular Weight
LMWG	Low Molecular Weight Gelator
log	Logarithm
logP	Partition Coefficient
m	metre
Nm	Newton metre
NMR	Nuclear Magnetic Resonance

Pa	Pascal
PXRD	Powder X-Ray Diffracion
SEM	Scanning Electron Microscopy
SMD	Solvent model based on density
SXRD	single Crystal X-Ray Diffraction
t	Time
ε	Extinction coefficient

Throughout this work standard three letter codes for amino acids have been used in the thesis, with the additional use of the one letter code, F, being used for phenylalanine.

List of Figures and Tables

Figure 1.9. (a) Interlocking of Fmoc groups from alternate β-sheets to create π-stacked pairs with interleaved phenyl rings. (b) Due to the twist of β-sheets, the second sheet must be rotated in relation the first to maintain the interaction between the fluorenyl groups. A cylindrical end view, (c), of the structure and side view, (d). (reproduced with permission from ref.[90])

Figure 1.10. Diagrams highlighting the structural difference between an oxygen centred BTA molecule (left) and a nitrogen centred BTA molecule (right).

Figure 1.11. Diagrams showing BTA gelators in the oxygen centred confirmation functionalised with pyridyl arm units.

Figure 1.12. Diagrams showing the chemical structures of TSA-TDAB and TSA-TDATA, examples of C_3 tripodal gelators.

Figure 1.13. Formation of the tripodal trihydrazone. Starting from the initial water soluble aldehyde and trihydrazide reactants, the formation of the trihydrazone resulted in supersaturation, followed by fibre formation. It is these fibres that entangle, forming a three-dimensional network, which ultimately leads to gelation of the solvent.

Figure 1.14. Representation of the three types of imine reaction: (a) imine condensation, (b) exchange reaction and (c) metathesis reaction.

Figure 1.15. The general reaction scheme for an autocatalytic reaction feature two starting products, **A** and **B**, which react to produce the autocatalytic species, **C**.

Figure 1.16. The general form for the rate equation that describes a template based auto-catalytic reaction. ac^p refers to the autocatalytic term (c defines product concentration). p is the order of the reaction with respect to the product. b relates to the non-catalysed reaction rate.

Figure 1.17. Kinetic signatures of autocatalysis. Top: exponential vs. parabolic growth. Bottom: the rate of reaction is proportional to initial concentration of product. (reproduced with permission from ref.[125]).

Figure 2.1. Proposed reaction scheme demonstrating the stepwise reaction between the trialdehyde (***II***) and hydrazide (***I***) through the mono- ($\boldsymbol{A_e}$), di- ($\boldsymbol{B_e}$) and tri- ($\boldsymbol{C_e}$) reacted species in order to form a C_3 LMWG. The tri- reacted species has the potential for tautomerisation from $\boldsymbol{C_e}$ to $\boldsymbol{C_k}$.

Figure 2.2. Synthesis of 1,3,5-triformylphloroglucinol (***II***) from phloroglucinol using hexamethylenetetramine in trifluoroacetic acid. Deprotonation of ***II***'s hydroxyl groups produces a water soluble form of ***II*** that is necessary for gel formation.

Figure 2.3. *In situ* reaction scheme for the formation of *N*',*N*''',*N*''''-((1*E*,1'*E*,1''*E*)-(2,4,6-trihydroxybenzene-1,3,5-triyl)tris(methanylylidene))tri(isonicotinohydrazide) (***Ce***) in its proposed deprotonated form. Reaction involves the combination of ***I*** and ***II*** in water at pH 8.

Figure 2.4. Close up photograph of gel set using concentrated HCl (left) and set with GdL (right). The differences in homogeneity are apparent with the GdL set gel having a highly uniform structure, when compared with the HCl set gel.

Figure 2.5. Time sweep experiment results for the ***Ce*** gel set using nine equivalents GdL (added four hours after the mixing of ***I*** and ***II***) . Blue diamonds (◆) represent the evolution of *G′* as a function of time.

Figure 2.6. Time sweep rheology experiment for gel ***Ce*** set using GdL (nine equivalents) four hours after mixing ***I*** and ***II*** in water at pH 8, with the point defining onset of gelation marked (left). Avrami (*D*) constant determination for ***Ce*** using previously outlined method (right) ($R^2 = 0.99$).

Figure 2.7. Frequency sweep experiment results for ***Ce*** gel set using GdL (nine equivalents) four hours after mixing ***I*** and ***II*** in water at pH 8. Experiment conducted immediately upon completion of the time sweep experiment. Values for *G′* represented as blue squares with *G″* represented as red diamonds.

Figure 2.8. Concentration study for *in situ* formed ***Ce*** gel. Straight line gives the relationship, $G' = 0.10[\boldsymbol{C_e}]^{2.02}$. Data points represent the *G′* value obtained at specific concentrations of ***Ce*** (●) This confirms the proportional relationship between *G′* and [gelator] for this system is in agreement with what would be expected for the cellular with the gradient of the line = 2.02 ($R^2 = 0.96$).

Figure 2.9. Stress sweep experiment results for the ***Ce*** gel set using GdL that was described previously. Blue diamonds represent the *G′* of the gel at any given time. Region of rapid decrease in *G′* represents yield point.

Figure 2.10. SEM images of dried samples of ***Ce*** gel. The fibrous morphology of the gel network can be clearly seen in the images along with crystallites that can be attributed to the presence of gluconic acid/gluconate salts or sodium salts that arise due to the addition of sodium hydroxide.

Figure 2.11. Photographs of gel ***Be*** in an inverted vial orientation (1) to demonstrate its gelatinous nature and a top view to highlight its bright orange colour (2). A top view of gel ***Ce*** (3) has been included to demonstrate the noticeable difference in colour between the two gels.

Figure 2.12. Time sweep experiment results for the ***Be*** gel set using nine equivalents GdL (added immediately after the mixing of ***I*** and ***II***). Blue diamonds (◆) represent the evolution of *G′* as a function of time.

Figure 2.13. Determination of the Avrami constant (*D*) for the ***B*$_e$** gel using the previously defined period of the onset of gelation. $D = 2.13$ ($R^2 = 0.99$).

Figure 2.14. Frequency sweep experiment results for ***B*$_e$** gel set using GdL (nine equivalents) immediately after mixing ***I*** and ***II*** in water at pH 8. Experiment conducted immediately upon completion of the time sweep experiment. Values for *G′* represented as blue squares with *G″* represented as red diamonds.

Figure 2.15. Stress sweep rheology experiment for the *in situ* produced gel ***B*$_e$**. The stress sweep experiment was performed on the same sample and immediately after the completion of the frequency sweep experiment. *G′* represented by blue squares (■) connected by a solid line in order to guide the eye. *G′* plotted on the y-axis linearly (in Pa) and applied stress in the form of applied torque plotted logarithmically on the x-axis (in μNm).

Figure 2.16. Reaction scheme for the formation of *N*',*N*"'-((1*E*,1'*E*)-(5-formyl-2,4,6-trihydroxy-1,3-phenylene)bis(methanylylidene))di(isonicotinohydrazide) (***B*$_e$**) from the combination of ***I*** and ***II*** in water at pH 8 with the immediate addition of GdL. By using a number of equivalents of ***I*** >3 the formation of ***B*$_e$**.

Figure 2.17. SEM images of dried samples of ***B*$_e$** gel. The fibrous morphology of the gel network can be clearly seen, with the sample in the left image having a thin gold coating applied, and the right image showing the gel sample uncoated.

Figure 2.18. Determination of the kinetic data of the reaction between ***I*** and ***II***. The graph shows how relative normalized percentage abundances of the species present within the reaction mixture change with time as determined by ESI-MS. ***C*$_e$** = ■, ***B*$_e$** = ▲, ***A*$_e$** = ◆ and ***II*** = ○.

Figure 2.19. UV-Vis spectra for samples of ***B*$_e$** (left) and ***C*$_e$** (right). Spectra obtained for samples of ***B*$_e$** and ***C*$_e$**, at a concentration of 1.25 μM, that had previously been isolated from their corresponding gels before being redissolved in water ,and their spectra recorded.

Figure 2.20. Collection of UV-Vis spectra for the reaction between ***I*** and ***II***. Spectra recorded at 10, 20, 30, 40, 50, 60, 70, 80, 90, 100, 110, 120, 130, 140, 150, 160, 170, 180, 360 and 1200 minutes with arrows highlighting the decrease in absorption at 300 nm and increase in absorption at 415 nm.

Figure 2.21. Kinetic data for the reaction between ***I*** and ***II***, recorded using UV-Vis spectroscopy, and the subsequent conformation of ***B*$_e$** (■) as a function of time. The reaction of ***B*$_e$** with ***I*** to form ***C*$_e$** is also reported (◆). Lines added between data points to guide the eye.

Figure 2.22. Photograph of gel ***C*$_k$** set from *in situ* reaction of ***I*** and ***II***, when the reaction was performed in a reaction solution at pH 10.5. This distinct yellow gel formed after one hour.

Figure 2.23. Time sweep rheology experiment for the *in situ* produced gel $\boldsymbol{C_k}$. Gel set at a pH of 11, resulting in the G' value of the gel beginning to plateau after approximately 22 minutes, at a value of 200 Pa, before achieving a final G' value of 460 Pa after 3 hours.

Figure 2.24. Frequency sweep rheology experiment for the *in situ* produced gel $\boldsymbol{C_k}$. The frequency experiment was performed on the same sample and immediately after the completion of the time sweep experiment. G' represented by blue squares (■) and G'' represented by red squares (■), with G' and G'' plotted on the y-axis logarithmically and frequency of oscillation in the applied stress plotted linearly on the x-axis. G' recorded 50 Hz has a value of 500 Pa and is the value used for comparisons with other gels.

Figure 2.25. Stress sweep rheology experiment for the *in situ* produced gel $\boldsymbol{C_k}$. The stress sweep experiment was performed on the same sample and immediately after the completion of the frequency sweep experiment. G' represented by blue squares (■) connected by a solid line in order to guide the eye. G' plotted on the y-axis linearly (in Pa) and applied stress in the form of applied torque plotted logarithmically on the x-axis (in μNm).

Figure 2.26. Molecular component of gel $\boldsymbol{C_k}$, the ligand $\boldsymbol{C_k}$. Two geometric isomers of the same ligand are shown, as both are evident in the ^{1}H and ^{13}C NMR spectra in the solution state. The C_3 symmetric geometric isomer is shown on the left, and the C_s symmetric is shown on the right.

Figure 2.27. Time sweep rheology experiment for the gel set using an *ex situ* prepared sample of the ligand $\boldsymbol{C_e}$. Gel was set with the addition of GdL (nine equivalents) to give a gel of 2 wt%. The setting of the gel resulted in the G' value of the gel beginning to plateauing after approximately 14 minutes and achieving a final G' value of 15000 Pa after 3 hours.

Figure 2.28. Time sweep rheology experiment for the gel set using a sample of the ligand $\boldsymbol{B_e}$. isolated from an *in situ* gel was set with the addition of GdL (nine equivalents) to give a gel of 2 wt%. The setting of the gel resulted in the G' value of the gel beginning to plateauing after approximately 30 minutes at a value of 2000 Pa before achieving a final G' value of 2300 Pa after 3 hours.

Figure 2.29. Frequency sweep rheology experiment for the $\boldsymbol{B_e}$ gel prepared using the described *ex situ* method. The frequency experiment was performed on the same sample and immediately after the completion of the time sweep experiment. G' represented by blue squares (■) and G'' represented by red squares (■) with G' and G'' plotted on the y-axis logarithmically and frequency of oscillation in the applied stress plotted linearly on the x-axis. G' recorded at 50 Hz has a value of 2300 Pa and is the value used for comparisons with other gels.

Figure 2.30. Stress sweep rheology experiment for the *ex situ* produced gel ***B*e**. The stress sweep experiment was performed on the same sample and immediately after the completion of the frequency sweep experiment. *G´*represented by blue squares (■) connected by a solid line in order to guide the eye. *G´*plotted on the y-axis linearly (in Pa) and applied stress in the form of applied torque plotted logarithmically on the x-axis (in μNm).

Figure 2.31. PXRD patterns for each of the three gels prepared by both the *in situ* and *ex situ* methods. ***B*e** *in situ* coloured light blue (—), ***B*e** *ex situ* coloured light orange (—), ***C*e** *in situ* coloured dark orange (—),***C*e** *ex situ* coloured dark blue (—), ***C*k** *in situ* coloured grey (—), and ***C*k** *ex situ* coloured green (—).

Figure 2.32. Crystal structure of ***C*e**·DMSO solvate. Asymmetric unit, top left, of the structure of ***C*e** showing labels of atoms, with atoms shown as ellipsoids at 50% probability. Complete molecule of ***C*e** (top middle) showing the hydrogen bonding between the OH groups and hydrazone N(imine) groups, as well as those between the DMSO molecules and ***C*e**. The flatness of the ***C*e** molecules is highlighted with the right-hand image. Stacking of ***C*e** into one-dimensional array, i.e. supramolecular polymers shown in bottom image. π- π interactions between the pydridyl groups clearly seen, as well as the concave:convex fit. Structure viewed diagonal to the c axis.

Figure 2.33. Calculated supramolecular arrangement of three molecules of ***B*e**. Top down view (left) and side view (right) of stack shown. Dashed lines show inter- and intramolecular hydrogen bonds.

Figure 2.34. Calculated supramolecular arrangement of three molecules of ***C*e**. Top down view (left) and side view (right) of stack shown. Dashed lines show inter- and intramolecular hydrogen bonds.

Figure 2.35. Calculated supramolecular arrangement of three molecules of ***C*k**. Dashed lines show inter- and intramolecular hydrogen bonds.

Figure 2.36. Pictorial representation of the various possible pathways within the gelation system. Included are all pathways that give rise to a gel as well the pathways that maybe result in the formation of an unobserved/non-gelator reaction product. ▲ represents the central keto core of products ***A*k**, ***B*k** and ***C*k**. ▲ represents the central enol core of products ***A*e**, ***B*e** and ***C*k**. * represents the start of the reaction upon mixing.

Figure 2.37. Predicted theoretical UV-Vis spectra for molecules ***C*e** and ***C*k** in DMSO (left). Experimental UV-Vis spectra for molecules ***C*e** and ***C*k** in DMSO (right). Data plotted for ***C*e** in red and data plotted for ***C*k** in blue.

Figure 2.38. Predicted theoretical UV-Vis spectra for the molecule ***B*e** in DMSO (left). Experimental UV-Vis spectra for the molecule ***B*e** in DMSO (right).

Figure 2.39. Pathway for the transition from $\boldsymbol{A_e}$ (minima 1) to $\boldsymbol{A_k}$ (minima 4) (left) showing the structure of the four minima that would result from the transition (TS = transition state). Plot of reaction coordinate (x-axis) against relative electronic energy (y-axis) for the $\boldsymbol{A_e}$ to $\boldsymbol{A_k}$ transition showing energy differences between the tautomers and the barrier size between them. B3LYP with 6-311G(d) basis set at 298K; electronic energy in kcal/(mol).

Figure 2.40. Pathway for the transition from $\boldsymbol{B_e}$ (minima 1) to $\boldsymbol{B_k}$ (minima 4) (left) showing the structure of the four minima that would result from the transition (TS = transition state). Plot of reaction coordinate (x-axis) against relative electronic energy (y-axis) for the $\boldsymbol{B_e}$ to $\boldsymbol{B_k}$ transition showing energy differences between the tautomers and the barrier size between them. B3LYP with 6-311G(d) basis set at 298K; electronic energy in kcal/(mol).

Figure 2.41. Pathway for the transition from $\boldsymbol{C_e}$ (minima 1) to $\boldsymbol{C_k}$ (minima 4) (left) showing the structure of the four minima that would result from the transition (TS = transition state). Plot of reaction coordinate (x-axis) against relative electronic energy (y-axis) for the $\boldsymbol{C_e}$ to $\boldsymbol{C_k}$ transition showing energy differences between the tautomers and the barrier size between them. B3LYP with 6-311G(d) basis set at 298K; electronic energy in kcal/(mol).

Figure 2.42. Samples of gels $\boldsymbol{B_e}$ (left) and $\boldsymbol{C_e}$ (right) prepared at 2 wt% and stored in the dark for 380 days (at the time the photograph was taken).

Figure 2.43. Samples of gel $\boldsymbol{C_k}$ prepared at 2 wt% and stored in the dark for 372 days (at the time the photograph was taken).

Figure 2.44. Gel $\boldsymbol{B_e}$ (left), Gel $\boldsymbol{C_e}$ (centre) and gel $\boldsymbol{C_k}$ (right). Photograph taken after gels had been heated to 90 ^{o}C in an oil bath, and held at this elevated temperature for two hours.

Figure 2.45. Reaction scheme for the formation of *N*',*N*''',*N*''''-((1*E*,1'*E*,1''*E*)-(2,4,6-trihydroxybenzene-1,3,5-triyl)tris(methanylylidene))tri(benzohydrazide) (C_{eB}) from the combination of I_B and *II* after four hours in water at pH 8.

Figure 2.46. The suspension that arises from the *in situ* preparation of ligand $\boldsymbol{C_{eB}}$ in solution at pH 8, followed by the addition of GdL after a reaction time of four hours.

Figure 2.47. Images of the asymmetic unit for the structure of $\boldsymbol{C_{eB}}$ with molecules of methanol. Atoms shown as elipsiods at 50 % probablity. Image on the left is the asymmetric unit with the central and right handside images showing the labels of the two non-symmetry related components of the asymetric unit.

Figure 2.48. The stacking of molecules of $\boldsymbol{C_{eB}}$ into high aspect ratio columns (right) through a hydrogen bonding pattern (left) that involves four molecules of $\boldsymbol{C_{eB}}$ and two molecules of methanol. A set of these bonds has been coloured yellow to highlight the ring pattern with the methanol molecules presented in a ball and stick representation for clarity, with the $\boldsymbol{C_{eB}}$ molecules shown in a close-dcapped representation.

Figure 3.1. Pictorial representations of three possible co-assembling and self-sorting supramolecular arrangements within a four component gelator system. Picture on left represents an ordered co-assembling arrangement where the gel fibres feature two of the four components in a regular pattern. Central picture shows a random co-assembly process where all fibres feature a random number and arrangement of all four components. Picture on right demonstrates self-sorting where each individual fibre consists of only one type of LMWG with no mixing in terms of the individual molecular components occurring.

Figure 3.2. Reaction scheme for the reaction between aniline and ***II*** at pH 8 in water, and the product that forms from the resulting reaction.

Figure 3.3. The 10 amines that were screened with ***II*** in order to test for gelation. $\mathbf{R_1}$ 4-aminobenzoic acid, $\mathbf{R_2}$ 5-amino-2-chlorobenzoic acid, $\mathbf{R_3}$ 4-amino-2-methoxybenzoic acid, $\mathbf{R_4}$ 4-amino-3-hydroxybenzoic acid, $\mathbf{R_5}$ 3-amino-4-hydroxybenzoic acid, $\mathbf{R_6}$ 3-amino-5-(trifluoromethyl)benzoic acid, $\mathbf{R_7}$ 3-amino-2-methoxybenzoic acid, $\mathbf{R_8}$ 4-amino-2-methylbenzoic acid, $\mathbf{R_9}$ 4-aminophenol, $\mathbf{R_{10}}$ 6-aminohexanoic acid.

Figure 3.4. Photo shows the gels resulting from an *in situ* preparation method (gels $\mathbf{R_1}$ to $\mathbf{R_9}$ shown left to right) with gels $\mathbf{R_1}$ to $\mathbf{R_8}$ set with the addition of GdL, and $\mathbf{R_9}$ setting using HCl. Photo on far right shows precipitate formed when $\mathbf{R_{10}}$ is used.

Figure 3.5. Potential tautomeric forms of the products for the reaction between ***II*** and general aromatic amine (aniline used for the purposes of demonstration). The enol-imine tautomer, not analytically observed, on the left with the observed keto-enamine tautomer on the right.

Figure 3.6. Structures of the central core when molecules adopt a C_3 geometric form or a C_s conformation. Dotted lines highlight the intramolecular hydrogen bonding patterns that are present within the molecules.

Figure 3.7. SEM images obtained for gels $\mathbf{R_1}$ to $\mathbf{R_9}$ with examples shown of gels set using both the *in situ* and *ex situ* method of ligand preparation. Samples are labelled accordingly in red text in top left of image.

Figure 3.8. Results of the frequency sweep rheology experiment for the gel prepared using both an *in situ* and *ex situ* synthesised sample of $\mathbf{R_1}$ at a concentration of 25 mM. The storage modulus G'(Pa) *in situ* (●) and *ex situ* (○) as well as the loss modulus G''(Pa) *in situ* (■) and *ex situ* (□) are shown as a log scale (y-axis) against the frequency (Hz) (x-axis).

Figure 3.9. Results of the stress sweep rheology experiment for the gel prepared using both an *in situ* and *ex situ* synthesised sample of $\mathbf{R_1}$ at a concentration of 25 mM. Storage modulus G' for *in situ* (■) and *ex situ* (□) synthesised samples (Pa) (y-axis) plotted against torque (μNm) shown as a log scale (x-axis).

Figure 3.10. Results of the frequency sweep rheology experiment for the gel prepared using both an *in situ* and *ex situ* synthesised sample of $\mathbf{R_2}$ at a concentration of 25 mM. The storage modulus *G′*(Pa) *in situ* (●) and *ex situ* (○) as well as the loss modulus *G″*(Pa) *in situ* (■) and *ex situ* (□) are shown as a log scale (y-axis) against the frequency (Hz) (x-axis).

Figure 3.11. Results of the stress sweep rheology experiment for the gel prepared using both an *in situ* and *ex situ* synthesised sample of $\mathbf{R_2}$ at a concentration of 25 mM. Storage modulus *G′* for *in situ* (■) and *ex situ* (□) synthesised samples (Pa) (y-axis) plotted against torque (μNm) shown as a log scale (x-axis).

Figure 3.12. Results of the frequency sweep rheology experiment for the gel prepared using both an *in situ* and *ex situ* synthesised sample of $\mathbf{R_3}$ at a concentration of 25 mM. The storage modulus *G′*(Pa) *in situ* (●) and *ex situ* (○) as well as the loss modulus *G″*(Pa) *in situ* (■) and *ex situ* (□) are shown as a log scale (y-axis) against the frequency (Hz) (x-axis).

Figure 3.13. Results of the stress sweep rheology experiment for the gel prepared using both an *in situ* and *ex situ* synthesised sample of $\mathbf{R_3}$ at a concentration of 25 mM. Storage modulus *G′* for *in situ* (■) and *ex situ* (□) synthesised samples (Pa) (y-axis) plotted against torque (μNm) shown as a log scale (x-axis).

Figure 3.14. Results of the frequency sweep rheology experiment for the gel prepared using both an *in situ* and *ex situ* synthesised sample of $\mathbf{R_4}$ at a concentration of 25 mM. The storage modulus *G′*(Pa) *in situ* (●) and *ex situ* (○) as well as the loss modulus *G″*(Pa) *in situ* (■) and *ex situ* (□) are shown as a log scale (y-axis) against the frequency (Hz) (x-axis).

Figure 3.15. Results of the stress sweep rheology experiment for the gel prepared using both an *in situ* and *ex situ* synthesised sample of $\mathbf{R_4}$ at a concentration of 25 mM. Storage modulus *G′* for *in situ* (■) and *ex situ* (□) synthesised samples (Pa) (y-axis) plotted against torque (μNm) shown as a log scale (x-axis).

Figure 3.16. Results of the frequency sweep rheology experiment for the gel prepared using both an *in situ* and *ex situ* synthesised sample of $\mathbf{R_5}$ at a concentration of 25 mM. The storage modulus *G′*(Pa) *in situ* (●) and *ex situ* (○) as well as the loss modulus *G″*(Pa) *in situ* (■) and *ex situ* (□) are shown as a log scale (y-axis) against the frequency (Hz) (x-axis).

Figure 3.17. Results of the stress sweep rheology experiment for the gel prepared using both an *in situ* and *ex situ* synthesised sample of $\mathbf{R_5}$ at a concentration of 25 mM. Storage modulus *G′* for *in situ* (■) and *ex situ* (□) synthesised samples (Pa) (y-axis) plotted against torque (μNm) shown as a log scale (x-axis).

Figure 3.18. Results of the frequency sweep rheology experiment for the gel prepared using both an *in situ* and *ex situ* synthesised sample of $\mathbf{R_6}$ at a concentration of 25 mM. The storage modulus *G′*(Pa) *in situ* (●) and *ex situ* (○) as well as the loss modulus *G″*(Pa) *in situ* (■) and *ex situ* (□) are shown as a log scale (y-axis) against the frequency (Hz) (x-axis).

Figure 3.19. Results of the stress sweep rheology experiment for the gel prepared using both an *in situ* and *ex situ* synthesised sample of $\mathbf{R_6}$ at a concentration of 25 mM. Storage modulus *G′* for *in situ* (■) and *ex situ* (□) synthesised samples (Pa) (y-axis) plotted against torque (μNm) shown as a log scale (x-axis).

Figure 3.20. Results of the frequency sweep rheology experiment for the gel prepared using both an *in situ* and *ex situ* synthesised sample of $\mathbf{R_7}$ at a concentration of 25 mM. The storage modulus *G′*(Pa) *in situ* (●) and *ex situ* (○) as well as the loss modulus *G″*(Pa) *in situ* (■) and *ex situ* (□) are shown as a log scale (y-axis) against the frequency (Hz) (x-axis).

Figure 3.21. Results of the stress sweep rheology experiment for the gel prepared using both an *in situ* and *ex situ* synthesised sample of $\mathbf{R_7}$ at a concentration of 25 mM. Storage modulus *G′* for *in situ* (■) and *ex situ* (□) synthesised samples (Pa) (y-axis) plotted against torque (μNm) shown as a log scale (x-axis).

Figure 3.22. Results of the frequency sweep rheology experiment for the gel prepared using both an *in situ* and *ex situ* synthesised sample of $\mathbf{R_8}$ at a concentration of 25 mM. The storage modulus *G′*(Pa) *in situ* (●) and *ex situ* (○) as well as the loss modulus *G″*(Pa) *in situ* (■) and *ex situ* (□) are shown as a log scale (y-axis) against the frequency (Hz) (x-axis).

Figure 3.23. Results of the stress sweep rheology experiment for the gel prepared using both an *in situ* and *ex situ* synthesised sample of $\mathbf{R_8}$ at a concentration of 25 mM. Storage modulus *G′* for *in situ* (■) and *ex situ* (□) synthesised samples (Pa) (y-axis) plotted against torque (μNm) shown as a log scale (x-axis).

Figure 3.24. Results of the frequency sweep rheology experiment for the gel prepared using both an *in situ* and *ex situ* synthesised sample of $\mathbf{R_9}$ at a concentration of 25 mM. The storage modulus *G′*(Pa) *in situ* (●) and *ex situ* (○) as well as the loss modulus *G″*(Pa) *in situ* (■) and *ex situ* (□) are shown as a log scale (y-axis) against the frequency (Hz) (x-axis).

Figure 3.25. Results of the stress sweep rheology experiment for the gel prepared using both an *in situ* and *ex situ* synthesised sample of $\mathbf{R_8}$ at a concentration of 25 mM. Storage modulus *G′* for *in situ* (■) and *ex situ* (□) synthesised samples (Pa) (y-axis) plotted against torque (μNm) shown as a log scale (x-axis).

Figure 3.26. Plot showing linear relationship between the *c*logP value of the gelating (protonated) for of molecules $\mathbf{R_1}$ – $\mathbf{R_8}$ (molecule $\mathbf{R_9}$ omitted owing to it being impossible to set a homogenous sample of a gel composed of it using the same method used for gels $\mathbf{R_1}$ – $\mathbf{R_8}$) and the *G′* for the corresponding gels. All gels setting using nine equivalents of GdL with *ex situ* synthesised gelator.

Figure 3.27. Graph showing the calculated values for the pK_a and clogP of gelators R1 to R9. *C*logP vs calculated pK_a (green Δ) neutral species, *c*log*P* vs calculated pK_a (blue ◊) trianionic species, and *c*log*P* vs measurement pK_a (red ○).

Figure 3.28. PXRD patterns for samples produced from dried gels **R_1, R_2, R_3, R_4 and R_5** recorded between 5 – 60 º over a time 30 minutes. An arbitrary scale is used for count intensity for the sake of comparisons. Data presented in this manner allows for direct comparison between samples.

Figure 3.29. PXRD patterns for samples produced from dried gels **R_6**, **R_7**, **R_8** and **R_9** recorded between 5 – 60 º over a time 30 minutes. An arbitrary scale is used for count intensity for the sake of comparisons. Data presented in this manner allows for direct comparison between samples.

Figure 3.30. PXRD pattern for the sample produced from the filtration of a suspension of **R_{10}** recorded between 5 – 60 º over a time 30 minutes.

Figure 3.31. Photograph of *ex situ* synthesised mixtures LMWGs **R_1** and **R_6** suspended in water after 20 minutes of sonication. From left to right vials contain (in terms of LMWGs) **A** = 100% **R_1**, **B** = 80% **R_1** 20% **R_6**, **C** = 60% **R_1** 40% **R_6**, **D** = 40% **R_1** 60% **R_6**, **E** = 20% **R_1** 80% **R_6**, and **F** = 100%.

Figure 3.32. Photograph of gels composed of *ex situ* synthesised samples LMWGs **R_1** and **R_6** in various ratios. Gels set from suspensions shown in Figure 3.31 through the addition of sodium hydroxide up to a pH of 8, before the addition of 9 equivalents of GdL. From left to right vials contain (in terms of LMWGs) **A** = 100% **R_1**, **B** = 80% **R_1** 20% **R_6**, **C** = 60% **R_1** 40% **R_6**, **D** = 40% **R_1** 60% **R_6**, **E** = 20% **R_1** 80% **R_6**, **F** = 100%.

Figure 3.33. Combined spectra for the transmission experiments conducted on 100% **R_1** at 10 mM (●), 75% **R_1** : 25% **R_6** (●), 50% **R_1** : 50% **R_6** (●), 25% **R_1** : 75% **R_6** (●),100% **R_6** (●).

Figure 3.34. PXRD patterns collection for dried samples of gels **R_1** and **R_6**, as well as three dried gel samples of gels composed of both **R_1** and **R_6** in the ratios defined in the Figure.

Figure 3.35. PXRD patterns collection for dried samples of gels **R_1** and **R_6** as well as three dried gel samples of gels composed of both **R_1** and **R_6** in the ratios defined in the Figure.

Figure 3.36. SEM analysis showing the consistency of morphology for gels set using various molar ratios of R_1 and R_6. a) R_1 100 : 0 R_6. b) R_1 75 : 25 R_6. c) R_1 50 : 50 R_6. d) R_1 25 : 75 R_6. e) R_1 0 : 100 R_6.

Figure 3.37. Apparent *p*K$_a$ determination for **R_1**/**R_6** mixed systems using a series of solutions of pH 10 – 10.5 containing a total of gelator concentration of 10 mM. Aliquots of HCl (0.1 M) were added to these solutions and the resulting pH recorded. Continuous stirring was used to stop a gel forming and the resultant convection problems associated with gelation. **R_1** (●), **R_1**:**R_6**, 80:20 (●), **R_1**:**R_6**, 60:40 (●), **R_1**:**R_6**, 50:50 (●), **R_1**:**R_6**, 40:60 (●), **R_1**:**R_6**, 20:80 (●), **R_1** (●).

Figure 3.38. Plot of the evolution of the percentage of gelators in the solid-phase over time. Percentage calculated from the integration of distinct peaks for each of the gelators in the ^{1}H NMR spectra for a sample contain a mixture of 50% **R$_1$** (●) and 50% **R$_6$** (●).

Figure 3.39. Plot demonstrating the effects of increasing **R$_{10}$** concentration (relative to the total concentration of both compounds) on *G′*.

Figure 3.40. PXRD patterns comparing the patterns for pure sample of gel **R$_6$**, a sample of **R$_{10}$** precipitated from water with GdL and the 50:50 mixed **R$_6$** and **R$_{10}$** Gel.

Figure 3.41. Apparent pK_a determination for **R$_1$** (●), **R$_{10}$** (●), and a 50:50, **R$_1$**:**R$_{10}$** mixed solution (●). The red circle highlights the step change in apparent pK_a, demonstrating the self-sorting nature of the system.

Figure 3.42. Plot of the evolution of the percentage of gelators in the solid-phase over time. Percentage calculated from the integration of distinct peaks for each of the gelators in the ^{1}H NMR spectra for a sample containing a mixture of 50% **R$_1$** (●) and 50% **R$_{10}$** (●).

Figure 3.43. Demonstrates the variation in *G′* of an **R$_1$** gel with increasing percentages of **R$_6$** (orange) and **R$_{10}$** (blue) relative to the total compound concentration.

Figure 3.44. Amines that will feature in the discussions in this section regarding the *in situ* formation of LMWGs when combining these amines with the trialdehyde core unit ***II***.

Figure 3.45. All possible reaction products for the *in situ* **R$_1$** + **R$_6$** + ***II***, including the gelators **R$_1$**, **R$_6$**, and products composed of mixed amines **R$_1^2$,$_6^1$** and **R$_1^1$,$_6^2$**.

Figure 3.46. All possible reaction products for the *in situ* **R$_1$** + **R$_{10}$** + ***II***, including the known molecules **R$_1$** and **R$_{10}$**, and products composed of mixed amines **R$_1^2$,$_{10}^1$** and **R$_1^1$,$_{10}^2$**.

Figure 3.47. HPLC trace for *ex situ* synthesised compound **R$_1$**, with a retention time of 323 seconds recorded.

Figure 3.48. HPLC trace for *ex situ* synthesised compound **R$_6$**, with a retention time of 391 seconds recorded.

Figure 3.49. HPLC trace for *in situ* reaction mixture containing **R$_1$** amine, **R$_6$** amine and ***II***. All components were dissolved in water at pH 8, with the HPLC analysis performed after 16 hours.

Figure 4.1. Example of the simplest possible manifestation of an autocatalytic reaction where A + B goes to C, with C then acting as a catalyst, resulting in an exponential increase in the concentration of C occurring as time progresses until the supply of A and B are exhausted.

Figure 4.2. Amino acids; phenylalanine, leucine, tyrosine and tryptophan were used in gel screening with the trialdehyde core unit ***II***. Amino acids highlighted in red to not produce a gel upon acidification, the unnatural amino acid 4-aminophenylalanine (***$_4$F***), highlighted in green, does form a gel upon acidification.

Figure 4.3. Diagrams showing all possible proposed reaction products for the reaction between ***II*** and ***$_4$F***. From top left and going clockwise reaction occurs at all three aromatic amines, two aromatic amines and one amino acid amine, one aromatic amine and two amino acid amines and all three amino acid amines.

Figure 4.4. IR spectra presented with wavelength (cm^{-1}) on the x-axis and percentage transmission on the y-axis. These spectra show L-phenylalanine (a), 4-aminobenzoic acid (b), 4-amino-L-phenylalanine (c), compound ***Z*** (d).

Figure 4.5. The ^{13}C NMR spectra obtained for ***$_4$F*** dissolved in D_2O at pD 9 (**a**) and for ***Z*** recorded under the same solvent conditions (**b**). Arrow highlights peak that has moved, with red lines added to guide the eye as to the size of the shift 144.4 to 141.9 ppm, and to demonstrate the lack of a shift in the other peaks. The peaks 59.8 ppm are used to exemplify this.

Figure 4.6. The *ex situ* reaction between three equivalents of ***$_4$F*** and one equivalent of ***II*** in ethanol. Reaction is performed at reflux for 16 hours, with the product being the tripodal LMWG ***Z***.

Figure 4.7. Results of the time sweep rheology experiment for the gel prepared using an *ex situ* synthesised sample of ***Z*** to produce a gel at 2 wt%. Storage modulus *G′*(●) (Pa) (y-axis) plotted (log scale) against time (s) (x-axis).

Figure 4.8. Results of the frequency sweep rheology experiment for the gel prepared using an *ex situ* synthesised sample of ***Z*** to produce a gel at 2 wt%. The storage modulus *G′*(Pa) (●) and the loss modulus *G″*(Pa) (○) are shown as a log scale (y-axis) against the frequency (Hz) (x-axis).

Figure 4.9. Results of the stress sweep rheology experiment for the gel prepared using an *ex situ* synthesised sample of ***Z*** to produce a gel at 2 wt%. The storage modulus *G′*(Pa) (●) and the loss modulus *G″*(Pa) (○) are shown as a log scale (y-axis) plotted against torque (μNm) (x-axis) shown in a log scale. A line between data points added to guide the eye.

Figure 4.10. Time sweep rheology experiment (left) and the derived Avrami plot (right) of the gel prepared using *ex situ* synthesized ***Z***. t_0 marks the point at which the onset of gelation begins and the region with which the Avrami constant is calculated.

Figure 4.11. Concentration study of the gel produced using *ex situ* synthesised ***Z*** used to determine the cellular solid model for the system presented in this chapter.

Figure 4.12. Results of the frequency sweep rheology experiment for the gel prepared using an *ex situ* synthesised sample of ***Z*** to produce a gel at 2 wt%, as well as a sample of the *in situ* prepared gel at 2 wt%. The storage modulus *G′*(Pa) for the *in situ* formed gel (●) and *ex situ* formed gel (■), as well as the loss modulus *G″*(Pa) for the *in situ* form gel (●) and *ex situ* formed gel (□), are shown as a log scale (Pa) (y-axis) against the frequency (Hz) (x-axis).

Figure 4.13. PXRD patterns obtained from dried samples of gels prepared using the *ex situ* method (left) and the *in situ* method (right).

Figure 4.14. Reaction scheme for the formation of ***Z*** for ***$_4$F*** and ***II*** with mono-, di- and tri- (enol and keto forms) reaction products shown as the proposed reaction pathway. Arrows indicate relative equilibriums, that arise because of the lack of stability of the imine species in water, between the species before the energetically irreversible enol to keto tautomerisation step.

Figure 4.15. HPLC trace for the *in situ* reaction to form ***Z***. Peak A (retention time 3 minutes and 20 seconds) is associated with ***II*** and peak B (retention time 5 minutes and 15 seconds) is associated with the reaction product ***Z***.

Figure 4.16. Concentration UV-vis absorption experiment for ***II*** using concentrations of: 4.0, 8.0, 12.0, 16.0, 20.0, 24.0, 28.0, 32.0, 36.0 and 40.0 mmol (left). Determination of molar absorptivity (ε) for ***II*** at 290 nm by plotting the absorption (AU) at 290 nm against each concentration. ε is defined as the slope of the straight line (67.9) (right).

Figure 4.17. Concentration UV-vis absorption experiment for ***Z*** using concentrations of: 4.0, 8.0, 12.0, 16.0, 20.0, 24.0, 28.0, 32.0, 36.0 and 40.0 mmol of an *ex situ* prepared sample of ***Z*** (left). Determination of molar absorptivity (ε) for ***Z*** at 290 nm by plotting the absorption (AU) at 290 nm against each concentration. ε is defined as the slope of the straight line (118) (right).

Figure 4.18. Frequency sweep experiments (G′ shown) for the gels resulting from the set using a 2 ml portion of a 25 ml stock solution with a potential maximum **Z** of 28.2 $mmoll^{-1}$.

figure 4.18. Graph showing the evolution of *G′* with time for gels set using portions of a stock *in situ* reaction mixture at times of 0.5, 1, 2, 3, 4, 8, 12, 24, 48, 72, 96 hours. Time on the x-axis is plotted using a log scale in order to highlight the sigmodal nature of the plot profile.

Figure 4.19. Graph showing the evolution of *G′* with time for gels set using portions of a stock *in situ* reaction mixture at times of 0.5, 1, 2, 3, 4, 8, 12, 24, 48, 72, 96 hours. Time on the x-axis is plotted using a log scale in order to highlight the sigmodal nature of the plot profile.

Figure 4.20. Concentration (in mM) of reaction product, ***Z***, monitored over time by rheology for the reaction **A** + $_4$**F** = ***Z***. calculated using the rheology data. Concentration (●) plotted against time (hours, log scale) with a line added between data points to guide the eye.

Figure 4.21. The rate of reaction of **A** + $_4$**F** = ***Z*** calculated using the previously determined concentration from the by rheology against time (hours, log scale) with a line added between data points to guide the eye.

Figure 4.22. Concentration (in mM) of reaction product, ***Z***, monitored over time by HPLC for the reaction **A** + $_4$**F** = ***Z***. calculated using the previously determined molar absorption coefficients against time (hours, log scale) with a line added between data points to guide the eye.

Figure 4.23. Measurements of the viscosity of various concentrations of solubilised samples of ***Z*** at pH 8.5 with increasing temperature: water (light blue ◆), 0.25 wt%, 3.59 mmol, below CGC (orange ▲), 0.5 wt%, 7.18 mmol at CGC (yellow ●), 1 wt% 14.36 mmol (grey ◆), 2 wt%, 28.72 mmol (dark blue ▲), 3 wt%, 43.08 mmol (green ●), 4 wt% 57.44 mmol (red ◆).

Figure 4.24. Pictorial representation of the dynamics that exist between the supramolecular polymer, the gel network and the free molecules. Protonation of the supramolecular polymers balances the charge resulting in a reduction in solubility and gelation.

Figure 4.25. Pictorial representation of the effects of mechanical agitation on the supramolecular fibres formed in aqueous conditions (20 ºC without mechanical agitation) by the anionic species $\mathbf{C}^{n-}$ and the subsequent increase in the number of catalytic sites.

Figure 4.26. Frequency sweep experiments (G′ shown) for the gels resulting from the set using a 2 ml portion of a 25 ml stock solution with a potential maximum **C** of 28.2 $mmoll^{-1}$ which was subjected to continuous mechanical agitation in the form of magnetic stirring at 1000 rpm.

Figure 4.27. Concentration (in mM) of reaction product ***Z*** formed under standard conditions with the addition of magnetic stirring at 1000 rpm, monitored by using frequency sweep rheological experiments and calculated using the cellular solid model. Concentration plotted against time (hours, log scale) with a line added between data points to guide the eye.

Figure 4.28. The rate of reaction for the formation of ***Z*** calculated using the previously determined concentration from the rheology (green ●), against time (hours, log scale), with a line added between data points to guide the eye.

Figure 4.29. Concentration (in mM) of reaction product Z formed under standard conditions with the addition of magnetic stirring at 1000 rpm,. monitored over time by ^{1}H NMR (yellow ▲) and HPLC (blue ■) against time (hours, log scale), with a line added between data points to guide the eye.

Figure 4.30. Concentration (in mM) of reaction product ***Z*** formed under standard conditions with the addition of magnetic stirring at 1000 rpm. Monitored over time by rheology (green ●), ^{1}H NMR (yellow ▲) and HPLC (blue ■) against time (hours, log scale) with a line added between data points to guide the eye.

Figure 4.31. The rate of reaction for the formation of $\boldsymbol{Z}^{-}$ calculated using the previously determined concentration from rheology (green ●), ^{1}H NMR (yellow ▲) and HPLC (blue ■) against time (hours, log scale), with a line added between data points to guide the eye.

F Figure 4.32. Total concentration of ***Z*** formed over time with different quantities of $\mathbf{C}^{\mathbf{n-}}$ added as a seed at time 0 h. $\mathbf{C}_{\text{catalyst}}$ = 0.5 mM (green ●), $\mathbf{C}_{\text{catalyst}}$ = 1.0 mM (red ■), $\mathbf{C}_{\text{catalyst}}$ = 1.5 mM (black ▲), $\mathbf{C}_{\text{catalyst}}$ = 2.0 mM (yellow ◆) and $\mathbf{C}_{\text{catalyst}}$ = 2.5 mM (blue ●).

Figure 4.33. Rate (d[***Z***]/dt) for the formation of ***Z*** with varying concentration of $\boldsymbol{Z}_{\text{catalyst}}$ added to the reaction mixture at time = 0 h. $\boldsymbol{Z}_{\text{catalyst}}$ = 0.5 mM (green ●), $\boldsymbol{Z}_{\text{catalyst}}$ = 1.0 mM (red ■), $\boldsymbol{Z}_{\text{catalyst}}$ = 1.5 mM (black ▲), $\boldsymbol{Z}_{\text{catalyst}}$ = 2.0 mM (yellow ◆) and $\mathbf{Z}_{\text{catalyst}}$ = 2.5 mM (blue ●).

Figure 4.34. Determination of the reaction order for $\mathbf{A + B \rightarrow C^{n-}}$ where $y = mx^{p}$ with *p* being equal to the order of the reaction (concentrations of seed $\mathbf{C}^{\mathbf{n-}}$ marked on graph).

Table 1.1. Summary of different chemical and supramolecular interactions with the an approximate value of the energy required to be break them.

Table 2.1 The determined molar absorption for $\boldsymbol{B_e}$ at 300 nm (ε_{B300}), 415 nm (ε_{B415}) and $\boldsymbol{C_e}$ at 300 nm (ε_{C300}) and 415 nm (ε_{C415}).

Table 3.1 Apparent pK_a determined for each of the LMWG presented in this chapter ($\mathbf{R_1}$ – $\mathbf{R_9}$).

Table 3.2. Summary of rheological properties for gels R_1 to R_9.

Table 3.3. Data used to plot Figure 3.27, calculated *c*logP values for molecules $\mathbf{R_1}$ – $\mathbf{R_8}$ with the *G´* for gels corresponding to each of these molecules. *G´* value corresponds that recorded during the frequency sweep experiments at 50 Hz for 2 wt% gels.

Table 3.4. Data on 2θ and corresponding *d*-spacing obtained from the PXRD patterns for the mixed $\mathbf{R_1}$/$\mathbf{R_6}$ systems presents in Figures 3.34 and 3.35.

Chapter 1 - Introduction

1.1 Hydrogels

Hydrogels, as the name implies, are a class of gelatinous material that consist primarily of water.[1] Despite this predominantly liquid composition, hydrogels are viscoelastic materials that behave more like a solid than a liquid. This solid-like behaviour arises from the presence of a solid phase fibrous network, composed of the gelator molecules, that ultimately results in the immobilisation of the water through surface tension and capillary forces. Interest in these materials has increased dramatically in recent years, largely due to the plethora of applications they can be associated with. Hydrogels have shown particular promise with a range of biological applications, such as drug delivery and cell growth, due the inherent biocompatibility of many hydrogel systems.[2–4] As previously mentioned, a hydrogel is dependent on the existence of a fibrous network, this matrix can be formed from a diverse set of materials. Broadly speaking there are two main classes of hydrogel, polymeric hydrogels and small molecule hydrogels, each defining a different means through which the fibrous network is assembled. A polymeric hydrogel describes a gel where the fibrous network consists of covalently linked polymers that are either chemically or physically cross-linked.[5] These polymers can be naturally occurring biopolymers, such as agarose or synthetic polymers, examples of which include poly(2-hydroxyethyl methacrylate).[6]

Small molecule gels are gels where the structure of the fibrous network is completely dependent on physical i.e. supramolecular interactions and not chemical bonds. These supramolecular interactions allow relatively low molecular weight molecules to self-assembly under the correct conditions to give supramolecular hydrogels. Such molecules are known as low molecular weight gelators (LMWGs) and are the subject of the work discussed in this thesis.

Despite the generally higher mechanical strength of polymeric hydrogels when compared to LMWGs, often in the MPa range,[7] they have several disadvantages, particularly when considering biological applications for the gels. The formation of a polymeric hydrogel involves a crosslinking/polymerisation process that can, for example, be initiated with UV-radiation,[8] this often results in the presence of radical material which can be damaging to cells. The use biopolymers circumvent the issue of radical material. However, the advantages of LMWGs, such as their ability to react to a range of external stimuli, have resulted in them being considered a promising and versatile class of

materials. This is particularly true for the afore-mentioned biological applications. Including, but not limited to, cell growth and drug delivery.[9] The diversity in the chemical structure of LMWGs is as remarkable as the range of solvents that can be gelled, when the correct LMWG is employed.[10] LMWGs are small molecules with a molecular weight typically < 1000 Da that self-assemble in the correct solvent, under the correct conditions, to form a gel. This self-assembly can be driven by the full spectra of supramolecular interactions, which include hydrogen bonding, π-π stacking and electrostatic interactions. These interactions allow the individual gelator molecules to assemble into high aspect ratio fibres which bundle into fibrals that entangle and immobilise the liquid component of the gel (Figure 1.1).

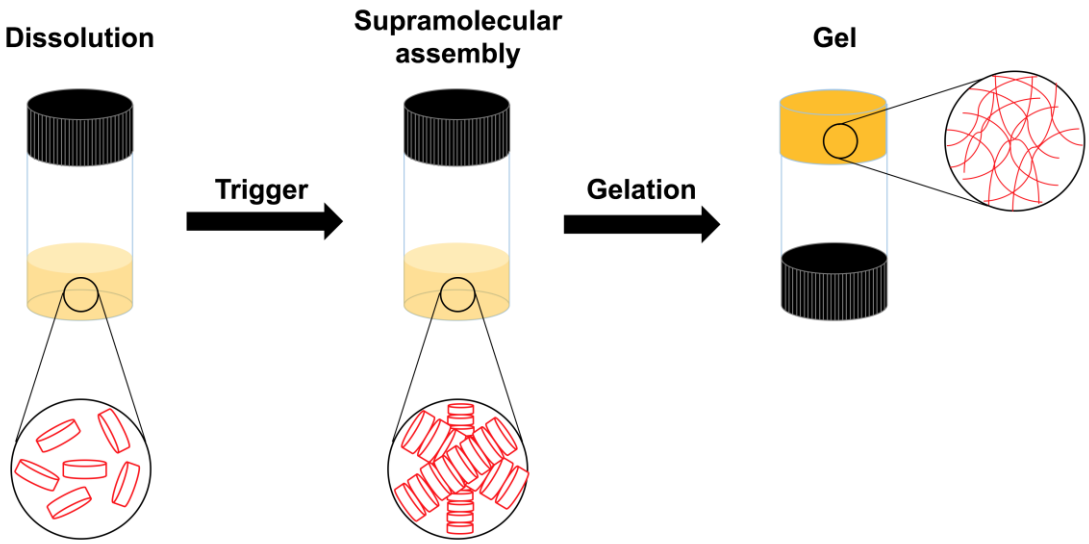

Figure 2.1 Pictorial representation of the gelation process involving a LMWG. Vial on left shows the LMWG dissolved in water. Central vial shows the supramolecular self-assembly process the occurs after an appropriate trigger is applied driven by molecular recognition. Inverted vial on right shows a gel formed through the entangled fibres consisting of LMWGs into the gel matrix that immobilises the water.

The gels formed with LMWGs are dependent on these physical supramolecular interactions, as opposed to the chemical cross-linking that a large number of polymeric hydrogels are dependent on. This gives rise to both the advantages and disadvantages when comparing and contrast small molecule and polymeric hydrogelators. As alluded to previously, polymeric hydrogels are often highly resilient to externally applied mechanical stress. This strength is derived from the chemical bonds that often cross-link the polymer chains to form the gel matrix, there are, however, examples of polymer gels where the crosslinking interactions are purely physical in nature. The strength of the

interactions that drive supramolecular small molecule hydrogel formation are considerably weaker than the covalent bonds of chemically cross-linked polymeric hydrogels, they are, however, reversible meaning supramolecular hydrogels are dynamic in nature. The fact the transition from gel to sol can be initiated easily means that LMWGs are highly promising materials for a range of applications. Table 1 provides a summary of the strength of various supramolecular interactions, as well as the strength of a carbon to carbon single covalent bond for comparison.

Table 1.1. Summary of different chemical and supramolecular interactions with the an approximate value of the energy required to be break them.

Type of interaction	Strength of interaction (kcal/mol)
Covalent bond (C-C)	86
Hydrogen bonding	2 - 30
Electrostatic interaction	1 - 20
π-π interaction	0 - 10
van der Waals forces	0.1 - 1

Although not prominent in this thesis, it is possible to gel solvents other than water using the same principles. Should an organic solvent be used as the liquid component of the gel, then the gel is known as an organogel. There are numerous examples of organogels in the literature, with which many of the same design principles one would consider for hydrogels still being apparent, as non-covalent interactions inducing the assembly of a three-dimensional network are still the driving force behind gelation.

This chapter will discuss a number of the elements one must consider when studying a supramolecular hydrogel system. The key analytical techniques used in developing an understanding of supramolecular gels, along with the interpretation of the results they may give will be examined. There are a number of different means by which gelation of a LMWG can be triggered. While not providing a completely comprehensive, this chapter will give an insight into a number of key gelation trigger methods and the mechanisms by which they operate. Although no hard and fast rules exist as to why some molecules form gels while others do not, the general design principles behind what makes a LMWG will be considered. This will also involve discussions on how groups that trigger gelation can be incorporated into the gelator molecule. Having summarised a number of the key concepts of supramolecular hydrogel science this work will then describe what is meant by *in situ* and *ex situ* gelator synthesis. What will then be looked

at are the chemical concepts of systems chemistry and autocatalysis, which are key areas of interest in the subsequent chapters of this thesis.

1.2 LMWG characterisation

The characterisation of LMWGs relies on two key components. Firstly, chemical characterisation of the LMWG itself, and secondly, the characterisation of the material properties of any resulting gel. The need for characterisation from the molecular to the macroscopic scale requires the use of a number of analytical techniques. These techniques focus on gaining an insist into the assembly process and final structure of the gel network, as well as the gels mechanical properties in terms of its response to an externally applied mechanical stress.[11,12]

1.2.1 Rheology

Rheology describes the study of the flow of matter. While this is classically thought of as a characterisation method for liquids, in terms of their viscosity, techniques exist that allow the rheological characterisation of supramolecular gelatinous materials. While viscosity measurements rely on the application of a unidirectional strain to the sample, rheological studies of gelatinous materials employ an oscillatory applied strain.[13] This way the gel can be deformed without shearing it. Supramolecular gels are what are known as viscoelastic materials, i.e. they possess both viscous and elastic properties. It is the elastic characteristics of the gel that allow them to behave as solids, and despite this behaviour, they are not ideal solids meaning they do not exhibit a stress that is proportional to the applied strain. By the same token, they are not ideal liquids as gels do not display a stress that is proportional to the applied rate of strain.

The oscillatory experiments used to characterise viscoelastic materials involves the application of a sinusoidal strain, defined as γ. This strain is applied with an angular frequency of ω and invokes a response from the gel with a sinusoidal stress, σ. These quantities are related by equation (1), with which the mechanical response of a viscoelastic material can be determined.

$$\sigma = \gamma_0(G'(\omega)\sin(\omega t) + G''(\omega)\cos(\omega t)) \qquad (1)$$

Equation (1) features the terms G' and G''. These denote the shear storage modulus (G') and the shear loss modulus (G''). When considering viscoelastic materials, G' can be thought of as being representative of solid-like characteristics of the material, as this is the in-phase, elastic response to the oscillatory strain, i.e. the elastic component. G'' conversely describes the liquid-like characteristics of the material represented by the out-of-phase component, relative to the applied strain, namely the viscous component. Figure 1.2 shows the results that can expected for an oscillatory strain experiment on a typical viscoelastic material. The applied strain and resultant stress are slightly out-of-phase, highlighting the imperfect response that can be expected for a typical real world material. This variable phase angle (δ) refers to how in or out of phase the applied strain and the measured stress are. with a true elastic solid having $\delta = 0$ and a viscous fluid having $\delta = \pi/2$. It is safe to say a supramolecular gel and other viscoelastic materials show $0 < \delta < \pi/2$. This arises because of the contributions from both the in-phase elastic behaviour of the material and the out of phase viscous liquid behaviour of the viscoelastic material. Once a set data, such as that depicted in Figure 1.2, has been collected the widely reported G' and G'' values can be calculated. Use of equations (2) and (3) to calculate G' and G'' relies on the experimentally determined values for γ (sinusoidal strain) and σ (sinusoidal stress), as well as that of δ.

$$G' = \sigma/\gamma \cos \delta \qquad (2)$$

$$G'' = \sigma/\gamma \sin \delta \qquad (3)$$

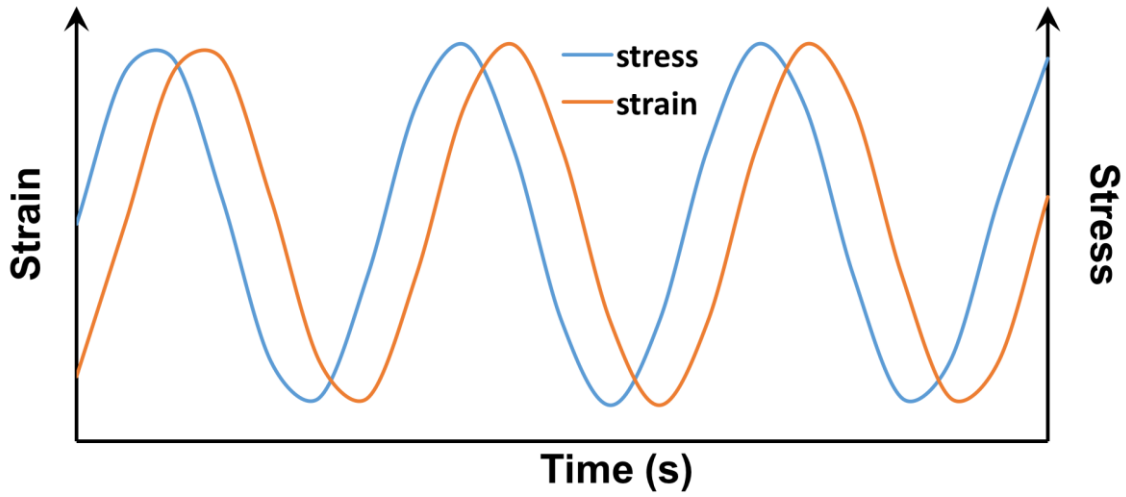

Figure 1.2. Arbitrary representation of the applied oscillatory strain shown as the orange line (—) and the typical resulting sinusoidal stress response of an imperfect viscoelastic material, shown as the blue line (—).

1.2.2 NMR spectroscopy

The vast majority of the literature reported NMR experiments pertain to the characterisation of the LMWG molecules themselves and not the supramolecular assembly. This, however, is changing, particularly because of the advancements in various solid-state NMR experiments and the increasing understanding and refinement of existing techniques. This is typified in supramolecular gel research by the ability to study supramolecular interactions, such as hydrogen bonding, using routine concentration and temperature dependent ^{1}H NMR experiments.[14] The dynamic nature of supramolecular gels with respect to their constituent LMWG components moving in and out of the solutions makes NMR an ideal tool for their study and characterisation. This can incorporate concepts such as variable temperature NMR.[15]

As alluded to previously, the probing of the ^{1}H nuclei by NMR is an incredibly useful technique, not just for molecular characterisation, but also for characterising the supramolecular assembly. This can be done through examination of the chemical shifts of ^{1}H nuclei that are involved with the non-covalent interactions that drive the self-assembly process and monitoring how they change as said process proceeds. This concept was demonstrated by Ma *et. al.* with a LMWG consisting of an anthraquinone unit attached to a long alkyl tail by a bridging hydrazide group.[16] They presented two separate studies, one involving a concentration-dependent ^{1}H NMR experiment and a second involving a temperature-dependent ^{1}H NMR experiment. In the case of the concentration study, the ^{1}H signals associated with the hydrazide N-H groups demonstrated a gradual shift downfield as the concentration of the LMWG was increased. This was determined to be due to the increasing number of intermolecular hydrogen bonds that existed between the hydrazide groups as the concentration of the LMWG is increased from 0.5 mM to 2.5 mM. The temperature-dependent study involved the analysis of ^{1}H signal shifts associated with aromatic type ^{1}H at a fixed concentration as the temperature of the sample was increased. This increase in experiment temperature results in an upfield shifting of the aromatic signals. This is due to a reduction in the number of possible π-π interactions that arise from the assembly process associated with intermolecular aggregation of the anthraquinone section of the molecules.

Recent research has developed solution state NMR tools to probe assembled, NMR invisible gelators. It has been shown that arrangement of the supramolecular gelators and resulting assembly process could be tracked by examining the residual

quadrupolar couplings of a number of molecular probes. The molecular probes in question are $^{14}NH_4^+$ and isopropanol-d_8 (IPA-d_8), this was done in conjunction with measuring the NMR relaxation rates of $^{23}Na^+$, all of which were dopants in the aqueous component of the gel.[17] The formation of fibrillar aggregates with certain LMWG has been shown to be influenced by NMR-strength magnetic fields. This induces a high degree of anisotropy in the arrangement of the constituent fibres.[18] It is this anisotropy that leads to the observed residual quadrupolar coupling in the ^{14}N and ^{2}H NMR spectra. When examining the gelation, an initial increase in the residual quadrupolar couplings for $^{14}NH_4^+$ can be observed which corresponds to the beginning of the assembly process, before the affect is observably reduced in the latter stages of gelation. This corresponds to an increase in the residual quadrupolar coupling for the IPA-d_8, with both NMR techniques showing a plateauing in the size of the coupling as the final steady state of the gel assembly is reached. These residual quadrupolar coupling variations also coincides with a decrease in the T_1 and T_2 relaxation times for the ^{23}Na nuclei. It is these NMR probes that allowed the tracking of a dipeptide LMWG's gelation process from the individual, free molecules as they aggregate into large fibrillar structures that possess a significant negative charge. This charge is then gradually lost which results in an increasing level of interactions between the various fibres, which in turns leads to the formation of a macroscopic gel network. This example of solution state NMR elegantly showcases how such a non-invasive technique can be used to gain information on the assembly and structure of a solid-like material. The utilisation of high resolution magic angle spinning (HRMAS) NMR for the characterisation of supramolecular gels is becoming increasingly prominent thanks to the publications of high profile work.[19]

The very first example of HRMAS ^{1}H NMR as a technique to characterise supramolecular gels was presented by Escuder, Miravet and co-workers. In their study, they utilised some of their previously published gelators, including amidocarbamate[20] and tetrapeptide[21] based gelators, which could either gel toluene-d_8 or deuterated acetonitrile (CD_3CN). This study was instrumental in proposing HRMAS ^{1}H NMR as a powerful technique that could be used to develop an understanding of the dynamic structural properties that are at play within the three-dimensional network of a supramolecular gel. Through their deployment of so-called diffusion filtered HRMAS NMR[22], they were able to remove the signals that arose due to the gelator molecules not included in the solid phase. Molecules that are free in the solvent phase, i.e. are translationally free, and molecules bound to the solid network but 'dipped' in the liquid phase, which gives them a degree of conformational freedom, could be segregated in terms of their ^{1}H NMR signal.

This was done through the use of a diffusion filter in pulsed field gradient spin echoes experiments. Before application of the diffusion filter, it was reported that the HRMAS ^{1}H NMR spectra for a proline functionalised gelators[23] was similar to that of obtained for a solution of the compound. Upon application of the filter there was a marked decrease in the intensity of the signals as the translational free molecules had been removed, leaving only the signal intensity that arises from molecules in the solid-state (see Figure 1.3). This work laid the foundations for many of the future studies that used HRMAS NMR as a characterisation method for the native gelatinous material. When using HRMAS NMR to characterise a supramolecular gel a number of practical considerations must be made. The technique may not be suitable for gels at the weaker end of the mechanical strength spectrum as the spinning of the sample holder at the several kHz rotation rate may be enough to shear weak gels, resulting in the collection of erroneous data.

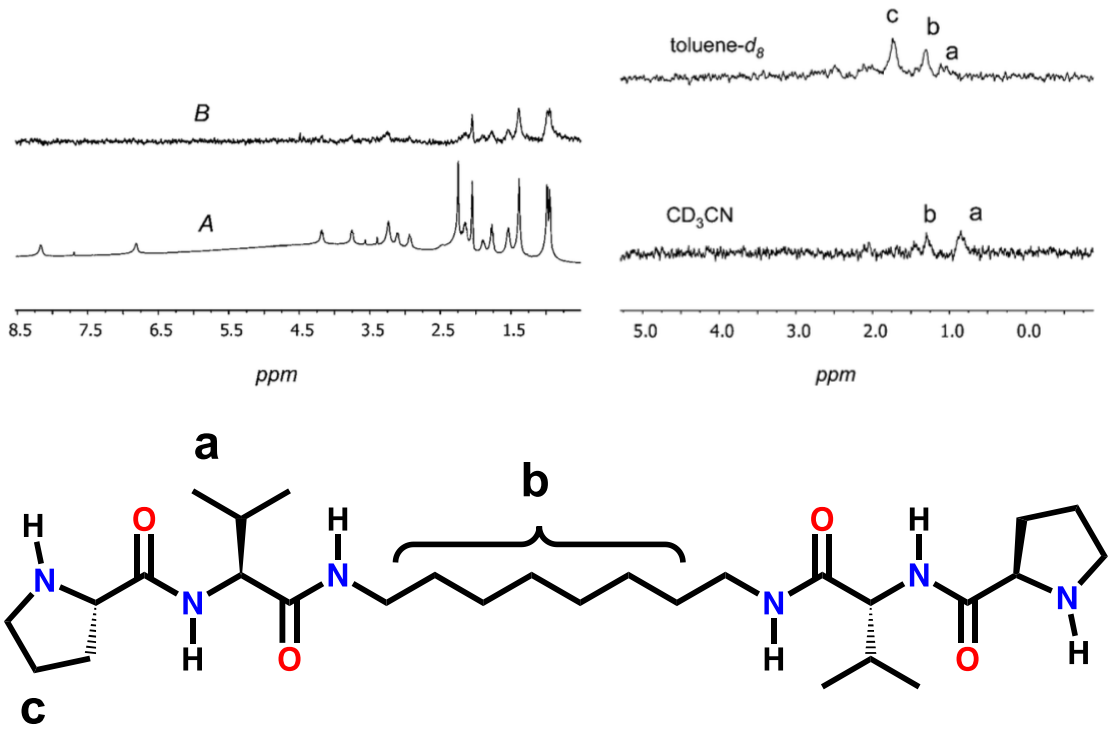

Figure 1.3. Results of the application of a diffusion filter to a HRMAS ^{1}H NMR experiment (reproduced with permission from ref.[19]). Spectra on the left shows the results of the diffusion filter application with **A** showing no diffusion filter and **B** showing a 50% diffusion filter, spectra recorded on the molecules at the bottom of the Figure. Spectra on the right shows HRMAS ^{1}H NMR results for molecule with 70% diffusion filter. Labelling of molecular drawing (labels a, b and c) match peaks with corresponding labels in the NMR spectra on right hand side of the figure.

1.2.3 Morphology determination

The fibrous morphology of supramolecular gels is a physical property that can give interesting qualitative insights into other physical properties, such as mechanical strength and the chirality of the gel fibres.[24] There are a number of different microscopic techniques that can be used to examine the morphology of supramolecular gels, often down to a resolution of several nanometers. What will be discussed in the following section is a number of the most popular microscopic techniques paying particular attention to their strengths and weaknesses when compared to each other.

1.2.3.1 Scanning electron microscopy

Scanning electron microscopy (SEM) is an imaging technique that relies on scanning a sample with a focused beam of electrons, these electrons then interact with the electrons of the sample. These interactions produce detectable signals, which contain information on the topography and elemental composition of the samples surface. By combining information on the incident electron beams position and the signal produced by the scattered electrons, it is possible to produce an image of the samples surface. When using SEM microscopy to image a supramolecular gel sample there are a number of positive attributes that are related to the technique. It is a cheap method of imaging, relative to other techniques, and as a result is often readily available at research institutions. The fact the incident electron beam has an incredibly small cross section results in a distinctive and useful characteristic for SEM images, that is a depth of field.[25] This results in the images often having a three-dimensional effect that is beneficial when considering materials such a supramolecular gels which rely on the formation of a three-dimensional network structure. Scanning electron microscopes also have a wide range of magnification meaning a large portion of the sample can be imaged at low magnification or a small area at high resolution, high magnification. While there are these positives for using a SEM for morphology studies, there are also several drawbacks that must be considered. Preparation of an SEM sample involves ensuring the sample is as dry as possible, when done using high vacuum or freeze dry techniques.[26] When dealing with samples of gel, which by definition are majority liquid, careful consideration has to be given to what the SEM image is actually showing. By drying a typical gel to completion, a xerogel is produced, where the inter-fibre space is occupied by air or indeed empty when under the vacuum required for SEM imaging. This means the drying process can

result in a collapsing of the three-dimensional gel network or phase change(s) in the gel fibres, which ultimately means the images obtained are not a true representation of the gel morphology. There is also the problem of potential phase changing within the gel sample upon drying. There is the potential to prepare SEM samples using the supercritical drying technique presented by Kistler, as a means of maintaining the original structure of the gel.[27] With that said, they do often give a good indication of the fibrous nature of the gel sample, which is often all that is desired. Another aspect of SEM sample preparation is the optional coating of the sample with a very thin layer of a conductive material,[28] usually gold or platinum. This is done to reduce the charging of the sample with the electron beam. Charging causes bright patches on the sample area being imaged, resulting in the image looking washed out. By providing a conductive pathway to earth for the incident electrons, charging is prevented. While coating will generally result in a better quality of image being obtained, care must be taken with regards to the thickness of the coating. If an excessively thick conductive coating is applied, then some of the finer structural details of the gel fibres may be lost. This loss of fine detail could prove potentially problematic when looking for features such as right or left handed chirally induced helix formation.[29] Although the native, undried and organo- or hydrogel state can be imaged using cryogenic scanning electron microscopy (cryo-SEM) or environmental SEM on wet samples, the necessary equipment is not nearly as common as a standard SEM.

1.2.3.2 Transmission electron microscopy

The use of transmission electron microscopy (TEM) has proven to be popular for the imaging of supramolecular gels. This is in part due to the techniques potential to provide remarkably high resolution, down to a subnanometer scale.[30] It is often used in conjunction with other imaging techniques, such as SEM, in order to obtain a range of images of the gels morphology.[31] It is similar to SEM in its requirement for extensive sample preparation in terms of drying and coating, usually with a carbon grid. The sample is also often negatively stained, in order to improve the contrast between background and sample.[32]

1.2.3.3 Confocal microscopy

The use of confocal microscopy as a technique to study the morphology of supramolecular gels[33,34] and supramolecular polymers[35] is proving increasingly popular.

There are a number of reasons that it appeals to those wishing to image materials with fine structure. These include its remarkable high resolution (sub-diffraction limit) and the fact that drying or surface coating of the sample is not required. Confocal microscopy involves the incorporation of a fluorescent dye into the supramolecular structure. Light emission from this dye is stimulated through the application of a laser light to the sample. The ability to study the growth of supramolecular fibres and their crosslinking to form a gel showcases confocal microscopy as a technique to image nanoscale fibre morphology. The ability to better understand these assembly principles may give rise to more functional supramolecular polymers.[36]

There are many different dyes that can be used for confocal microscopy, each requiring a specific wavelength of light to cause their fluorescence. This offers the means to investigate systems with two different assembling species functionalised with different dyes and see how they interact with one another. Figure 1.4 highlights this multiple dye approach to image different supramolecular fibre networks demonstrated by Onogi *et al.*[37]

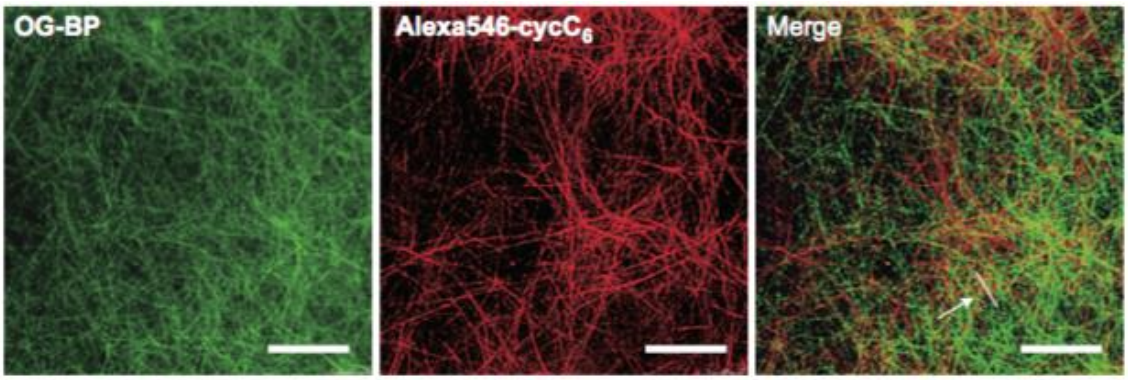

Figure 1.4. Confocal images showing two different supramolecular fibre structures consisting of two different monomer units each functionalised with a different dye. The fibre structures that arise from each of the monomers are shown left and centre, while the image on right shows the complete supramolecular structure (scale bars 10 μm). Arrow on right hand side image with white line used to highlight the orientation of the fibres. (Figure reproduced with permission from ref. 37).

1.3 Gelation triggers and effects on supramolecular structure

In the majority of cases, immobilisation of the liquid medium by the assembly of the LMWG is the product of a nucleation event that results in the growth of a fibrous network.[38] The nucleation event must be triggered in some way, causing the gelator

molecules to transform from a soluble entity into its insoluble form that makes up the solid, fibrous phase of the gel. There are numerous ways of triggering gelation, with each LMWG having one or more trigger methods that can be associated with it. The type of trigger and the way it is applied can have a dramatic effect on the physical properties of the gel formed.[39–42] Generally, the trigger and the way it is applied, is optimised in order to give the most homogenous network structure. This homogeneity of network structure results in gels that are more mechanically resilient and have more predictable optical and structural properties, over those that have larger regions of imperfect gelation. A number of methods of triggering the assembly of LMWGs and resultant gelation will now be described. The use of temperature, solvent, enzyme, pH and salt trigger method will be discussed in relation to examples of gelation systems that utilise them.

1.3.1 Temperature induced gelation

The balance a LMWG must strike between being soluble and insoluble may give rise to the possibility of inducing gelation through a heat-cool cycle. The fact many molecules may act as LMWG is often due the hydrophobic nature of such molecules. This results in them being soluble in an aqueous environment either in very low concentrations or at elevated temperatures. If it is possible to dissolve a concentration of gelator in water greater or equal to the critical gelation concentration (CGC) by heating the solution, then as its solubility decreases, once the source of heat has been remove, the formation of a three-dimensional network driven by non-covalent interactions between the gelator molecules will be realised. Gels formed using a heat-cool cycle will feature a gel transition temperature or T_{gel}.[43] The T_{gel} value for a gel is most accurately determined through rheological measurements. This is because through measuring the rheological properties of the gel sample, in conjunction with a temperature sweep, the temperature at which the interactions between and within the fibres break down can be determined. The temperature at which flow within the sample begins is the T_{gel} value.[10] There are many examples of the implementation of a heat-cool cycle to induce gelation with LMWGs.[44] The method is also used widely in the setting of gels formed with covalent polymers. The same principle of raising then lowering the apparent solubility of the LMWG can be applied to supramolecular organogel systems. An example is the study by Weiss *et. al.* on the gelator 5R-cholestan-3-yl *N*-(2-naphthyl)-carbamate (CNC)[45], one of the famed aromatic linker steroid (ALS) class of organogelators.[46,47] This detailed study exams the kinetics of the assembly of the gel network constructed from CNC in *n*-alkane solvents,

namely *n*-octane and *n*-dodecane. The temporal stability of the resulting gels was dependant on the concentration of the gelator, but more important for stability is the cooling protocol used to form the gel. Gels that where formed by incubation at the lower temperatures (0.0 and 15.6 ^{o}C) (after dissolution of the CNC by heating) consisted of small spherulitic colloidal aggregates. Incubation at higher temperatures (but below the T_{gel}) produces gels with a much more fibrous morphology, giving rise to a cellular structure. It is this fibrous morphology that gives the qualitatively higher mechanical strength to the gels formed through incubation temperatures closer to that of the T_{gel}. This higher incubation temperature results in a slower nucleation/growth period which, in turn, allows the large fibrous morphology to form, with its superior load bearing capabilities. Another example of temperature trigger gelation has been presented by Das and co-workers in the form of protected dipeptide hydrogelators with cationic C-termini.[48] It is also possible to use small peptides as LMWG with thermal gelation triggers. The peptide MAX3 was shown to be an effective gelator by the group of Haines, it could immobilise water through a completely reversible heat-cool cycle, with the gel formed by subsequent cycles after the initial formation matching the mechanical strength of the initially gel formed.[49] There are further literature examples where heating the LMWG in water is not enough to induce dissolution. In such cases, the addition of a small quantity of a water miscible organic solvent in which the gelator is soluble often aids solubilisation enough to allow the heat/cool cycle to be an effective gelation trigger mechanism.[50]

1.3.2 Solvent switch gelation

The hydrophobic nature of supramolecular hydrogelators is something that can be exploited in order to induce their assembly. Many hydrogelators, while completely insoluble in water, will readily dissolve in an organic solvent that is miscible in water, such as dimethylformamide (DMF) and dimethyl sulfoxide (DMSO). This organic solvent solubility offers a way of overcoming the inherent hydrophobicity of the LMWG. By creating a saturated solution of gelator in the water miscibility organic solvent and then diluting the solution with water, the hydrophobic interactions start to dominate and a hydrogel can be produced through molecular assembly.[51] Solvent switching has proven itself to be a popular method for inducing gelation. Not only is it an easy method to employ but it also is associated with speed. It, normally, very rapidly causes gel formation relative to other triggered methods discussed in this section.[52,53] While changing the nature of the solution in a physical way offers an effective means to induce gelation, it is

not the only option. Using a LMWG which must undergo a chemical change in order to be an effective gelator proves another, chemical rather than physical, class of trigger methods.

1.3.3 Enzyme triggered gelation

Another method of triggering gelation involves the incorporation of an enzymatically cleavable group into the potential LMWG. The reason for the addition of an enzymatically cleavable group is to solubilise the molecule before assembly occurs.[54] Owing to the biocompatibility of many amino acid based LMWGs, research is being pursued into using such hydrogel systems in biological based application.[55,56] One issue that frequently needs to be overcome when considering a particular LMWG for biological applications is the method used to trigger self-assembly. In order for enzyme triggered gelation to be viable for biological applications the self-assembly must be triggered under physiological conditions. One proposed trigger method that by definition would be possible under physiological conditions would be to adopt an enzyme triggered approach to the self-assembly process. The enzyme would act as catalyst in the transformation of a soluble species to an insoluble, self-assembling LMWG through the enzymatic cleavage of a particular solubilising group. Another possible method would be to use the catalytic enzyme to aid in the synthesis of a self-assembling hydrogelator molecule from two or more soluble components.

The groups Xu and Uljin have elegantly demonstrated both approaches to enzymatically triggered gelation. One of Xu's systems starts as an Fmoc (fluorenylmethyloxycarbonyl) protected tyrosine phosphate, a species that is soluble in an aqueous buffer solution.[57] As can be seen in Figure 1.5, the addition of the enzyme alkaline phosphatase catalyses the dephosphorylation of the species resulting in the production of the insoluble molecule Fmoc-tyrosine hydrogelator. The loss of phosphate group results in an increase of the overall hydrophobicity of the molecule, an effect that drives the self-assembly process.

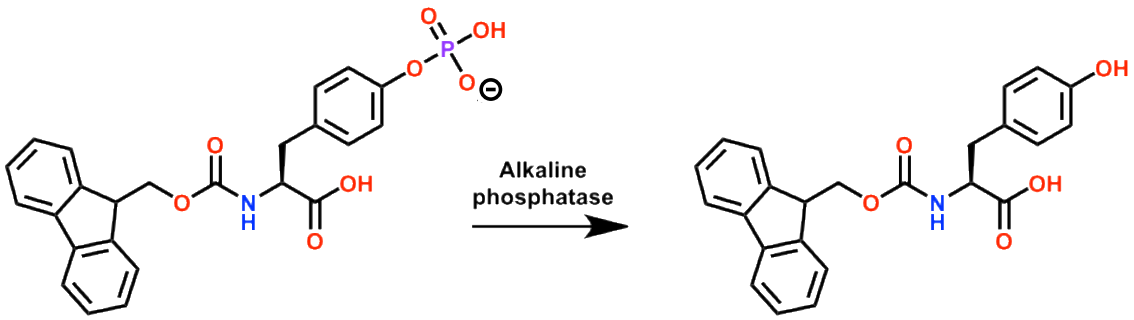

Figure 1.5. Reaction scheme highlighting the enzymatic cleavage of a phosphate group for an Fmoc protected tyrosine molecule using alkaline phosphatase. The phosphate group solubilises the molecule its removal increases the molecules overall hydrophobicity inducing gelation.

The approach of the Ulijn group involves the use of a condensation process to enzymatically produce short peptide hydrogelators.[58,59] By using an protease, or the endoprotease enzyme thermolysin, enzymes that normal hydrolyses peptide bonds, to perform the resverse reaction (reverse hydrolysis, peptide synthesis),[60] it was possible to synthesis peptide hydrogelators that self-assembly to form macroscopic structures from water soluble components. This reaction system has the advantage of the only by-product being one equivalent of water per peptide bond. The assembly process is essential for the reverse hydrolysis reaction to be favoured over the hydrolysis of the peptide bonds. This is due to the fact that the amide hydrolysis process is very close to equilibrium when occurring in dilute, aqueous conditions.[61] This equilibrium can be shifted towards the formation of amide bonds by stabilising the amide component of the reaction through self-assembly into a hierarchal structure, providing $\Delta G_{self\text{-}assembly} - \Delta G_{amide\ hydrolysis} < 0$.

The use of enzymatically triggered gelation for biological applications has been showcased by Yang and Xu.[62] By using their tyrosine phosphate gelation system, discussed previously, it is possible to screen for enzyme inhibitors. Should the enzyme inhibitor be effective at blocking the active site of the alkaline phosphatase enzyme, then the dephosphorylation reaction would not occur resulting in no gel formation. This concept allows the visual assay produced to show which inhibitors were effective without the need to deploy more complicated spectroscopic techniques. By their very nature enzymes are very specific in their behaviour. Their ability to trigger gelation is dependent on the ability of a molecule to be synthesised that utilises an enzymatically cleavable group to inhibit gelation. Such synthetic targets may not always be possible or, at least, not economical to produce. With this in mind, pH triggered gelation, an arguably similar and more versatile gelation method, will now be discussed.

1.3.4 pH triggered gelation

The utilisation of a change in pH to induce formation of a supramolecular gel from the sol state has become increasingly prevalent in the field. The functional groups within many LMWGs induce a sensitivity towards pH. This is true with many protected amino acid and peptide based hydrogel systems[63] with which most of the investigations into pH triggered gelation have been conducted. Protection at the N-terminus of an amino acid, or coupling via the N-terminus to another amino acid to construct di- or higher order peptides, leaves the C-terminus carboxyl group free. This carboxylic acid group will be deprotonated at pH's above its pK_a resulting the molecule bearing a negative charge. This charge results in solubilisation of the molecule in water. Lowering the pH to a level below the pK_a protonates the carboxylate group removing the charge, this now neutral molecule can then go on to assembly and ultimately form the gel network. However, it is not uncommon for there to be a degree of assembly at high pH resulting in an increase of the apparent viscosity of the solution when compared to that of water at the same pH. This has been hypothesised to be due the formation of tubular micelles or supramolecular polymers.[64,65]

It is not uncommon to see the addition of mineral acids, usually hydrochloric acid (HCl), being employed to lower the pH. Such a method was employed by Jayawarna *et al.* with an Fmoc protected dipeptide hydrogelator.[66] In order to induce gelation, their gelator was dissolved at elevated pH (8) before concentrated HCl was added drop wise until a clear gel had formed. This system will be discussed in more detail in subsequent sections of this chapter. There are further examples of pH sensitive dipeptide hydrogel systems, the work of Xu and co-workers demonstrates such systems with pH triggers synonymous with the previously discussed system.[67] What is noteworthy about this Xu example is how the gel responds to the addition of a biological ligand in the form of the antibiotic, vancomycin: Van. Addition of Van to a number of the presented dipeptide hydrogels can trigger a gel-sol should the LMWG be able to bind to the Van molecules through specific biological ligand – receptor interactions. This demonstrates a method where by the sol-gel transition can be induced with a pH trigger and a subsequent, irreversible gel-sol transition can be induced through the addition of a competitor ligand.

One of the most important developments in pH triggered gelation can be attributed to Adams and coworkers. This group developed a method for slowly lowering the pH of a sol through the use of the sugar derivative glucono-δ-lactone (GdL),[68] When in an

aqueous environment, GdL hydrolyses to produce gluconic acid (Figure 1.6), importantly this hydrolysis occurs at a rate much slower than that of the rate of dissolution of GdL. This results in a homogenous lowering of the pH throughout the solution, which in turn results in the formation of a gel with a homogenous structure. The importance of the implementation of GdL to set supramolecular gels cannot be overstated. It ensures a high degree of consistency and reproducibility of gelation. As a result, this method of inducing gelation has been employed by a large number of groups on a wide variety of gelator systems. More recently, the Adams group has shown the hydrolysis of a number of anhydrides to their corresponding acids as an effective means of lowering the pH for self-assembly and gelation.[69] The different anhydrides used in the study and their corresponding rates of dissolution and hydrolysis, while not affecting the primary assembly process, did have an effect on the mechanical strength of the resulting gel. This provides another handle with which to control the material properties of supramolecular gelatinous materials. Changing the pH alters the charge carried by the gelator molecule, generally creating a charge neutral species. Other charge balancing triggers, such as the addition of salt are also well documented.

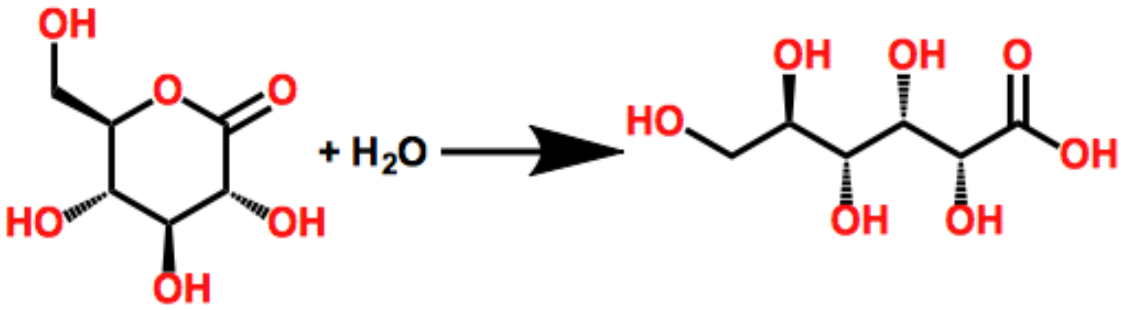

Figure 1.6. Reaction scheme for the hydrolysis of glucono-delta-lactone to gluconic acid. The presence of gluconic acid in an aqueous environment in which a LMWG is present may result in the formation of a gel through the protonation and subsequent change in the solubility of the dissolved LMWG.

1.3.5 Salt triggered gelation

The addition of a salt into the aqueous solution containing the unassembled gelator is another method that has proven effective in inducing the assembly of the individual gelator molecules into the three-dimensional gel network. This method has proven effective with dipeptide based LMWGs which can be dissolved with an increase in pH, above the pK_a of the terminal carboxylic acid group,[70] before the addition of a salt induces

self-assembly.[64,71] The addition of salt to amino acid based gelation systems is an attractive prospect when considering the biological applications that many such LMWGs are considered for, owing to the method being relatively biocompatible.

The use of salt triggers with peptide gelation systems has also introduced some interesting elements of control with respect to the assembled structure. By far and away, the most common salt that is used to induce gelation is calcium chloride ($CaCl_2$).[72–74] $CaCl_2$ is highly water soluble and has a high degree of biological compatibility. It induces gelation through intermolecular calcium mediated ionic bridging, generally between oxygen containing carboxylate groups of separate gelator molecules. Of course, $CaCl_2$ is not the only salt that can induce gelation.[75,76] Work done in the Ulijn group demonstrates the effects of different salts on peptide-based hydrogelators. They show how a change in the salt can have a dramatic effect on the physical properties of the gel. The preparation of the gels took place in phosphate buffer solutions with the addition of various sodium salts including sodium citrate, sodium bromide and sodium nitrate. What was discovered was that the ability of the LMWG molecules in solutions to form the nanofibers required for gelation followed the Hofmeister series. This involved the addition of sodium citrate at the kosmotrope end of the series, resulting in the formation of a dense fibrous network. The addition of the chaotrope sodium nitrate induced the formation of spherical aggregates, rather than the high aspect ratio fibres required for gelation. The supramolecular structures formed upon the addition of sodium bromide lie between these two morphologies. Using salts in order to induce gelation is an easily deployed and convenient trigger method. However, care should be taken when choosing a salt because, as has been discussed, not all salts are created equally with regards to their ability to induce a gel assembly process. This results in a method of controlling the material properties of the gel, such as mechanical robustness, through changing the trigger salt as opposed to the alternative, which is a complete redesign with regards to the chemical structure of the LMWG itself.

1.4 Design Principles of LMWGs and supramolecular assembly

There are a huge number of structurally diverse LMWGs reported in the literature. Examples include those derived from carbohydrates,[77,78] cholesterols, fatty acids,[79–82] functionalised peptide systems[64,83] and calixarene-based systems,[84,85] to name but a few. Although the various types of gelator may bare no immediate similarities to each other, with regards to their chemical structure, they all share a number of design principles that

allow them to act as LMWGs. They all have the ability to form the directional supramolecular interactions (see Figure 1.7) necessary for high aspect ratio fibre formation, whether it be through hydrogen bonding or some other form of physical interaction. Hydrogelators must also strike a careful balance between hydrophobicity and hydrophilicity. To this end, LMWGs generally consist of two distinct regions, a hydrophilic zone that will allow solubilisation, and a hydrophobic zone that drives the self-assembly in water. This regional distinction means many LMWG can often be classified as amphiphilic molecules.

There are numerous examples of amino acids, di- and tripeptides functionalised with a Fmoc protected N-terminus showing themselves to be effective hydrogelators (Figure 1.8). The facile reaction to add the Fmoc group to amino acids is part of the reason for the large number of Fmoc bearing LMWGs. The first such examples of dipeptides conjugated to Fmoc groups behaving as gelators was presented by Vegners *et al.* in a study that involved Fmoc-Leu-Asp, Fmoc-Ala-Asp and Fmoc-Ile-Asp. All three examples formed hydrogels when subjected to a heat/cool cycle at concentrations between 0.5 and 6.7 wt%.[86] Unsurprisingly, it was the most water-soluble example Fmoc-Ala-Asp that required the highest concentration to induce gelation. More recently, Fmoc-diphenylalanine, Fmoc-Phe-Phe, has emerged as one of the most well characterised of the Fmoc-dipeptide gelators, with the first examples of these Fmoc-dipeptide gelators emerging in 2006.[51,66] There are several different trigger methods that can be employed to set gels using Fmoc-Phe-Phe, with resulting differences in the supramolecular assembly being apparent.

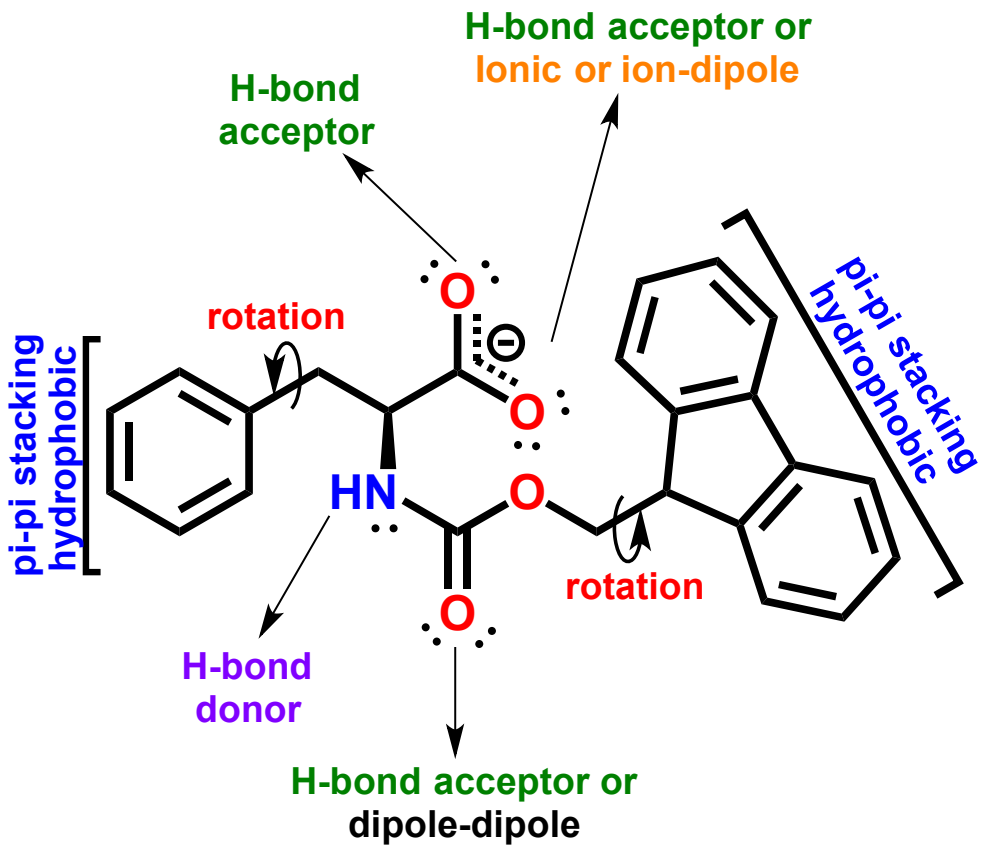

Figure 1.7. Structure of Fmoc-phenylalanine highlighting the sites for potential interaction with both other gelator molecules and solvent molecules, which will drive the formation of the three-dimensional gel network.

The earlier methods of gelation involved dissolution of Fmoc-Phe-Phe in an effective solvent such as DMSO or hexafluoroisopropanol (HFIP).[87,88] The addition of water, as an anti-solvent, induced gelation at concentrations of 0.5 wt%. Unsurprisingly, a higher concentration of gelator would result in a more mechanically robust gel. By performing FT-IR spectroscopy on the gels it was possible to observe peaks at 1607, 1658, and 1691 cm^{-1}, which is indicative of the existence of β-sheets and β-turns.[51] An alternative gelation strategy has been presented by Ulijn and co-workers utilising a pH trigger.

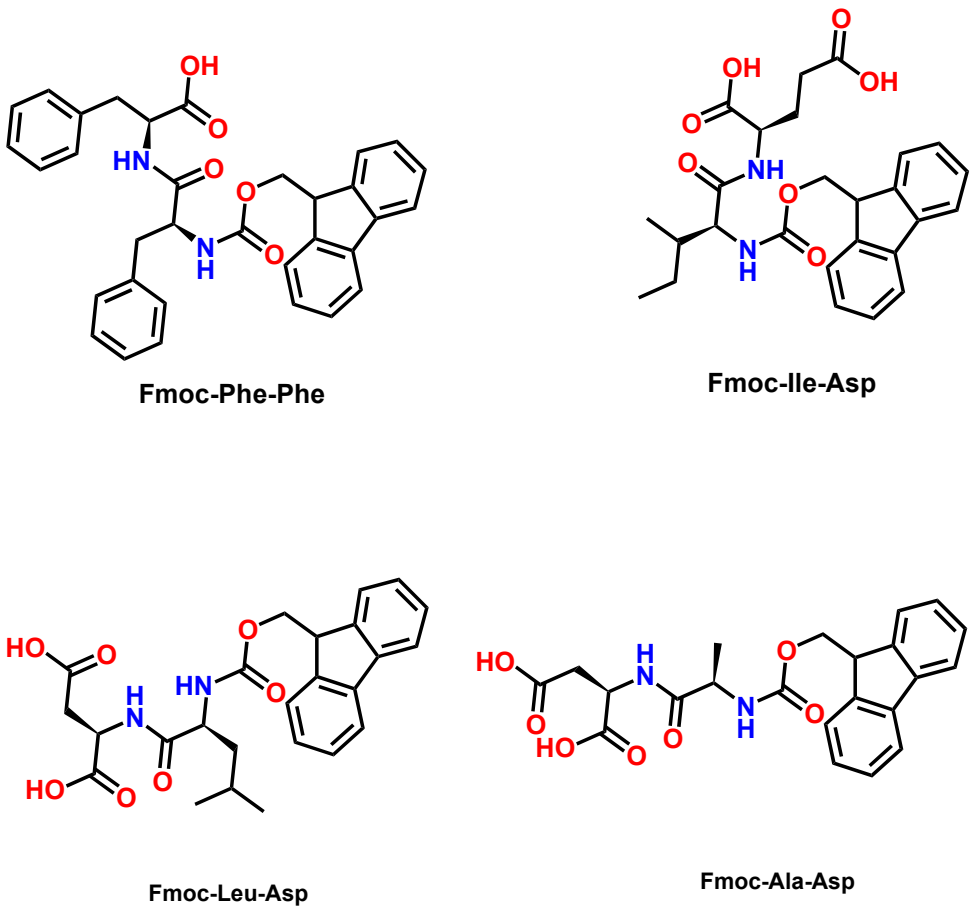

Figure 1.8. Fmoc-dipeptide species that have shown effective hydrogelation properties. In these examples, aromatic groups and extended alkyl sections represent the hydrophobic region.

By dissolving Fmoc-Phe-Phe in a basic solution, taking care not to cleave the Fmoc protecting group which is sensitive to base, before lowering the pH with the addition of HCl, resulted in a gel being set.[66] This gel again relies on a fibrous network for solvent immobilisation with an elastic modulus that could range from 1900 – 21000 Pa. FT-IR spectroscopy conducted on gels set using this pH trigger method showed absorption at 1630 and 1690 cm^{-1}, absorptions that are characteristic of anti-parallel β-sheets.[89] The presence of β-sheets could also be demonstrated with circular dichroism with an observable minimum of 218 nm (see Figure 1.9).[90] These Fmoc-Phe-Phe examples highlight the importance in considering the supramolecular assembly when different trigger mechanisms are employed. Despite the design of the LMWG being the same, solvent switch and pH switch triggers gave different supramolecular assemblies within the gels structure.

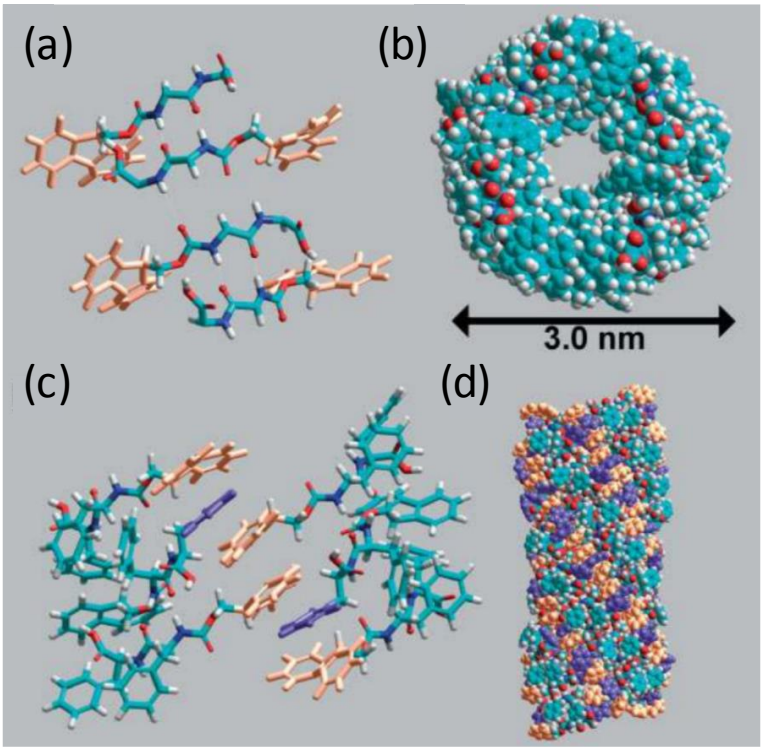

Figure 1.9. (a) Interlocking of Fmoc groups from alternate β-sheets to create π-stacked pairs with interleaved phenyl rings. (b) Due to the twist of β-sheets, the second sheet must be rotated in relation the first to maintain the interaction between the fluorenyl groups. A cylindrical end view, (c), of the structure and side view, (d). (reproduced with permission from ref.[90])

1.4.1 *C*$_3$ symmetric tripodal gelators

There are an ever increasing number of LMWGs that follow the same overall design layout and obey the same symmetry rules, namely the *C*$_3$ symmetric LMWGs. This design strategy will be utilised extensively in the design of gels in this thesis. Their overall chemical layout lends itself to the formation of planar, discotic molecules. This design principle has long been associated with liquid crystallinity and the discogen liquid crystals, with many examples exhibiting *C*$_3$ symmetry.[91] These traits allow effective columnar stacking,[92] often through the formation of intermolecular hydrogen bonds.[93] With the presence of such effective columnar stacking, it is of little surprise that molecules with similar designs and layouts have shown to produce fibrous supramolecular gels.

One of the most common structural motifs for *C*$_3$ symmetric gelators is that of the 1,3,5-benzenze tricarboxamide (BTA) gelators. As can be seen in Figure 1.10, a typical BTA gelator consists of a benzene core and three amides connected to the central core unit at the 1, 3 and 5 positions. These 1,3,5 periphery groups are often described as arms.

There is the potential for BTA species to be asymmetric with one of the arms differing from the other two. However, most likely due to the far more complex synthetic strategy that must be employed when producing such a species, there are significantly fewer examples in the literature when compared to a species with three identical arms. The structure of C_3 BTA gelator is reminiscent of the archetypal cyclohexane centred triamide gelators introduced over ten years ago as a hydrogelator by the group of van Esch.[94] Their work presents a family of gelators where the central 1,3,5-trisamide cyclohexane unit is extended with hydrophobic amino acid groups. This effectively shelters the amide functionalities from the potential competitive interactions with water. This forces the anisotropic self-assembly of the molecules into the high aspect ratio fibres required for gelation through the complimentary amide-amide hydrogen bonding and the hydrophobic effects of the amino acid groups. The concept of hydrogen bond driven anisotropic self-assembly is also the key feature in the assembly of BTA molecules.

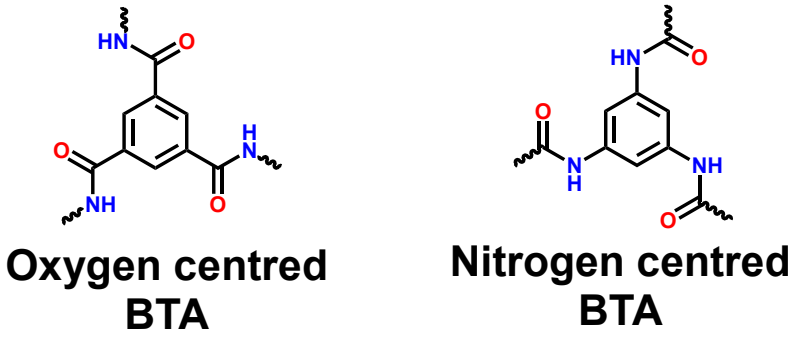

Figure 1.10. Diagrams highlighting the structural difference between an oxygen centred BTA molecule (left) and a nitrogen centred BTA molecule (right).

The BTA class of molecules has long been considered as a supramolecular building block, with the earliest examples emerging from the field of a liquid crystallinity.[95] The lyotropic, liquid crystalline behaviour of certain BTA species arises because of the hydrogen bond driven face-to-face stacking of the molecules, results in a dramatic increase in the viscosity of solution in which they are synthesised.[96] Something that can be attributed to the formation of supramolecular polymers.[97] The earliest example of a BTA species acting as a LMWG was reported by Yasuda *et al.* in 1996.[98] The use of an oxygen centred core functionalised with long alkyl arm groups (C_{17}) producing an effective gelator in a range of solvents, including, but not limited to, 1,2-dichloroethane, nitrobenzene and DMSO. The development of further BTA organogelators has shown the

versatility of system. However, the inherent insolubility in water of BTA species has proven problematic in the development of a hydrogel-based system. It was not until 2004, when the group of Das presented their BTA derivatives, that a hydrogelating BTA system was realised.[99] The gelators were both oxygen centred, as opposed to nitrogen centred[100,101], BTA cores appended with pyridyl arms with the pyridyl nitrogen, either in the three or four position (Figure 1.11).

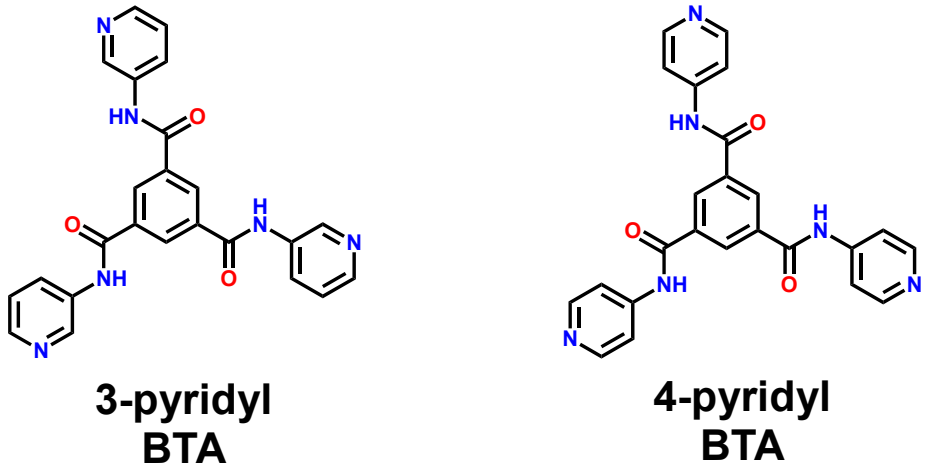

Figure 1.11. Diagrams showing BTA gelators in the oxygen centred confirmation functionalised with pyridyl arm units.

Although termed as hydrogel gels, the setting using the discussed pyridyl BTAs employed an organic solvent/water mixture before a heat/cool is used to induce gelation. The organic solvents typically used to aid solubility included DMSO, ethanol, and DMF, in a 3:7 ratio with water. The application of such a gel system was demonstrated by Shi and co-workers.[102] Their utilisation of the surface of a 3-pyridyl BTA hydrogel as a growth centre for biominerals elegantly demonstrates the possibility to produce calcium phosphate nanostructures by using the gel network as a scaffold. This has important implications for the repair and grafting of broken bones, something that will prove increasingly useful as the world's population ages.

In order to remove the necessity for the solubilising solvent for the BTA and produce a true hydrogelator, an alternative trigger mechanism would have to be realised. This was achieved by Schmidt and Albuquerque *et. al.* through the use of benzoic acid-type groups as the arms of BTA, in place of the pyridyl groups.[103] The presence of the carboxylic acid groups allowed the molecule to be deprotonated with NaOH, before reprotonation by the addition of GdL, resulted in the formation of an organic solvent free hydrogel. This fully pH reversible hydrogel also has the interesting characteristic of being

photoluminecent, in that it displays a strong blue emission when irradiated with UV light. The only comparable previous work featured a BTA organogel and concluded the photolumenicent activity arose from the molecular aggregation driven by the H-bonding groups, without giving further details on the origin of the phenomena.[104] The work of Schmidt and Albuquerque went further and elucidated the means by which the photoluminescence occurs. They established, through use of DFT calculations, that the blue luminescence arises solely because of the columnar stacking that occurs and involves a large number of monomers. Aggregation of the BTA results in a lowering of the energy of the S_1 and T_1 excited states, the two lowest energy LUMOs making them more accessible for the excitation process for fluorescence. The work of Schmidt and Albuquerque was expanded upon by Howe *et. al.*, with the introduction of a family of BTA-based pH triggered gelators. They introduced a number of modified gelators with the use of alternative aminobenzoic acid and naphthyl carboxylic acid groups as the three constituent arm groups of the BTA. Their study highlights how minor chemical changes to the BTA molecules can make dramatic changes to the properties of the bulk assembly. This is particularly true in terms of the materials response to externally applied mechanical stress and the visual appearance of the gels.[105]

Further examples of tripodal, C_3 symmetric gelators include 1,3,5-tris(*N*-phenyl-*N*-4-stearoylaminophenylamino)benzene (TSA-TDAB) and 4,4′,4′′-tris(*N*-phenyl-*N*-4-stearoylaminophenylamino)triphenylamine (TSA-TDATA) developed by Shirota and co-workers, see Figure 1.12.[98] The ability to modify the chemical structures of the discussed C_3 symmetric gelators means there is potential to produce further supramolecular gelators based on a discotic, C_3 design strategy with different physical properties.

Despite the recent advances made, it is still correct to say that the overall supramolecular gelation process is not entirely understood. These advances have gone a long way to further our understanding of the gelation phenomenon. The point we are at now means we can, to some degree of confidence, rationally design new LMWGs and even predict a molecules potential gelation ability at the theoretical level.[106] What has been demonstrated in this section is that the most important properties of a LWMG is its ability to form or not form supramolecular interactions with other gelator molecules, or indeed the solvent in which it is present. The incorporation of hydrophobic components, such as Fmoc, has the ability to tune the solubility of the LMWG, allowing dissolution at high temperature, before the hydrophobic effect driven supramolecular assembly occurs upon the solution cooling. The supramolecular interactions that induce assembly are dependent on the functional groups that are built into the LMWG. An excellent example

of this concept are gels containing urea groups. These gels assemble through the formation of the well-documented intermolecular urea tape hydrogen bonding motif.[107,108] The introduction of other groups into the structure of LMWGs that are incorporated as a means to trigger gelation, may also involve the use of the chemical reactivity as the trigger mechanism.

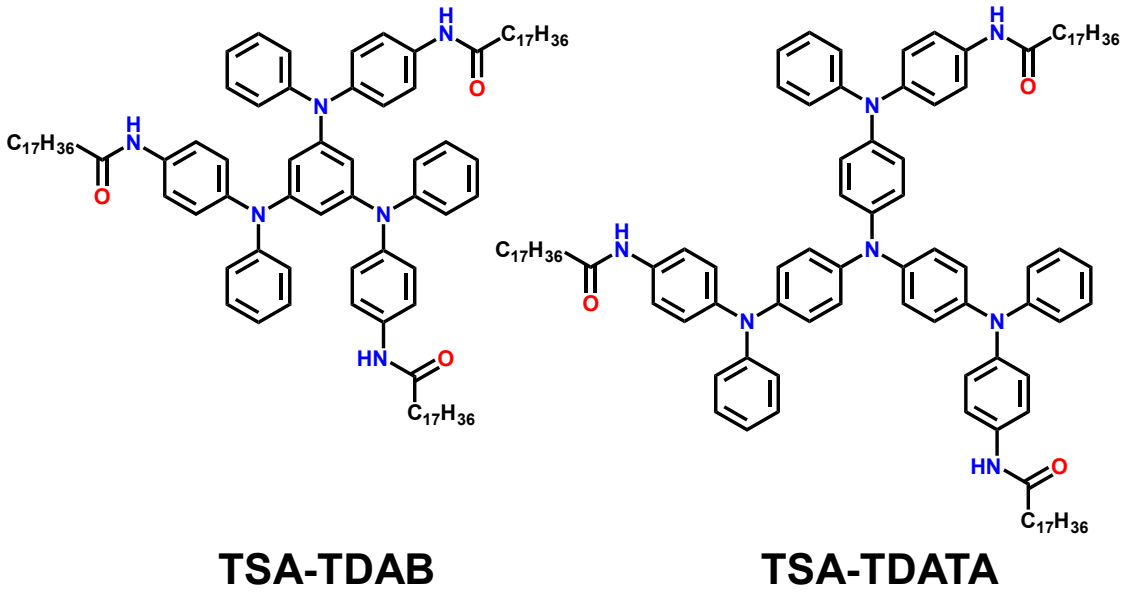

Figure 1.12. Diagrams showing the chemical structures of TSA-TDAB and TSA-TDATA, examples of C_3 tripodal gelators.

1.5 In situ vs Ex situ LMWG formation

When discussing LMWGs, we are referring to relatively small organic molecules. The vast majority of these molecules are produced through a traditional chemical synthesis route. What this means is that two or more chemical components are reacted together, usually in an organic solvent, before various isolation and purification methods are employed to yield the LMWG. An example of which would be the classic organic reactions such as the Schotten-Baumann reaction.[105] With the gelator now isolated, it can be dissolved in the desired solvent phase, usually with heating, sonication or with the addition of base. Once dissolved, gelation is triggered most often by allowing the solution to cool or by lowering the pH with the addition of acid, as discussed previously in section 1.3. This method of producing a LMWG is referred to as an *ex situ* gelator synthesis and is by far the most common way of making gelators.

An alternative, and far less common, way of gelling a solvent is to perform a chemical reaction in the liquid medium you wish to gel, between two or more molecules, thus creating a LMWG. Once formed at a concentration greater than or equal to the CGC of the LMWG, the solution will solidify resulting in gel formation. There are very few examples of this methodology being used to synthesise a LMWG and successfully gel a solvent.[109,110] However, one such study by Eelkema, van Esch and co-workers elegantly demonstrates such a gelation system. The combination of a water soluble aldehyde and a cyclohexane based 1,3,5-trihydrazide (see Figure 1.13) results in the formation of a tripodal hydrazone.[111]

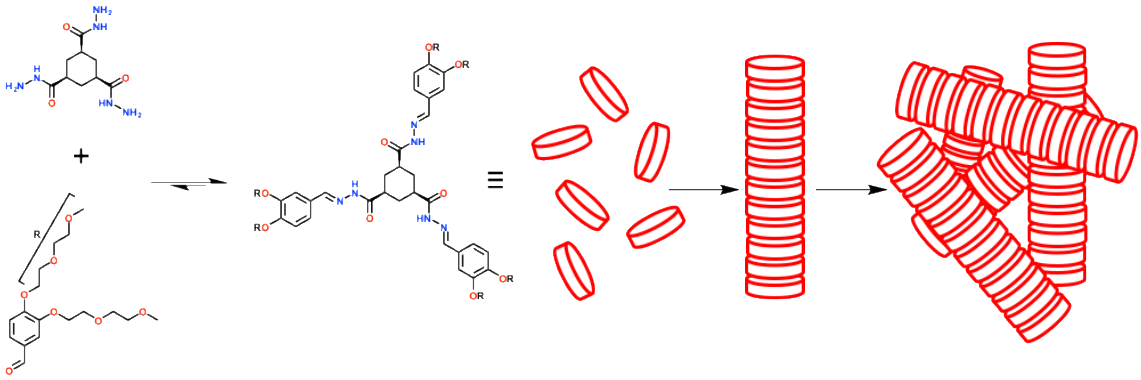

Figure 1.13. Formation of the tripodal trihydrazone. Starting from the initial water soluble aldehyde and trihydrazide reactants, the formation of the trihydrazone resulted in supersaturation, followed by fibre formation. It is these fibres that entangle, forming a three-dimensional network, which ultimately leads to gelation of the solvent.

These individual hydrazone molecules can be considered as a planar, discotic C_3 symmetric supramolecular building units that undergo face-to-face stacking driven by hydrogen bonding between the hydrazone groups. The fact that this reaction occurs *in situ* with respect to water, which is to be gelled, means that by controlling the chemical reaction between the hydrazide and the aldehyde the authors were able to greatly influence the bulk properties of the resulting gel material. The dynamic covalent chemistry between an aldehyde and a hydrazide to produce a hydrazone is a reaction that is well-known to be catalysed by either acidic conditions[112] or aniline and its various derivatives.[113,114] This was utilised in the study to influence not only the time the gel took to form but also the ultimate mechanical strength of the gel with respect to an externally applied mechanical stress. A low pH of 5 results in the lowest gelation time. The use of aniline as a catalyst results in lower gelation times as the concentration of aniline is increased. With an aniline catalyst, the strongest gel is achieved at relatively low

concentrations, approximately 10 mM, compared to an acid catalyst. This was thought to be the case because at higher concentrations a competing side reaction producing the aniline derived imine with the aldehyde occurs. The catalysed formation of the tripodal gelator, whether by acid or aniline, is thought to produce mechanically more robust gels because of the at higher rates of formation. These increased rates result in an increase in the number of defects in the gel fibres, which in turn increases fibre branching and ultimately the cross linking of the fibres. This example has provided a source of inspiration for much of work presented in this thesis, with the dynamic nature of the hydrazone bonds being of particular interest.

1.6 Dynamic Covalent Chemistry

Dynamic covalent chemistry (DCvC) is a synthetic strategy that is akin to supramolecular chemistry, in that it allows dynamic change to a structure, albeit at a molecular level instead of a supramolecular assembly. With both supramolecular chemistry and DCvC allowing dynamic changes to either the supramolecular or molecular components, they are both encompassed by constitutional dynamic chemistry (CDC), as defined by Lehn.[115] This term is similar to dynamic combinatorial chemistry (DCC), which Sanders and Otto described as combinatorial supramolecular or molecular chemistry that operates under thermodynamic control.[116]

Using DCvC as a synthetic strategy relies on two key features. There is a dynamic reaction, which allows an exchange process, resulting in the system being able access stable thermodynamic minima. The ratio of reaction products resulting from these thermodynamic minima can be influenced through external factors. These factors include, but are not limited to, reaction solvent, temperature, pH or the presence of stabilisation sources in the form of templates or metal ions. The fact that this synthetic strategy is adaptable, based on a variety of stimuli, gives rise to a number of applications. This is particularly true with the development of stimuli responsive dynamic functional materials. Such materials are proving to be exciting areas of research in technologies such as self-healing materials.

Relative to the number of chemical reactions, examples of reactions that exhibit DCvC are limited. However, there are examples of key chemical functionalities that feature dynamic bonds, these include but are not limited to hydrazone[117] and imine based[118] functional groups. These groups rely on the reaction of an aldehyde with a hydrazide or amine, respectively, with both examples producing one equivalent of H_2O

for each product group that is formed. The release of the H_2O requires special consideration with these systems, as its presence effects the position of the reaction equilibrium. Imines, of which hydrazones are a subset, can generally be thought of as undergoing three different types of equilibrium controlled reactions; hydrolysis, exchange and metathesis (see Figure 1.14). The hydrolysis of the imine is dependent on the addition of water, this is reason for the use of a Dean-Stark apparatus, or a chemical drying agent such as $MgSO_4$, when synthesising imine based compounds. As a result, addition of H_2O to the reaction will induce a reversion back to the aldehyde and amine starting materials.

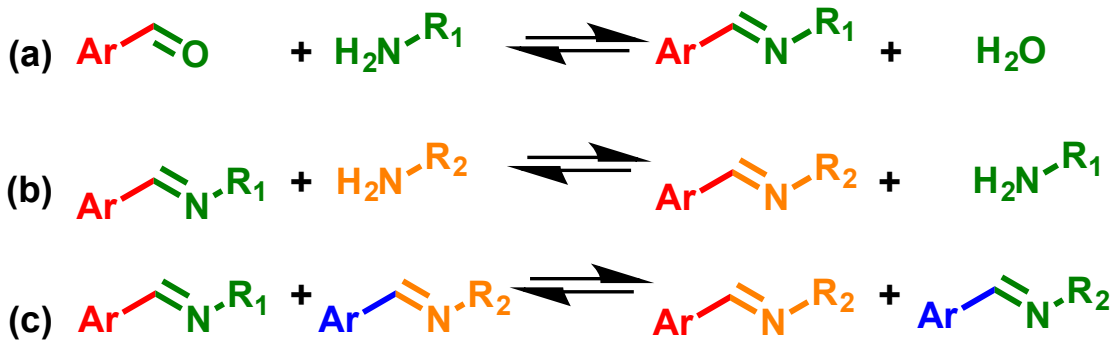

Figure 1.14. Representation of the three types of imine reaction: (a) imine condensation, (b) exchange reaction and (c) metathesis reaction.

The dynamic covalent nature of imine formation, and the ability for the group to undergo exchange reactions, allows for the emergence of self-sorting systems. When considered at the molecular level, where DCvC is involved, self-sorting can be thought of as a spontaneous reorganisation of a disordered system with numerous components to a system with fewer components and more order. Like many synthetic ideas, nature has developed self-sorting systems to perfection. This is prevalent with highly targeted enzymes, which operate in a highly selective manner. Self-sorting systems that operate under kinetic control are born out the concepts discussed in the Curtin-Hammet principle. This principle says that should a reaction give rise to reactive intermediates or reactants that interconvert rapidly, then the ratios of the reactant products will depend not on the equilibrium constants between the intermediates or reactants but on the free energies of the transition states that lead to each of the products. This principle has been demonstrated by the fact that 'imine' products can be trapped by reduction of the C=N bond, which gives rise to a secondary amine functionality. When such a method is used, it can be said

that the product is obtained under thermodynamic control in a kinetic fashion. In a system where a variety of amines are combined with an aldehyde, the kinetically favoured imine product will emerge. Reduction of this product to the secondary amine will result in the formation of more of the kinetically favoured product being formed through adjustment of the equilibrium, as dictated by Le Châtelier's principle. Further imine formation will result in further oxidation to the secondary amine until the materials required to make the kinetically favoured imine are consumed. Such techniques can be used to produce high yield, high purity products from a potential complex reaction mixture.

There are numerous literature examples of the imine, or indeed hydrazone, chemistry being utilised as complex supramolecular building blocks. The work of Cooper and co-workers has involved the preparation of a number of organic cages through the reaction of 1,3,5-triformylbenzene and diamines.[119] The nature of these cages meant they feature windows large enough for guest molecules to enter through. This has allowed them to be thought of as potentially applicable to applications such as gas or solvent separation. Arguably more interesting is the fact that because these cages have been constructed through imine formation, they exhibit a dynamic nature which can be exploited.[120] By adjusting the ratio of the starting materials, and the introduction of a second diamine, it was possible to employ dynamic covalent scrambling to produce a variety of cages. Due to the fact there was a large number of different cages that could not pack effectively, the supramolecular assembly of them, i.e. the growth of a single crystal, was massively effected. The different cages all had different sizes which reduced the packing effectiveness, resulting in the formation of an amorphous porous material.

The use of DCvC, such as the discussed imine examples, provides an exciting synthetic tool with which to develop new supramolecular gelatinous materials. The combination of the *in situ* LMWG synthesis method with DCvC has the potential to allow exploration of some of the concepts associated with DCvC (such as self-sorting). This can be explored not just a chemical level, but also at the level involved with the formation of the supramolecular gel network.

1.7 Auto-catalysis

Auto-catalysis, or self-replication, is the description of an entity that aids the production of more copies of itself (see Figure 1.15), and as a concept, has been investigated for a considerable length of time.[121] The importance of auto-catalytic processes is near

impossible to overstate, in part due to them being generally accepted as playing a central role in the emergence of life.[122] Demonstration of a reactions tendency to exhibit auto-cataylsis can be done in two ways. The plot of product concentration against time will exhibit an exponential curve with the corresponding rate of product (replicator) formation plot giving rise to a 'bell' shaped profile. The other demonstration is the positive correlation between the initial concentration of the product and the rate of the reaction.

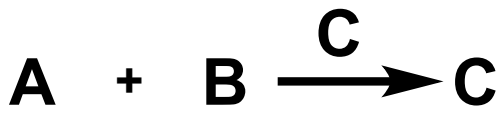

Figure 1.15. The general reaction scheme for an autocatalytic reaction feature two starting products, **A** and **B**, which react to produce the autocatalytic species, **C**.

When discussing an auto-catalytic reaction it is important to consider the mechanism by which the catalytic process operates. Template based auto-cataylsis is a common mechanistic concept. It involves the replicator reversibly binding two or more chemical fragments of itself, which effectively increases their local concentration, resulting in the catalysis of the chemical reaction that couples them. While this template directed auto-catalysis is an elegant concept, it also explains why auto-catalytic reactions often do not display the level of catalytic activity that would be theoretically possible when operating under ideal conditions. This is due to the potential for a template-based auto-catalytic reaction to be affected by a process known as product inhibition. Product inhibition describes the process where the templating molecule and the newly formed template fail to dissociate from one another. This results in the formation of dimers or multimers that are catalytically inactive. A perfect template based auto-catalytic reaction results in an exponential increase in product concentration The general rate equation, Figure 1.16, features the term *p* which is the order of the reaction with respect to the product.[123]

$$\frac{dc}{dt} = ac^p + b$$

Figure 1.16. The general form for the rate equation that describes a template based auto-catalytic reaction. ac^p refers to the autocatalytic term (*c* defines product concentration). *p* is the order of the reaction with respect to the product. *b* relates to the non-catalysed reaction rate.

While auto-catalysis is not a particular rare principle in the literature, most synthetic examples exhibit parabolic[124] rather than exponential increase in the product/replicator/template concentration, as shown in Figure 1.17.[125,126]

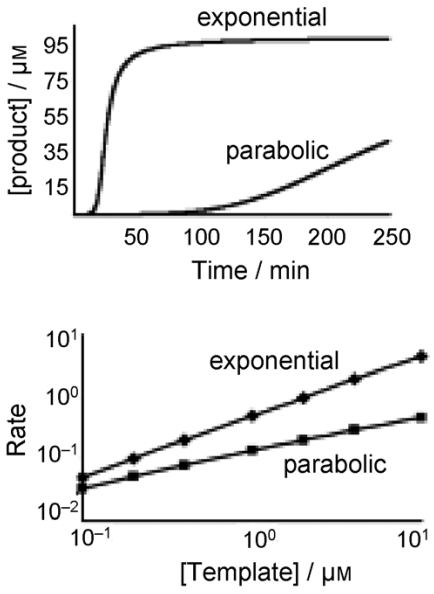

Figure 1.17. Kinetic signatures of autocatalysis. Top: exponential vs. parabolic growth. Bottom: the rate of reaction is proportional to initial concentration of product. (reproduced with permission from ref.[125]).

With nature, once again, proving itself to be far superior and consistent in demonstrating exponential auto-catalytic processes, synthetic systems that show exponential increase in product concentration are highly sought after. One such synthetic system, and one that is particularly pertinent to some of the work discussed in this thesis, is an example presented by the Otto group. They discuss a system where there is an obvious templating effect which results in the growth of fibres composed of the replicators. Mechanical agititation of the reaction solution results in a breaking of these fibres, and as a result, an increase in the rate of the auto-catalytic reaction to the point at which it exhibits exponential self-replication is seen.[127]

1.8 Presented work

The work presented in this thesis seeks to build on previously demonstrated C_3 symmetrical design strategies.[128–130] The utilisation of a C_3 architecture to develop the next generation of discotic LMWGs has proven successful across a range of different chemical systems. The goal of bringing together the concepts of chemical reactivity and

supramolecular assembly in the form of hydrogels was investigated across a number of systems.

By using an *in situ* synthesis protocol to form certain LMWGs many new concepts have been introduced into the gelation process. These processes such as chemical and physical self-sorting and co-assembly at various stages of the hierarchal assembly process. This in combination with pathway complexity have allowed tuning of the gels physical properties, in particular the gels responses to an externally applied mechanical stimulus. The ability to analysis the hierarchal assembly in a top down fashion is also possible whereby kinetic information on the in situ chemical reactions can be obtained from the material properties of the gel they form.

Chapter 2 discusses a single gelation system that gives rise to three distinctly different gelatinous materials through utilisation of dynamic hydrazone chemistry along with a reversible tautomerisation This arises through control of the pathway complexity of the system with respect to both the thermodynamics and kinetics of the chemical reaction. A complete study of this reaction both experimentally and theoretically has led to an accurate mapping of the systems energy landscape, which can be used to control the material properties of the gel.

Chapter 3 presents a number of different gelators that can be formed either using an in situ or an ex situ synthesis method. They are based on an initial imine forming reaction before a highly energetically favourable enol-imine to keto-enamine tautomerisation occurs resulting in a thermodynamic trapping of the gelator species. Owing to the use of the in situ synthesis method the chapter will discuss the possibility to introduce gelators formed from a more complex mix of starting materials. This allows probing of the systems kinetics and thermodynamics at the chemical level and exploration of aspects of systems chemistry.

Chapter 4 studies an individual gelation system similar to the systems discussed in chapter 3, however, with a much slower in situ reaction time. This allowed for a thorough and accurate study of the reaction kinetics. The chemical system exhibited auto-catalysis to the extent where an exponential increase in the concentration of the reaction product (gelator) molecule. Links between the chemical kinetics and the mechanical strength of the gel were then sought.

1.9 References

1 L. A. Estroff and A. D. Hamilton, *Chem. Rev.*, 2004, **104**, 1201–1218.

2 G. M. Peters and J. T. Davis, *Chem. Soc. Rev.*, 2016, **45**, 3188–3206.

3 X. Li, Y. Kuang, J. Shi, Y. Gao, H.-C. Lin and B. Xu, *J. Am. Chem. Soc.*, 2011, **133**, 17513–17518.

4 R. Parveen and P. Dastidar, *Chem. Eur. J.*, 2016, **22**, 9257–9266.

5 E. A. Appel, J. del Barrio, X. J. Loh and O. A. Scherman, *Chem. Soc. Rev.*, 2012, **41**, 6195–6214.

6 W. Nierzwicki and W. Prins, *J. Appl. Polym. Sci.*, 1975, **19**, 1885–1892.

7 J. Yang, C. Gong, F.-K. Shi and X.-M. Xie, *J. Phys. Chem. B*, 2012, **116**, 12038–12047.

8 G. D'Errico, M. De Lellis, G. Mangiapia, A. Tedeschi, O. Ortona, S. Fusco, A. Borzacchiello and L. Ambrosio, *Biomacromolecules*, 2008, **9**, 231–240.

9 R. Dong, Y. Pang, Y. Su and X. Zhu, *Biomater. Sci.*, 2015, **3**, 937–954.

10 P. Terech and R. G. Weiss, *Chem. Rev.*, 1997, **97**, 3133–3160.

11 F. M. Menger and K. L. Caran, *J. Am. Chem. Soc.*, 2000, **122**, 11679–11691.

12 G. Yu, X. Yan, C. Han and F. Huang, *Chem. Soc. Rev.*, 2013, **42**, 6697–6722.

13 F. H. Gaskins and W. Philippoff, *J. Appl. Polym. Sci.*, 1959, **2**, 143–154.

14 J. Liu, P. He, J. Yan, X. Fang, J. Peng, K. Liu and Y. Fang, *Adv. Mater.*, 2008, **20**, 2508–2511.

15 W. Edwards and D. K. Smith, *J. Am. Chem. Soc.*, 2013, **135**, 5911–5920.

16 J.-W. Liu, Y. Yang, C.-F. Chen and J.-T. Ma, *Langmuir*, 2010, **26**, 9040–9044.

17 M. Wallace, J. A. Iggo and D. J. Adams, *Soft Matter*, 2015, **11**, 7739–7747.

18 M. Wallace, A. Z. Cardoso, W. J. Frith, J. A. Iggo and D. J. Adams, *Chemistry*, 2014, **20**, 16484–16487.

19 S. Iqbal, F. Rodríguez-Llansola, B. Escuder, J. F. Miravet, I. Verbruggen and R. Willem, *Soft Matter*, 2010, **6**, 1875–1878.

20 B. Escuder, S. Martí and J. F. Miravet, *Langmuir*, 2005, **21**, 6776–6787.

21 S. Iqbal, J. F. Miravet and B. Escuder, *Eur. J. Org. Chem.*, 2008, **2008**, 4580–4590.

22 W. S. Price, *Concepts Magn. Reson.*, 1998, **10**, 197–237.

23 F. Rodríguez-Llansola, B. Escuder and J. F. Miravet, *Org. Biomol. Chem.*, 2009, **7**, 3091–3094.

24 S. J. James, A. Perrin, C. D. Jones, D. S. Yufit and J. W. Steed, *Chem. Commun.*, 2014, **50**, 12851–12854.

25 M. Sato, T. Ishitani, S. Watanabe and M. Nakagawa, *Nucl. Instruments Methods Phys. Res. Sect. A Accel. Spectrometers, Detect. Assoc. Equip.*, 2004, **519**, 280–285.

26 P. Byrne, G. O. Lloyd, L. Applegarth, K. M. Anderson, N. Clarke and J. W. Steed, *New J. Chem.*, 2010, **34**, 2261–2274.

27 S. S. Kistler, *J. Phys. Chem.*, 1931, **36**, 52–64.

28 S. Nandi, H.-J. Altenbach, B. Jakob, K. Lange, R. Ihizane, M. P. Schneider, U. Gün and A. Mayer, *Org. Lett.*, 2012, **14**, 3826–3829.

29 J. H. Jung, Y. Ono, K. Hanabusa and S. Shinkai, *J. Am. Chem. Soc.*, 2000, **122**, 5008–5009.

30 B. Freitag, M. Bischoff, H. Mueller, P. Hartel and H. von Harrach, *Microsc. Microanal.*, 2009, **15**, 184–185.

31 G. Bühler, M. C. Feiters, R. J. M. Nolte and K. H. Dötz, *Angew. Chem. Int. Ed.*, 2003, **42**, 2494–2497.

32 S. P. Patil, H. S. Jeong and B. H. Kim, *Chem. Commun.*, 2012, **48**, 8901–8903.

33 A. C. H. Pape, M. M. C. Bastings, R. E. Kieltyka, H. M. Wyss, I. K. Voets, E. W. Meijer and P. Y. W. Dankers, *Int. J. Mol. Sci.*, 2014, **15**, 1096–1111.

34 J. Raeburn, C. Mendoza-Cuenca, B. N. Cattoz, M. a. Little, A. E. Terry, A. Zamith Cardoso, P. C. Griffiths and D. J. Adams, *Soft Matter*, 2015, **11**, 927–935.

35 L. R. Hart, S. Li, C. Sturgess, R. Wildman, J. R. Jones and W. Hayes, *ACS Appl. Mater. Interfaces*, 2016, **8**, 3115–3122.

36 T. Aida, E. W. Meijer and S. I. Stupp, *Science*, 2012, **335**, 813–817.

37 S. Onogi, H. Shigemitsu, T. Yoshii, T. Tanida, M. Ikeda, R. Kubota and I. Hamachi, *Nature Chem.*, 2016, **8**, 743–752.

38 R. G. Weiss, *J. Am. Chem. Soc.*, 2014, 136, 7519–7530.

39 D. Sağlam, P. Venema, R. de Vries, A. van Aelst and E. van der Linden, *Langmuir*, 2012, **28**, 6551–6560.

40 Q. Zhong and C. R. Daubert, *J. Colloid Interface Sci.*, 2004, **279**, 88–94.

41 W. Tian, J. Song, Y. Wang, L. Yue, J. Wang, T. Dan, B. Menghe and H. Zhang, *RSC Adv.*, 2015, **5**, 73352–73362.

42 M. C. Puppo, C. E. Lupano and M. C. Anon, *J. Agric. Food Chem.*, 1995, **43**, 2356–2361.

43 H. Kobayashi, A. Friggeri, K. Koumoto, M. Amaike, S. Shinkai and D. N. Reinhoudt, *Org. Lett.*, 2002, **4**, 1423–1426.

44 I. Furman and R. G. Weiss, *Langmuir*, 1993, **9**, 2084–2088.

45 X. Huang, P. Terech, S. R. Raghavan and R. G. Weiss, *J. Am. Chem. Soc.*, 2005, **127**, 4336–4344.

46 L. Lu, T. M. Cocker, R. E. Bachman and R. G. Weiss, *Langmuir*, 2000, **16**, 20–34.

47 Y. C. Lin, B. Kachar and R. G. Weiss, *J. Am. Chem. Soc.*, 1989, **111**, 5542–5551.

48 S. Debnath, A. Shome, D. Das and P. K. Das, *J. Phys. Chem. B*, 2010, **114**, 4407–4415.

49 D. J. Pochan, J. P. Schneider, J. Kretsinger, B. Ozbas, K. Rajagopal and L. Haines, *J. Am. Chem. Soc.*, 2003, **125**, 11802–11803.

50 K. J. Skilling, A. Ndungu, B. Kellam, M. Ashford, T. D. Bradshaw and M. Marlow, *J. Mater. Chem. B*, 2014, **2**, 8412–8417.

51 A. Mahler, M. Reches, M. Rechter, S. Cohen and E. Gazit, *Adv. Mater.*, 2006, **18**, 1365–1370.

52 C. Tang, A. M. Smith, R. F. Collins, R. V Ulijn and A. Saiani, *Langmuir*, 2009, **25**, 9447–9453.

53 L. Chen, J. Raeburn, S. Sutton, D. G. Spiller, J. Williams, J. S. Sharp, P. C. Griffiths, R. K. Heenan, S. M. King, A. Paul, S. Furzeland, D. Atkins and D. J. Adams, *Soft Matter*, 2011, **7**, 9721–9727.

54 C. Yang, X. Ren, D. Ding, L. Wang and Z. Yang, *Nanoscale*, 2016, **8**, 10768–10773.

55 Z. Yang, G. Liang, Z. Guo, Z. Guo and B. Xu, *Angew. Chem. Int. Ed.*, 2007, **46**, 8216–8219.

56 Y. Zhang, Z. Yang, F. Yuan, H. Gu, P. Gao and B. Xu, *J. Am. Chem. Soc.*, 2004, **126**, 15028–15029.

57 Z. Yang, G. Liang and B. Xu, *Acc. Chem. Res.*, 2008, **41**, 315–326.

58 S. Toledano, R. J. Williams, V. Jayawarna and R. V Ulijn, *J. Am. Chem. Soc.*, 2006, **128**, 1070–1071.

59 R. J. Williams, A. M. Smith, R. Collins, N. Hodson, A. K. Das and R. V Ulijn, *Nat. Nanotechnol.*, 2009, **4**, 19–24.

60 A. Trusek-Holownia, *J. Biotechnol.*, 2003, **102**, 153–163.

61 F. H. Carpenter, *J. Am. Chem. Soc.*, 1960, **82**, 1111–1122.

62 Z. Yang and B. Xu, *Chem. Commun.*, 2004, 2424–2425.

63 D. J. Adams and P. D. Topham, *Soft Matter*, 2010, **6**, 3707–3721.

64 L. Chen, G. Pont, K. Morris, G. Lotze, A. Squires, L. C. Serpell and D. J. Adams, *Chem. Commun.*, 2011, **47**, 12071–12073.

65 L. Chen, T. O. McDonald and D. J. Adams, *RSC Adv.*, 2013, **3**, 8714–8720.

66 V. Jayawarna, M. Ali, T. A. Jowitt, A. F. Miller, A. Saiani, J. E. Gough and R. V. Ulijn, *Adv. Mater.*, 2006, **18**, 611–614.

67 Y. Zhang, H. Gu, Z. Yang and B. Xu, *J. Am. Chem. Soc.*, 2003, **125**, 13680–13681.

68 D. J. Adams, M. F. Butler, W. J. Frith, M. Kirkland, L. Mullen and P. Sanderson, *Soft Matter*, 2009, **5**, 1856–1862.

69 E. R. Draper, L. L. E. Mears, A. M. Castilla, S. M. King, T. O. McDonald, R. Akhtar and D. J. Adams, *RSC Adv.*, 2015, **5**, 95369–95378.

70 L. Chen, S. Revel, K. Morris, L. C Serpell and D. J. Adams, *Langmuir*, 2010, **26**, 13466–13471.

71 S. Roy, N. Javid, P. W. J. M. Frederix, D. A. Lamprou, A. J. Urquhart, N. T. Hunt, P. J. Halling and R. V Ulijn, *Chemistry*, 2012, **18**, 11723–11731.

72 M. A. Greenfield, J. R. Hoffman, M. O. de la Cruz and S. I. Stupp, *Langmuir*, 2010, **26**, 3641–3647.

73 S. Zhang, M. A. Greenfield, A. Mata, L. C. Palmer, R. Bitton, J. R. Mantei, C. Aparicio, M. O. de la Cruz and S. I. Stupp, *Nat. Mater.*, 2010, **9**, 594–601.

74 J. C. Stendahl, M. S. Rao, M. O. Guler and S. I. Stupp, *Adv. Funct. Mater.*, 2006, **16**, 499–508.

75 M.-O. M. Piepenbrock, G. O. Lloyd, N. Clarke and J. W. Steed, *Chem. Rev.*, 2010, **110**, 1960–2004.

76 A. Y.-Y. Tam and V. W.-W. Yam, *Chem. Soc. Rev.*, 2013, **42**, 1540–1567.

77 A. Vidyasagar, K. Handore and K. M. Sureshan, *Angew. Chem. Int. Ed.*, 2011, **50**, 8021–8024.

78 D. J. Cornwell, B. O. Okesola and D. K. Smith, *Soft Matter*, 2013, **9**, 8730–8736.

79 J. Yan, J. Liu, P. Jing, C. Xu, J. Wu, D. Gao and Y. Fang, *Soft Matter*, 2012, **8**, 11697–11703.

80 S. W. Jeong, K. Murata and S. Shinkai, *Supramol. Sci.*, 1996, **3**, 83–86.

81 M. Zhang and R. G. Weiss, *Phys. Chem. Chem. Phys.*, 2016, **18**, 20399–20409.

82 R. da C. Duarte, R. Ongaratto, L. A. Piovesan, V. R. de Lima, V. Soldi, A. A. Merlo and M. G. M. D'Oca, *tetrahedron Lett.*, 2012, **53**, 2454 - 2460.

83 J. Raeburn, T. O. McDonald and D. J. Adams, *Chem. Commun.*, 2012, **48**, 9355–9357.

84 X. Cai, K. Liu, J. Yan, H. Zhang, X. Hou, Z. Liu and Y. Fang, *Soft Matter*, 2012, **8**, 3756–3761.

85 Y. Wu, K. Liu, X. Chen, Y. Chen, S. Zhang, J. Peng and Y. Fang, *New J. Chem.*, 2015, **39**, 639–649.

86 R. Vegners, I. Shestakova, I. Kalvinsh, R. M. Ezzell and P. A. Janmey, *J. Pept. Sci.*, **1**, 371–378.

87 R. Orbach, L. Adler-Abramovich, S. Zigerson, I. Mironi-Harpaz, D. Seliktar and E. Gazit, *Biomacromolecules*, 2009, **10**, 2646–2651.

88 T. Liebmann, S. Rydholm, V. Akpe and H. Brismar, *BMC Biotechnol.*, 2007, **7**, 88.

89 V. Jayawarna, S. M. Richardson, A. R. Hirst, N. W. Hodson, A. Saiani, J. E. Gough and R. V Ulijn, *Acta Biomater.*, 2009, **5**, 934–943.

90 A. M. Smith, R. J. Williams, C. Tang, P. Coppo, R. F. Collins, M. L. Turner, A. Saiani and R. V. Ulijn, *Adv. Mater.*, 2008, **20**, 37–41.

91 R. J. Bushby and O. R. Lozman, *Curr. Opin. Colloid Interface Sci.*, 2002, **7**, 343–354.

92 G. Hennrich, A. Omenat, I. Asselberghs, S. Foerier, K. Clays, T. Verbiest and J. L. Serrano, *Angew. Chem. Int. Ed.*, 2006, **45**, 4203–426.

93 S. Park, M.-H. Ryu, T. J. Shin and B.-K. Cho, *Soft Matter*, 2014, **10**, 5804–5809.

94 A. Heeres, C. van der Pol, M. Stuart, A. Friggeri, B. L. Feringa and J. van Esch, *J. Am. Chem. Soc.*, 2003, **125**, 14252–14253.

95 A. R. Palmans, J. A. Vekemans, H. Fischer, R. A. Hikmet and E. W. Meijer, *Chemistry*, 1997, **3**, 300–307.

96 A. R. A. Palmans, J. A. J. M. Vekemans, R. A. Hikmet, H. Fischer and E. W. Meijer, *Adv. Mater.*, 1998, **10**, 873–876.

97 C. M. A. Leenders, L. Albertazzi, T. Mes, M. M. E. Koenigs, A. R. A. Palmans and E. W. Meijer, *Chem. Commun.*, 2013, **49**, 1963–1965.

98 Y. Yasuda, E. Iishi, H. Inada and Y. Shirota, *Chem. Lett.*, 1996, **7**, 575–576.

99 D. K. Kumar, D. A. Jose, P. Dastidar and A. Das, *Chem. Mater.*, 2004, **16**, 2332–2335.

100 J. E. Gill, R. MacGillivray and J. Munro, *J. Chem. Soc.*, 1949, 1753–1754.

101 H. Stetter, D. Theise and G. J. Steffens, *Chem. Ber.*, 1970, **103**, 200–204.

102 N. Shi, G. Yin, M. Han and Z. Xu, *Colloids Surf. B. Biointerfaces*, 2008, **66**, 84–89.

103 A. Bernet, R. Q. Albuquerque, M. Behr, S. T. Hoffmann and H.-W. Schmidt, *Soft Matter*, 2012, **8**, 66–69.

104 S. Y. Ryu, S. Kim, J. Seo, Y.-W. Kim, O.-H. Kwon, D.-J. Jang and S. Y. Park, *Chem. Commun.*, 2004, 70–71.

105 R. C. T. Howe, A. P. Smalley, A. P. M. Guttenplan, M. W. R. Doggett, M. D. Eddleston, J. C. Tan and G. O. Lloyd, *Chem. Commun.*, 2013, **49**, 4268–4270.

106 J. K. Gupta, D. J. Adams and N. G. Berry, *Chem. Sci.*, 2016, **7**, 4713–4719.

107 J. van Esch, S. De Feyter, R. M. Kellogg, F. De Schryver and B. L. Feringa, *Chem. Eur. J.*, 1997, **3**, 1238–1243.

108 G. O. Lloyd, M.-O. M. Piepenbrock, J. A. Foster, N. Clarke and J. W. Steed, *Soft Matter*, 2012, **8**, 204–216.

109 S. C. Bremmer, A. J. McNeil and M. B. Soellner, *Chem. Commun.*, 2014, **50**, 1691–1693.

110 M. J. Webber, C. J. Newcomb, R. Bitton, S. I. Stupp, M. J. Webber, J. A. Kessler and S. I. Stupp, *Soft Matter*, 2011, **7**, 9665–9672.

111 J. Boekhoven, J. M. Poolman, C. Maity, F. Li, L. van der Mee, C. B. Minkenberg, E. Mendes, J. H. van Esch and R. Eelkema, *Nature Chem.*, 2013, **5**, 433–437.

112 E. T. Kool, D.-H. Park and P. Crisalli, *J. Am. Chem. Soc.*, 2013, **135**, 17663–17666.

113 P. Crisalli and E. T. Kool, *J. Org. Chem.*, 2013, **78**, 1184–1189.

114 P. Crisalli and E. T. Kool, *Org. Lett.*, 2013, **15**, 1646–1649.

115 J.-M. Lehn, *Chem. Soc. Rev.*, 2007, **36**, 151–160.

116 P. T. Corbett, J. Leclaire, L. Vial, K. R. West, J.-L. Wietor, J. K. M. Sanders and S. Otto, *Chem. Rev.*, 2006, **106**, 3652–3711.

117 B. Levrand, Y. Ruff, J.-M. Lehn and A. Herrmann, *Chem. Commun.*, 2006, 2965–2967.

118 M. E. Belowich and J. F. Stoddart, *Chem. Soc. Rev.*, 2012, **41**, 2003–2024.

119 T. Tozawa, J. T. A. Jones, S. I. Swamy, S. Jiang, D. J. Adams, S. Shakespeare, R. Clowes, D. Bradshaw, T. Hasell, S. Y. Chong, C. Tang, S. Thompson, J. Parker, A. Trewin, J. Bacsa, A. M. Z. Slawin, A. Steiner and A. I. Cooper, *Nat. Mater.*, 2009, **8**, 973–978.

120 S. Jiang, J. T. A. Jones, T. Hasell, C. E. Blythe, D. J. Adams, A. Trewin and A. I. Cooper, *Nat. Commun.*, 2011, **2**, 207.

121 G. N. Lewis, *Proc. Am. Acad. Arts Sci.*, 1905, **40**, 719–733.

122 V. Vasas, C. Fernando, M. Santos, S. Kauffman and E. Szathmáry, *Biol. Direct*, 2012, **7**, 1; discussion 1.

123 B. G. Bag and G. von Kiedrowski, *Pure Appl. Chem.*, 1996, **68**, 2145–2152.

124 N. Paul and G. F. Joyce, *Curr. Opin. Chem. Biol.*, 2004, **8**, 634–639.

125 A. J. Bissette and S. P. Fletcher, *Angew. Chem. Int. Ed.*, 2013, **52**, 12800–12826.

126 Z. Dadon, N. Wagner and G. Ashkenasy, *Angew. Chem. Int. Ed.*, 2008, **47**, 6128–6136.

127 M. Colomb-Delsuc, E. Mattia, J. W. Sadownik and S. Otto, *Nat. Commun.*, 2015, **6**, 7427.

128 M. de Loos, J. H. van Esch, R. M. Kellogg and B. L. Feringa, *Tetrahedron*, 2007, **63**, 7285–7301.

129 M. Yamanaka, *Chem. Rec.*, 2016, **16**, 768–782.

130 I. Danila, F. Riobé, J. Puigmartí-Luis, Á. Pérez del Pino, J. D. Wallis, D. B. Amabilino and N. Avarvari, *J. Mater. Chem.*, 2009, **19**, 4495–4504.

Chapter 2 – Hydrazone based multi-reactive gelation system

2.1 Chapter preface

The study presented in this chapter features the work of several contributors. The work involved in the computational study, in sections 2.5.2 and 2.6, are the work of Dr Justyna M. Żurek and Nuno M. S. Almeida of Professor Martin J. Paterson's research group at Heriot-Watt University. The SCXRD data discussed in section 2.5.2 was collected and solved by Dr Amber L. Thompson of Oxford University, aided by Dr Gareth O. Lloyd.[1–5] All other work was performed by Jamie Foster.

2.2 Introduction

The manipulation of thermodynamic and kinetic parameters is increasingly being shown to determine the form of the assembly adopted by the molecular building blocks in supramolecular materials, through a process known as pathway selection. The final assembly, driven by recognition at the molecular level, is a direct result of the pathway adopted by the supramolecular assembly process. Although it is possible to identify the single initial starting point for any supramolecular construction, the final assembly can be markedly different depending on the pathway taken. This concept of pathway complexity was elegantly demonstrated by Korevaar *et al.* with the use of S-chiral oligo(*p*-phenylenevinylene) (SOPV). SOPV could form helical supramolecular polymers with opposite chirality, which chirality depending on whether they were formed under kinetic or thermodynamic control.[6] Although the concept of different assemblies competing due to different pathways is not a new one, and has been documented in nature in the case of protein fibrils.[7] It is also making an increasing impact in the world of synthetic supramolecular assembly.

The desire to develop a synthetic system that incorporate pathway complexity is interesting, particular when considering the biological systems that utilise such a process. These processes include, but are not limited, to the emergence of viruses[8] and the formation of protein networks.[7,9] A chemical reactivity system that displays pathway complexity will generally result in a number of different products being produced, despite the reaction beginning from a single initial starting point. The different reaction products

can be obtained through following different reaction pathways from starting material(s) to product. Selection or preference for one these pathways can be influenced by external[10] or temporal effects. This results in a degree of control over the thermodynamics and kinetics of the reaction system. This concept is best described in terms of the systems energy landscape. The energy landscape for a system that demonstrates pathway complexity can be thought of as a terrain that features a number of different energy minima for the system. Energetically less stable minima are generally the result of the trapping of kinetic products or energised, out-of-equilibrium products. More stable energy minima, including the global energy minimum for the system, represent thermodynamically more stable reaction products. The heights of the energy barriers between these thermodynamic states influences the potential for the reaction product to transform from one thermodynamic state to another, depending on the application of external stimuli. Of course, should the size of the energy barrier be too large to overcome, then the reaction product will reside in whatever thermodynamic state was selected through determination of a specific pathway.

As previously mentioned in chapter 1, there are numerous examples of planar, C_3 symmetric tripodal gelators.[11,12] These consist of a central core unit, from which the C_3 symmetry is derived and three identical periphery or 'arm units'. Most of these examples, along with the vast majority of gelators, are formed in an *ex situ* manner, using standard synthetic techniques, before being dissolved in the desired solvent by appropriate means.[13] Upon application of the necessary trigger, the self-assembly process will begin, ultimately resulting in the formation of a supramolecular gel. With a view to introducing pathway complexity into a gelation system at the molecular level of the hierarchal assembly process, an *in situ* gelator synthesis method would have to be employed. This could also encompass elements of DCvC, which would indeed introduce pathway complexity in the system, as rapidly formed kinetic products would give way to thermodynamically more stable reaction products.[14–16]

This chapter discusses a system where pathway complexity emerges as the dominant concept. Unlike previous examples of a supramolecular assembly featuring pathway complexity, this system will feature the emergence of pathway complexity with formation of the individual supramolecular chemical building blocks, rather than with the supramolecular assembly itself.

2.3 Study aims

The aim of this study was to bring together dynamic covalent chemistry (DCvC) and an *in situ* method of synthesis as a means of creating a new LMWG. DCvC could be introduced through forming the gelator using dynamic hydrazone chemistry.[17] The use of the previously discussed C_3 symmetric gelator design principles and the desire to produce a hydrogelator required special considerations of the starting materials. The components will be examined in more detail in the following section, but for the purposes of this discussion, the reaction pathway for the components should be considered. The C_3 symmetry is derived from the central core unit of the molecule, with the position of the aldehyde groups imposing this symmetry. Figure 2.1 demonstrates the reaction pathway that will lead to the formation of a C_3 potential LMWG. The reaction pathway induced through the stepwise reaction through the mono-, di- and tri- reacted species, relative to the aldehyde core, offers a means of obtaining three reaction products from a single starting point. These three reaction products and their potential to be isolated is dependent on the kinetics of this stepwise reaction, of course, thermodynamics must also be considered. Systems similar to this are well known for their enol to keto tautomerisation. While this tautomerisation is in theory reversible, the keto product is far more thermodynamically stable than the enol product. This means systems reported in the literature all reside in the keto tautomeric form.[18,19]

2.4 Experimental results and discussion

As discussed in section 2.3, the chemical reaction system proposed involves two separate components, a hydrazide (***I***) and an aldehyde (***II***),[20–24] with a view to make a hydrazone-based supramolecular gelator.[20] Both components had to be water soluble in order to get them into the aqueous environment required for hydrogel formation. The aldehyde selected, 1,3,5-triformylphloroglucinol (***II***), would form the central core of the gelator molecule. While not soluble in water at pH 7, raising the pH to 8-8.5 does result in a highly soluble deprotonated form of ***II***. See Figure 2.2 for the synthesis of ***II*** and Figure 2.3 for its deprotonated form, i.e. the hydroxyl groups can be easily deprotonated and the number of deprotonated groups is dependent on pH.

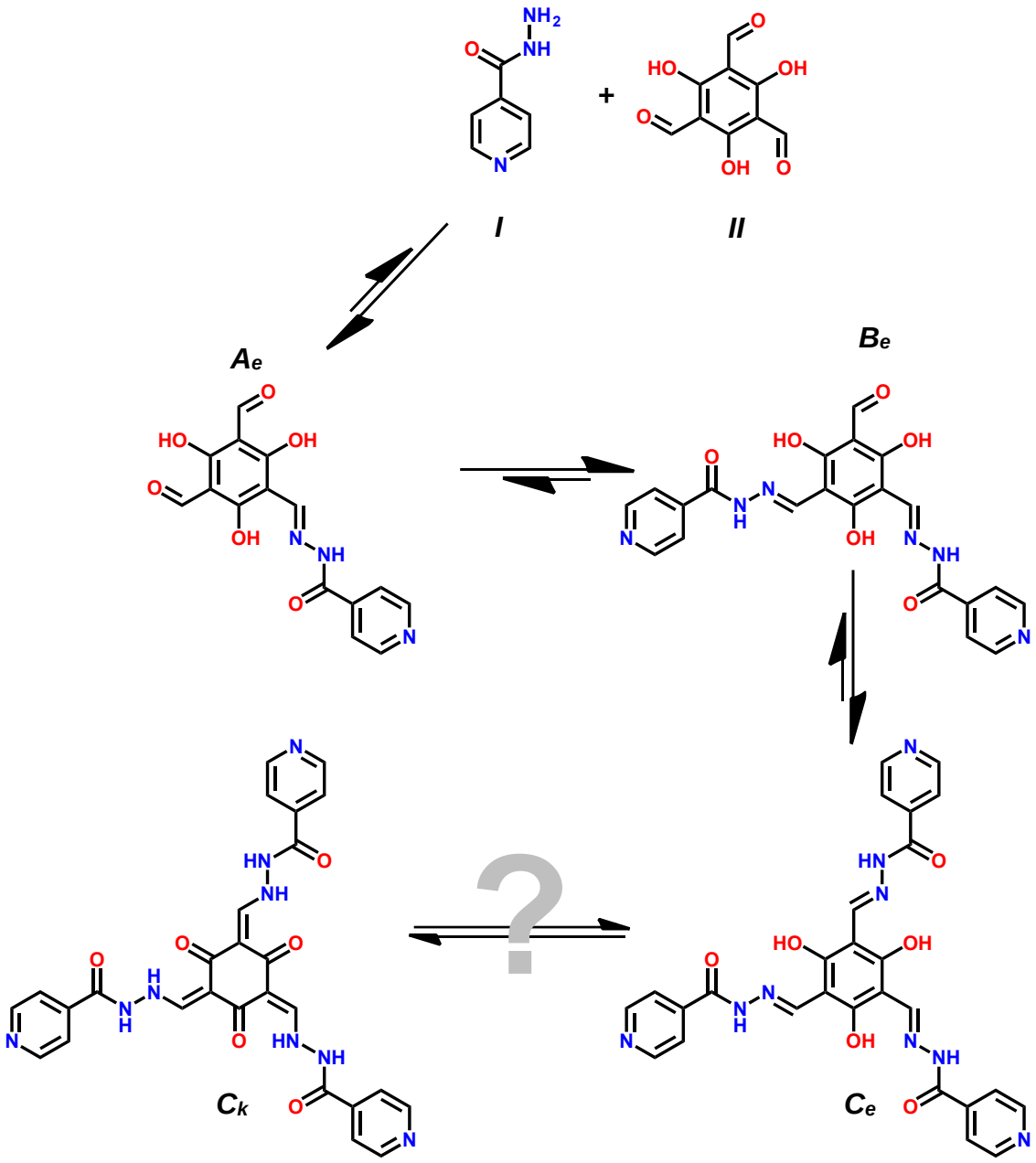

Figure 2.1. Proposed reaction scheme demonstrating the stepwise reaction between the trialdehyde (***II***) and hydrazide (***I***) through the mono- (***A*****e**), di- (***B*****e**) and tri- (***C*****e**) reacted species in order to form a C_3 LMWG. The tri- reacted species has the potential for tautomerisation from ***C*****e** to ***C*****k**.

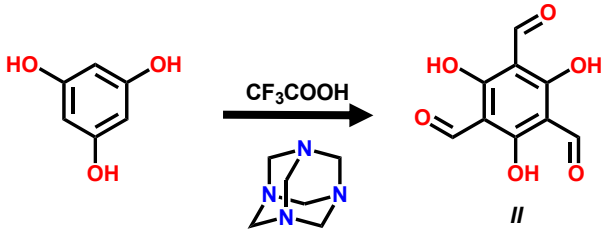

Figure 2.2. Synthesis of 1,3,5-triformylphloroglucinol (***II***) from phloroglucinol using hexamethylenetetramine in trifluoroacetic acid. Deprotonation of ***II***'s hydroxyl groups produces a water soluble form of ***II*** that is necessary for gel formation.

The hydrazide component (***I***), which once reacted would form the three peripheral arms of the gelator molecules, was isonicotinic acid hydrazide. Isonicotinic acid hydrazide is also known as isoniazid, owing to its use as a drug molecule. It has been proven to be an effective first-line antibiotic in the treatment, and indeed prevention, of both latent and active tuberculosis.[25–27] ***I*** has a relatively high solubility in water, this would allow it to be introduced into the *in situ* reaction mixture with ***II*** without any special considerations (see Figure 2.3).

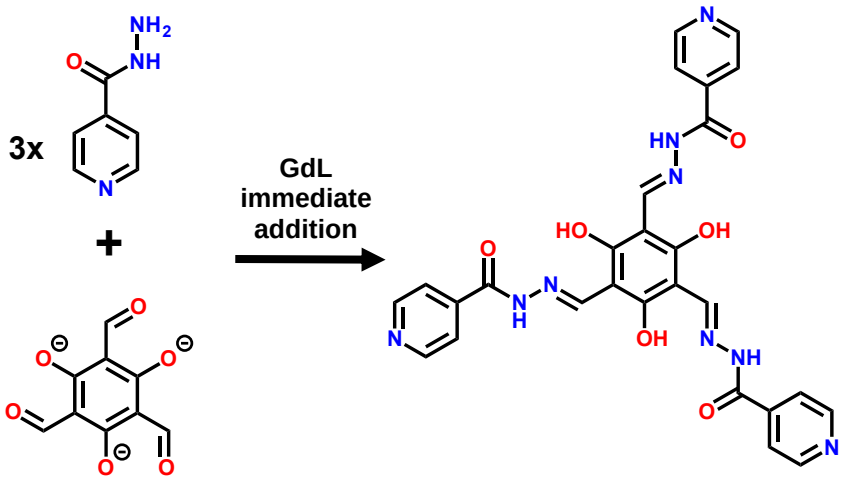

Figure 2.3. *In situ* reaction scheme for the formation of *N*',*N*''',*N*''''-((1*E*,1'*E*,1''*E*)-(2,4,6-trihydroxybenzene-1,3,5-triyl)tris(methanylylidene))tri(isonicotinohydrazide) (***C$_e$***) in its proposed deprotonated form. Reaction involves the combination of ***I*** and ***II*** in water at pH 8.

An *in situ* combination of ***I*** and ***II*** was proposed to result in the formation of a tri-hydrazone based tripodal C_3 symmetric gelator. This system could be described as similar to the previously discussed work of Eelkema, van Esch and coworkers, in that it would form a tri-hydrazone based tripodal C_3 symmetric gelator.[28] However, the gelation system presented here would have the aldehyde reactive groups delivered by the central core and the hydrazide groups delivered by the isoniazid molecules, the reverse chemistry. The ability of a molecule to form a supramolecular hydrogel depends on how it interacts with the molecules around it. That is its hydrophobicity with regards to the aqueous phase[29,30] and its ability to form supramolecular interactions with other molecules of itself.[31–33]

The combination of ***II*** and three equivalents ***I*** in water at pH 8 resulted in a solution that would gradually darken from a clear pale yellow to a clear dark yellow as the reaction proceeded (generally left for over four hours to set). Acidification of this solution with HCl resulted in the formation of red gel, determined by use of the vial

inversion method. This method of setting results in a lack of homogeneity, visually observable in the gels macroscopic structure. With this in mind, setting was attempted using GdL, with the results shown in Figure 2.4.

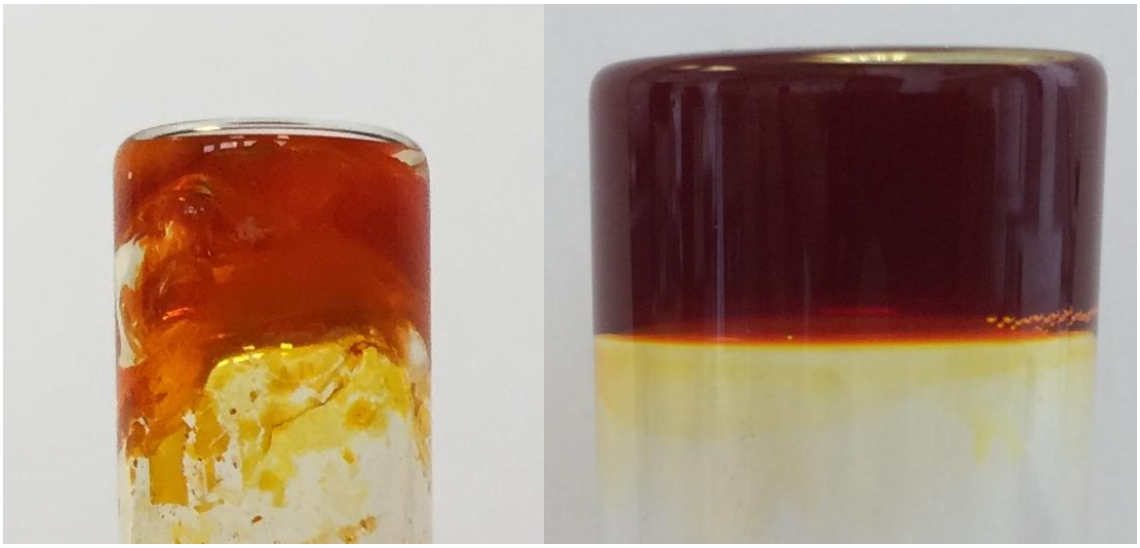

Figure 2.4. Close up photograph of gel set using concentrated HCl (left) and set with GdL (right). The differences in homogeneity are apparent with the GdL set gel having a highly uniform structure, when compared with the HCl set gel.

GdL offers the means to slowly reprotonate the LMWG, resulting in a gel that is more reproducible and likely exhibit a higher final mechanical strength.[34,35] Using GdL with this system did indeed result in the formation of a homogeneous and highly reproducible supramolecular hydrogel. In order to obtain chemical characterisation of the gelator molecules themselves, the gel was dried and the residue repeatedly washed with water, a process that was essential to remove any residual gluconic acid/gluconate salt that had arisen from the hydrolysis of GdL.[35] The use of ^{1}H NMR, ^{13}C NMR, FTIR and mass spectroscopy confirmed the formation of the trihydrazone species, ***C*$_{e}$**. All chemical analyses are presented in Chapter 6.4.

Rheological characterisation of the gels set using GdL materials properties was preformed and gave insight into the supramolecular network structure of the solid phase of the material. After the addition of GdL, time sweep rheology experiments were used to characterise the transition from sol to gel of the reaction mixture. Using nine mole equivalents of GdL resulted in the gel reaching its most mechanically robust state, in terms of maximum *G′*, after approximately three hours (Figure 2.5).

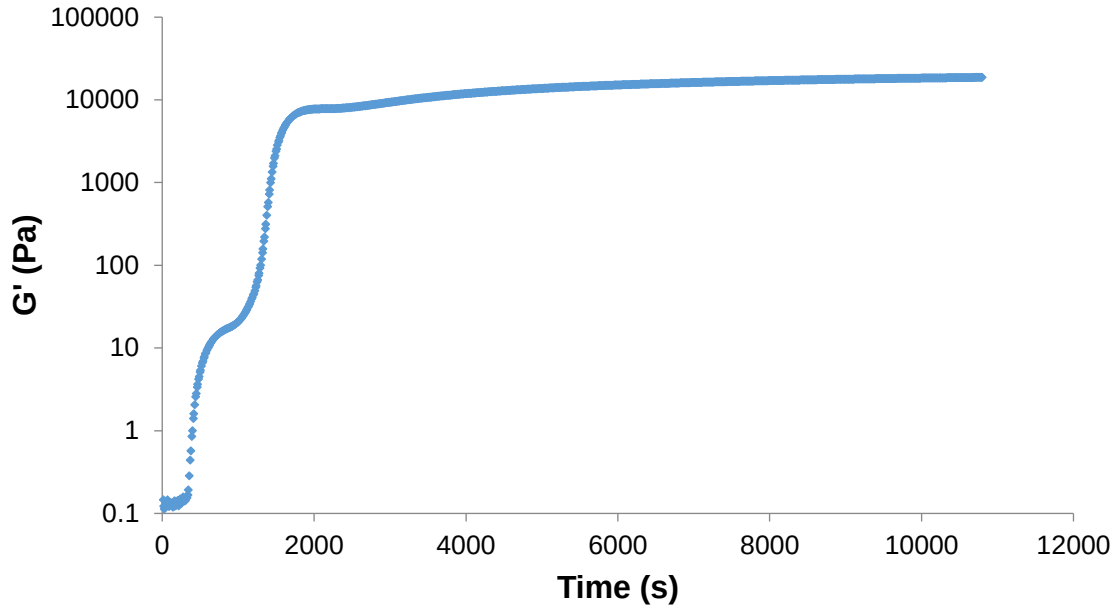

Figure 2.5. Time sweep experiment results for the ***C*$_e$** gel set using nine equivalents GdL (added four hours after the mixing of ***I*** and ***II***) . Blue diamonds (◆) represent the evolution of *G′* as a function of time.

By preforming a time sweep, the data acquired allowed determination of the Avrami constant for gelation sample. The Avrami constant is a useful method of quantifying the kinetics of a phase change.[36,37] More recently it has been used to describe the sol to gel transition for supramolecular gelation systems.[38,39] The use of the Avrami equation, which is used to determine the Avrami constant, relies on the general sigmoidal profile for the extent of transformation from one phase to another.

$$\ln(1 - X_{cr}) = -kt^{D} \qquad \textbf{(equation 1.)}$$

The work of Avrami is generally thought of as relating to the formation of bulk crystals, it describes how phase and ordered growth kinetics relate to physical properties such as temperature and concentration. This also means that different morphologies can arise from different growth rates.[36,37] Liu used the foundations laid by Avrami to develop a method where by the growth of the fibres involved in the formation of the three-dimensional supramolecular gel networks could be characterised *in situ*. The work of Liu describes the Avrami constant as the fractal dimension, however, throughout this work the term Avrami constant will be used.[40] The general form of the Avrami constant (equation 1.) where k = constant, t = time and X_{cr} = the systems crystallinity which is

equal to $\phi(t)/\phi(\infty)$, where $\phi(t)$ is the volume fraction of crystal materials t, and $\phi(\infty)$ is $\phi(t)$ at $t \rightarrow \infty$. D describes the dimensions in which the bulk crystal grows, with rod-like growth described by $D = 1$, plate like crystals described by $D = 2$ and spherulite growth described by $D = 3$. By considering the relationship proposed by Einstein between relative viscosity and volume concentration of suspension of spheres[41,42] it is possible to relate X_{cr} to specific viscosity η_{sp}. Equation 2 describes specific viscosity of a system in terms of the complex viscosity η^*, and the viscosity of the medium in which the phase change is taking place, η_0.

$$\eta_{sp} = \frac{\eta^* - \eta_0}{\eta_0} \qquad \textbf{(equation 2.)}$$

It is possible to define the crystallinity of the solution in terms of η^* and η_0 with respect to time as can be seen in equation 3.

$$X_{cr}(t) = \frac{\phi(t)}{\phi(\infty)} = \frac{\eta_{sp}(t)}{\eta_{sp}(\infty)} = \frac{\eta^*(t) - \eta_0}{\eta^*(\infty) - \eta_0} \qquad \textbf{(equation 3.)}$$

With equation 3 it possible to observe how the viscosity of the solution as a function of time can be used to determine X_{cr}. Viscosity is a rheological property, with this in mind it is possible to use other rheological material properties to determine X_{cr}. Although gels do exhibit a relatively high degree of long-range order, they are not strictly crystalline, in most cases. With this in mind, from now on X_{cr} will be discussed as X, which represents gelation as opposed to crystallinity. With a supramolecular gel's rheological characterisation the elastic modulus G' is representative of the materials elastic, solid-like behaviour.

$$X = \frac{G'(t)}{G'(\infty)} \qquad \textbf{(equation 4.)}$$

Equation 4 shows the relationship between the elastic modulus at time t, $G'(t)$ and it as $t \rightarrow \infty$, $G'(\infty)$. The information required to solve for X can be obtained from the time sweep experiments that were performed on the gel as it set. $G'(\infty)$ is defined as the average value for the last 20 measurements of G'. The values of $G'(t)$ used are up to ~ 10 Pa,

where generally the rate of increase in G' is less than 0.1 Pa per measurement. The rate of increase in G' is important, as below 0.1 Pa per measurement, fibre growth is the key factor in the increase in G'. When this rate exceeds 0.1 Pa per measurement the branching and entangling of the existing fibres becomes an increasingly significant factor, as this marks the point at which the system moves from fibre growth to the onset of gelation.[40] With these factors in mind, the Avrami constant can be determined from equation 5.

$$ln\left(ln\left(\frac{1}{1-X}\right)\right) = ln(K) + Dln(t) \qquad \textbf{(equation 5.)}$$

X can be replaced with equation 4, K represents a constant that is related to temperature, t is time and D is the Avrami constant itself. The *in situ* reaction system discussed here relies on the addition of GdL to set the gel meaning that the term K does not have to be considered. A plot of $ln(ln(1/1\text{-}X))$ against $ln(t)$ will result in a straight line with a gradient equal to D, as shown in Figure 2.6.

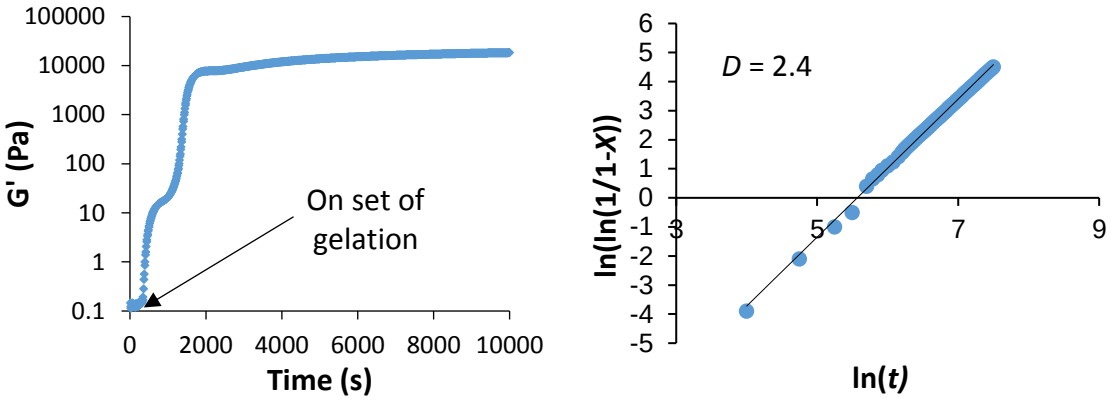

Figure 2.6. Time sweep rheology experiment for gel $\boldsymbol{C_e}$ set using GdL (nine equivalents) four hours after mixing ***I*** and ***II*** in water at pH 8, with the point defining onset of gelation marked (left). Avrami (D) constant determination for $\boldsymbol{C_e}$ using previously outlined method (right) ($R^2 = 0.99$).

In Figure 2.6 it is possible to observe an inflection point in the G' during the initial stages of gelation before the plateau is reached in the time sweep experiment. This is a known characteristic of gels set using GdL. The work of Adams defines this as the point at which protonation of the gelators removes the residual charge from the system and the possibility for inter fibril aggregation occurs.[43] The determination of the Avrami constant for the $\boldsymbol{C_e}$ gel shows that D = 2.4. This is a typical value for a system that exhibits the

fractal growth necessary for the formation of a relatively robust mechanical gel. Previous examples of this type of kinetic analysis has shown that when one gelation is used, the conditions used to test the gel can have a dramatic effect on the Avrami constant. Mechanical weaker gels will have a lower *D* value ca. ~ 1.4, this results in a gel network that exhibits a lower degree of fractal growth meaning a network with fewer, less cross-linked fibres. A *D* value in excess of the three would suggest a nucleation event that results in crystallisation as opposed to gelation, although this would mostly likely not be measureable with rheology.

After the time sweep experiment was completed, a frequency sweep experiment was performed on the same gel sample (Figure 2.7). A normal gelatinous material's response to an applied external oscillatory stress should be independent of the frequency at which that oscillatory stress is applied.[44] This results in the values of *G′* recorded over a range of frequencies being similar, resulting in a characteristic linear plot. The values for the viscous modulus *G″* should also be linear and independent of frequent, and ideally should be at least an order of magnitude less than *G′*.[45]

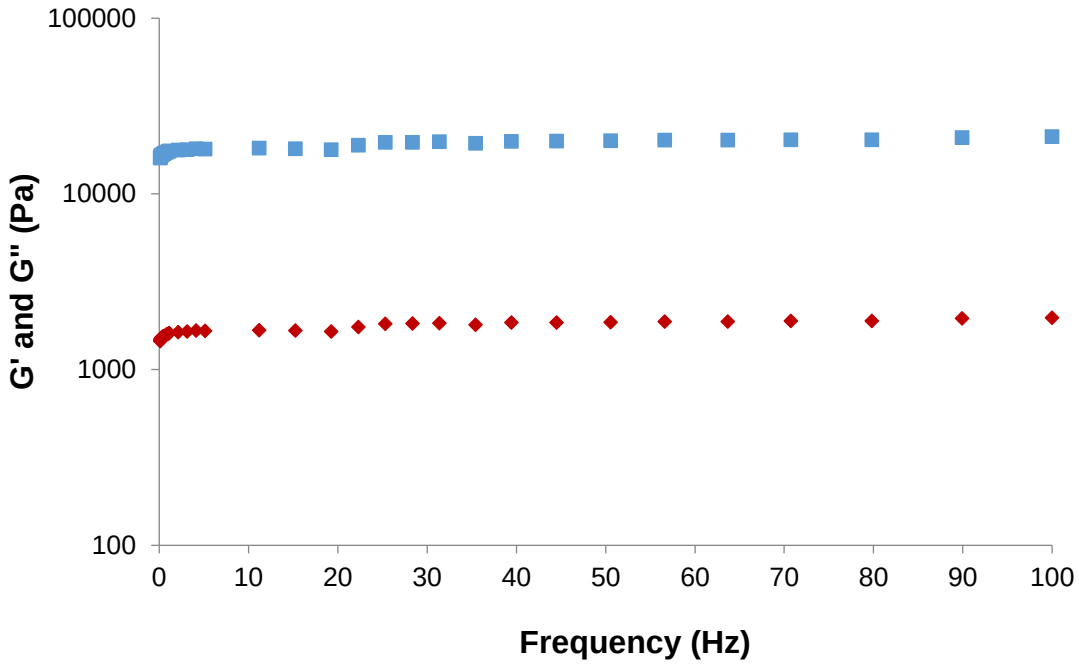

Figure 2.7. Frequency sweep experiment results for C_e gel set using GdL (nine equivalents) four hours after mixing ***I*** and ***II*** in water at pH 8. Experiment conducted immediately upon completion of the time sweep experiment. Values for *G′* represented as blue squares with *G″* represented as red diamonds.

The results of the frequency sweep experiment preformed on the *in situ* sample of the C_e confirm the gelatinous nature of the material, the G' and G'' shown to be independent of the frequency. Another example of using rheological data as a means of determining structural morphology involves the use of the cellular solid model. The cellular solid model is a model, when used to discuss the structure of supramolecular gels, that suggests a relationship of $G' \propto [\text{conc}]^{\sim 2}$.[46,47] The cellular solid model can be thought of as describing three-dimensional structure with open 'cell' areas made up of load bearing rods or struts with interconnecting crosslinks or junction points. These three-dimensionally arrange rods and junction points will deform by bending which would give rise to the material elastic properties. The C_e gel could be analysed in terms of the cellular solid model by preforming a number of frequency sweep experiments on various mixtures of ***I*** and ***II*** that will give different final concentrations of the gelator molecule C_e.

As can be seen from Figure 2.8, the C_e gel does show a good fit with the cellular solid model with a relationship of $G' = 0.10[C_e]^{2.02}$. When this is considered along with the previously determined Avrami constant, which describes the fractal growth nature of fibres that entangle with one another, we can comfortably say the gels show a cellular solid structure/network.

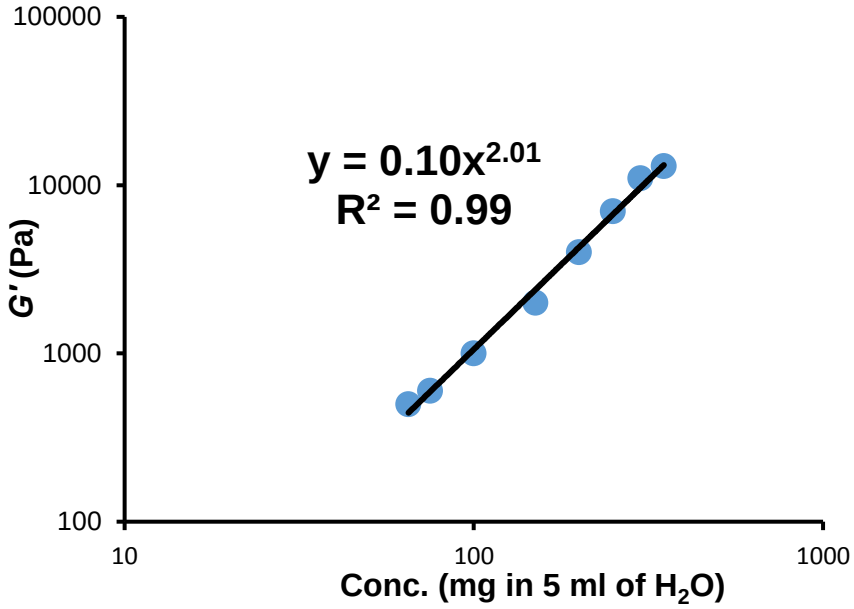

Figure 2.8. Concentration study for *in situ* formed C_e gel. Straight line gives the relationship, $G' = 0.10[C_e]^{2.02}$. Data points represent the G' value obtained at specific concentrations of C_e (●) This confirms the proportional relationship between G' and [gelator] for this system agrees with what would be expected for the cellular with the gradient of the line = 2.02 ($R^2 = 0.96$).

With time sweep experiments showing the transition of the material from sol to gel, and frequency sweep experiments proving that the material formed is indeed gelatinous in nature, an experiment should be performed on the gel that measures its mechanical strength. This can be quantified as the maximum external stress that can be applied to the gel before it yields and breaks. As can be seen in Figure 2.9, when the applied external force reaches a value of approximately 450 μNm, the gel begins to yield and break. This sheering of the gel is an important value in the characterisation of supramolecular gels as it defines the point at which the gel structure is perturbed to the point of collapse. The rheological studies conducted on this gel have predicted a cellular structure formed through an entangled fibrous network, something that had not yet been directly observed visually.

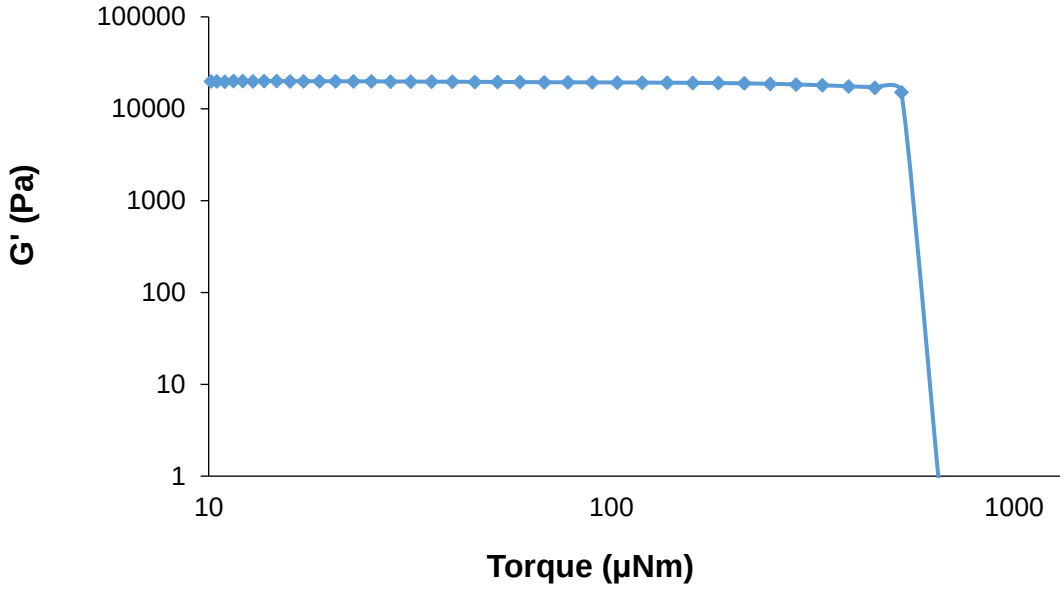

Figure 2.9. Stress sweep experiment results for the C_e gel set using GdL that was described previously. Blue diamonds represent the G' of the gel at any given time. Region of rapid decrease in G' represents yield point.

In order to determine the morphology, and confirm the cellular solid network of the C_e, SEM was utilised in order to give an impression of the gels microscale structure. While it must be appreciated that in order to image gel samples using SEM they must be well dried and in general have a thin gold coating applied to aid conductivity, this may result in a collapse of the cellular network and potential loss of fine detail. However, it can still give an accurate impression of the native gels morphology.

The SEM images obtained for dried samples of C_e (Figure 2.10) clearly shows the high aspect ratio gel fibres that were expected for this particular gelation system. These fibres would appear to average approximately 65 nm in diameter, with molecules of C_e having an approximate diameter of 18 Å. It could be calculated that the fibres imaged by SEM had an approximate cross-section equivalent to 36 molecules of C_e lying edge to edge. While this number is may not be completely accurate, it does offer an approximation of scale for the size of these supramolecular fibres.

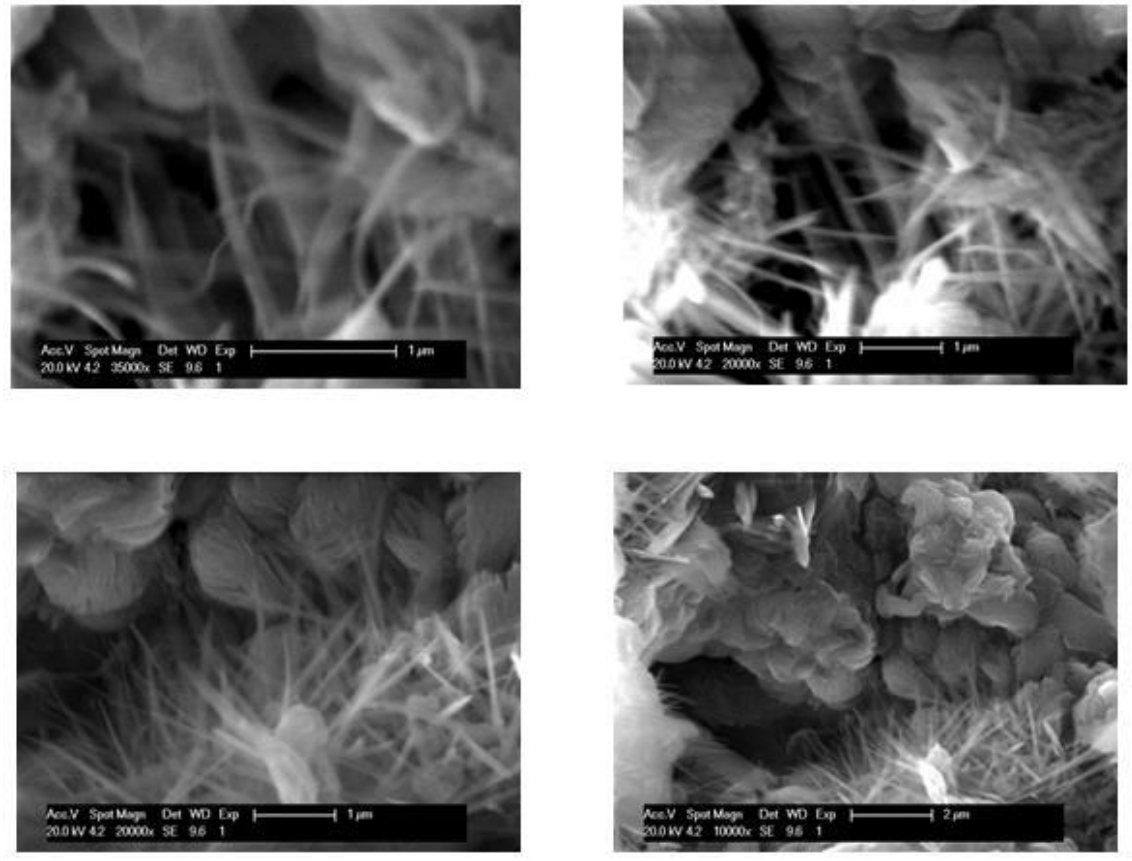

Figure 2.10. SEM images of dried samples of C_e gel. The fibrous morphology of the gel network can be clearly seen in the images along with crystallites that can be attributed to the presence of gluconic acid/gluconate salts or sodium salts that arise due to the addition of sodium hydroxide.

In attempts to set gel C_e GdL was added to the reaction mixture immediately after the addition of components ***I*** and ***II***. Previously the formation of the C_e had resulted from ***I*** and ***II*** being mixed in water and allowed to react for four hours before the addition of GdL. Instant addition of the GdL did indeed result in the formation of a gel, however it was visual different to what one would expect for the gel C_e. This early addition of GdL gave rise to a gel with a striking orange colour as opposed to the dark red hue of gel C_e

(see Figure 2.11). This observation suggests the gel resulted in the formation of a ligand that was chemically different to the one that resulted in the formation of gel $\boldsymbol{C_e}$. With this in mind, this apparent new form of the gel was designated gel $\boldsymbol{B_e}$ as it was likely that it lay on the reaction pathway between ***I*** + ***II*** and $\boldsymbol{C_e}$.

1  **2**  **3**

Figure 2.11. Photographs of gel $\boldsymbol{B_e}$ in an inverted vial orientation (1) to demonstrate its gelatinous nature and a top view to highlight its bright orange colour (2). A top view of gel $\boldsymbol{C_e}$ (3) has been included to demonstrate the noticeable difference in colour between the two gels.

Rheological characterisation of the early set gel, $\boldsymbol{B_e}$, revealed its interesting mechanical properties with respect to gel $\boldsymbol{C_e}$. While the time sweeps recorded for both gels show a similar profile, the final value of G' exhibited by the $\boldsymbol{B_e}$ gel is significantly lower than that of $\boldsymbol{C_e}$, at the same concentration. It is likely that this difference is a result of the chemical structure of the supramolecular building blocks as opposed to the form of the supramolecular assembly, something that may arise from the differences in the kinetics of the assembly process.[43] Overall the time sweep experiment showed a similar profile to that reported for gel $\boldsymbol{C_e}$, with a couple of key differences. As can be seen in Figure 2.12 there is very little incubation time, i.e. the time before the gel starts forming is minimal, with a rapid increase in G' occurring very quickly. The G' plateaus after one hour 45 minutes at a value of 2400 Pa. This G' value is almost an order of magnitude lower than the G' value recorded for the gel $\boldsymbol{C_e}$ (22000 Pa). As with the $\boldsymbol{C_e}$ gel it is possible to determine the Avrami constant for the $\boldsymbol{B_e}$ gel. This is done in the same manner as outlined previously for the $\boldsymbol{C_e}$ gel. Figure 2.13 shows the plot of ln(ln(t/1-X)) against ln(t) for the initial stages of formation for the $\boldsymbol{B_e}$ gel. The Avrami constant for the $\boldsymbol{B_e}$ is 2.2. This value is again constant with the fractal growth required for the formation of a mechanically robust hydrogel. The difference between $\boldsymbol{B_e}$ and $\boldsymbol{C_e}$ is also apparent when comparing the results of their respective frequency sweep (Figure 2.14) and stress sweep

experiments (Figure 2.15). The linear *G′* and *G″* plots that can be observed in Figure 2.14 for the ***B*$_e$** gel show it is truly gelatinous and provide a means of comparing gel samples. The yield point of the ***B*$_e$** gel is also considerably lower, indicating a weaker gel.

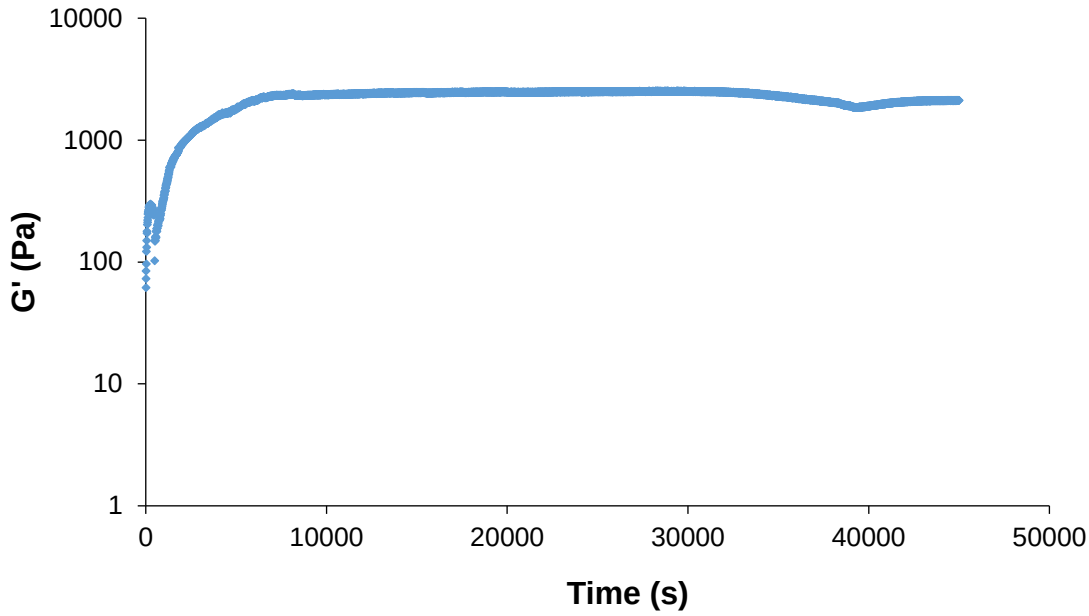

Figure 2.12. Time sweep experiment results for the ***B*$_e$** gel set using nine equivalents GdL (added immediately after the mixing of ***I*** and ***II***). Blue diamonds (◆) represent the evolution of *G′* as a function of time.

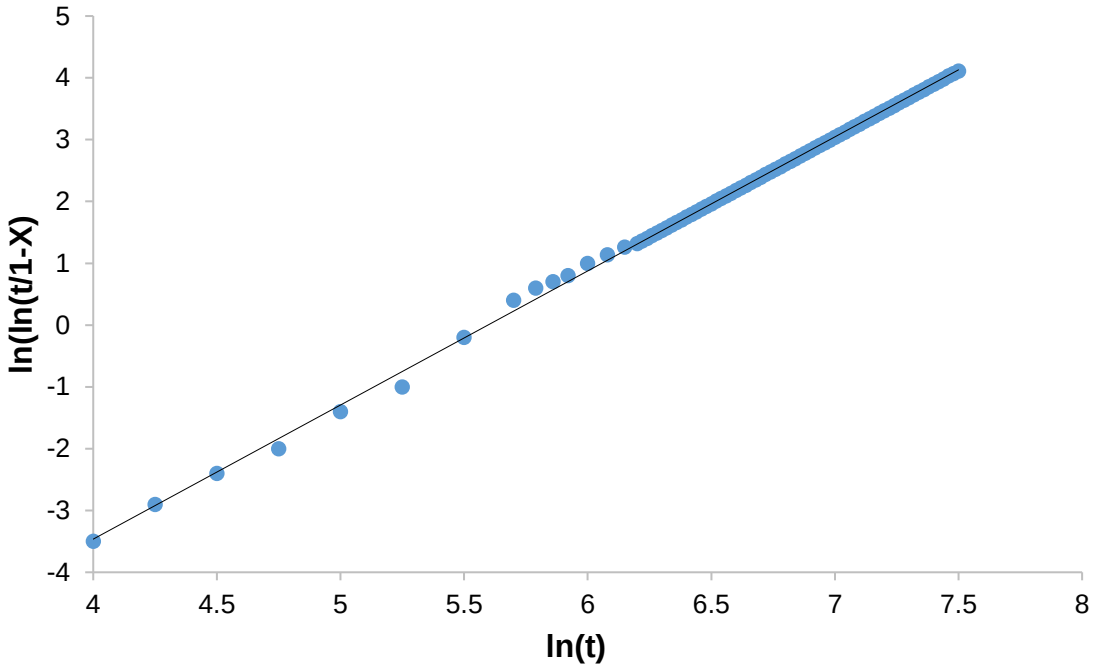

Figure 2.13. Determination of the Avrami constant (*D*) for the ***B*$_e$** gel using the previously defined period of the onset of gelation. $D = 2.13$ ($R^2 = 0.99$).

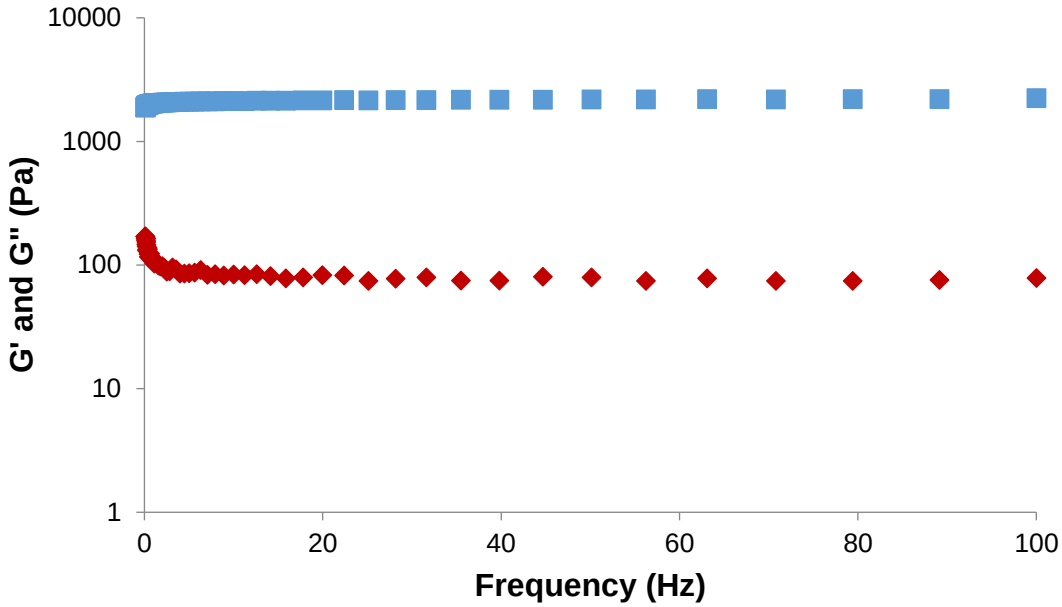

Figure 2.14. Frequency sweep experiment results for $\boldsymbol{B_e}$ gel set using GdL (nine equivalents) immediately after mixing ***I*** and ***II*** in water at pH 8. Experiment conducted immediately upon completion of the time sweep experiment. Values for *G′* represented as blue squares with *G″* represented as red diamonds.

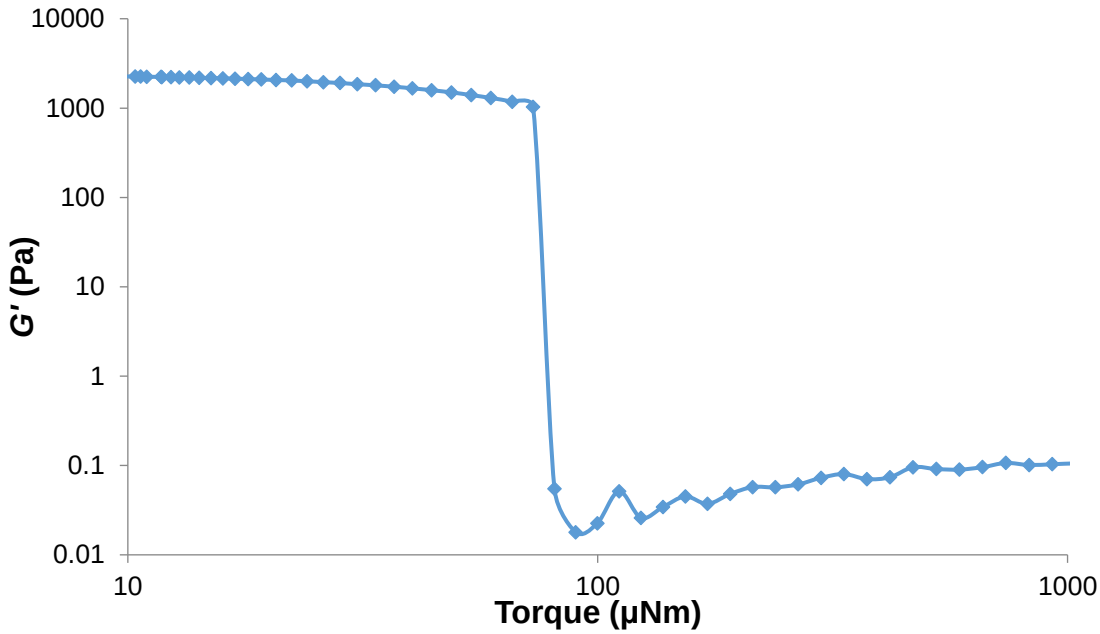

Figure 2.15. Stress sweep rheology experiment for the *in situ* produced gel $\boldsymbol{B_e}$. The stress sweep experiment was performed on the same sample and immediately after the completion of the frequency sweep experiment. *G′* represented by blue squares (■) connected by a solid line in order to guide the eye. *G′* plotted on the y-axis linearly (in Pa) and applied stress in the form of applied torque plotted logarithmically on the x-axis (in μNm).

Drying of this ***B*$_e$** gel through vacuum filtration and water washing produced a dark red powder, which could be subjected to chemical analysis in order to determine the nature of the species that had assembled in order to form gel ***B*$_e$**. What was discovered was that the ligand that was forming gel ***B*$_e$** was indeed chemically different to the ligand ***C*$_e$** that was giving rise to the formation of gel ***C*$_e$**. The emergence of the chemical species ***B*$_e$** resulted from the reaction between ***I*** and ***II*** failing to go to completion, i.e. not giving rise to ***C*$_e$**. This resulted in the formation of a di-hydrazone (Figure 2.16), with two of the aldehyde groups of ***II*** having each reacted with a molecule of ***I***. Despite this obvious chemical difference between ***B*$_e$** and ***C*$_e$**, SEM analysis showed that they demonstrated a very similar fibrous morphology (Figures 2.10 compared to 2.17). Despite there being a sufficient number of molar equivalents of ***I*** in the initial reaction mixture to result in the formation of ***C*$_e$**, the reduction of the time before the addition of the GdL always resulted in the formation of ***B*$_e$**. This was true regardless of the number of equivalents of ***II*** included in the initial reaction mixture. With the fact the reaction to form ***B*$_e$**, as opposed to ***C*$_e$**, is solely dependent on time rather than available ***II***, it can be said that this initial stage of the reaction operates under kinetic control rather than thermodynamic control.

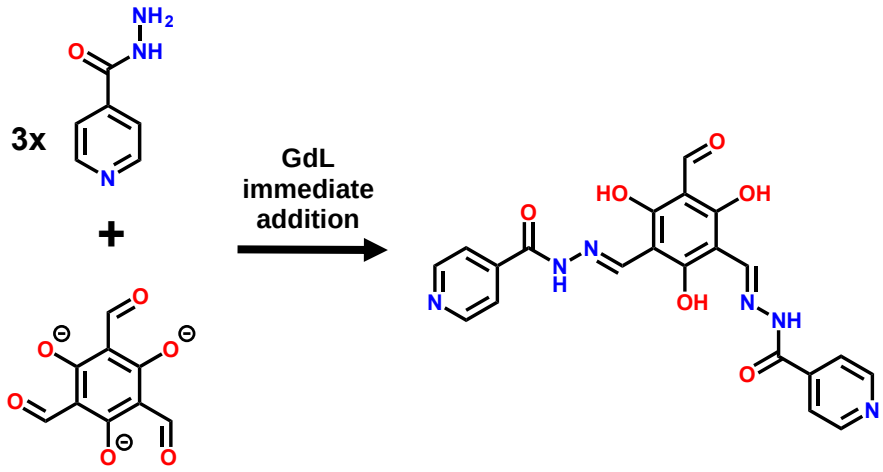

Figure 2.16. Reaction scheme for the formation of *N*',*N*'''-((1*E*,1'*E*)-(5-formyl-2,4,6-trihydroxy-1,3-phenylene)bis(methanylylidene))di(isonicotinohydrazide) (***B*$_e$**) from the combination of ***I*** and ***II*** in water at pH 8 with the immediate addition of GdL. By using a number of equivalents of ***I*** >3 the formation of ***B*$_e$**.

The presence of ***B*$_e$** and the formation of the gel ***B*$_e$** being somewhat surprising, however, it did mean there was the opportunity to conducting an interesting study into

the reaction kinetics after the mixing of ***I*** and ***II***. This was done using several different techniques to monitor the progress of the reaction.

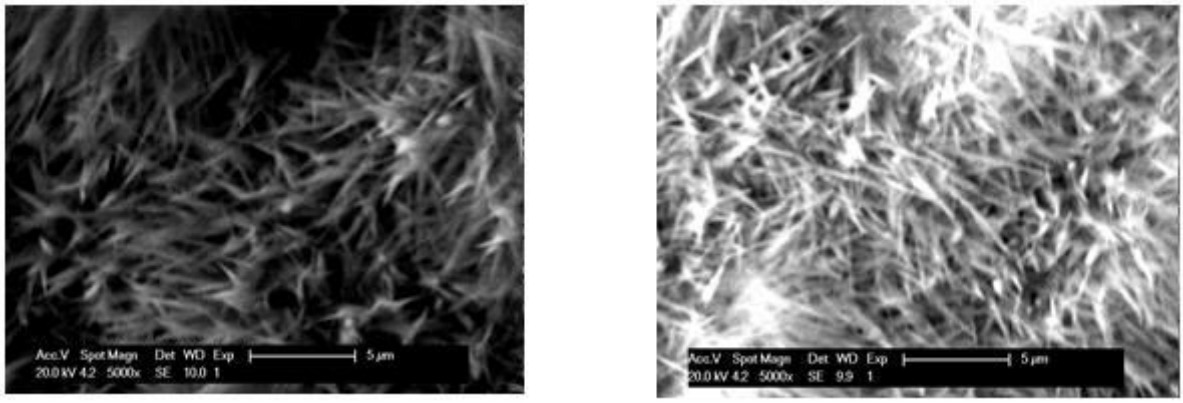

Figure 2.17. SEM images of dried samples of B_e gel. The fibrous morphology of the gel network can be clearly seen, with the sample in the left image having a thin gold coating applied, and the right image showing the gel sample uncoated.

One method that was employed involved periodically preforming an electro-spray ionization mass spec (ESI-MS) experiment on the contents of the reaction mixture. This would give an idea of the relative abundances of ***I*** relative to both B_e and C_e. What this analysis revealed was a more complete picture of the reaction pathway from ***I*** to C_e. The combination of ***I*** and ***II*** results in a stepwise reaction to form C_e, with the reaction proceeding through a singly reacted mono-hydrazone (A_e) before the di-hydrazone B_e is formed, with this finally giving way to the tri-hydrazone C_e.

The existence of A_e, while not entirely surprising, had not been observed in any quantity in the chemical analysis conducted on the B_e and C_e gels that had been set previously. By plotting the normalised relative abundances against time, a graph of reaction kinetics can be produced (Figure 2.18). From this graph it is possible to see the reason that A_e had not been observed until now, this is due to its very short lifespan relative to the other incompletely reacted species B_e. A key feature of the data is that the ESI-MS experiment preformed 15 minutes after the reaction had begun shows the species B_e representing 98.3 % of the maximum possible total composition of the mixture relative to ***II***. C_e makes up the rest of the maximum theoretical hydrazone composition at 1.7 %, with no evidence of ***I*** or A_e being present. Although the conversion of starting materials through A_e to B_e is relatively quick, the reaction from B_e to C_e takes much longer, something that is perhaps surprising given the excess of ***I*** present. A reason for this maybe the formation of soluble supramolecular aggregates that act as a retardant to the chemical reaction.

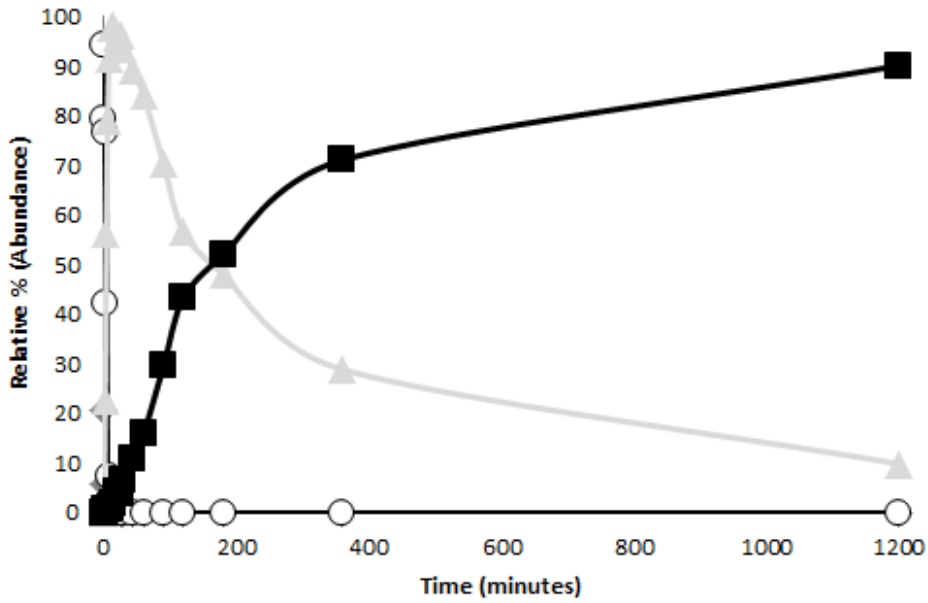

Figure 2.18. Determination of the kinetic data of the reaction between ***I*** and ***II***. The graph shows how relative normalized percentage abundances of the species present within the reaction mixture change with time as determined by ESI-MS. C_e = ■, B_e = ▲, A_e = ◆ and ***II*** = ○.

As well as using ESI-MS to determine relative abundances of the reaction products, UV-Vis spectroscopy could be used to determine the concentration of ***II***, B_e and C_e, or their respective dissolved anionic species, in solution at any given time as the reaction progresses. In order to monitor the reaction using UV-Vis spectroscopy in combination with the Beer-Lambert law, it was first necessary to determine the molar absorption coefficients (ε) for both B_e and C_e. This was done using samples of B_e and C_e that had been previously isolated and purified from corresponding gel samples. These sample were then used to make solutions with different, known concentrations, with each of these samples having their absorption recorded at specific wavelengths. A plot of concentration against absorption should give a straight line when relatively small concentrations are used. The gradient of this straight line represents the molar absorption coefficient, a measure of how effectively a species absorbs UV-Vis light. In recording the various UV-Vis spectra at different concentrations of both B_e and C_e required for molar absorption coefficient determination, the best wavelengths at which to determine the concentration of each of the species became apparent. As can be seen in Figure 2.19, the spectra for B_e features a significant secondary absorption at 300 nm, with no feature in the C_e spectra.

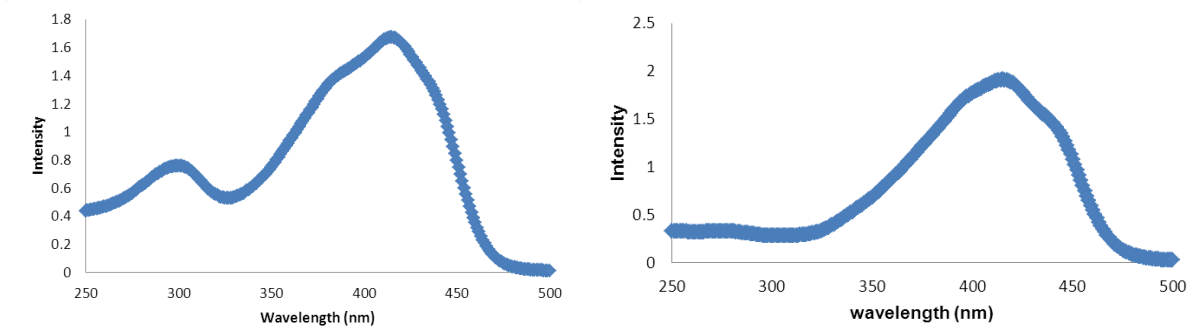

Figure 2.19. UV-Vis spectra for samples of B_e (left) and C_e (right). Spectra obtained for samples of B_e and C_e, at a concentration of 1.25 μM, that had previously been isolated from their corresponding gels before being redissolved in water ,and their spectra recorded.

This 300nm peak is in addition the primary absorption centred on 415 nm, that is present in the spectra of both B_e and C_e. This would suggest that as the reaction processes, a decrease in the absorption at 300 nm would be observed coinciding with an increase in the absorption value observed at 415 nm. With this theory in mind the molar absorption coefficients for B_e and C_e were determined at both 300 and 415 nm (Table 2.1).

Table 2.1 The determined molar absorption for B_e at 300 nm (ε_{B300}), 415 nm (ε_{B415}) and C_e at 300 nm (ε_{C300}) and 415 nm (ε_{C415}).

Coefficient	Value ($molL^{-1}cm^{-1}$)
ε_{B300}	378000
ε_{B415}	846000
ε_{C300}	141000
ε_{C415}	945000

Once the ε values had been determined using previously isolated samples of B_e and C_e, a UV-Vis experiment was preformed where ***I*** and ***II*** were mixed in water at pH 8 and an absorption spectra was recorded periodically. The pH 8 reference water sample contained an equal quantity of ***I***, this was to ensure that any absorption recorded arose solely from the presence of B_e and C_e and potentially A_e, in the initial stages of the reaction. However, because absorption spectra were only recorded ten minutes after the mixing of ***I*** and ***II***, the findings of the ESI-MS kinetic experiments would suggest that the presence A_e would be not significant at the times at which absorption were recorded. As can be seen in Figure 2.20, the predicted decrease in the absorption at 300 nm did occur, along with the corresponding increase in the absorption at 415 nm as the

conversion from $\boldsymbol{B_e}$ to $\boldsymbol{C_e}$ occurred. Recording of the spectra was done until the there was no significant change in the spectra, at which point the reaction was thought to have gone to completion and the maximum possible concentration of $\boldsymbol{C_e}$ had been reached.

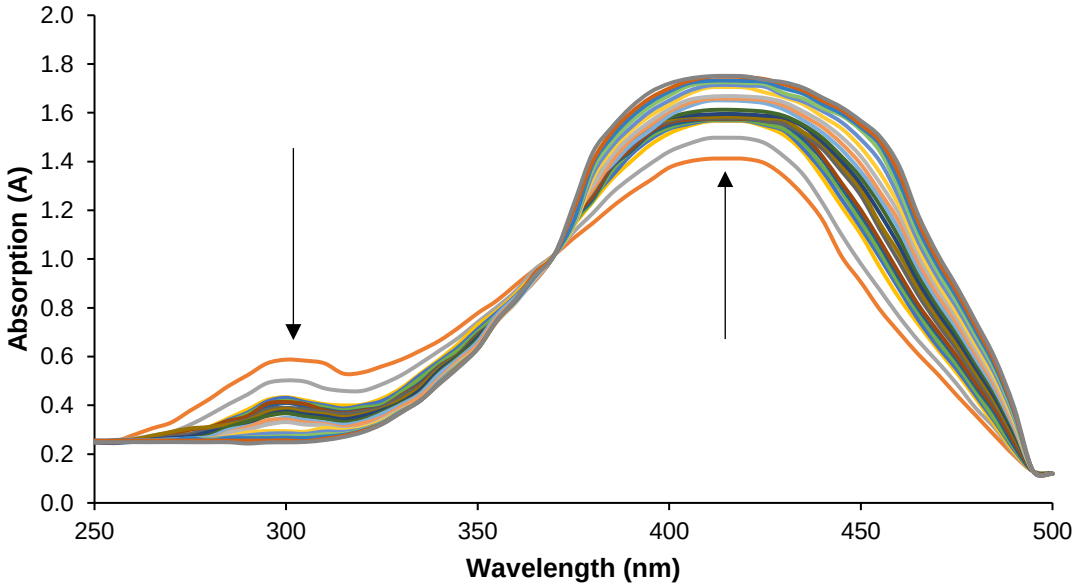

Figure 2.20. Collection of UV-Vis spectra for the reaction between ***I*** and ***II***. Spectra recorded at 10, 20, 30, 40, 50, 60, 70, 80, 90, 100, 110, 120, 130, 140, 150, 160, 170, 180, 360 and 1200 minutes with arrows highlighting the decrease in absorption at 300 nm and increase in absorption at 415 nm.

Equation 6 represents the Beer-Lambert law, where C is the concentration of the species being measured, A is the absorption at a given wavelength and ε is the molar absorption coefficient of that species measured at that given wavelength. l is the path length of the sample, i.e. the distance of solution the incident light has had to travel through. However, during this experiment l = 1, so this simplifies the equation. The absorption is assumed to be a direct addition of two species in the solution. Calculation of the of the concentrations of $\boldsymbol{B_e}$ to $\boldsymbol{C_e}$ and a subsequent plot against time gave rise to a very similar kinetic profile as that obtained from the ESI-MS experiment (Figure 2.21).

$$c = \frac{A}{\varepsilon l} \qquad \textbf{(equation 6.)}$$

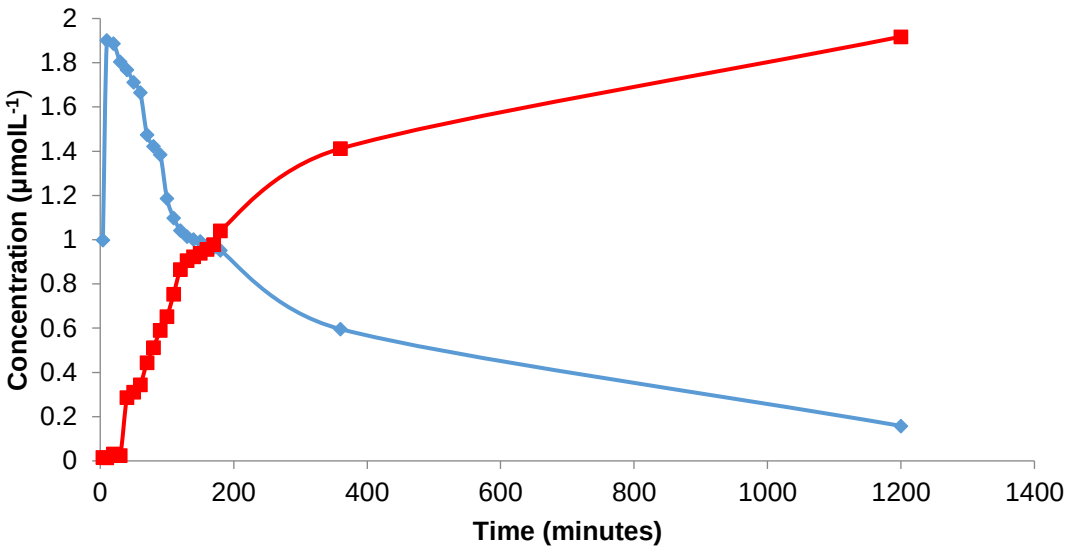

Figure 2.21. Kinetic data for the reaction between ***I*** and ***II***, recorded using UV-Vis spectroscopy, and the subsequent conformation of $\boldsymbol{B_e}$ (■) as a function of time. The reaction of $\boldsymbol{B_e}$ with ***I*** to form $\boldsymbol{C_e}$ is also reported (◆). Lines added between data points to guide the eye.

When incorporated into the solid-phase of the gel state, $\boldsymbol{B_e}$ demonstrates a high level of stability, that is to say a high purity sample of $\boldsymbol{B_e}$ can be isolated from the gel through vacuum filtration many months after the initial setting of the gel. The reason for this perceived thermodynamic stability of $\boldsymbol{B_e}$ in the solid-state, despite there still being a significant amount of unreacted ***I*** present within the gel solution, is that a mass transfer limitation mechanism becomes significant once the gel has formed. There is no detectable $\boldsymbol{B_e}$ in the solution. This stops the ***I*** molecules reacting with the aldehyde group of $\boldsymbol{B_e}$, meaning that $\boldsymbol{C_e}$ is not formed.

2.4.1 High pH set gel

Conceptually the system that has been outlined so far is not particularly difficult to understand. It involves the stepwise formation of a trihydrazone-based gelator that is arrived at through going through the mono- and di- hydrazone "intermediates" starting from a trialdehyde. There is however an additional layer of complexity that can be added to this system, it is this complexity that allows a third gel to be set from the single ***I*** + ***II*** starting point.

Pathway complexity is a term used to describe a system where the product of a reaction or assembly process can be altered based on any number of external factors.

Chemical pathway complexity may arise from a multi-reactivity dynamic reaction system as has been demonstrated so far in this study. The existence of the enol tautomeric form in the gels discussed so far is interesting in that most similar species reported in the literature exist in the keto form.[18,48,19] This raised the question, is the keto form of $\boldsymbol{C_e}$ accessible for this system? If so, what species would represent the more stable of the discussed products for this system. The serendipitous discovery of a yellow gel that merged from the same reaction mixture that produced the $\boldsymbol{B_e}$ and $\boldsymbol{C_e}$ gels offered hope that the keto form had been found.

The method for producing the gels formed with *in situ* synthesised $\boldsymbol{B_e}$ and $\boldsymbol{C_e}$ requires the aqueous solution where the *in situ* reaction takes place to have a pH of 8-9 in order to ensure the solubility of ***II*** and the reaction products $\boldsymbol{B_e}$ and $\boldsymbol{C_e}$. However, examples of the *in situ* reaction were produced where the pH of the reaction exceeded pH 9. When this reaction was allowed to proceed in this pH range of 9 – 10, the yellow reaction solution solidified producing a yellow gel over a period of two hours (see Figure 2.22). This time could be reduced by increasing the pH further to the region of 10 – 12.

Figure 2.22. Photograph of gel $\boldsymbol{C_k}$ set from *in situ* reaction of ***I*** and ***II***, when the reaction was performed in a reaction solution at pH 10.5. This distinct yellow gel formed after one hour.

With the formation of this yellow gel, again starting with the reaction of ***I*** + ***II***, there are now three distinct gels that have been produced from this single chemical starting point. Rheological studies revealed the differences between this new gel, $\boldsymbol{C_k}$, and the previously characterised gels $\boldsymbol{B_e}$ and $\boldsymbol{C_e}$. The most noticeable feature of gel $\boldsymbol{C_k}$ is its relatively low mechanical strength. When examining the data collected for the time sweep experiment it can be seen that the G' value for gel $\boldsymbol{C_k}$ is significantly lower than the values recorded for gels $\boldsymbol{B_e}$ and $\boldsymbol{C_e}$ (see Figure 2.23). As with the previously discussed gels, a frequency

sweep rheology experiment was performed, the results of which can be seen in Figure 2.24.

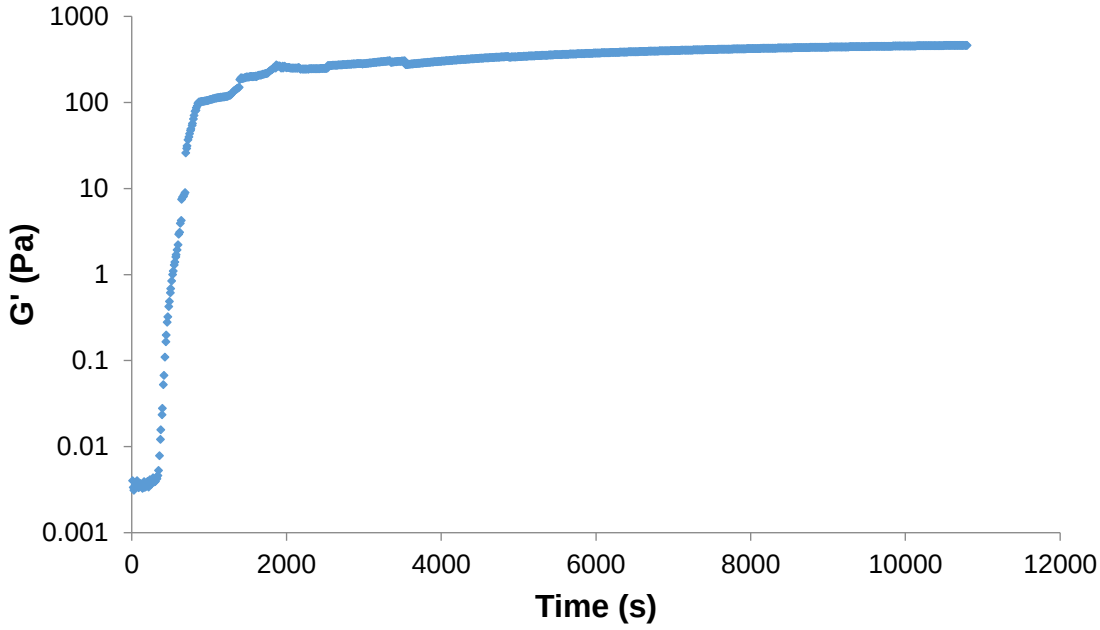

Figure 2.23. Time sweep rheology experiment for the *in situ* produced gel C_k. Gel set at a pH of 11, resulting in the G' value of the gel beginning to plateau after approximately 22 minutes, at a value of 200 Pa, before achieving a final G' value of 460 Pa after 3 hours.

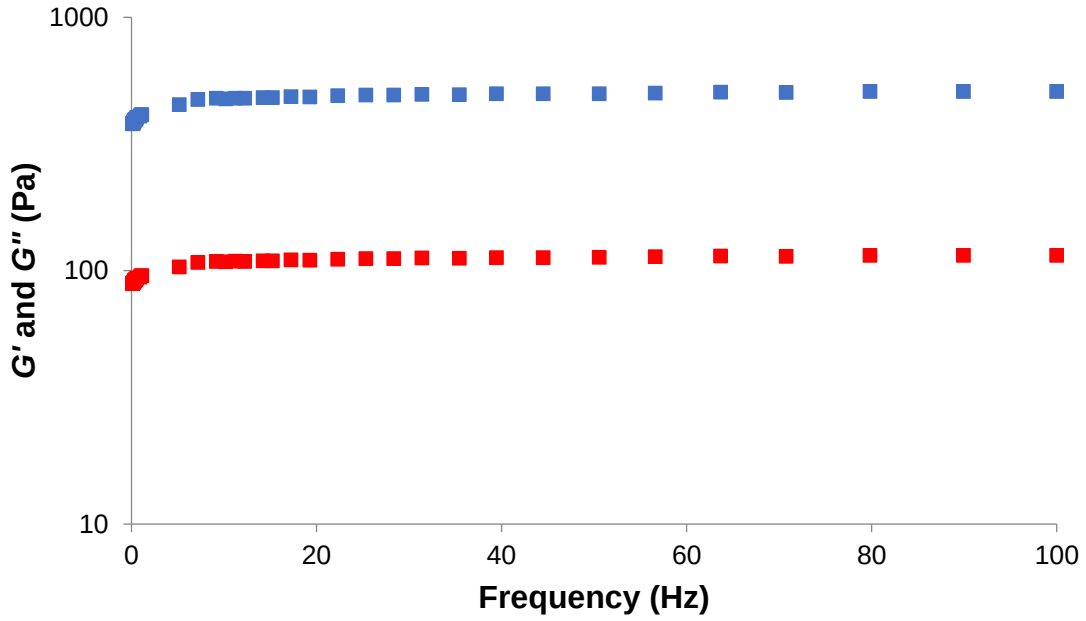

Figure 2.24. Frequency sweep rheology experiment for the *in situ* produced gel C_k. The frequency experiment was performed on the same sample and immediately after the completion of the time sweep experiment. G' represented by blue squares (■) and G'' represented by red squares (■), with G' and G'' plotted on the y-axis logarithmically and frequency of oscillation in the applied stress plotted linearly on the x-axis. G' recorded 50 Hz has a value of 500 Pa and is the value used for comparisons with other gels.

The results of the frequency sweep experiment that are shown in Figure 2.24 confirm the gelatinous nature of the gel $\boldsymbol{C_k}$. The response G' and G'' to an externally applied oscillatory stress is independent of the frequency at which that stress is applied. This is also true in cases of the gels $\boldsymbol{C_e}$ and $\boldsymbol{C_k}$. The other important aspect of the frequency sweep experiment, the ratio of G' to G'', shows that G' is significantly larger than G'' (five times great), a fact that again confirms the gelatinous nature of the material $\boldsymbol{C_k}$. As with the previous gels, the final experiment to be performed was the stress sweep experiment to determine the yield stress of the gel. The results of this experiment are shown in Figure 2.25.

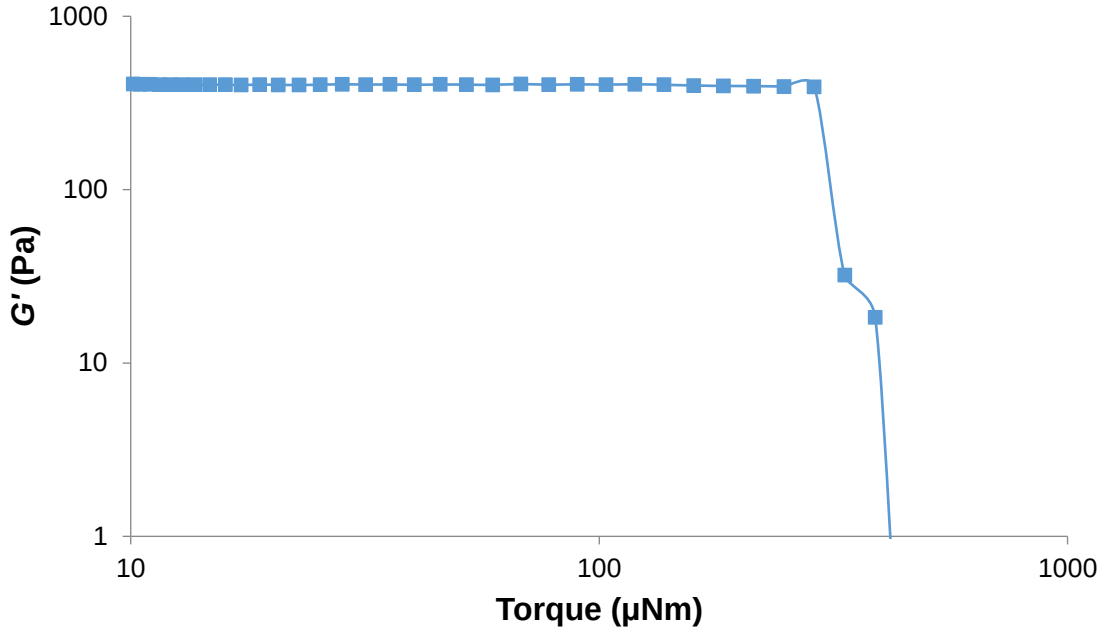

Figure 2.25. Stress sweep rheology experiment for the *in situ* produced gel $\boldsymbol{C_k}$. The stress sweep experiment was performed on the same sample and immediately after the completion of the frequency sweep experiment. G' represented by blue squares (■) connected by a solid line in order to guide the eye. G' plotted on the y-axis linearly (in Pa) and applied stress in the form of applied torque plotted logarithmically on the x-axis (in µNm).

From the stress sweep data presented in Figure 2.25 it can be seen that the yield point for gel $\boldsymbol{C_k}$ occurs when the force applied to the gel is around 290 µNm. This yield point value is less than that of the $\boldsymbol{C_e}$ (525 µNm) but higher than the yield point recorded for the gel $\boldsymbol{B_e}$ (73 µNm). The results of these rheology experiments demonstrate how three distinctly different materials have been produced from effectively the same starting point. The difference in the rheology between the gels arises not due to different assemblies or

gelators concentrations, but the difference in the chemical entities. With this in mind it stands to reason that this new yellow gel $\boldsymbol{C_k}$ set through a raise in pH of the reaction solution arises because of a third pathway within the system which gives rise to a third distinct reaction product. By drying a sample of the $\boldsymbol{C_k}$ gel, a dark yellow product could be isolated. The use of ^{1}H NMR, ^{13}C NMR and FTIR chemical analysis highlighted the difference between the chemical components of this gel, $\boldsymbol{C_k}$ and the gels $\boldsymbol{C_e}$ and $\boldsymbol{B_e}$. The analysis of the ^{1}H and ^{13}C NMR spectra allowed determination of the structure of ligand $\boldsymbol{C_k}$, which is highlighted in Figure 2.26. The $\boldsymbol{C_k}$ tautomer shows to conformers in solution, similar to what has been seen in the literature.[18,48,19]

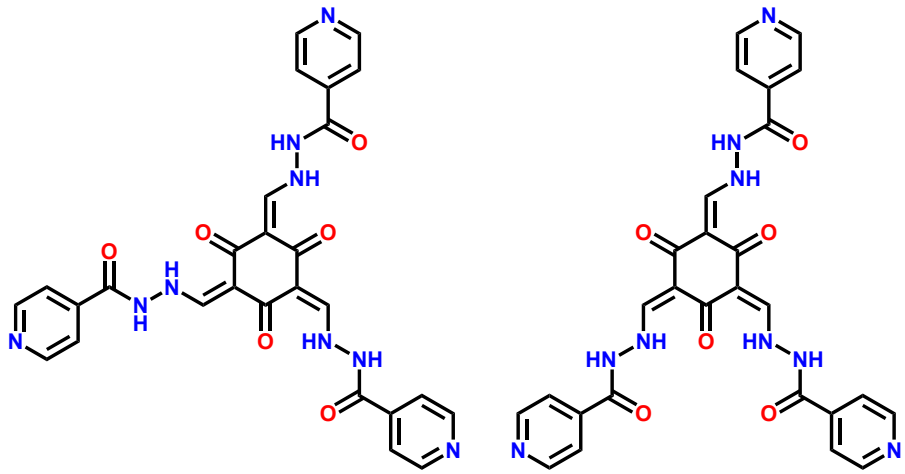

Figure 2.26. Molecular component of gel $\boldsymbol{C_k}$, the ligand $\boldsymbol{C_k}$. Two geometric isomers of the same ligand are shown, as both are evident in the ^{1}H and ^{13}C NMR spectra in the solution state. The C_3 symmetric geometric isomer is shown on the left, and the C_s symmetric is shown on the right.

2.4.2 Ex situ gelation method

The LMWGs presented so far in this chapter have all arisen through the *in situ* combination of ***I*** and ***II***, that is the solvent in which the chemical reaction occurs is the solvent that is gelled. When the ***I*** + ***II*** *in situ* reaction goes to completion, the product $\boldsymbol{C_e}$ is arrived at. There is an alternative method of preparing $\boldsymbol{C_e}$ and that is through an *ex situ* reaction. This is done through the combination of ***I*** and ***II*** in ethanol, with the resulting suspension being refluxed overnight. This *ex situ* reaction offers a convenient method to produce $\boldsymbol{C_e}$ in very good yields and high purity.

The $\boldsymbol{C_e}$ produced through this *ex situ* reaction allows for gels of $\boldsymbol{C_e}$ and $\boldsymbol{C_k}$ to be set. The *ex situ* synthesised ligand $\boldsymbol{C_e}$ can be dissolved in water, at the desired weight percentage, through the addition of NaOH until the *ex situ* synthesised $\boldsymbol{C_e}$ is fully

dissolved with the aqueous solution then having its pH adjusted up to pH 8. Once this pH had been reached two gels could be set from this solution, the addition of the GdL resulted in the setting of the red gel, $\boldsymbol{C_e}$. Raising the pH further with the addition of more NaOH produced the yellow gel, $\boldsymbol{C_k}$. Through visual inspection with the naked eye there was no way to discern between $\boldsymbol{C_e}$ and $\boldsymbol{C_k}$ gels prepared through either the *in situ* or *ex situ* synthesis methods. Chemical analysis of the dried gels showed that the chemical components of the gels remained the same when comparing like with like, prepared using either *in situ* or *ex situ* synthesis. With the gels being chemically identical, it would have been surprising if there had been any difference between the gels rheologically. This was investigated through the three standard rheology experiments. As can be seen in Figure 2.27, the $\boldsymbol{C_e}$ gel that is set using *ex situ* prepared $\boldsymbol{C_e}$ follows a similar profile for the sol to gel transition over time, after the addition of GdL, as the $\boldsymbol{C_e}$ gel prepared using an *in situ* reaction. Both samples enter the *G´*plateau region after approximately 20 minutes

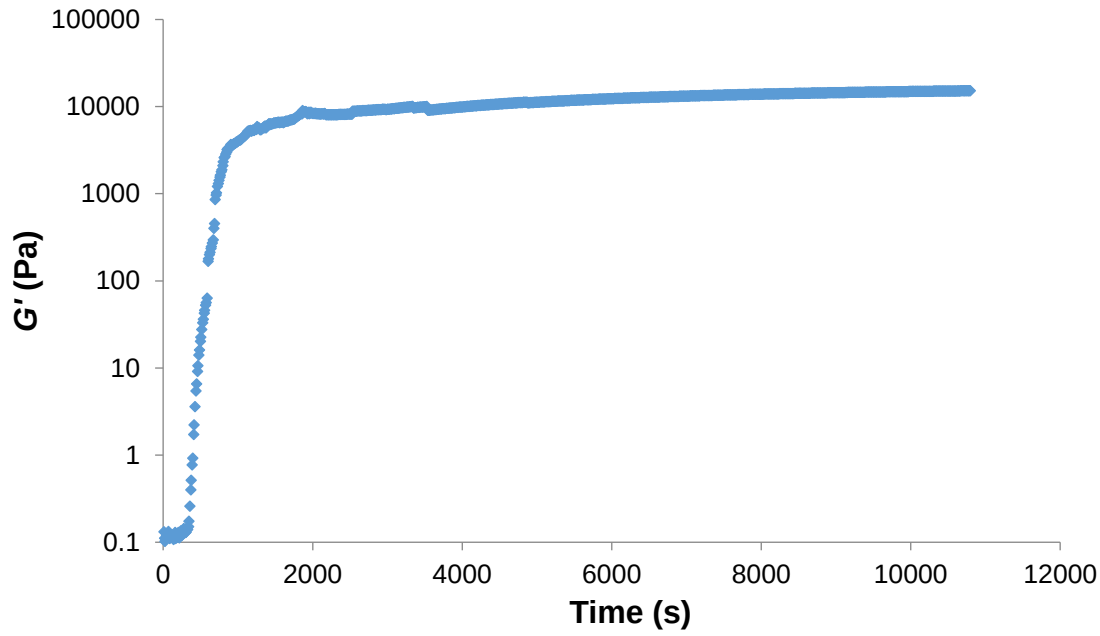

Figure 2.27. Time sweep rheology experiment for the gel set using an *ex situ* prepared sample of the ligand $\boldsymbol{C_e}$. Gel was set with the addition of GdL (nine equivalents) to give a gel of 2 wt%. The setting of the gel resulted in the *G´*value of the gel beginning to plateauing after approximately 14 minutes and achieving a final *G´*value of 15000 Pa after 3 hours.

The method for producing the gel $\boldsymbol{B_e}$ from an *ex situ* synthesised sample of the ligand $\boldsymbol{B_e}$ is also possible, although it does follow a different protocol to that discussed for *ex situ* prepared $\boldsymbol{C_e}$ and $\boldsymbol{C_k}$ gels. The production of $\boldsymbol{B_e}$ is reliant on the mass transfer

mechanism that arises because of the formation of the three-dimensional gel network composed of molecules of $\boldsymbol{B_e}$. The *ex situ* method, in ethanol, that has been described to synthesise $\boldsymbol{C_e}$ does not offer the potential for mass transfer limitation to occur. There is the potential to reduce the number of equivalents of ***I*** from in excess of three, relative to ***II***, to two. This was attempted, however, the dynamic nature of the hydrazone bonds means the product of such a reaction contains all three potential products $\boldsymbol{A_e}$, $\boldsymbol{B_e}$ and $\boldsymbol{C_e}$ in some quantity. However, $\boldsymbol{C_e}$ composed the bulk of the reaction product in ethanol. This also shows how important the gel formation is in the formation of $\boldsymbol{B_e}$. Gel $\boldsymbol{B_e}$ could be set through dissolving a sample of the $\boldsymbol{B_e}$ ligand, isolated from a previously *in situ* set $\boldsymbol{B_e}$ gel in water, with the addition of sodium hydroxide. GdL, nine equivalents, is then added to set the gels. The $\boldsymbol{B_e}$ gel prepared using the outlined *ex situ* method is again similar to the *in situ* prepared $\boldsymbol{B_e}$, when comparing the time sweep experiments (Figure 2.28).

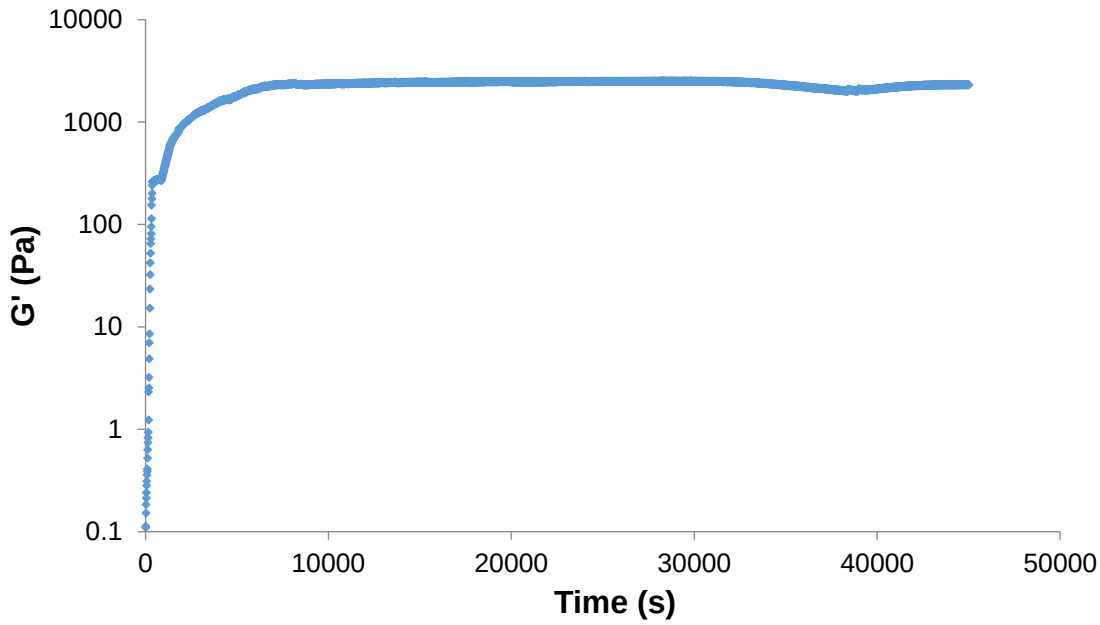

Figure 2.28. Time sweep rheology experiment for the gel set using a sample of the ligand $\boldsymbol{B_e}$. isolated from an *in situ* gel was set with the addition of GdL (nine equivalents) to give a gel of 2 wt%. The setting of the gel resulted in the *G′* value of the gel beginning to plateauing after approximately 30 minutes at a value of 2000 Pa before achieving a final *G′* value of 2300 Pa after 3 hours.

This is also true of the frequency sweeps for the *in situ* and *ex situ* prepared gels. When comparing the frequency sweeps for two $\boldsymbol{B_e}$ gels of the same wt%, one prepared with *in situ* synthesised ligand and one with *ex situ* synthesised ligand, the plots show highly comparable values for *G′* and *G″* between the two data sets. When examining the *G′* values recorded for both gels at an oscillatory frequency of 50 Hz, it was found that

both gels give rise to very similar values; 2350 Pa for the *in situ* prepared gel, and 2300 for the *ex situ* gel The results of the final rheology experiment to be conducted on the *ex situ* prepared $\boldsymbol{B_e}$, the stress sweep, can be seen in Figure 2.29.

The difference between the stress sweep experiments for the *in situ* and *ex situ* prepared $\boldsymbol{B_e}$ gels are apparent. The *in situ* prepared gel shows a gradual yield before a final decisive break occurs at 76 μNm. The stress sweep data for the *ex situ* prepared gel follows a noticeably different profile, with a sudden breaking in the gel occurring at a higher applied torque of 154 μNm (Figure 2.30). The gradual yielding of the *ex situ* prepared gel may be the result of the gel sample slipping on the rheometer, as one of the features of the $\boldsymbol{B_e}$ gel (prepared with both methods) is that it shrinks resulting in water being effectively expelled from the gel sample.[49,50]

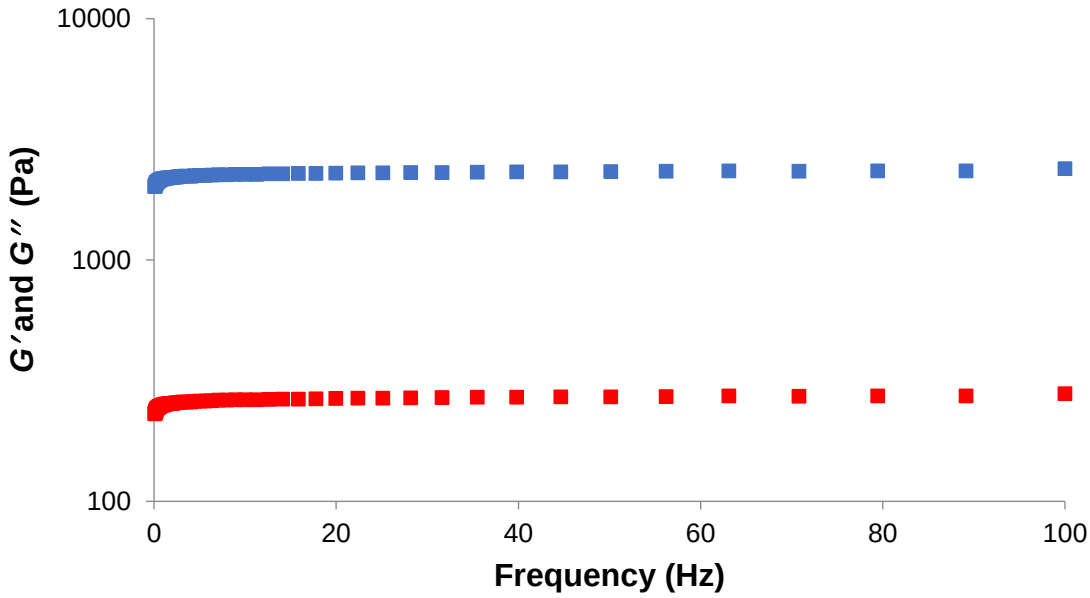

Figure 2.29. Frequency sweep rheology experiment for the $\boldsymbol{B_e}$ gel prepared using the described *ex situ* method. The frequency experiment was performed on the same sample and immediately after the completion of the time sweep experiment. *G′* represented by blue squares (■) and *G″* represented by red squares (■) with *G′* and *G″* plotted on the y-axis logarithmically and frequency of oscillation in the applied stress plotted linearly on the x-axis. *G′* recorded at 50 Hz has a value of 2300 Pa and is the value used for comparisons with other gels.

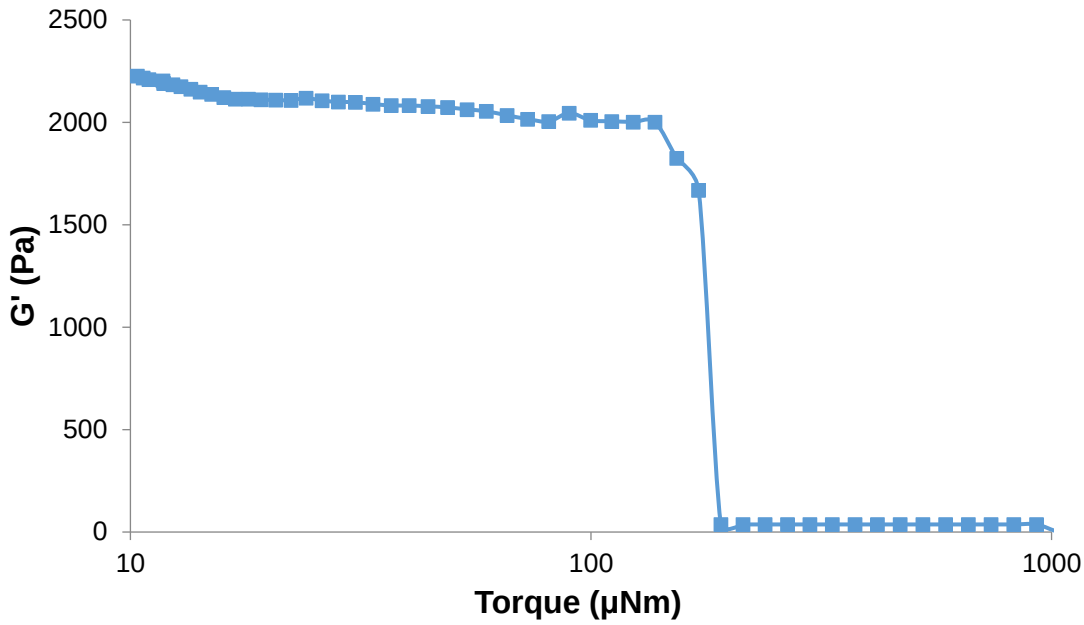

Figure 2.30. Stress sweep rheology experiment for the *ex situ* produced gel $\boldsymbol{B_e}$. The stress sweep experiment was performed on the same sample and immediately after the completion of the frequency sweep experiment. *G´*represented by blue squares (■) connected by a solid line in order to guide the eye. *G´*plotted on the y-axis linearly (in Pa) and applied stress in the form of applied torque plotted logarithmically on the x-axis (in μNm).

The comparisons between the gels $\boldsymbol{B_e}$, $\boldsymbol{C_e}$ and $\boldsymbol{C_k}$ prepared using *in situ* and *ex situ* revealed no significant difference in terms of the gels responses to mechanical stress. Regardless of whether the gels are prepared *in situ* or *ex situ*, the mechanical properties of the gels remain the same. This implies that regardless of the method used to synthesis the ligand, the supramolecular structure that gives rise to the formation of the gel is identical.

2.5 Supramolecular assembly

As mentioned previously, the use of SEM and TEM imaging has shown the presence of a fibrous network in all three gels discussed in this chapter, $\boldsymbol{B_e}$, $\boldsymbol{C_e}$ and $\boldsymbol{C_k}$. The nature of these three-dimensional assemblies could be characterised further through the use of x-ray diffraction techniques. The diffraction techniques used where powder x-ray diffraction (PXRD) and single crystal x-ray diffraction (SCXRD). Both techniques have advantages and limitations when used in the analysis of a system such as the one discussed in this chapter. While SCXRD offers the opportunity to obtain atomic resolution information on the crystal structure of the gelator molecules, it relies on the

growing of a single crystal of the gelator of sufficient size and quality required for diffraction experiments. The production of such a crystal can often present a significant challenge.[51,52] PXRD is a much more versatile technique, with it being possible to collect diffraction patterns on any sample that displays any long-range order. Of course with this versatility comes the caveat that significantly less information is collected, making full structural characterisation of the gelator sample much more difficult. While samples of the gelators may indeed feature long-range order, they are not crystalline, resulting in PXRD patterns that are not sufficiently detailed to allow solving of the crystal structure. This however does not mean that no useful information can be obtained from the PXRD patterns. Of course, in order to obtain a PXRD pattern for a gel sample, it has to be dried first. While this means the diffraction is not due to the gels three-dimensional network in its native state, drying is likely not to affect many of the important supramolecular interactions that will be discussed in this section.[53] It is worth noting here that drying of supramolecular gel samples may induce a phase change. While it is difficult to know if a phase change has occurred when analysing a dried sample, it is something that is worth considering when examining the obtained diffraction data.

2.5.1 PXRD

The formation of the three-dimensional network within supramolecular gels mean this type of material lies somewhere between crystalline and amorphous. While not highly ordered in the way a single crystal is, gels do exhibit a degree of long-range one-dimensional order. This order is the product of the self-assembly that occurs through a nucleation growth mechanism. Because of this, PXRD analysis can be used to gain an insight into the structure of the gels discussed in this chapter.

In situ and *ex situ* prepared samples of each of the individual gels were produced, before being dried out to yield the corresponding powder samples. This drying of the gel samples may have a profound effect on the structure of the three-dimensional solid-phase network. With this in mind, there are examples of analyses of gels in the literature developing techniques, such as fibre x-ray diffraction[54] and small-angle neutron scattering experiment,[55] in which partially dried or wet gels are analysed. However, even with the potential alterations to the three-dimensional network, the interactions and spacing between the individual constituent molecules that make up the fibres often are unaffected. The powder patterns for all three gels, $\boldsymbol{B_e}$, $\boldsymbol{C_e}$ and $\boldsymbol{C_k}$ prepared through both the *in situ* and *ex situ* methods can be seen in Figure 2.31. All six patterns are dominated

by a reflection centred on an average angle of 26.3 °, which correpsonds to an average *d*-spacing of 3.36 Å . This *d*-spacing likely arises from the distance between opposing faces of adjacent gelator molecules within the fibre columns, and represents recognisable π-π interactions. There is the possibilty to obtain additional structure and confirmational information about each of the gelators should a single crystal be obtained.

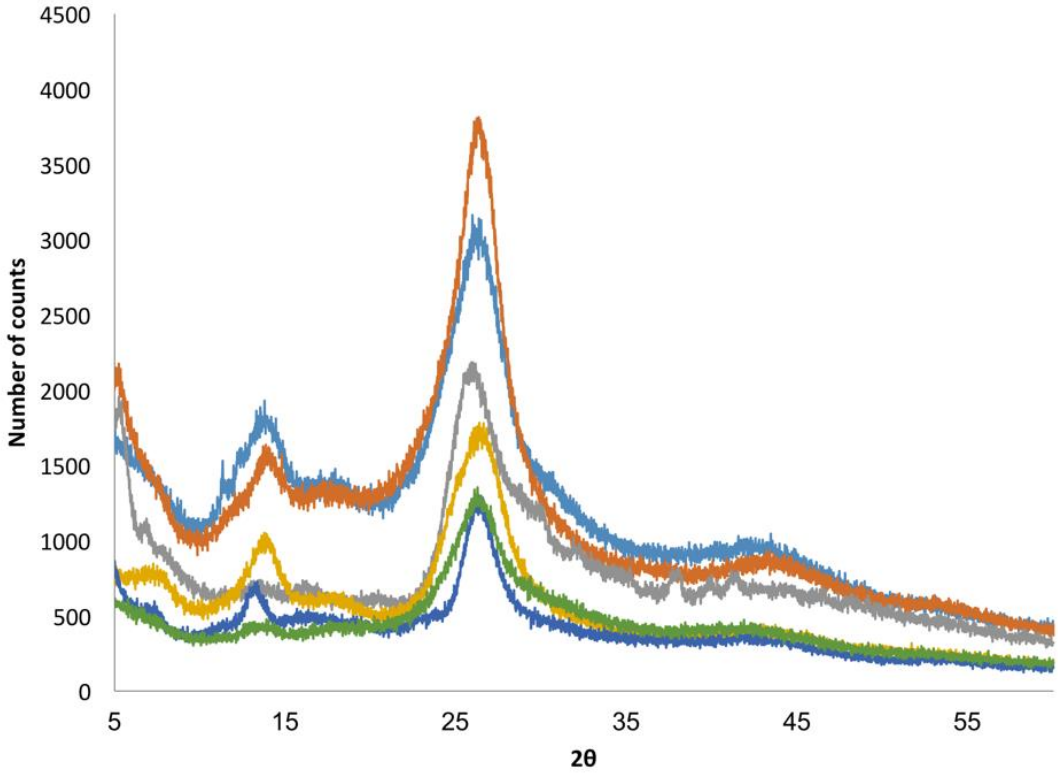

Figure 2.31. PXRD patterns for each of the three gels prepared by both the *in situ* and *ex situ* methods. ***B*ₑ** *in situ* coloured light blue (—), ***B*ₑ** *ex situ* coloured light orange (—), ***C*ₑ** *in situ* coloured dark orange (—),***C*ₑ** *ex situ* coloured dark blue (—), ***C*ₖ** *in situ* coloured grey (—), and ***C*ₖ** *ex situ* coloured green (—).

2.5.2 SCXRD and Conformational computational determination

Owing to the insolubility of the charge neutral ligands ***B*ₑ**, ***C*ₑ** and ***C*ₖ**, the growth of an appropriate single crystal presented a significant challenge. DMSO presented the only viable solvent for the dissolution of these ligands. However, use of this solvent introduces a new set of problems with regards to some of the most common methods used to produce single crystals. DMSO has a high boiling, this coupled with a remarkable low vapour pressure effectively rules out the option to use slow evaporation. The option to cool the solution down, decreasing the solubility of the ligand, thus inducing crystal formation is problematic owing to the high freezing point of DMSO. This meant that conventional cooling methods could not be used. Because of this the crystallisation method selected

was vapour diffusion, where an anti-solvent with a lower boiling point and a higher vapour pressure than DSMO is allowed to defuse into the solution containing the ligand resulting in the formation of single crystals. The diffusion of simple alcohols such as ethanol and methanol into the DMSO solution demonstrated the most promise for the obtainment of single crystals with a quality suitable for SCXRD. However, of the three gelators discussed in this chapter, only $\boldsymbol{C_e}$ crystallises in a form suitable for routine data collection techniques reliably yielding large, clear pale yellow needles. Crystalline fibres of both $\boldsymbol{B_e}$ and $\boldsymbol{C_k}$ have been produced that may field solvable data sets should a synchrotron radiation source be used, however, these experiments have not yet be performed. The needle-like morphology of the $\boldsymbol{C_e}$ crystals was unsurprising given the species tendency to form high aspect ratio fibres in the gel state. $\boldsymbol{C_e}$ was found to crystallise in the trigonal space group *P*31*c*, with a third of the molecule as the asymmetric unit (Figure 3.32). This third of the $\boldsymbol{C_e}$ molecule in the asymmetric unit is accompanied by one molecule of DMSO, which is hydrogen bonded to the NH group. The most significant feature of the structure is the columnar, face-to-face stacking that arises between the $\boldsymbol{C_e}$ molecules. This occurs with a slight offset from one molecule to the next, which involves a 30 ° rotation around the column axis. Formation of these columns is driven by a number of factors. The geometry of the $\boldsymbol{C_e}$ molecules allows them to adopt a slight shallow bowl shape. This bowl shape allows a concave-to-convex fitting pattern to occur between the adjacent molecules of $\boldsymbol{C_e}$ which in turn allows for there to be a large number of weak supramolecular dispersion interactions, such as π-π interactions, between the molecules as can be seen in Figure 3.32.

A computational study involving the molecules $\boldsymbol{B_e}$, $\boldsymbol{C_e}$ and $\boldsymbol{C_k}$ was performed in order to establish the nature and form of the supramolecular interactions between the respective molecules. The experiment was conducted using B97D with a 6-311g(d) basis set and a three molecule stack for each of the three ligands. A similar DFT approach has been used previously to determine the supramolecular stacking geometry of comparable C_3 symmetric gelator molecules.[56] The supramolecular structures that were determined by this DFT geometry optimisation study were confirmed as minima through the use of analytical frequency calculations. During the course of preforming the geometry optimisations on the three molecules stacks, it became apparent that accurate structural predictions required the addition of dispersion corrections. Calculation of all three molecules assemblies demonstrated that face-to-face stacking was possible between the molecules, as observed in fibres by SEM, TEM, PXRD and SCXRD analysis.

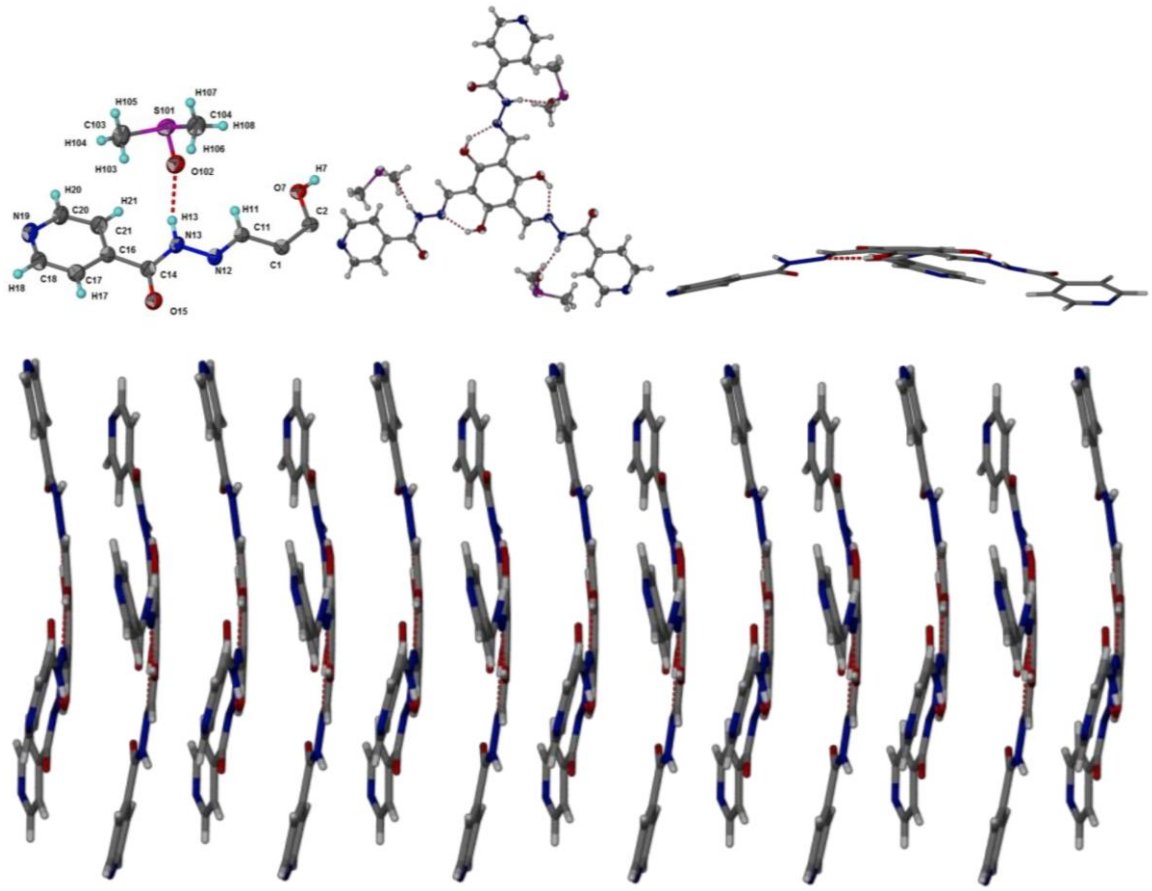

Figure 2.32. Crystal structure of C_e·DMSO solvate. Asymmetric unit, top left, of the structure of C_e showing labels of atoms, with atoms shown as ellipsoids at 50% probability. Complete molecule of C_e (top middle) showing the hydrogen bonding between the OH groups and hydrazone N(imine) groups, as well as those between the DMSO molecules and C_e. The flatness of the C_e molecules is highlighted with the right-hand image. Stacking of C_e into one-dimensional array, i.e. supramolecular polymers shown in bottom image. π- π interactions between the pydridyl groups clearly seen, as well as the concave:convex fit. Structure viewed diagonal to the c axis.

As can be seen in Figure 2.33, face-to-face stacking of molecules of B_e does appear to occur. The central core units of one molecule to the next is separated by a distance of approximately 3.4 Å, this distance is not to dissimilar to the intermolecular *d*-spacing values determined for dried samples of the B_e gel prepared by both the *in situ* and *ex situ* method (3.36 Å and 3.34 Å respectively). The stacking also appears to be driven by the formation of intermolecular hydrogen bonds. These occur between the hydrazone carbonyl group of one molecule to the hydrogen atom on the hydrazone nitrogen of another molecule. There is also intramolecular hydrogen bonding between the hydroxyl group hydrogen on the central core and either the oxygen of the adjacent aldehyde group or the nitrogen of any adjacent hydrazone group. This intramolecular hydrogen bonding would appear to lead to the relative planarity of the molecules, particularly with regards to central region in which this intramolecular hydrogen bonding occurs. The

concave:convex fit of the molecules and their corresponding interactions, as seen in the crystal structure of ***C*****e**, are also present.

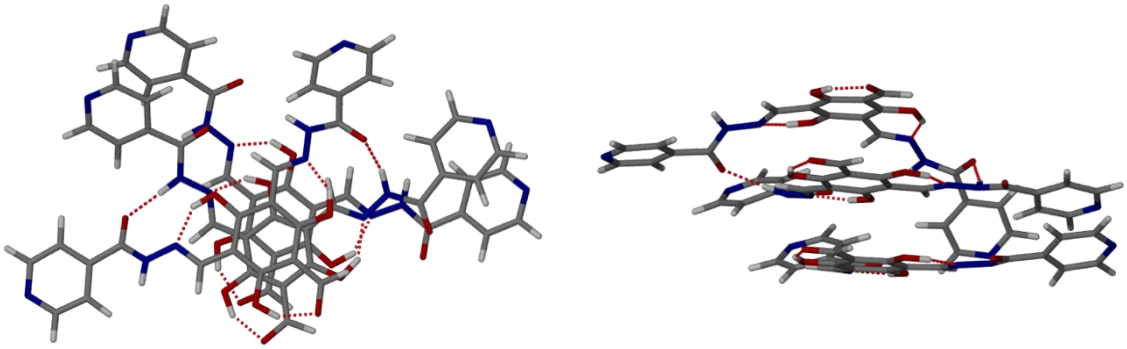

Figure 2.33. Calculated supramolecular arrangement of three molecules of ***B*****e**. Top down view (left) and side view (right) of stack shown. Dashed lines show inter- and intramolecular hydrogen bonds.

The calculated stack of three molecules of ***C*****e** can be seen in Figure 2.34. Similar to what was calculated for the stack of ***B*****e**, face-to-face stacking between the molecules is the obvious dominant structural feature. This, again, is driven by the intermolecular amide-amide hydrogen bonding between the amide portions of the hydrazone groups. The planar nature of the central region is again enforced by the intramolecular hydrogen bonding that occurs between the three hydroxyl groups hydrogen atoms on the core and the closest nitrogen of the adjacent hydrazone group. There is again favourable comparisons that can be made with PXRD patterns for the isolates of *in situ* and *ex situ* prepared samples of the gel, with regards to the intermolecular spacing. A comparison of these calculated stacks with the DMSO crystal structure is now possible.

The most significant difference to note is that the DMSO solvate, due to the strong hydrogen bonding acceptor nature of the DMSO, does not have any amide-amide interactions as the N−H is hydrogen bonded to the DMSO. There are many discussions on the relevance of the 1,3,5-triamide hydrogen bonding in these types of discotic gelators, and the results for the computational work and crystal structure of ***C*****e** indicate that the columnar packing of the molecules does not full require these triamide interactions. This fact is important to the design of the gelators in the following chapters.

A computational optimised stack of three molecules of ***C*****k** is shown in Figure 2.35. This serves to once again highlight the potential for face-to-face stacking to occur between the molecules. The computationally determined hydrogen bonds are shown, demonstrating the reason for the planar geometry of the individual molecules as well as the potential to form the supramolecular stack. These interactions are very similar to that of ***B*****e** and ***C*****e**, and indicates why all three molecules form gels, i.e. their supramolecular

packing is similar.

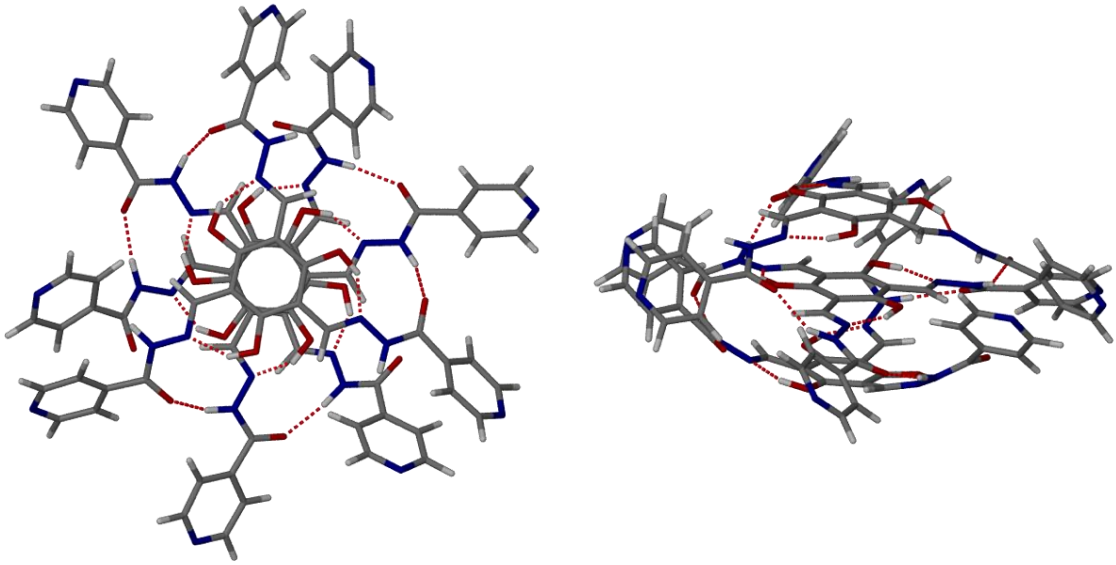

Figure 2.34. Calculated supramolecular arrangement of three molecules of C_e. Top down view (left) and side view (right) of stack shown. Dashed lines show inter- and intramolecular hydrogen bonds.

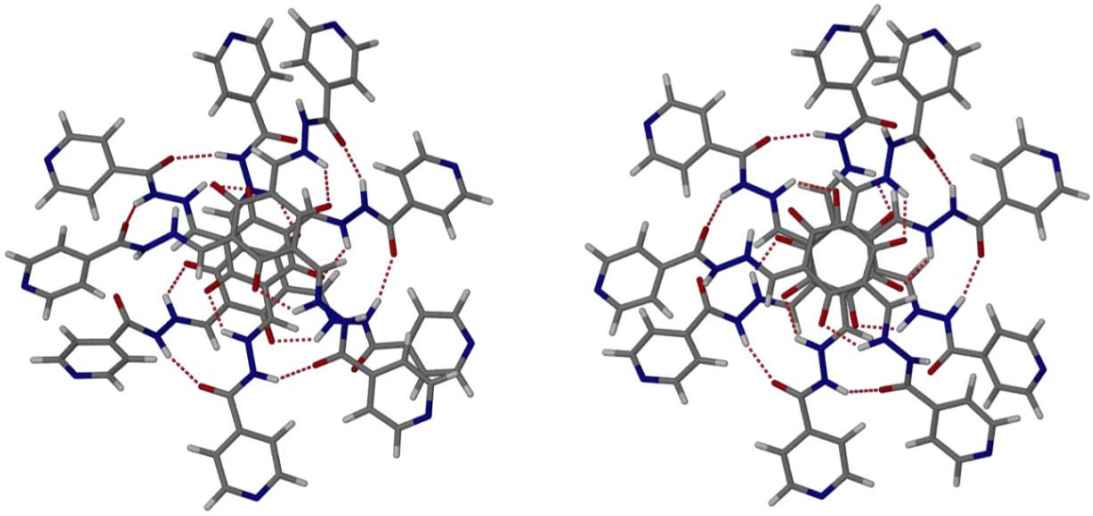

Figure 2.35. Calculated supramolecular arrangement of three molecules of C_k. Dashed lines show inter- and intramolecular hydrogen bonds.

2.6 Landscape determination

Determination of the selected pathway depends very much on the relative thermodynamic stabilities of the species in question and kinetic pathways to those species. While the formation gel B_e, and the existence of the B_e ligand, are resultant of kinetic trapping through a mass transfer mechanism, the difference in terms of thermodynamic stability

between C_e and C_k is much more difficult to intuitively determine. Therefore, DFT calculations are needed to explain the experimental observations. C_e and C_k are both isolatable and represent the first example where this process is reversible. There are a significant number of similar systems reported in the literature, particularly in terms of the reaction between ***I*** and various amines to form imine functionalities, of which hydrazones are a subset.[17] However, none of these examples report the existence of the enol form, instead only the keto form is reported. This suggests that, as reported in the literature, the keto form is energetically more favourable,[18] indeed thus far this system is the only reported example of such a system being isolated in the enol form.

This enol to keto tautomerisation results in an additional layer of complexity being added to the pathway selection within this system. While not observed there is no reason there should not be a keto tautomer of A_e (A_k) and B_e (B_k). This means that in theory, the single starting point for this system has the potential to yield six chemical different products, A_e, A_k, B_e, B_k, C_e and C_k, as demonstrated in Figure 2.36. This figure represents a summary of the three accessible pathways that have been identified within this gelation system. The reasoning behind, and justifying calculations for, these particular pathways will now be discussed.

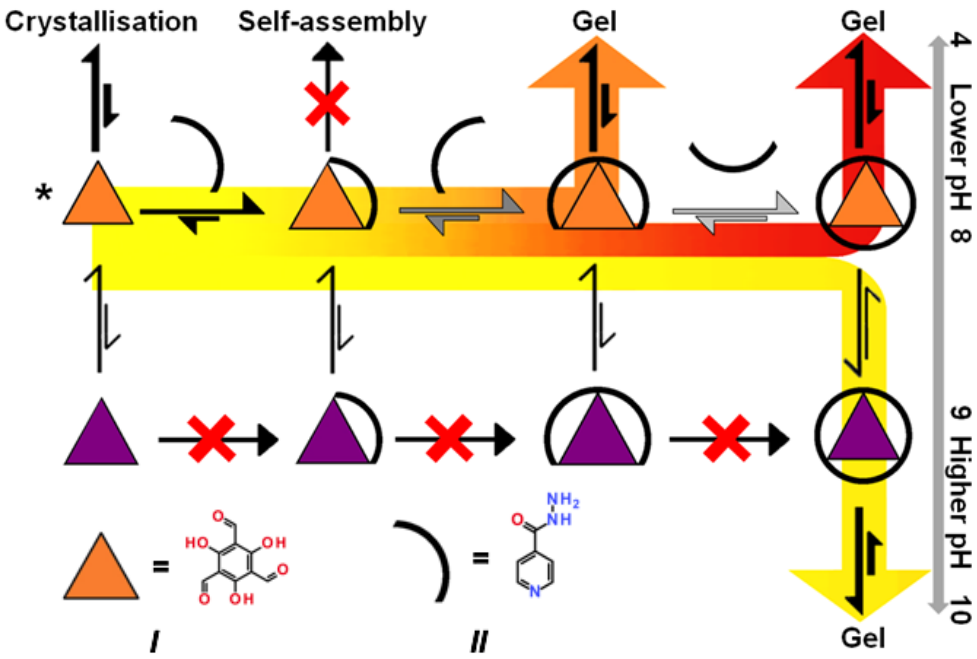

Figure 2.36. Pictorial representation of the various possible pathways within the gelation system. Included are all pathways that give rise to a gel as well the pathways that maybe result in the formation of an unobserved/non-gelator reaction product. ▲ represents the central keto core of products A_k, B_k and C_k. ▲ represents the central enol core of products A_e, B_e and C_k. * represents the start of the reaction upon mixing.

In order to better understand the pathway complexity within the system and determine the relative energies between the various potential reaction products, a computational study was required. The computational study consisted of two parts, firstly, the prediction of UV-Vis spectra, which will then be compared to the spectra of experimentally obtained products, thus confirming formation of these products. The second part of the study will focus on the calculated relative energies between the three different molecular species ***B*$_e$**, ***C*$_e$** and ***C*$_k$** with a view to understanding the thermodynamic and kinetic dimensions to this energy landscape.

Prediction of the UV-Vis spectra for the molecules ***C*$_e$** and ***C*$_k$** was done using TD-B97D3/6-31G(d) level of theory, with the spectra predicted using the first six bright states. The systems were modelled with SMD solvation model using DMSO as the solvent. Samples of ***C*$_e$** and ***C*$_k$** isolated from their corresponding gels were dissolved in DMSO and their UV-Vis spectra recorded. Figure 2.37 offers a comparison between the theoretical and experimental spectra for ***C*$_e$** and ***C*$_k$** in DMSO. As can be seen there is a good correlation between the theoretical and experimental results with the molecule ***C*$_e$** absorbing at noticeably longer wavelengths than the molecule ***C*$_k$**. Slight differences between the experimental and theoretical values in the exact wavelength of maximum absorption for ***C*$_e$**, and particularly ***C*$_k$**, were apparent, but within acceptable tolerances for the nature of this study. The results of these experiments confirmed the enol to keto tautomerisation of ***C*$_e$** to ***C*$_k$**, the reversible nature of this process and the exact nature of the chemical species.

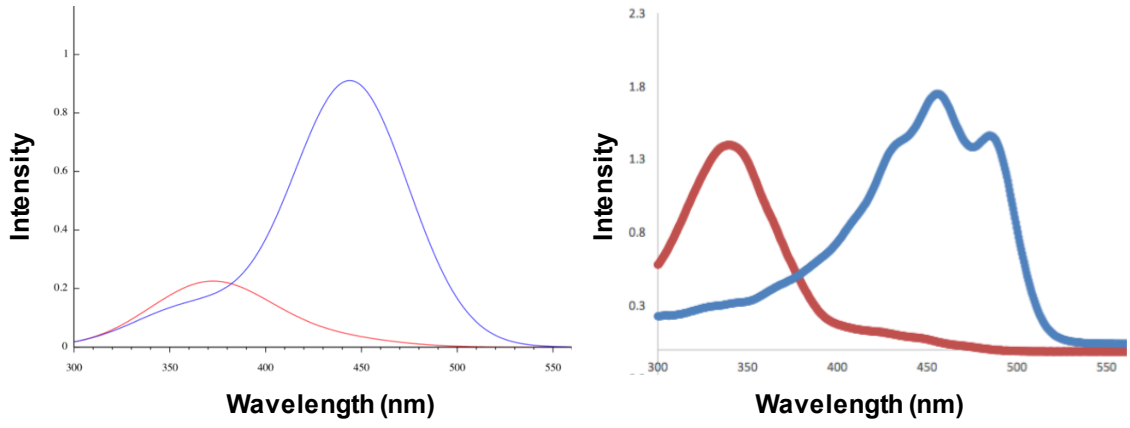

Figure 2.37. Predicted theoretical UV-Vis spectra for molecules ***C*$_e$** and ***C*$_k$** in DMSO (left). Experimental UV-Vis spectra for molecules ***C*$_e$** and ***C*$_k$** in DMSO (right). Data plotted for ***C*$_e$** in red and data plotted for ***C*$_k$** in blue.

Similar comparisons could be made between the theoretical and experimental UV-Vis spectra of obtained for the molecule $\boldsymbol{B_e}$. Again there is a good fit between both sets of data. As discussed previously, the UV-Vis spectra for $\boldsymbol{B_e}$ features two key absorption features. These features are both also clearly visible in the calculated spectra, as can be seen in Figure 2.38. The computational study shows the absorption at 300 nm has the higher intensity of the two features, rather than the 415 nm absorption in the experimental result. Intensity of absorption is difficult to predict using the computational techniques used in this study. However, seeing a correlation between the computational and experimental profiles was highly satisfactory with regards to the scope of this investigation, and again confirms the chemical species of $\boldsymbol{B_e}$ as the enol form.

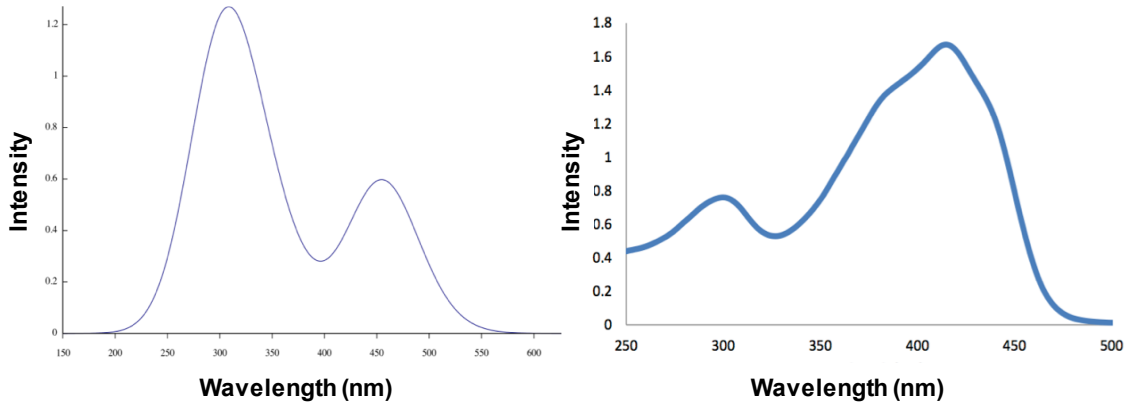

Figure 2.38. Predicted theoretical UV-Vis spectra for the molecule $\boldsymbol{B_e}$ in DMSO (left). Experimental UV-Vis spectra for the molecule $\boldsymbol{B_e}$ in DMSO (right).

The second part of the computational study was the calculation of the relative energies of the potential products from the different reaction pathways within the system. This was done using DFT calculations with B3LYP density functional and 6-31G(d) basis set. Owing to the enol version of $\boldsymbol{I}$ being the solely observed tautomer, the calculations were only performed in a way that simulated the enol to keto tautomerisation for $\boldsymbol{A_e}$ to $\boldsymbol{A_k}$, $\boldsymbol{B_e}$ to $\boldsymbol{B_k}$ and $\boldsymbol{C_e}$ to $\boldsymbol{C_k}$. Should the tautomerisation be an energetically uphill process, then the process would be unfavourable, being the enol form would represent the more stable of the two tautomers. An energetically downhill process would mean the keto tautomer would be the favoured of the two forms. Both of these theories are of course dependent on any barriers to these transition being surmountable at room temperature. These calculations are of particular interest with regards to the species $\boldsymbol{C_e}$ to $\boldsymbol{C_k}$ because of $\boldsymbol{C_k}$ being the only isolatable keto tautomer to emerge from this system. The reversible nature of the $\boldsymbol{C_e}$ to $\boldsymbol{C_k}$ tautomerisation process has already been established, suggesting

an energy barrier to this conversion that is easily overcome at room temperature. This computational study allowed the energy minimum for this system, with regards to the calculated species, to be determined.

All conversions from the corresponding keto to enol species were found to go through a stepwise process with a number of different intermediates and transitional states. The conversion from $\boldsymbol{A_e}$ to $\boldsymbol{A_k}$ (Figure 2.39) was determined to go through three transition states and two intermediates, with each corresponding to an –OH to =O (enol to keto) conversion, with regards to the –OH groups on the core unit. Transition states were found to be when the proton was moving from one functional group to another and with corresponding bond making and breaking, as expected. The overall process was calculated as being an energetically uphill process with barriers separating the energy minima. This demonstrated that had the ***A*** product been isolatable, it would exist in the enol ($\boldsymbol{A_e}$) form. The $\boldsymbol{A_e}$ to $\boldsymbol{A_k}$ transformation results in an overall increase in the molecules electronic energy of 4.4 kcal/mol, with the biggest barrier to this transition being 7.4 kcal/mol.

The reaction coordinate against energy plot for the $\boldsymbol{B_e}$ to $\boldsymbol{B_k}$ tautomerisation followed a similar trend to that witnessed for the $\boldsymbol{A_e}$ to $\boldsymbol{A_k}$. The overall electronic energy of the molecule increases by 1.5 kcal/mol, with noticeably larger electronic barriers existing. The transition state 2 being particularly high in energy giving rise to an energy barrier of 11.2 kcal/mol, when moving from the local minima (Figure 2.40). This theoretical finding is again in line with what is found experimentally, with $\boldsymbol{B_e}$ representing a product that can be isolated from the gel state, and $\boldsymbol{B_k}$ being a species that is not observed.

The final calculation, and arguably most important, of this study involves the tautomerisation of $\boldsymbol{C_e}$ to $\boldsymbol{C_k}$. As mentioned previously, both these products are observed experimentally, and the tautomerisation process between the two products has been found to be fully reversible. The computationally level of the energy barriers between the various transitions the molecules must move through during the tautomerisation process are not sufficiently high in energy to act as barriers that cannot be overcome at room temperature. Also, the determination of the relative energies of $\boldsymbol{C_e}$ and $\boldsymbol{C_k}$ will provide evidence of which one of the two species is the thermodynamic minimum for this system, in relation to the species whose energies have been calculated during the course of this study. Figure 2.41 outlines the energy of conversion determination for $\boldsymbol{C_e}$ to $\boldsymbol{C_k}$. The most

apparent feature of the energy profile plot is that the conversion is an overall downhill process, with C_k proving to be -0.6 kcal/mol more energetically stable than the C_e form of the molecule. This difference in electronic energies does show that the C_k product represents the energy minimum for species calculated and is also an energy minimum for this gelation system. The barriers between the various transition states also do not represent a significant enough barrier to the tautomerisation, in either direction. As a result, both the enol C_e and the keto C_k tautomer are observed experimentally and able to be isolated in bulk with a high degree of purity.

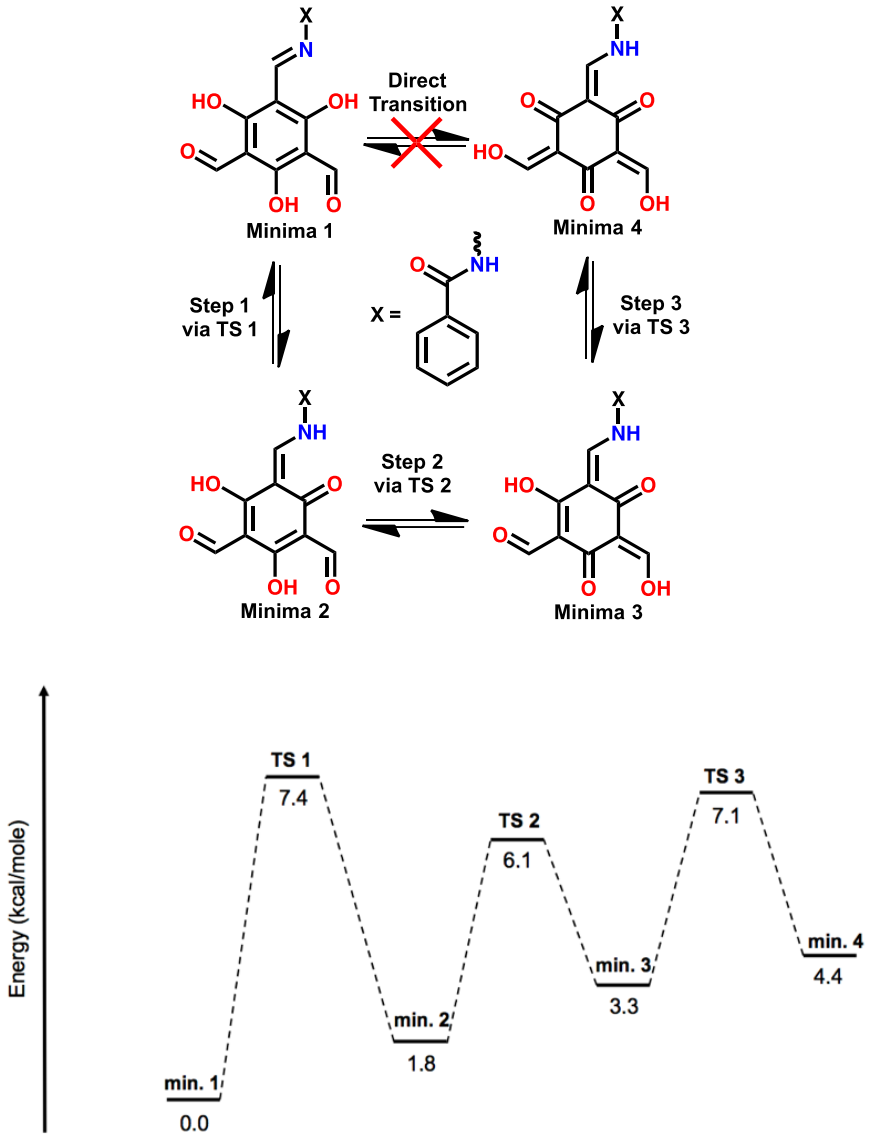

Figure 2.39. Pathway for the transition from A_e (minima 1) to A_k (minima 4) (left) showing the structure of the four minima that would result from the transition (TS = transition state). Plot of reaction coordinate (x-axis) against relative electronic energy (y-axis) for the A_e to A_k transition showing energy differences between the tautomers and the barrier size between them. B3LYP with 6-311G(d) basis set at 298K; electronic energy in kcal/(mol).

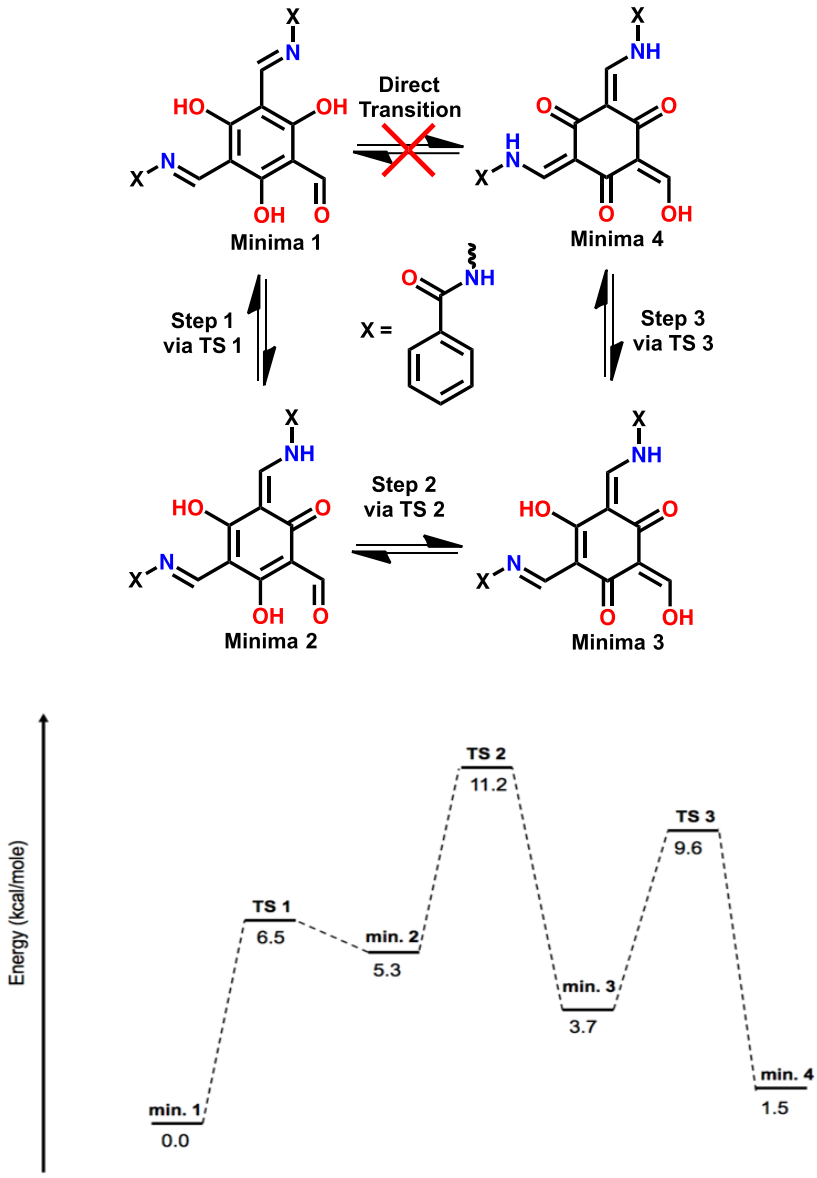

Figure 2.40. Pathway for the transition from B_e (minima 1) to B_k (minima 4) (left) showing the structure of the four minima that would result from the transition (TS = transition state). Plot of reaction coordinate (x-axis) against relative electronic energy (y-axis) for the B_e to B_k transition showing energy differences between the tautomers and the barrier size between them. B3LYP with 6-311G(d) basis set at 298K; electronic energy in kcal/(mol).

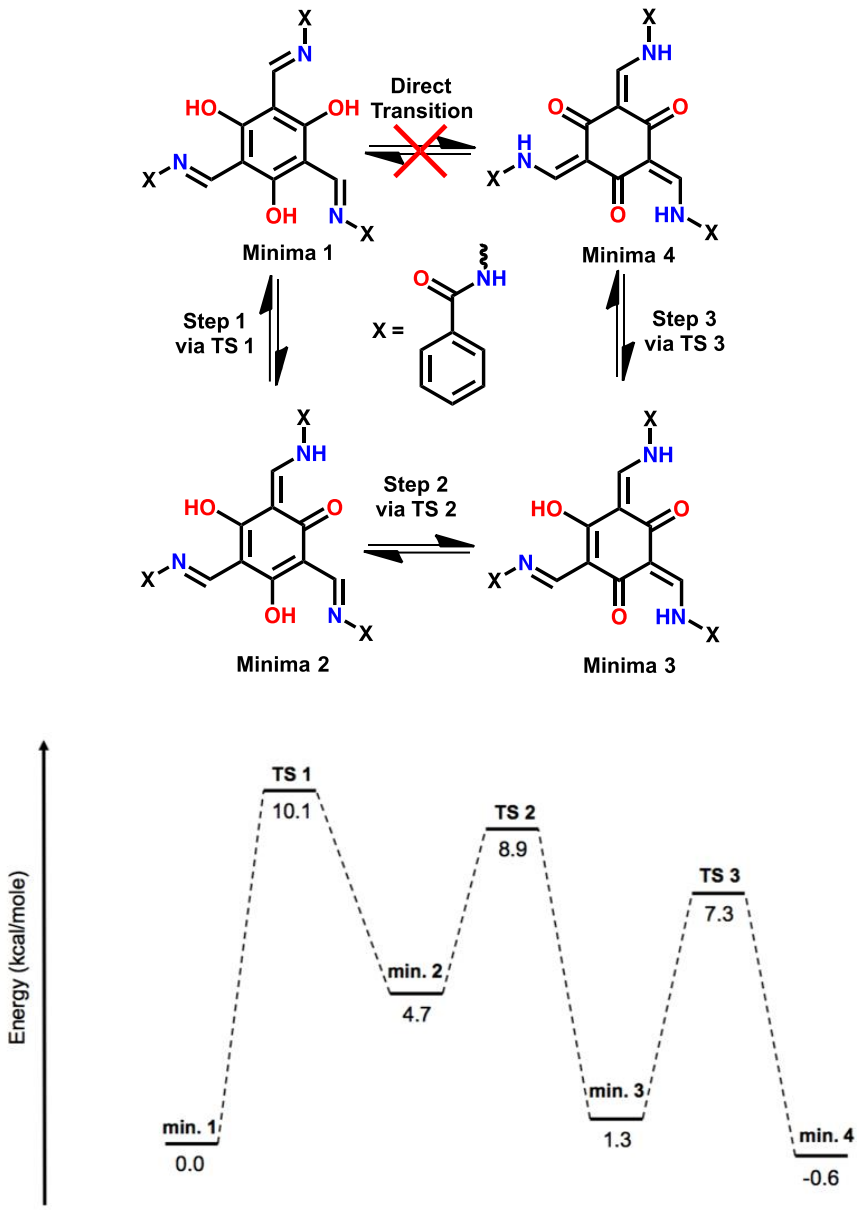

Figure 2.41. Pathway for the transition from C_e (minima 1) to C_k (minima 4) (left) showing the structure of the four minima that would result from the transition (TS = transition state). Plot of reaction coordinate (x-axis) against relative electronic energy (y-axis) for the C_e to C_k transition showing energy differences between the tautomers and the barrier size between them. B3LYP with 6-311G(d) basis set at 298K; electronic energy in kcal/(mol).

2.7 Thermodynamic Stability of the gelatinous material

While gels are generally considered to be relatively stable materials, it is often the case that the fibrous network that gives rise to the formation of the gel is not the thermodynamically most stable supramolecular assembly.[57,58] In this vein there has been little investigation into the total lifespan of supramolecular gels, as most supramolecular gels are stable enough in relation to typical experimental timescales.

In order to investigate the temporal stability of the supramolecular assembly within the gels presented in this chapter, various samples were prepared and stored for a period of time, well in excess of what would be considered a normal experimental timescale. Samples of all gels $\boldsymbol{B_e}$, $\boldsymbol{C_e}$ and $\boldsymbol{C_k}$ were prepared using the *in situ* method of preparation. As can be seen from Figure 2.42 the temporal stability of the gels $\boldsymbol{B_e}$ and $\boldsymbol{C_e}$ is proven over a 380-day timescale.

Figure 2.42. Samples of gels $\boldsymbol{B_e}$ (left) and $\boldsymbol{C_e}$ (right) prepared at 2 wt% and stored in the dark for 380 days (at the time the photograph was taken).

The vial inversion test demonstrates the materials have retained their gelatinous properties with no obvious phase transition or loss of mechanical robustness. Of course, the inverting of the vial only gives qualitative analysis of the gels mechanical properties and because removing the gel samples from the vials would inevitably have a detrimental effect on these mechanical properties, no quantitative rheological data was obtainable with this particular set of experiments. Similar analysis of the $\boldsymbol{C_k}$ gel was performed for almost the same length of time as the $\boldsymbol{B_e}$ and $\boldsymbol{C_e}$ gels. Again, upon inversion of the vial the material had appeared to remain as a supramolecular gel, even though small pieces of the gel had become detached from the bulk of the material (see Figure 2.43). While the gel certainly still exists, there is the possibility that this apparent structural deterioration is the result of a phase change process. This however seemed unlikely owing

to the PXRD patterns of dried product of both this sample and a freshly prepared sample being identical. The partial loss of structural integrity was therefore more likely to be a result of loss of water through evaporation.

Figure 2.43. Samples of gel C_k prepared at 2 wt% and stored in the dark for 372 days (at the time the photograph was taken).

The thermodynamic stability of the gels was further investigated through the application of heat to samples of each of the three gels. This was done by placing vials containing the gel samples in an oil bath and heating to 90 ^{o}C. This temperature was maintained for two hours before the samples were removed from the oil bath and the vials were inverted. This demonstrated that heating did not appear to have an obvious adverse effect on solid-phases of the supramolecular structure. There was also no obvious visual change to the gel samples (Figure 2.44), which suggested that the C_e to C_k, or indeed C_k to C_e tautomerisation process or any decomposition of ligands does not occur. The tautomerisation is often described in the literature as being thermally induced. This was confirmed through chemical characterisation of these gel samples after they were heated.

Figure 2.44. Gel B_e (left), Gel C_e (centre) and gel C_k (right). Photograph taken after gels had been heated to 90 ^{o}C in an oil bath, and held at this elevated temperature for two hours.

2.8 Alternative hydrazides

With the success of the ***I*** + ***II*** gelation system, investigations into another possible system that utilises the same hydrazone chemistry was conducted. In order to preserve the C_3 symmetry of any potential gelator molecules, ***I*** was replaced with an alternative hydrazide, while the tri-aldehyde ***II*** was maintained. The hydrazide selected for this additional study was benzhydrazide (***I*$_B$**) (Figure 2.45), this would allow exploration of the versatility of the system with regards to the use of hydrazide but also give insight into how important the pyridyl nitrogen atom of ***I*** is for the assembly process.[59,60]

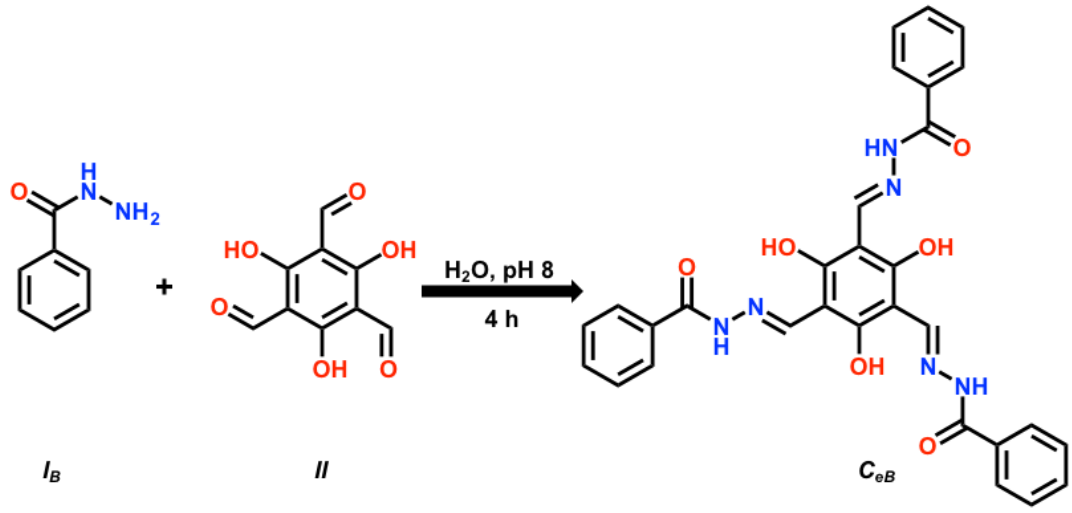

Figure 2.45. Reaction scheme for the formation of *N*',*N*''',*N*''''-((1*E*,1'*E*,1''*E*)-(2,4,6-trihydroxybenzene-1,3,5-triyl)tris(methanylylidene))tri(benzohydrazide) (C_{eB}) from the combination of I_B and *II* after four hours in water at pH 8.

Attempts to set a gel using ***I*$_B$** using the same *in situ* method that resulted in the formation of gel ***C*$_e$** proved unsuccessful. Chemical analysis did show that the desired product ***C*$_{eB}$** was formed, despite that lack of gelation occurring. Due to the system being unable to produce a gel, it was impossible to isolate to dihydrazone equivalent product, ***B*$_{eB}$**. The system did exhibit tautomerisation at increased pH (pH 10) to the keto product ***C*$_{kB}$**, however, this also did not demonstrate any gelation abilities. When attempting to set an *in situ* formed gel of ligand ***C*$_{eB}$** using GdL the formation of a yellow suspension was observed as seen in Figure 2.46. It should be noted that the ligand ***C*$_{eB}$** can be synthesised in the *ex situ* manner. Attempts to produce a gel by dissolving the ligand in water at pH 8, before the addition of GdL, were unsuccessful.

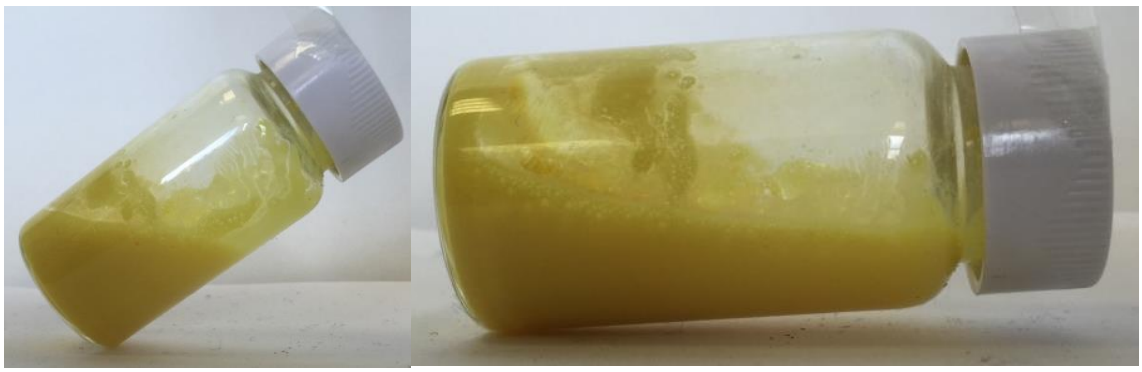

Figure 2.46. The suspension that arises from the *in situ* preparation of ligand ***C**eB* in solution at pH 8, followed by the addition of GdL after a reaction time of four hours.

Despite ligand ***C**eB* not being successful as a supramolecular gelator, attempts were made to produce single crystals of ***C**eB*. As with the ligand ***C**e*, the solubility of ***C**eB* is limited in any solvent other than DMSO. As a result attempts to grow crystals through the vapour diffusion of anti-solvents into the DMSO solution were again used. The use of water, methanol and ethanol as the anti-solvents all resulted in the formation of crystals suitable for SCXRD analysis. The structure obtained from this analysis can be seen in Figure 2.47.

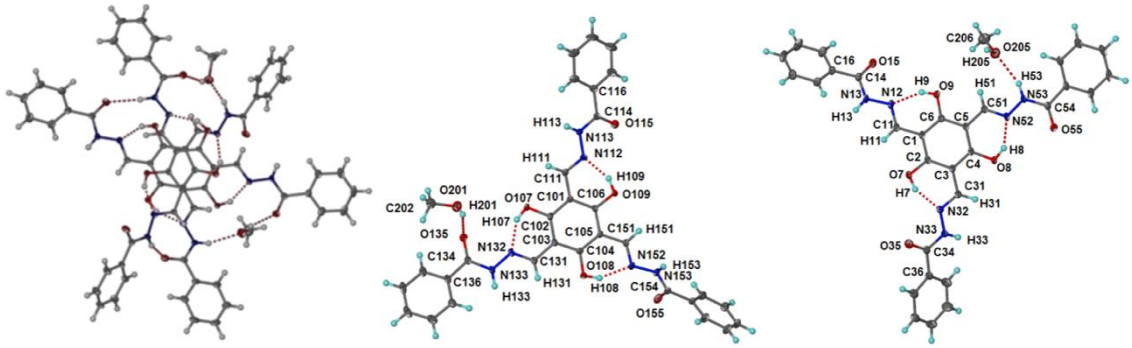

Figure 2.47. Images of the asymmetic unit for the structure of ***C**eB* with molecules of methanol. Atoms shown as elipsiods at 50 % probablity. Image on the left is the asymmetric unit with the central and right handside images showing the labels of the two non-symmetry related components of the asymetric unit.

Analysis of the crystals produced through the diffusion of methanol was conducted. ***C**eB* was shown to crystallise in the P-1 space group, with the asymmetric unit consisting of two molecules of ***C**eB* accompanied by two molecules of methanol. The crystal structure shows seperation between the core units of approximately 6.9 Å and unlike with the structure of ***C**e*, the face-to-face molecular stacking is not present. The

molecules of C_{eB} interdigitate with each other, with hydrogen bonding occuring between the hydrazone carbonyl and the hydrogen of the hydrazone group NHs through a bridging methanol molecules resulting the doubling of the core to core seperation distance (Figure 2.48). Similar to C_e, the planarity of the central part of the C_{eB} molecule is enforced by intramolecular hydrogen bonding between the hydrogen atom of the hydroxyl groups on the central core and imine-type nitrogen of the adjcent arm units.

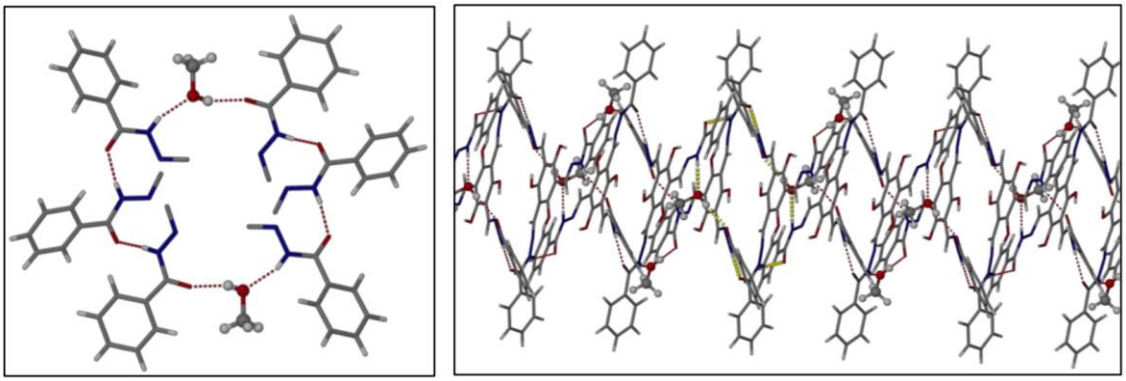

Figure 2.48. The stacking of molecules of C_{eB} into high aspect ratio columns (right) through a hydrogen bonding pattern (left) that involves four molecules of C_{eB} and two molecules of methanol. A set of these bonds has been coloured yellow to highlight the ring pattern with the methanol molecules presented in a ball and stick representation for clarity, with the C_{eB} molecules shown in a close-dcapped representation.

2.9 Conclusion

The gelation system discussed in this chapter is unique in that it allows three chemically different gels, with each of the three gels having two different methods of preparation to be arrived at from a single chemical starting point. Method one refers to the setting of a C_e gel using an *in situ* method where the core unit ***I*** is mixed with a minimum of three equivalents of ***II***. This mixture was allowed to react for a minimum of four hours in water at pH 8 before the addition of GdL, resulting in the setting of a dark red gel, C_e. If the previous method is used with the GdL added instantly after the mixing of ***I*** and ***II***, a more vivid orange gel is produce, B_e. Gel C_k could be prepared using a third method. This begins the same way as method one but instead of lowering the pH after four hours with the addition of GdL, the pH is raised to 10 with the addition of sodium hydroxide. This results in the setting of gel C_k, a distinct yellow gel. Gel C_e can be set using an *ex situ* method, method four. This involves a previously synthesised sample of the ligand C_e,

whether from an in ethanol reflux of ***I*** and ***II*** or isolated from a previously prepared sample of the C_e being dissolved with the addition of sodium hydroxide and gelled with the addition of GdL. Similarly, to method four, methods five and six involve the resetting of gels B_e and C_k, respectively. In the case of method five and gel B_e, this is done with the addition of GdL after dissolving the ligand in water with sodium hydroxide. Method six for gel C_k arises as the product of dissolving C_e or C_k in water at pH 8, before addition of further sodium hydroxide in order to set the gel. Overall, one starting point and three unique gels, each with two methods of preparation.

This gelation system's energy landscape has been fully characterised both at the experimental and theoretical levels. While supramolecular gels themselves are generally considered to be metastable assemblies, that is their properties are at least partially controlled by kinetics rather than thermodynamics, this system introduces another level of complexity into this concept by introducing pathway complexity at the chemical level. Initial setting of the B_e gel at low pH results in a mass transfer limitation mechanism coming into play arising from the assembly of the gel fibres themselves. This is means that the B_e gel arises from the trapping of a kinetic chemical product, B_e. Should the hydrazone reaction be allowed to go to completion, i.e. complete conversion of the aldehyde groups of ***I***, and a gel set using acidic conditions, the system arrives at the C_e gel. The C_e molecule represents a dramatically more thermodynamically stable species relative to B_e. However, it is not until the keto-enol tautomerisation from C_e to C_k occurs through the setting a gel of the fully reacted reaction mixture at high pH, that we arrive at the chemical energetic thermodynamic minimum for this system.

The work presented in this chapter has created a bridge between the chemical reactivity involved in the ligand formation and the self-assembly process that results in gel formation. The introduction of the chemical pathway complexity has allowed control over the gels physical properties within the boundaries of this specific system. It stands to reason that by connecting chemical reactivity and self-assembly this work will lead to new pathway complexity studies in a number of different research fields where multi-step reactivity can be introduced. This system has answered the questions that were asked of it, by allowing pathway complexity to be introduced to the formation of an *in situ* formed hydrogel.

2.10 References

1 R. I. Cooper, A. L. Thompson and D. J. Watkin, *J. Appl. Crystallogr.*, 2010, **43**, 1100–1107.

2 A. L. Thompson and D. J. Watkin, *J. Appl. Crystallogr.*, 2011, **44**, 1017–1022.

3 H. D. Flack, *Acta Crystallogr. Sect. A Found. Crystallogr.*, 1983, **39**, 876–881.

4 L. Palatinus and G. Chapuis, *J. Appl. Crystallogr.*, 2007, **40**, 786–790.

5 P. Parois, R. I. Cooper and A. L. Thompson, *Chem. Cent. J.*, 2015, **9**, 30.

6 P. a. Korevaar, S. J. George, A. J. Markvoort, M. M. J. Smulders, P. A. J. Hilbers, A. P. H. J. Schenning, T. F. A. De Greef and E. W. Meijer, *Nature*, 2012, **481**, 492–496.

7 I. V Baskakov, G. Legname, M. A. Baldwin, S. B. Prusiner and F. E. Cohen, *J. Biol. Chem.*, 2002, **277**, 21140–21148.

8 N. Misra, D. Lees, T. Zhang and R. Schwartz, *Comput. Math. Methods Med.*, 2008, **9**, 277–293.

9 A. Di Cola, E. Klostermann and C. Robinson, *Biochem. Soc. Trans.*, 2005, **33**, 1024–7.

10 J. Raeburn, C. Mendoza-Cuenca, B. N. Cattoz, M. a. Little, A. E. Terry, A. Zamith Cardoso, P. C. Griffiths and D. J. Adams, *Soft Matter*, 2015, **11**, 927–935.

11 F. Aparicio, F. García and L. Sánchez, *Chem. - A Eur. J.*, 2013, **19**, 3239–3248.

12 M. Yamanaka, *Chem. Rec.*, 2016, **16**, 768–782.

13 X. Cai, K. Liu, J. Yan, H. Zhang, X. Hou, Z. Liu and Y. Fang, *Soft Matter*, 2012, **8**, 3756–3761.

14 S. J. Rowan, S. J. Cantrill, G. R. L. Cousins, J. K. M. Sanders and J. F. Stoddart, *Angew. Chem. Int. Ed.*, 2002, **41**, 898–952.

15 S. Ogi, T. Fukui, M. L. Jue, M. Takeuchi and K. Sugiyasu, *Angew. Chem. Int. Ed.*, 2014, **53**, 14363–14367.

16 D. van der Zwaag, P. A. Pieters, P. A. Korevaar, A. J. Markvoort, A. J. H. Spiering, T. F. A. de Greef and E. W. Meijer, *J. Am. Chem. Soc.*, 2015, **137**, 12677–12688.

17 M. E. Belowich and J. F. Stoddart, *Chem. Soc. Rev.*, 2012, **41**, 2003–2024.

18 J. H. Chong, M. Sauer, B. O. Patrick and M. J. MacLachlan, *Org. Lett.*, 2003, **5**, 3823–3826.

19 C. V Yelamaggad, A. S. Achalkumar, D. S. S. Rao and S. K. Prasad, *J. Org. Chem.*, 2007, **72**, 8308–18.

20 M. M. Smith, W. Edwards and D. K. Smith, *Chem. Sci.*, 2013, **4**, 671–676.

21 V. T. Bhat, A. M. Caniard, T. Luksch, R. Brenk, D. J. Campopiano and M. F. Greaney, *Nature Chem.*, 2010, **2**, 490–497.

22 A. Dirksen, S. Dirksen, T. M. Hackeng and P. E. Dawson, *J. Am. Chem. Soc.*, 2006, **128**, 15602–15603.

23 B. Levrand, Y. Ruff, J.-M. Lehn and A. Herrmann, *Chem. Commun.*, 2006, 2965–2967.

24 E. T. Kool, D.-H. Park and P. Crisalli, *J. Am. Chem. Soc.*, 2013, **135**, 17663–17666.

25 G. J. Churchyard, K. L. Fielding, J. J. Lewis, L. Coetzee, E. L. Corbett, P. Godfrey-Faussett, R. J. Hayes, R. E. Chaisson and A. D. Grant, *N. Engl. J. Med.*, 2014, **370**, 301–310.

26 M. C. Hosseinipour, G. P. Bisson, S. Miyahara, X. Sun, A. Moses, C. Riviere, F. K. Kirui, S. Badal-Faesen, D. Lagat, M. Nyirenda, K. Naidoo, J. Hakim, P. Mugyenyi, G. Henostroza, P. D. Leger, J. R. Lama, L. Mohapi, J. Alave, V. Mave, V. G. Veloso, S. Pillay, N. Kumarasamy, J. Bao, E. Hogg, L. Jones, A. Zolopa, J. Kumwenda and A. Gupta, *Lancet*, 2016, **387**, 1198–1209.

27 F. Bardou, C. Raynaud, C. Ramos, M. A. Lanéelle and G. Lanéelle, *Microbiology*, 1998, **144**, 2539–2544.

28 J. Boekhoven, J. M. Poolman, C. Maity, F. Li, L. van der Mee, C. B. Minkenberg, E. Mendes, J. H. van Esch and R. Eelkema, *Nature Chem.*, 2013, **5**, 433–437.

29 K. Liu and J. W. Steed, *Soft Matter*, 2013, **9**, 11699–11705.

30 D. J. Pochan, J. P. Schneider, J. Kretsinger, B. Ozbas, K. Rajagopal and L. Haines, *J. Am. Chem. Soc.*, 2003, **125**, 11802–11803.

31 S. Park, M.-H. Ryu, T. J. Shin and B.-K. Cho, *Soft Matter*, 2014, **10**, 5804–5809.

32 C. M. A. Leenders, L. Albertazzi, T. Mes, M. M. E. Koenigs, A. R. A. Palmans and E. W. Meijer, *Chem. Commun.*, 2013, **49**, 1963–1965.

33 P. J. M. Stals, M. M. J. Smulders, R. Martín-Rapún, A. R. A. Palmans and E. W. Meijer, *Chem. Eur. J.*, 2009, **15**, 2071–2080.

34 E. R. Draper, J. R. Lee, M. Wallace, F. Jackel, A. J. Cowan and D. J. Adams, *Chem. Sci.*, 2016, **7**, 6499–6505.

35 D. J. Adams, M. F. Butler, W. J. Frith, M. Kirkland, L. Mullen and P. Sanderson, *Soft Matter*, 2009, **5**, 1856–1862.

36 M. Avrami, *J. Chem. Phys.*, 1939, **7**, 1103–1112.

37 M. Avrami, *J. Chem. Phys.*, 1940, **8**, 212.

38 X. Huang, S. R. Raghavan, P. Terech and R. G. Weiss, *J. Am. Chem. Soc.*, 2006,

128, 15341–15352.

39 R. C. T. Howe, A. P. Smalley, A. P. M. Guttenplan, M. W. R. Doggett, M. D. Eddleston, J. C. Tan and G. O. Lloyd, *Chem. Commun.*, 2013, **49**, 4268–4270.

40 X. Y. Liu and P. D. Sawant, *Appl. Phys. Lett.*, 2001, **79**, 3518–3520.

41 A. Einstein, *Ann. Phys.*, 2005, **14**, 229–247.

42 A. Einstein, *Ann. Phys.*, 2005, **14**, 406–407.

43 A. Z. Cardoso, A. E. Alvarez Alvarez, B. N. Cattoz, P. C. Griffiths, S. M. King, W. J. Frith and D. J. Adams, *Faraday Discuss.*, 2013, **166**, 101–116.

44 G. Yu, X. Yan, C. Han and F. Huang, *Chem. Soc. Rev.*, 2013, **42**, 6697–6722.

45 M. Zhang, D. Xu, X. Yan, J. Chen, S. Dong, B. Zheng and F. Huang, *Angew. Chem. Int. Ed.*, 2012, **51**, 7011–7015.

46 P. Terech, D. Pasquier, V. Bordas and C. Rossat, *Langmuir*, 2000, **16**, 4485–4494.

47 G. A. Buxton and N. Clarke, *Phys. Rev. Lett.*, 2007, **98**, 238103–238107.

48 C. V Yelamaggad, A. S. Achalkumar, D. S. Shankar Rao and S. K. Prasad, *J. Am. Chem. Soc.*, 2004, **126**, 6506–6507.

49 L. Qin, F. Xie, P. Duan and M. Liu, *Chem. Eur. J.*, 2014, **20**, 15419–15425.

50 S. Kiyonaka, K. Sugiyasu, S. Shinkai and I. Hamachi, *J. Am. Chem. Soc.*, 2002, **124**, 10954–10955.

51 A. E. Hooper, S. R. Kennedy, C. D. Jones and J. W. Steed, *Chem. Commun.*, 2016, **52**, 198–201.

52 N. N. Adarsh, D. K. Kumar and P. Dastidar, *Tetrahedron*, 2007, **63**, 7386–7396.

53 E. Ostuni, P. Kamaras and R. G. Weiss, *Angew. Chem. Int. Ed.*, 1996, **35**, 1324–1326.

54 K. A. Houton, K. L. Morris, L. Chen, M. Schmidtmann, J. T. A. Jones, L. C. Serpell, G. O. Lloyd and D. J. Adams, *Langmuir*, 2012, **28**, 9797–806.

55 K. L. Morris, L. Chen, J. Raeburn, O. R. Sellick, P. Cotanda, A. Paul, P. C. Griffiths, S. M. King, R. K. O'Reilly, L. C. Serpell and D. J. Adams, *Nat. Commun*, 2013, **4**, 1480.

56 A. Bernet, R. Q. Albuquerque, M. Behr, S. T. Hoffmann and H.-W. Schmidt, *Soft Matter*, 2012, **8**, 66–69.

57 J. Raeburn, A. Zamith Cardoso and D. J. Adams, *Chem. Soc. Rev.*, 2013, **42**, 5143–5156.

58 C. D. Jones, J. C. Tan and G. O. Lloyd, *Chem. Commun.*, 2012, **48**, 2110–2112.

59 K. Ghosh, S. Panja and S. Bhattacharya, *RSC Adv.*, 2015, **5**, 72772–72779.

60 M.-O. M. Piepenbrock, N. Clarke and J. W. Steed, *Langmuir*, 2009, **25**, 8451–

8456.

Chapter - 3 Targetable mechanical properties with *in-situ* formed tripodal ketoenamine supramolecular hydrogels

3.1 Introduction

The vast majority of LMWG systems reported in the literature feature a solid-phase that consist of only one type of LMWG. That is, all the gelator molecules within the gel are chemically identical. This approach results in the formation of gels with reproducible, predictable physical properties. The techniques used to characterise single component gels are now also highly refined, making most characterisation requirements, such as rheological measurements and SEM analysis, almost routine in nature.

With the physical properties of single LMWG gels so well defined the next logical step in this area of research would be to investigate gels formed not of a single LMWG, but with two or more molecular components making up the solid-phase. There are a number of different reasons for wanting to explore this area of gel science, however, control in one form or another is the most often cited in the literature.[1] Be it, spatial[2,3] or control over physical properties such as mechanical robustness or fluorescence.[4] There is also the idea that multicomponent gel systems can give rise to a "best of both worlds" material. This is particular true with investigations into combining LMWGs with polymeric gelators,[5] the idea being to combine the stimuli responsive nature of the LMWG with the physical robustness that can be achieved with a polymeric gelator.[6] It is, however, supramolecular gels formed from multiple LMWGs that the research momentum seems to be with.[7]

With multi-component LMWG gels, it is the nature of the supramolecular assembly that has received particular attention, with these multi-component being generally separated into two categories, those that co-assembly[8–10] and those that self-sort,[11,12] with the latter appearing to be far and away the most common. This is perhaps unsurprising when thinking of it as merely two chemical species that do not mix. However, should the two (or more) LMWGs be close enough in structure, as to provide a similar assembly driving force, co-assembly may occur. This similarity will be in terms of the supramolecular interactions, when comparing two identical molecules, then there

is a strong possibility that a co-assembling system could be arrived at, as pictorially represented in Figure 3.1.

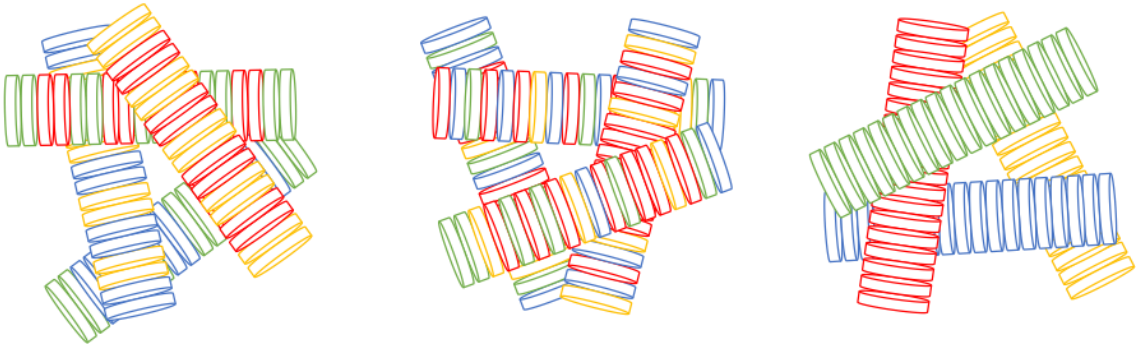

Figure 3.1. Pictorial representations of three possible co-assembling and self-sorting supramolecular arrangements within a four component gelator system. Picture on left represents an ordered co-assembling arrangement where the gel fibres feature two of the four components in a regular pattern. Central picture shows a random co-assembly process where all fibres feature a random number and arrangement of all four components. Picture on right demonstrates self-sorting where each individual fibre consists of only one type of LMWG with no mixing in terms of the individual molecular components occurring.

So far discussion on this chapter has focused on self-sorting or co-assembly at the supramolecular level, it is also true, however, that self-sorting can occur at the chemical level. The idea of self-sorting is a fundamental aspect of systems chemistry where the presence of a favoured product is amplified through its relative thermodynamic stability. This is while the other molecules within the system can undergo an "error checking" process, until the energetically favoured species is arrived at. Despite this focus on thermodynamic stability, the effects of kinetics should not be dismissed i.e. where a self-sorted system is produced due to one product forming much faster than the other with a lack of DC_vC, resulting in no error checking process occurring.

This chapter introduces a chemical diverse family of new LMWGs, with all members related chemically, but the gels that form differing significantly in terms of their mechanical properties. With the gelators being related so closely chemically, the supramolecular assembly concepts of self-sorting and co-assembly could be explored within multi-component gel systems containing one or more of the gelators. The effects of mixing two LMWGs, one that gave rise to a gel with a high G' value and one with a low G' value, could also be investigated with a view to producing a gelation system where the mechanical properties of the gel could be controlled by varying the ratio of the two substituent gelators. As each of these LMWG can be formed either *in situ* or *ex situ*, it

gave the possibility to explore not just the idea of self-sorting, co-assembly, and the supramolecular end of the assembly process, but also provided the possibility to investigate the idea of chemical self-sorting during the initial formation of the gelator molecules. By looking at the gelation process from the chemical formation of the individual gelator molecules at the start of the hierarchal assembly process, to the way in which the gel fibres form at the end of the process resulted in the study presented in this chapter.

3.2 Gelator design strategy

The hydrazine-based tripodal gelator system presented in the previous chapter provided the inspiration for the work presented here. While combining the chemical components ***I*** and ***II*** did result in a species that could effectively gel water, there was a very apparent limitation to the system. The system was highly specific in that it would only form a gel when the correct hydrazide was used. Indeed, something as apparently trivial as switch from a pyridyl to a benzyl ring within ***II*** could completely turn off the molecules gelation ability. In order to further the groups investigations into *in situ* formed LMWGs, a new system had to be developed.

Owing to the success of the hydrazone system and tripodal-shaped gelators in general it seemed appropriate to in some way modify the hydrazone system to come up with a more versatile and adaptable gelation system. Hydrazone chemistry is a subset of imine chemistry, with hydrazones resulting from the reaction between a hydrazide and an aldehyde, and imines from the reaction between an amine and an aldehyde. Investigating the gelation potential of the tri-aldehyde core unit *II* combined with a variety of amines was envisioned. This was logically not simply because of hydrazone gelator, but because of previous literature reports involving the combination of *II* with various aromatic primary amines. These showed the resulting tripodal species resulted solely in the keto tautomeric form[13] and perhaps more interestingly is this type of molecule, Tris(N-salicylideneanilines), demonstrate a planar discotic shape that lends itself to columnar stacking.[14] Finally, the crystal structure of $\boldsymbol{C_e}$ also showed that the shape of the molecules as well as the intermolecular hydrogen bonding are necessary for one-dimensional assembly, in DMSO at least.

The initial testing of this chemistry with a view of producing a gel involved the combination of aniline with ***II*** in water at pH, 8 in order to aid the solubility of ***II*** (Figure 3.2). This, however, was unsuccessful at form a gel for two reasons. Aniline has a

relatively low solubility in water, this meant it would be very difficult to form a gel with a wt% greater than 0.3 wt%. This value is relatively low and is actually lower than a number of molecules that are deemed to be highly effectively LMWGs. The second issue is the insolubility of the product due to rigidity of the planar core unit. The *in situ* reaction rapidly resulted in the formation of a pale yellow precipitate, this rapid precipitation means that there is a crystallisation process occurring rather than the formation of a desired cross-linked fibrous network.

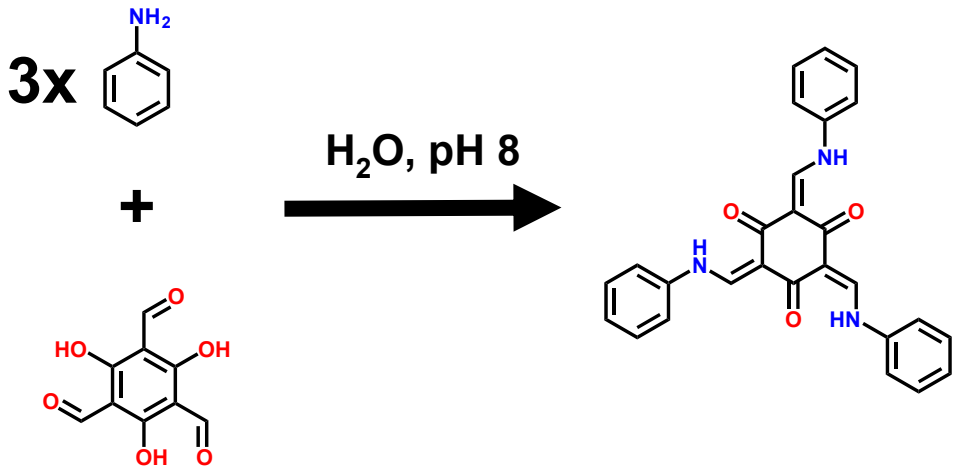

Figure 3.2. Reaction scheme for the reaction between aniline and ***II*** at pH 8 in water, and the product that forms from the resulting reaction.

With this finding in mind, modifications would have to be made to the system if this imine-based gelation system was to be successful. The insolubility of the aromatic amine had to be overcome. This could be done by switching to benzoic acid-derived amines, with the presence of the carboxylic acid group acting as a solubilising entity when deprotonated at the raised pH of the typical reaction conditions. This would also solve the issue of the rapid precipitation of the product molecule as the carboxylic acid groups would remain deprotonated after the imine formation/tautomerisation process before acidification, and the resulting reprotonation process inducing gelation.

The aminobenzoic acid approach was tested with a variety of derivatives, $\mathbf{R_1}$ to $\mathbf{R_8}$ (Figure 3.3) tested. In addition, $\mathbf{R_9}$, which would determine if the trigger groups besides the carboxylic acid group could be used, and $\mathbf{R_{10}}$, which would demonstrate whether aromatic arms are necessary for the columnar stacking subsequent gelation, were also tested. Testing of the gelation was done by preparing separate solutions of ***II*** and each of the ten amines $\mathbf{R_1}$ – $\mathbf{R_{10}}$, all of which were adjusted to pH 8 with the addition of

sodium hydroxide. This resulted in the dissolution of all compounds. Each of the amine solutions was then mixed with a solution of ***II*** resulting in a 10 reaction mixtures, each of which had the potential to produce gels of 2 wt% with a total volume of 5 ml.

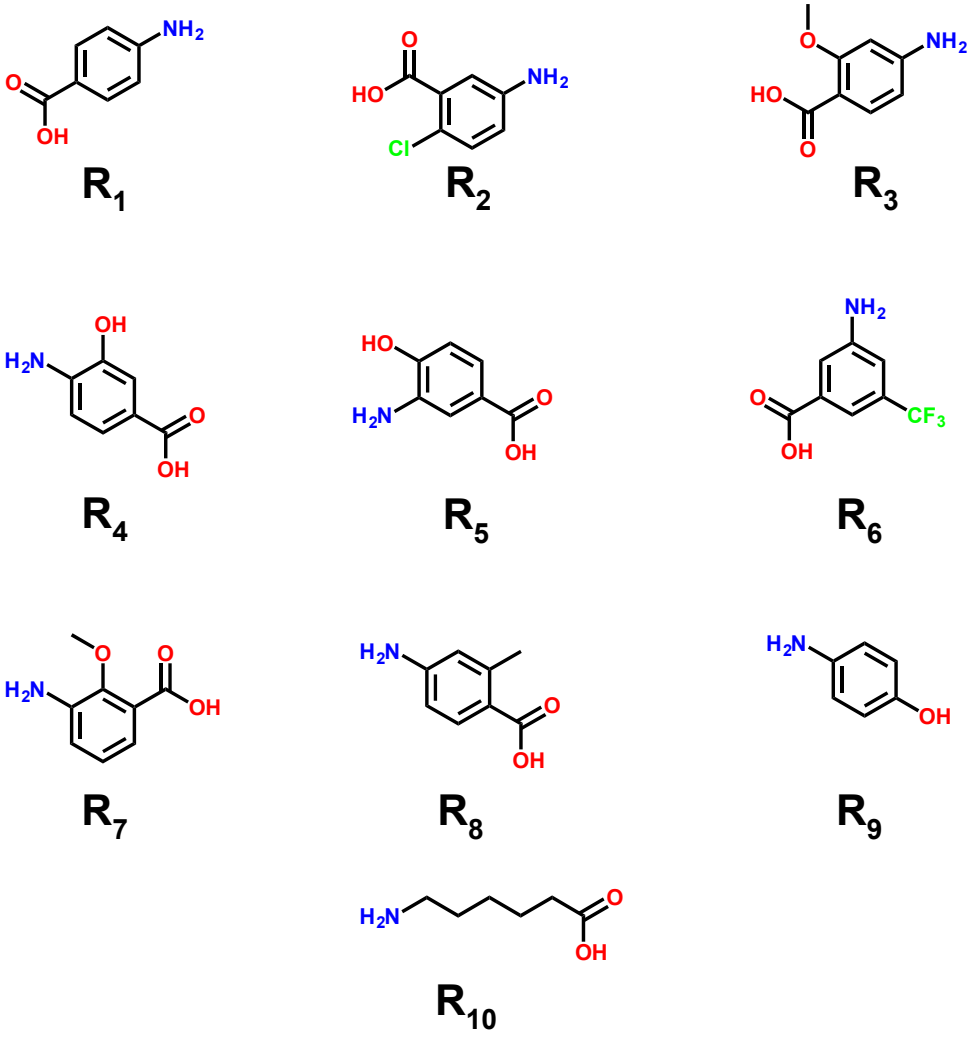

Figure 3.3. The 10 amines that were screened with ***II*** in order to test for gelation. **R1** 4-aminobenzoic acid, **R2** 5-amino-2-chlorobenzoic acid, **R3** 4-amino-2-methoxybenzoic acid, **R4** 4-amino-3-hydroxybenzoic acid, **R5** 3-amino-4-hydroxybenzoic acid, **R6** 3-amino-5-(trifluoromethyl)benzoic acid, **R7** 3-amino-2-methoxybenzoic acid, **R8** 4-amino-2-methylbenzoic acid, **R9** 4-aminophenol, **R10** 6-aminohexanoic acid.

The reactions solutions were then held at 20 ^{o}C for 4 hours, which resulted in the colours of the solutions changing from pale yellow to a dark yellow/orange. The exception was the **R10** solution, which adopted a relatively dark red colour. After the 4 hour reaction time had passed, nine equivalents of GdL relative to the ***II*** quantity was added to each of the solutions was added. This acidification through GdL hydrolysis resulted in the formation of gels with the samples of **R1** – **R8** (Figure 3.4). In order to set

a gel using **R**$_9$, acidification had to be performed with 100 μL of 4M HCl. While this did result in the formation of a gel, the structure was visibly less homogenous than the examples set with GdL (Figure 3.4). Regardless of the acidification method used on **R**$_{10}$, a gel could not be set, with precipitation always resulting.

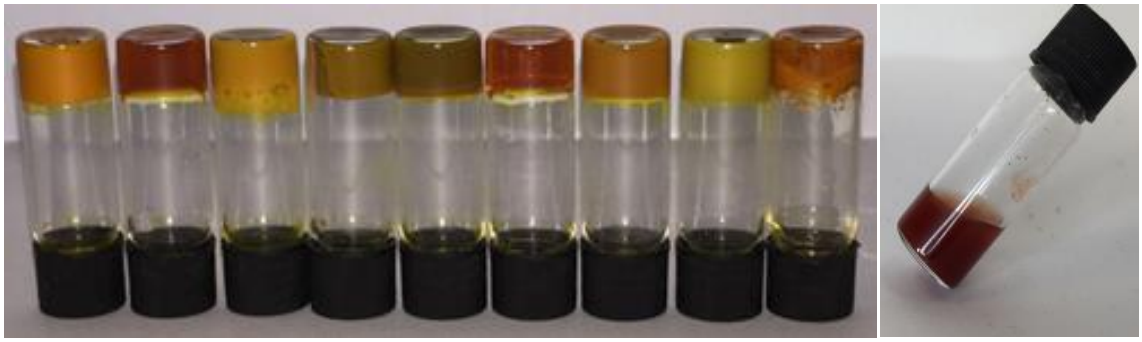

Figure 3.4. Photo shows the gels resulting from an *in situ* preparation method (gels **R**$_1$ to **R**$_9$ shown left to right) with gels **R**$_1$ to **R**$_8$ set with the addition of GdL, and **R**$_9$ setting using HCl. Photo on far right shows precipitate formed when **R**$_{10}$ is used.

Figure 3.4 highlights the differences in the gels that can be noticed simply through visual inspection of the gels. There is a range of colours from yellow through to oranges and browns, it is also worth noting the difference in transparency between the gels with gels **R**$_2$ being relatively transparent when compared to gels **R**$_1$, **R**$_3$, **R**$_4$, **R**$_5$, **R**$_7$, **R**$_8$ and **R**$_9$, which are all opaque. The exception to this is gel **R**$_6$, which is highly transparent. Figure 3.4 demonstrates the highly effective combination of aminobenzoic acid derivatives and ***II*** with an *in situ* synthesis method in forming a supramolecular gel when combined with a pH trigger mechanism. The realisation of this family of gels is an important required step in the exploration of self-sorting and co-assembling systems.

3.3 Characterisation of the gelators

With nine gelating (**R**$_1$ to **R**$_9$) and one non-gelating (**R**$_{10}$) compound synthesised through the *in situ* method, a full range of chemical characterisations were performed in order to determine what the actual gelating (or non-gelating) chemical species were in each case. To achieve this, all the vials' solid components were separated from the water through vacuum filtration before the filtrate was oven dried overnight in order to remove any residual water. With the use of ^{1}H NMR, ^{13}C NMR, FTIR and mass spectroscopy, the molecular components of the gels could be fully characterised. This showed that in all

cases the isolated species existed in the keto-enamine tautomeric form as opposed to the potential enol-imine version (Figure 3.5).

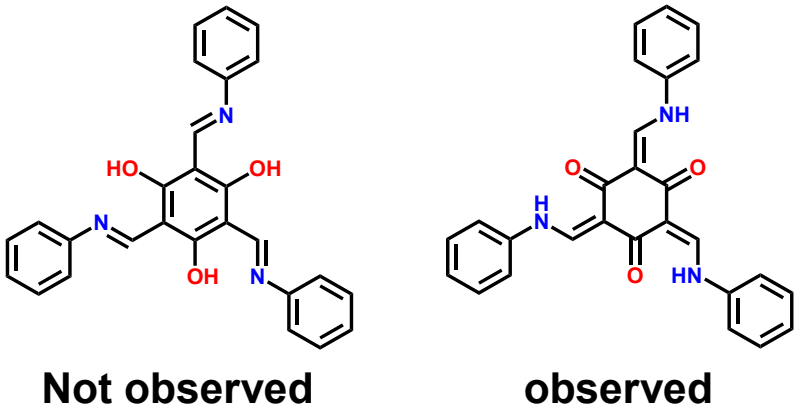

Figure 3.5. Potential tautomeric forms of the products for the reaction between ***II*** and general aromatic amine (aniline used for the purposes of demonstration). The enol-imine tautomer, not analytically observed, on the left, with the observed keto-enamine tautomer on the right.

With these compounds it was not just the enol-imine/keto-enamine tautomerisations that had to be considered. The work of Chong *et. al.* highlights the potential for two geometric tautomers to exist. Their work demonstrated how each of their salicylideneanilines could exist in two symmetric forms, either with a C_3 or C_s symmetry operation through the centre of the core unit. These geometric tautomers exist as two distinct entities in a random statistical mixture for two reasons. Firstly, there is the hydrogen bonding pattern, cited by Chong, that exists between the N-H and O=C groups. This results the high degree of planarity that these molecules demonstrate. Secondly, the enamine bonds with the sp^2 centres will resist any rotation meaning the molecules will reside in the geometric tautomer in which they initially formed. Full structures of all compounds presented in this chapter, in both their C_3 and C_s geometries are presented in chapter 6, section 6.4.2.1.

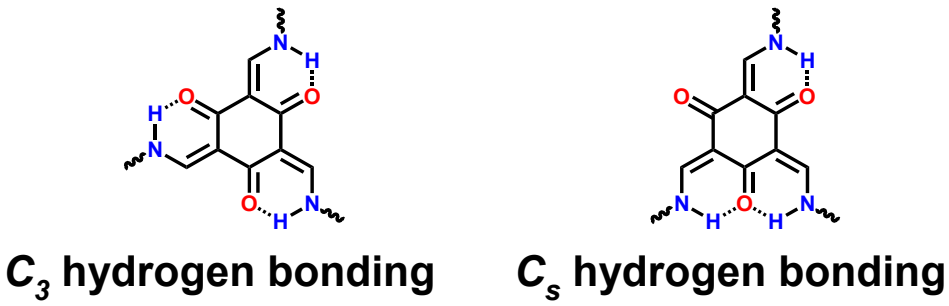

Figure 3.6. Structures of the central core when molecules adopt a C_3 geometric form or a C_s conformation. Dotted lines highlight the intramolecular hydrogen bonding patterns that are present within the molecules.

It is initially surprising when inspection of the structures presented in Figure 3.6 are studied, especially when considering the enol tautomeric version which loses its aromatic character with respect to the central ring. This loss of a highly stable aromatic structure must therefore be accompanied by a net stabilisation effect that occurs through one or more other factors. This net stabilisation is likely to arise from the strength of the hydrogen bonding between the hydrogens of the –NH groups and oxygen of the keto groups energetically compensating for the loss of aromaticity.

The compounds reported here do correspond to the literature data on the similar systems reported by Chong *et. al.*, in that the keto-enamine tautomer is significantly more stable, something they proved with ab initio DFT calculations to the order of ΔH_f = -75 kJ/mol. The keto-enamine to enol-imine tautomerisation, perhaps surprisingly never seems to occur. This is true even under conditions as harsh as being heated to 120 ^{o}C in an aprotic solvent, at least on an NMR timescale.

The calculations reported by Chong *et. al.*, also confirmed the planarity of the central core region was maintained through the hydrogen bonding pattern outlined in Figure 3.6, similar to those gelators with the hydrazone chemistry. Chong and coworkers also examined the geometric isomers, specifically whether there was any energetic preference when comparing the C_3 and the C_s conformations. It was determined that the C_3 form represented a more energetically favourable conformation, although the energy difference was negligible. Interestingly, ^{1}H NMR experiments of Chong *et. al.*, preformed in methanol-d_4 seemed to imply a changing in the ratio between C_3 and C_s that would suggest the C_s was the favoured geometric isomer in this polar protic solvent. This contradicts the lack of rotation possible around the sp^2 hybridised centres, so there may be dynamics present between the C_3 and C_s forms.

3.4 Ex situ ligand synthesis and subsequent gel setting

As with the hydrazine-based gelator in the previous chapter, it is possible to synthesise all compounds presented in this chapter so far through an *ex situ* method, as well as the so far discussed *in situ* method. This *ex situ* approach is the method most commonly presented in the literature for the synthesis of compounds of this type.[15] With the *ex situ* synthesised compounds **R$_1$** – **R$_9$**, a gel can be set through dissolving these compounds in water, at the desired wt%, through the addition of sodium hydroxide, complete dissolution occurring around pH 8, with the subsequent addition of nine equivalents of GdL resulting

in gelation. This resulted in the production of gels that were at least, when considered with the naked eye, identical to those produced using the *in situ* method. The similarity between the *in situ* and *ex situ* prepared gels did not end at their visual appearance, perhaps unsurprising when considering the identical chemical structure of the compounds. These similarities will be discussed in detail in the following sections both in terms of the gels rheological and morphological characteristics.

3.5 Apparent pK_a Determination

With the LMWG presented in this chapter, whether they are synthesised *in situ* or *ex situ*, the trigger to induce their transition from sol to gel is a change in pH from high to low. The use of GdL, in order to produce a homogenous gel network, in a quantity of 9 equivalents generally results in a gel with a pH between 3 and 4. This pH is far below the pH at which the protonation process of carboxylic acid begins, which signifies the start of the gelation process.

There is a way to determine the point at which this reprotonation process begins, and this is through determination of the apparent pK_a for the LMWG.[16,17] This involves dissolving the LMWG in water with the addition of sodium hydroxide, with the addition of base continuing until the pH is recorded to be around pH 10. A mildy acidic HCl solution (pH 3) is then added to the gelator solution in aliquots, with the pH of the gelator solution recorded after each addition. This will result in a decreasing pH down to the point at which significant protonation of the LMWG molecules begins. This protonation process results in a dramatic decrease in the rate of change of pH as deprotonated LMWG molecules effective "mop up" the additional H^+, essentially buffering the solution. This buffering effect results in a plateau region when the pH is plotted against volume of acidic solution added, this region represents the apparent pK_a of the gelator molecule. This titration experiment was performed on *ex situ* synthesised samples of compounds **R$_1$** – **R$_9$** in order to determine the minimum pH range (the apparent pK_a) which is critical for the gelation process. Something that will be of great importance during discussions in the later sections of this chapter.

Table 3.1 displays the results of these titration experiments and highlights the region that can be described as the apparent pK_a for each of the molecules. For compounds **R$_1$** – **R$_8$** the plot profiles and apparent pK_as are all relatively similar. This is to be expected as the protonation event with all these compounds is occurring at an aromatic carboxylate group. There are minor differences between the compounds in terms of the plateau region

with regards to the y-axis (pH). This can be explained by considering the substituent groups on the benzoic acid arms of each of the molecules. Depending on whether these groups are electron donating or electron withdrawing, the groups will influence the pK_a of the carboxylic acid group. For example **R6**, which features an electron withdrawing – CF_3 group, has the apparent pK_a of its benzoic acid group effectively lowered by this effect. The hydrophobicity of the molecules will also affect the pK_a, with more hydrophobic molecules protonating easier as to move out of the aqueous environment. These two effects combine to give the resultant changes that can be observed in the experimentally determined apparent pK_a of the molecules.

Table 3.1 Apparent pK_a determined for each of the LMWG presented in this chapter (**R1** – **R9**).

Gelator	Apparent pK_a range
R1	5.8 – 6.1
R2	5.5 – 5.8
R3	5.7 – 6.1
R4	6.2 – 6.5
R5	5.8 – 6.1
R6	5.0 – 5.2
R7	6.3 – 6.5
R8	6.0 – 6.4
R9	9.0 – 9.9

The significant outlier, both in terms of plot profile and apparent pK_a, is compound **R9**. This does not come as any great surprise given that **R1** – **R8** rely on protonation of a carboxylic acid group to induce gelation, rather the protonation of a phenolic-type O^- groups of **R9**. When considering the pK_a of phenol, it is clear it is significantly higher than that of a carboxylic acid, including of course benzoic acid (phenol pK_a = 9.95 vs. benzoic acid pK_a = 4.2). This results in a much strong conjugate base, which will effectively "mop up" protons at a much higher pH than is possible for benzoic acid. This results in the LMWG **R9** having an apparent pK_a of 9.0 – 9.9, significantly different to the atypical carboxylic acid-based gelator from this family, **R1**, having an apparent pK_a of 5.8-6.1.

These apparent pK_a values demonstrate the minimum pH the solutions would have to be adjusted to in order to start setting a gel. Even the gels in this family with the highest apparent pK_as have a pK_a too acidic to be used for any biological applications. With this in mind, the continued use of GdL was recognised as the best way to set future gel samples

using these LMWGs, mostly as the high level of structural homogeneity that could be achieved with GdL is deemed to be of greater importance than setting a gel with a minimal addition of acid.

3.6 Morphology and supramolecular structural characterisation

Characterisation of the network structure of the gels was conducted using SEM. As with the examples in the previous chapter, imaging was conducted on samples of the gels that had been dried out. Before the SEM analysis was conducted a fibrous morphology was expected. This would be in line similar tripodal gelator systems published in the literature and seen in columnar stacking liquid crystalline species.[14]

SEM images could be gathered for the dried samples, with a thin gold coating applied as can be seen in Figure 3.7. This has allowed comparisons to be made between the apparent supramolecular structure of the gels that were formed using the *in situ* and *ex situ* methods of preparation. Upon inspection of these images it is clear that all gels would appear to be reliant on a three-dimensional fibrous network for solvent immobilisation, which is a well-recognised motif for gelation by LMWGs.[18–22] When comparing the SEM images for samples of *in situ* and *ex situ* prepared gels, there is very little, if any, noticeable difference between the images resulting in it being impossible to distinguish between the preparation methods based solely on SEM. Something else that was can be seen is the lack of difference between the gels in terms of their morphology. This was perhaps surprising given that gels **R**$_2$ and **R**$_6$ are more transparent than the other members of the family (this is especially true in the case of **R**$_6$). The transparency of supramolecular gels is related to the width of the fibres that make up their three-dimensional network. The wider the fibres the more light that will be scattered, meaning that gels with thick fibres will look much more opaque than gels with narrow fibres. With this in mind, it was expected that gels **R**$_2$ and **R**$_6$ would exhibit narrower fibres than the rest, however, fibre width was similar between all the family members. This could be down to the requirement of a gold coating resulting in the loss of some of the finer structural detail, or the SEM resolution being high enough or the drying process concealing the fibre width.

While the SEM images presented in Figure 3.7 are compelling in their demonstration of the gels fibrous morphology, they perhaps lack the sufficient detail to allow recognition of the gel based solely on their morphology. Even the **R**$_9$ gel, which as mentioned previous has a visibly less homogeneous structure than gels **R**$_1$ – **R**$_8$, appears

to have an identical morphology, at least as far as SEM at the available resolutions is concerned. A limitation of this SEM study and the images presented are the differences in magnification between images. This was unfortunately unavoidable due to focusing limitations of the instrument and the requirement to stop charging of the samples occurring (charging was prevalent with these samples even with gold coating). Despite these limitations the SEM imaging has provided confirmation of the expected fibrous morphology, which will be important when considering results of other analytical techniques.

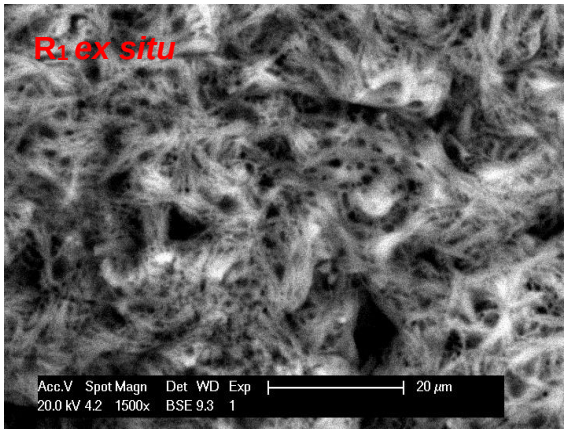

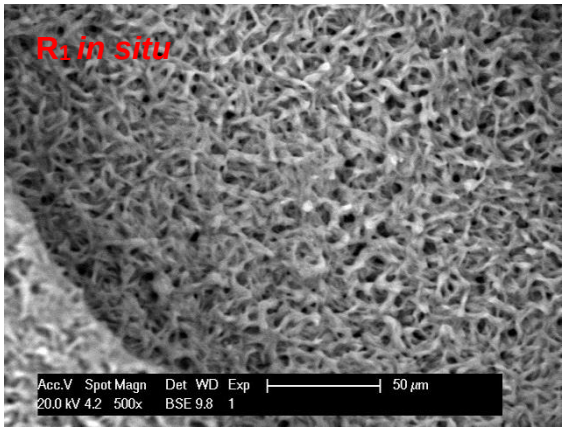

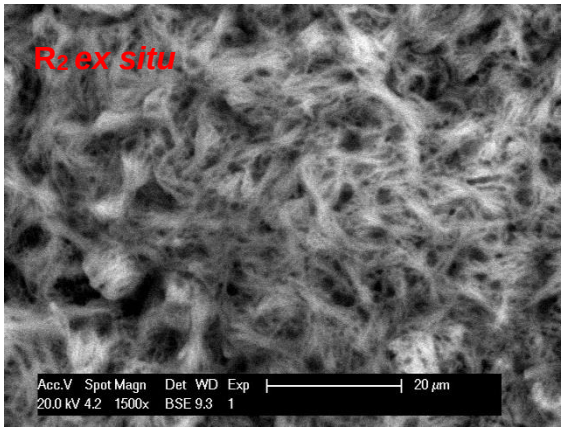

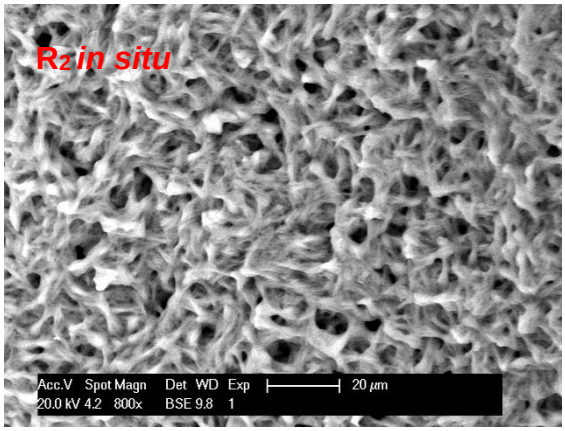

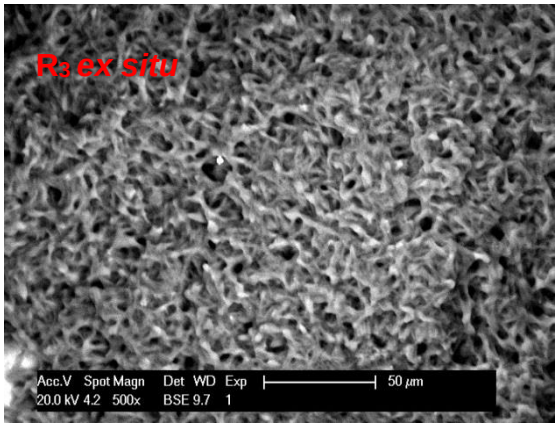

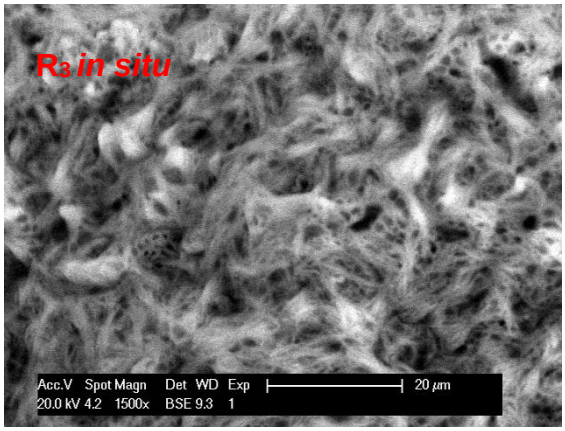

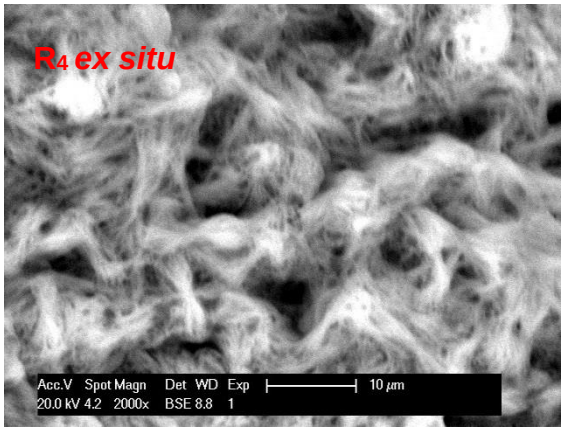
R4 ex situ
Acc.V Spot Magn Det WD Exp 10 µm
20.0 kV 4.2 2000x BSE 8.8 1

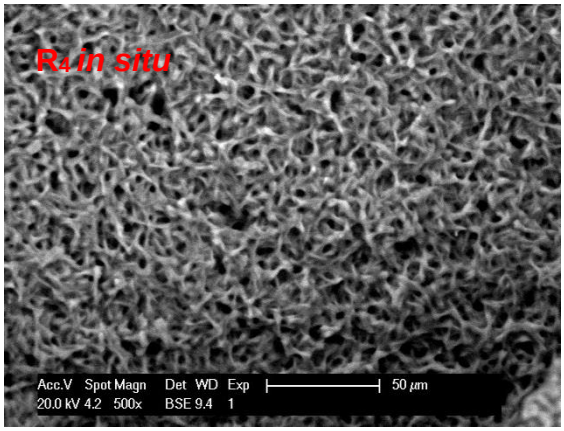
R4 in situ
Acc.V Spot Magn Det WD Exp 50 µm
20.0 kV 4.2 500x BSE 9.4 1

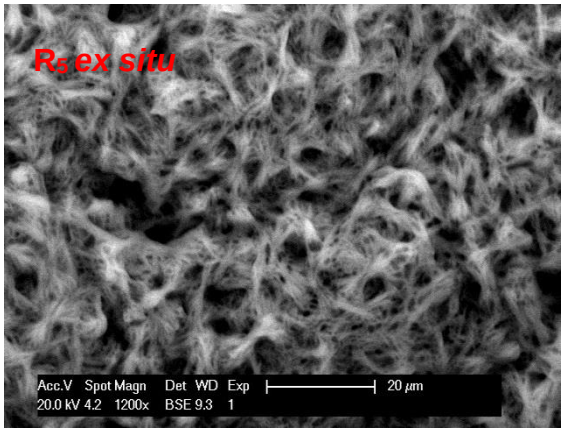
R5 ex situ
Acc.V Spot Magn Det WD Exp 20 µm
20.0 kV 4.2 1200x BSE 9.3 1

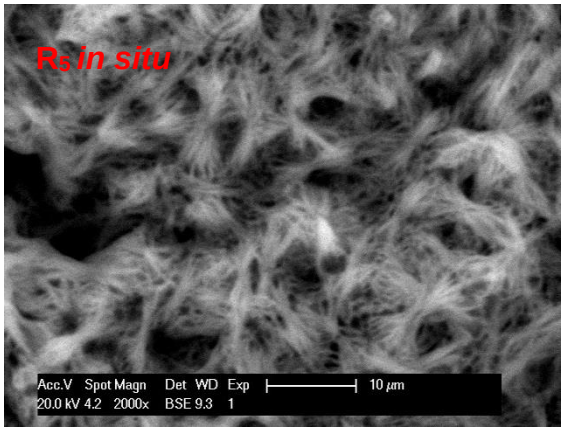
R5 in situ
Acc.V Spot Magn Det WD Exp 10 µm
20.0 kV 4.2 2000x BSE 9.3 1

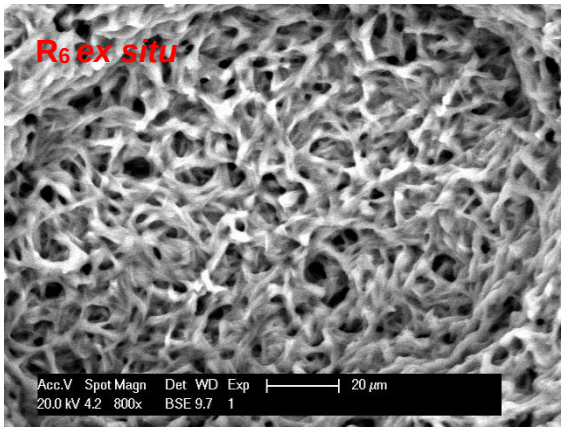
R6 ex situ
Acc.V Spot Magn Det WD Exp 20 µm
20.0 kV 4.2 800x BSE 9.7 1

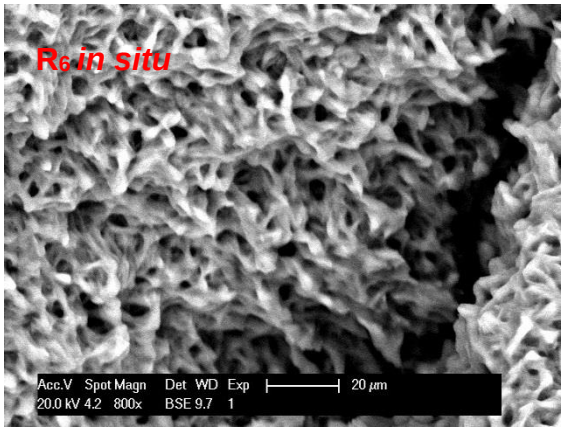
R6 in situ
Acc.V Spot Magn Det WD Exp 20 µm
20.0 kV 4.2 800x BSE 9.7 1

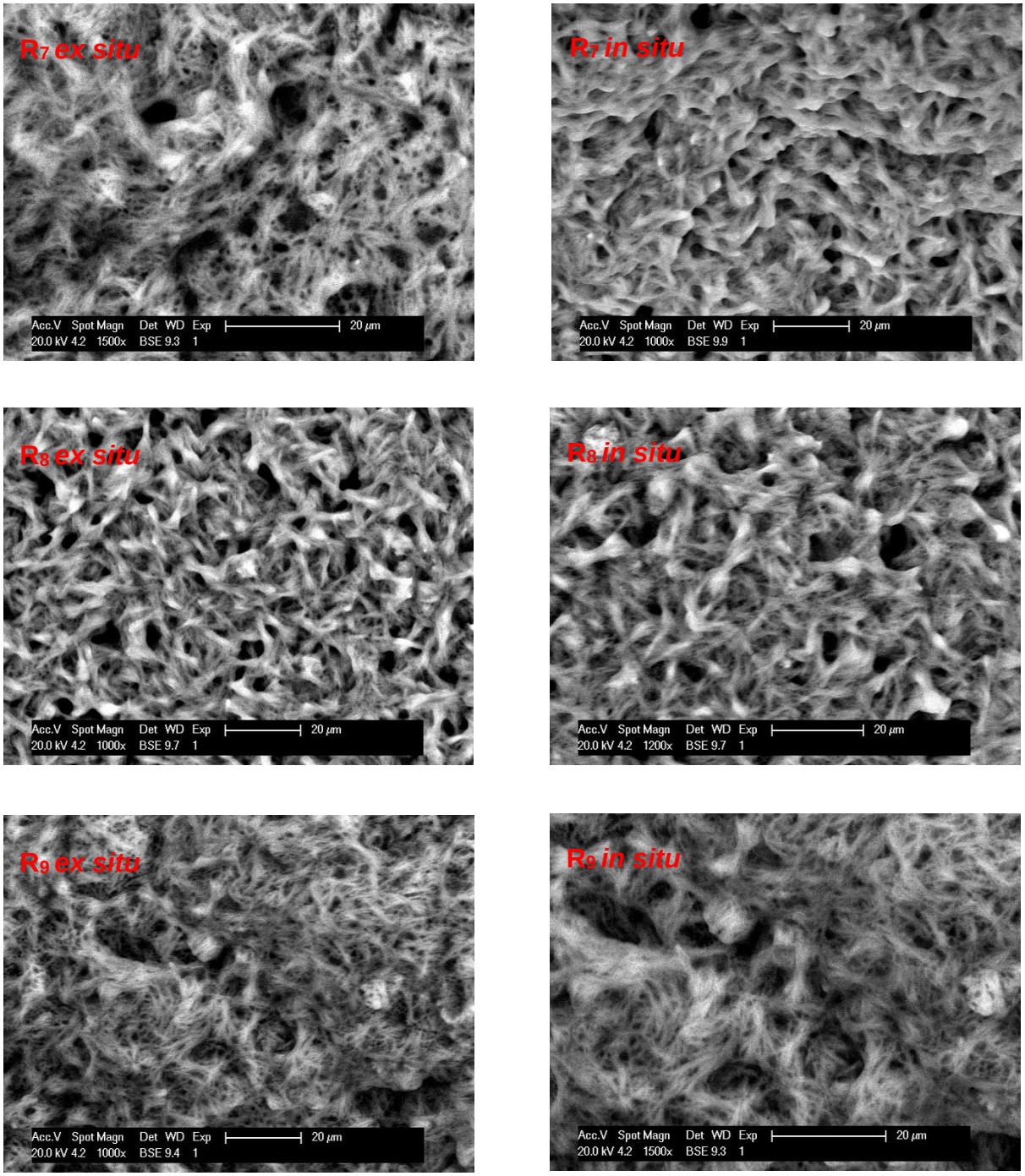

Figure 3.7. SEM images obtained for gels $\mathbf{R_1}$ to $\mathbf{R_9}$ with examples shown of gels set using both the *in situ* and *ex situ* method of ligand preparation. Samples are labelled accordingly in red text in top left of image. Note the difference in scale bars when comparing images.

3.7 Rheological characterisation

Characterisation of the rheological properties of the gels highlighted the differences between these gels formed with closely related LMWGs. The standard experiments of

frequency and stress sweeps were performed on samples of all the gels produced. All gels were set with GdL The exception to this was gel **R9**, because its reaction solution required the addition of conc. HCl, which resulted in an instantaneous gelation. The data produced allowed comparisons between the individual gels to be made and highlights the diversity in terms of the mechanical strength for the chemically very similar gels presented in this chapter.

The data presented in Figures 3.8 to 3.25 (pages 126 to 135) highlights the similarities and differences between the different LMWGs. All the gels behave similarly in terms of their response to an externally applied mechanical force, resulting in broadly similar plots for all data. For all gels, *G′* was at least two times greater than *G″*, and all gels showed typical yield torques, i.e. highlighting that these materials are indeed gels. All data is summarised in Table 3.2 (page 135), along with the CGCs of the LMWGs. These CGCs for the majority of the presented samples fall into the category of being a "super-gelator".[23,24]

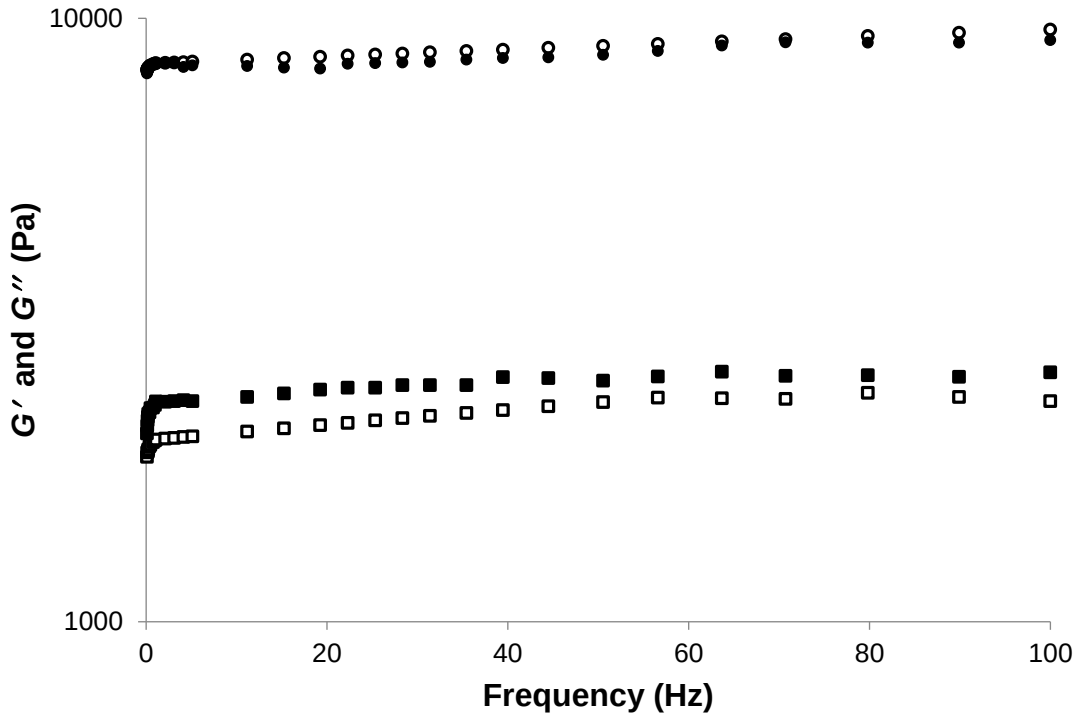

Figure 3.8. Results of the frequency sweep rheology experiment for the gel prepared using both an *in situ* and *ex situ* synthesised sample of **R1** at a concentration of 25 mM. The storage modulus *G′*(Pa) *in situ* (●) and *ex situ* (○) as well as the loss modulus *G″*(Pa) *in situ* (■) and *ex situ* (□) are shown as a log scale (y-axis) against the frequency (Hz) (x-axis).

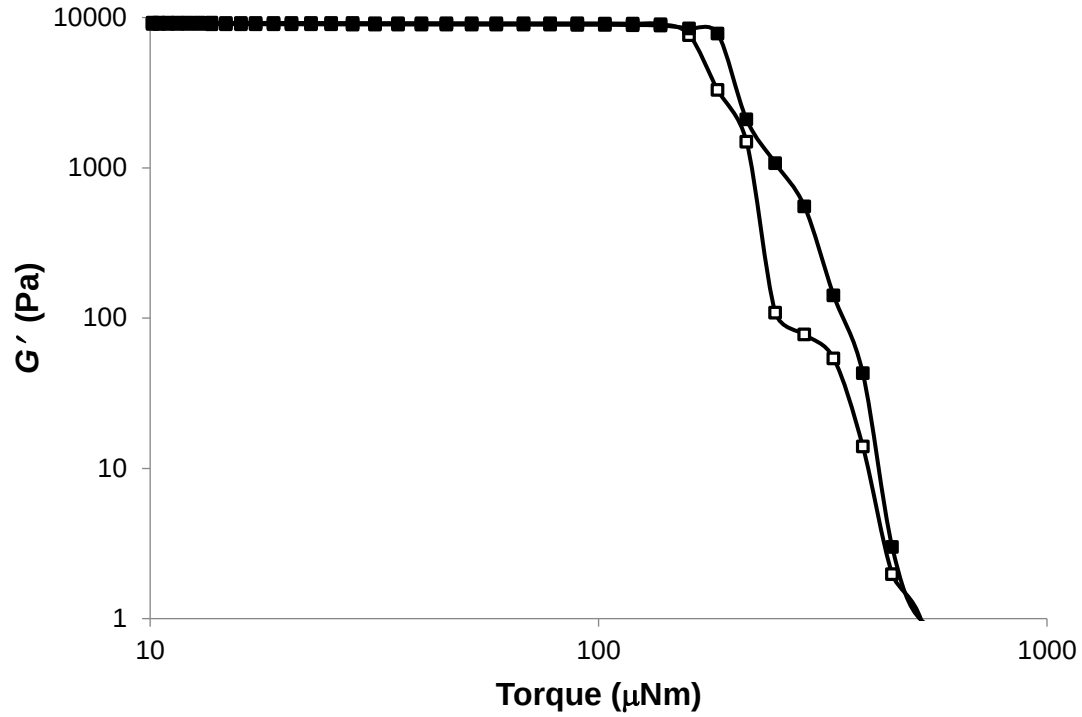

Figure 3.9. Results of the stress sweep rheology experiment for the gel prepared using both an *in situ* and *ex situ* synthesised sample of **R**$_1$ at a concentration of 25 mM. Storage modulus *G′* for *in situ* (■) and *ex situ* (□) synthesised samples (Pa) (y-axis) plotted against torque (μNm) shown as a log scale (x-axis).

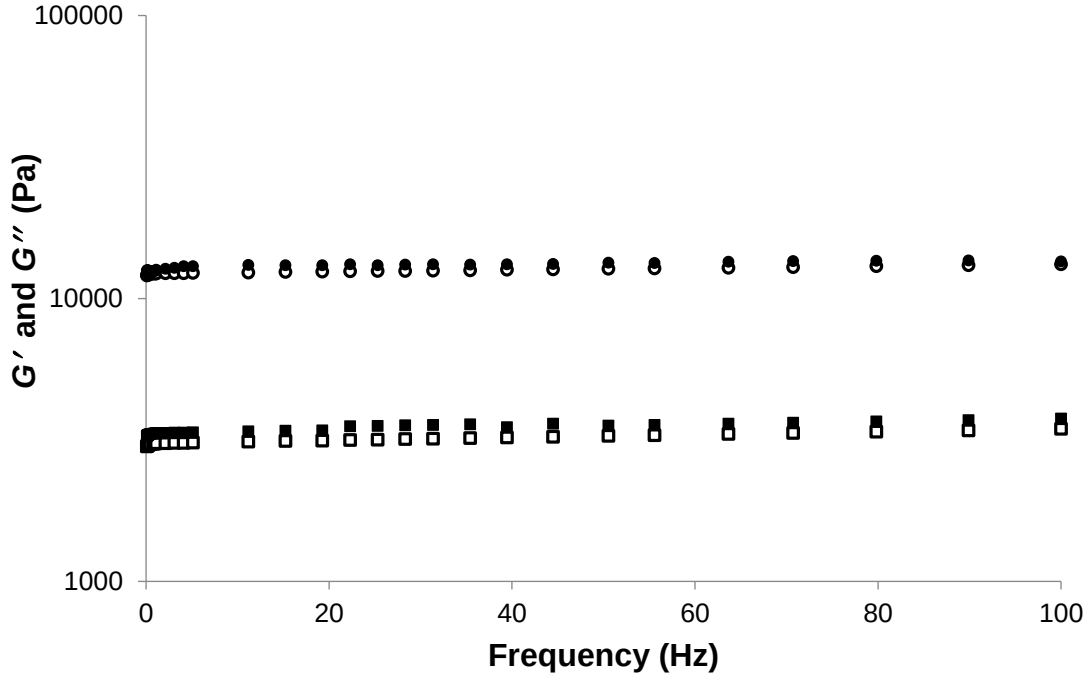

Figure 3.10. Results of the frequency sweep rheology experiment for the gel prepared using both an *in situ* and *ex situ* synthesised sample of **R**$_2$ at a concentration of 25 mM. The storage modulus *G′*(Pa) *in situ* (●) and *ex situ* (○) as well as the loss modulus *G″*(Pa) *in situ* (■) and *ex situ* (□) are shown as a log scale (y-axis) against the frequency (Hz) (x-axis).

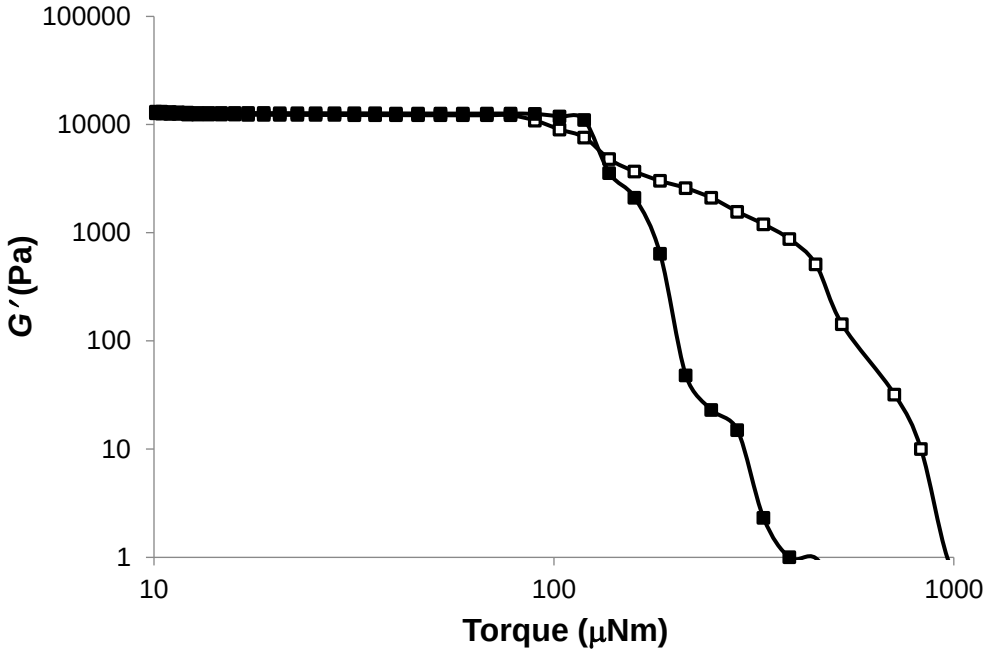

Figure 3.11. Results of the stress sweep rheology experiment for the gel prepared using both an *in situ* and *ex situ* synthesised sample of **R**$_2$ at a concentration of 25 mM. Storage modulus *G′* for *in situ* (■) and *ex situ* (□) synthesised samples (Pa) (y-axis) plotted against torque (μNm) shown as a log scale (x-axis).

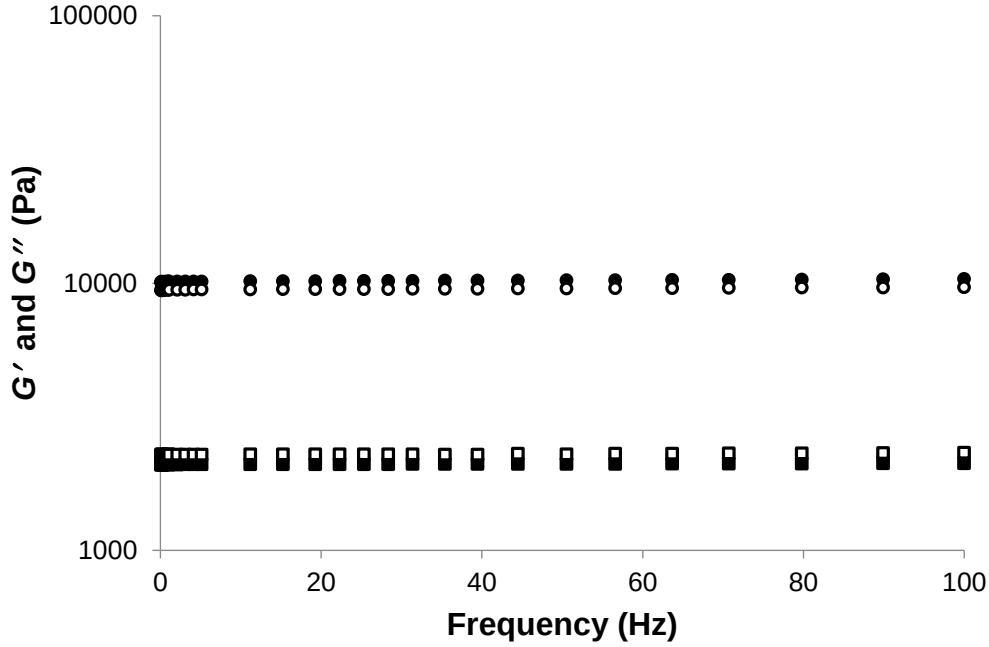

Figure 3.12. Results of the frequency sweep rheology experiment for the gel prepared using both an *in situ* and *ex situ* synthesised sample of **R**$_3$ at a concentration of 25 mM. The storage modulus *G′*(Pa) *in situ* (●) and *ex situ* (○) as well as the loss modulus *G″*(Pa) *in situ* (■) and *ex situ* (□) are shown as a log scale (y-axis) against the frequency (Hz) (x-axis).

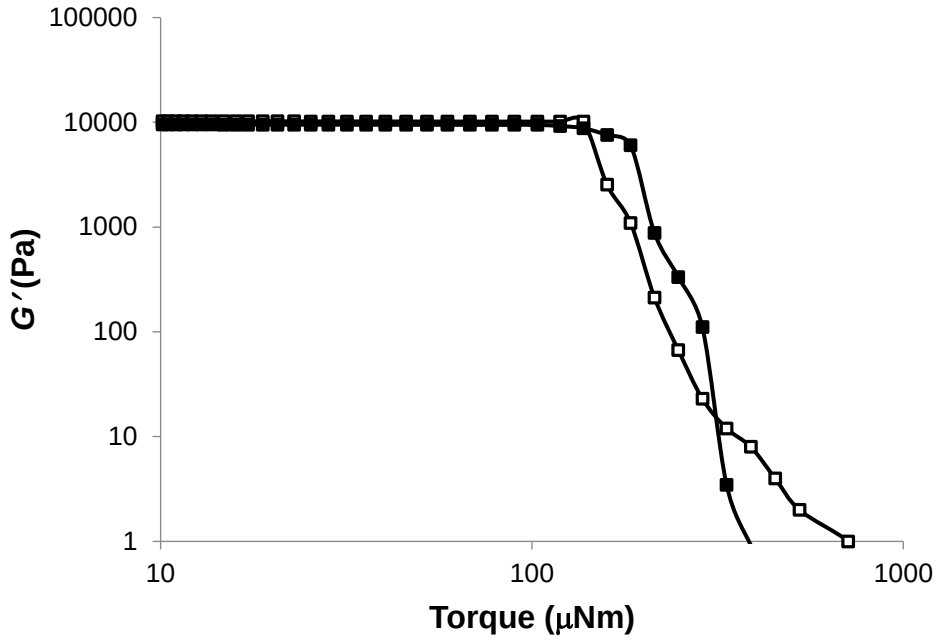

Figure 3.13. Results of the stress sweep rheology experiment for the gel prepared using both an *in situ* and *ex situ* synthesised sample of **R**$_3$ at a concentration of 25 mM. Storage modulus *G′* for *in situ* (■) and *ex situ* (□) synthesised samples (Pa) (y-axis) plotted against torque (μNm) shown as a log scale (x-axis).

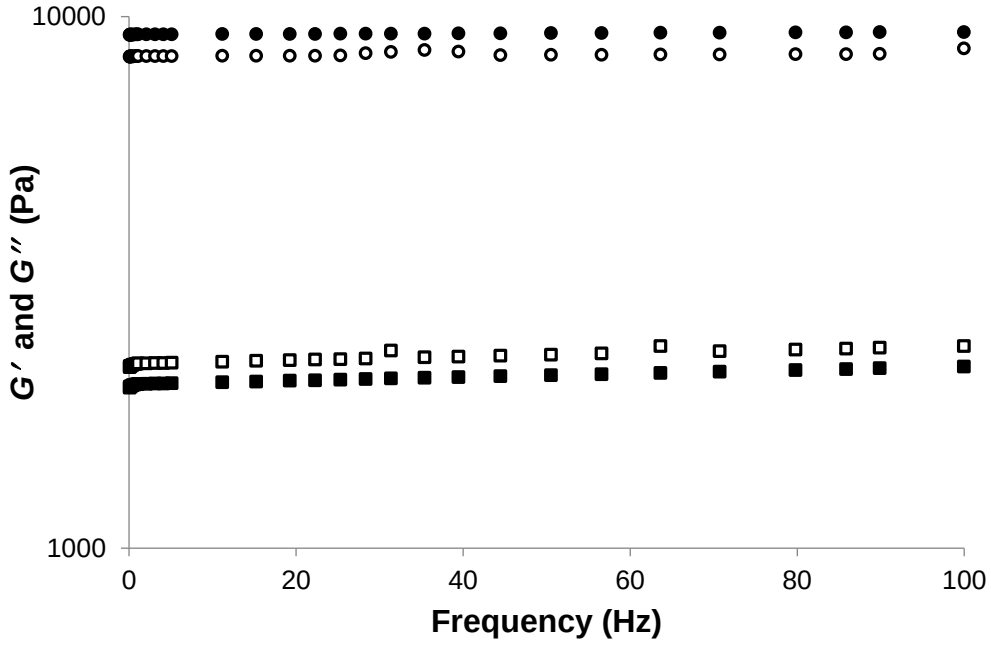

Figure 3.14. Results of the frequency sweep rheology experiment for the gel prepared using both an *in situ* and *ex situ* synthesised sample of **R**$_4$ at a concentration of 25 mM. The storage modulus *G′*(Pa) *in situ* (●) and *ex situ* (○) as well as the loss modulus *G″*(Pa) *in situ* (■) and *ex situ* (□) are shown as a log scale (y-axis) against the frequency (Hz) (x-axis).

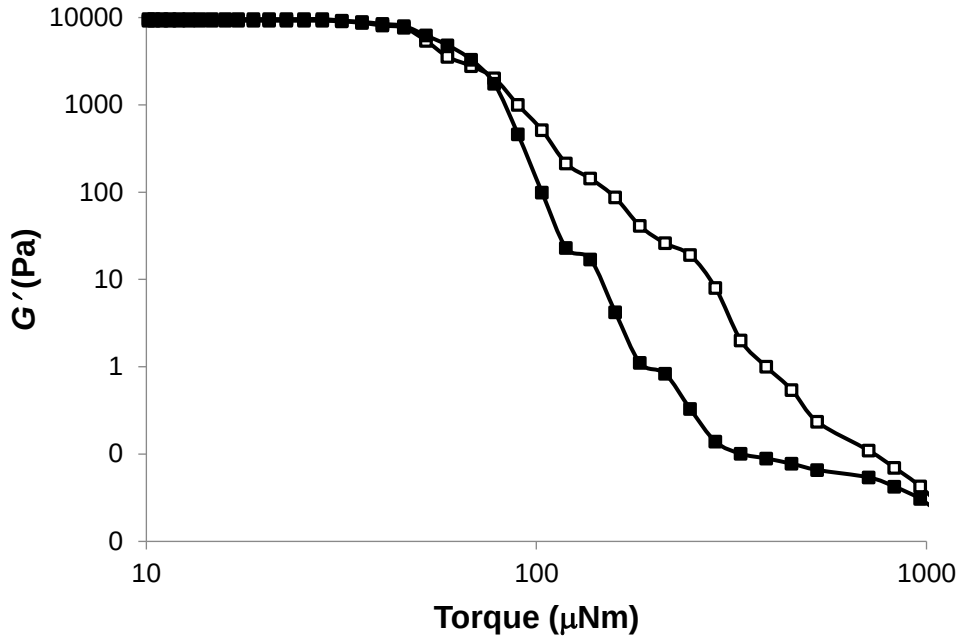

Figure 3.15. Results of the stress sweep rheology experiment for the gel prepared using both an *in situ* and *ex situ* synthesised sample of **R₄** at a concentration of 25 mM. Storage modulus *G′* for *in situ* (■) and *ex situ* (□) synthesised samples (Pa) (y-axis) plotted against torque (μNm) shown as a log scale (x-axis).

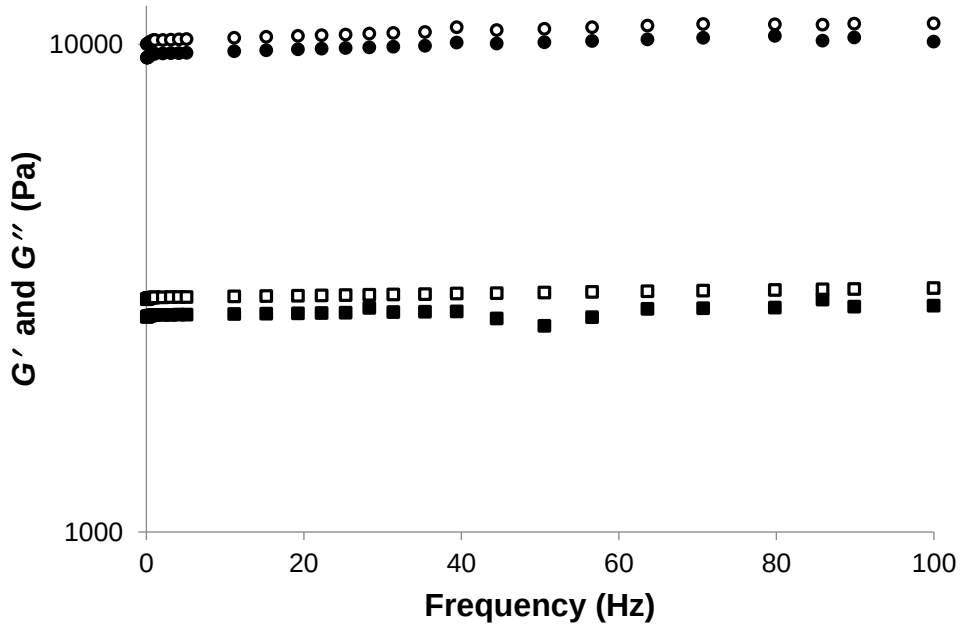

Figure 3.16. Results of the frequency sweep rheology experiment for the gel prepared using both an *in situ* and *ex situ* synthesised sample of **R₅** at a concentration of 25 mM. The storage modulus *G′*(Pa) *in situ* (●) and *ex situ* (○) as well as the loss modulus *G″*(Pa) *in situ* (■) and *ex situ* (□) are shown as a log scale (y-axis) against the frequency (Hz) (x-axis).

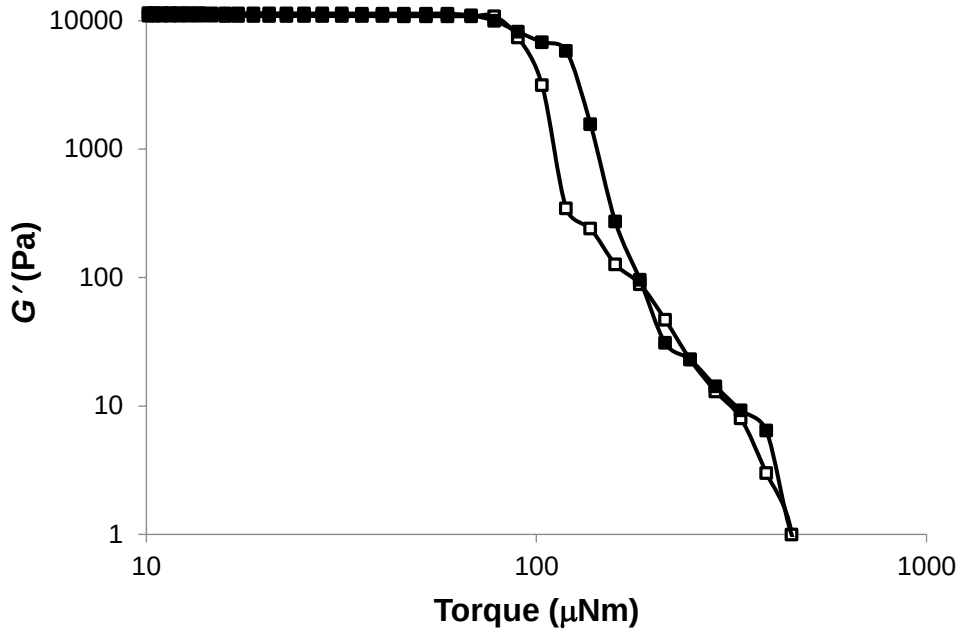

Figure 3.17. Results of the stress sweep rheology experiment for the gel prepared using both an *in situ* and *ex situ* synthesised sample of $\mathbf{R_5}$ at a concentration of 25 mM. Storage modulus *G′* for *in situ* (■) and *ex situ* (□) synthesised samples (Pa) (y-axis) plotted against torque (μNm) shown as a log scale (x-axis).

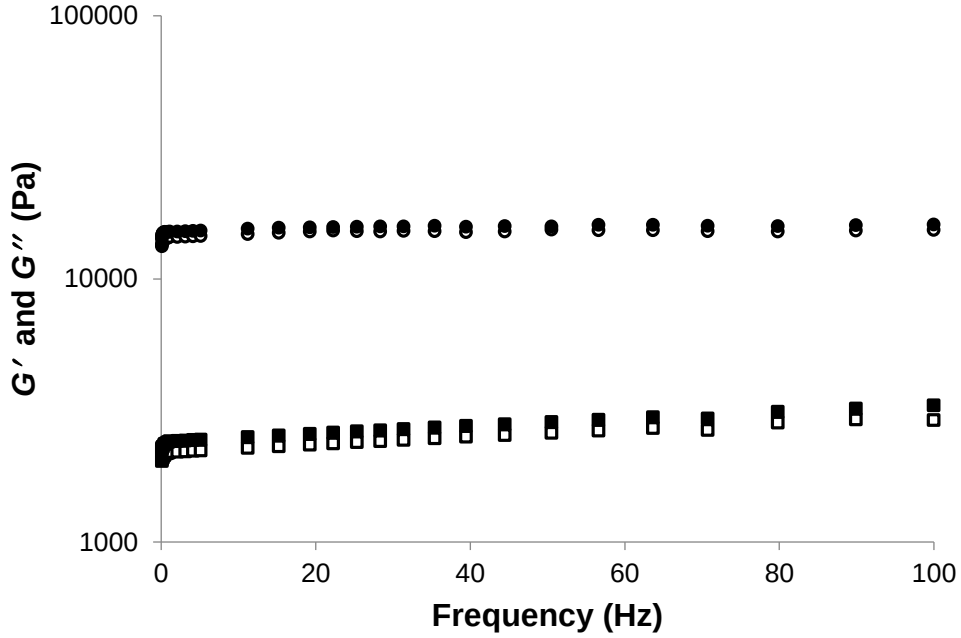

Figure 3.18. Results of the frequency sweep rheology experiment for the gel prepared using both an *in situ* and *ex situ* synthesised sample of $\mathbf{R_6}$ at a concentration of 25 mM. The storage modulus *G′*(Pa) *in situ* (●) and *ex situ* (○) as well as the loss modulus *G″*(Pa) *in situ* (■) and *ex situ* (□) are shown as a log scale (y-axis) against the frequency (Hz) (x-axis).

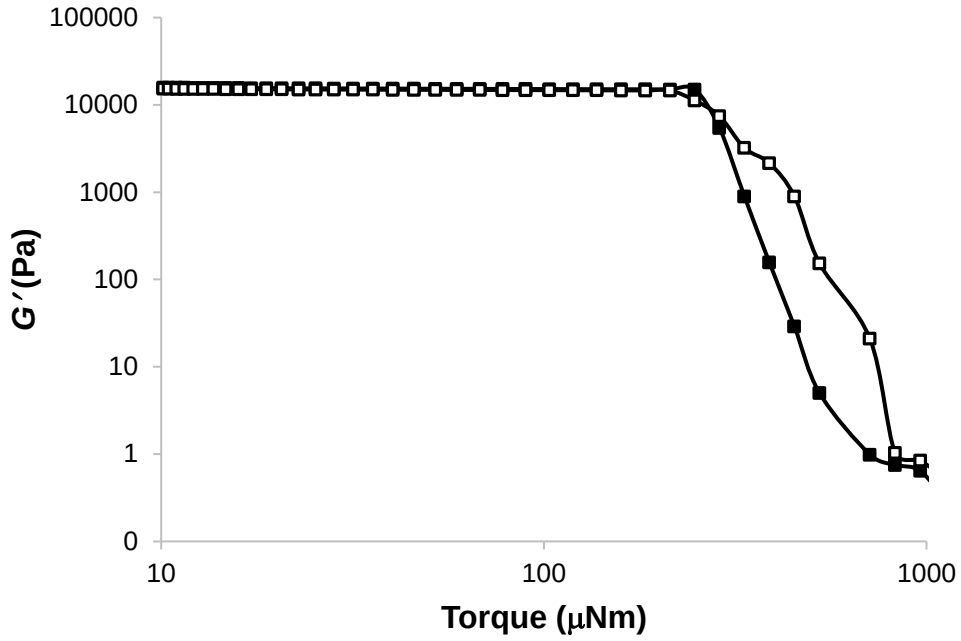

Figure 3.19. Results of the stress sweep rheology experiment for the gel prepared using both an *in situ* and *ex situ* synthesised sample of $\mathbf{R_6}$ at a concentration of 25 mM. Storage modulus *G′* for *in situ* (■) and *ex situ* (□) synthesised samples (Pa) (y-axis) plotted against torque (μNm) shown as a log scale (x-axis).

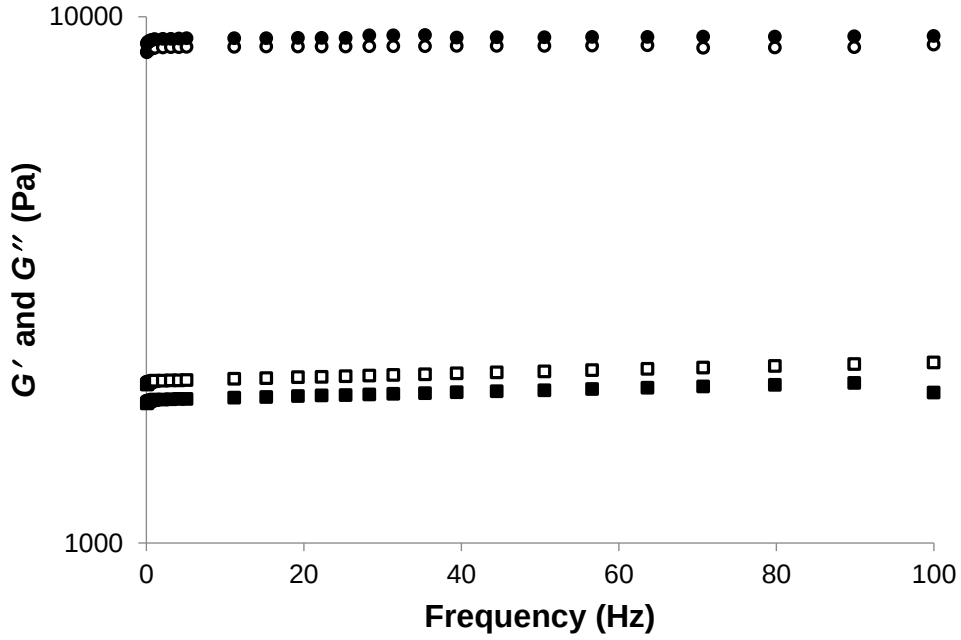

Figure 3.20. Results of the frequency sweep rheology experiment for the gel prepared using both an *in situ* and *ex situ* synthesised sample of $\mathbf{R_7}$ at a concentration of 25 mM. The storage modulus *G′*(Pa) *in situ* (●) and *ex situ* (○) as well as the loss modulus *G″*(Pa) *in situ* (■) and *ex situ* (□) are shown as a log scale (y-axis) against the frequency (Hz) (x-axis).

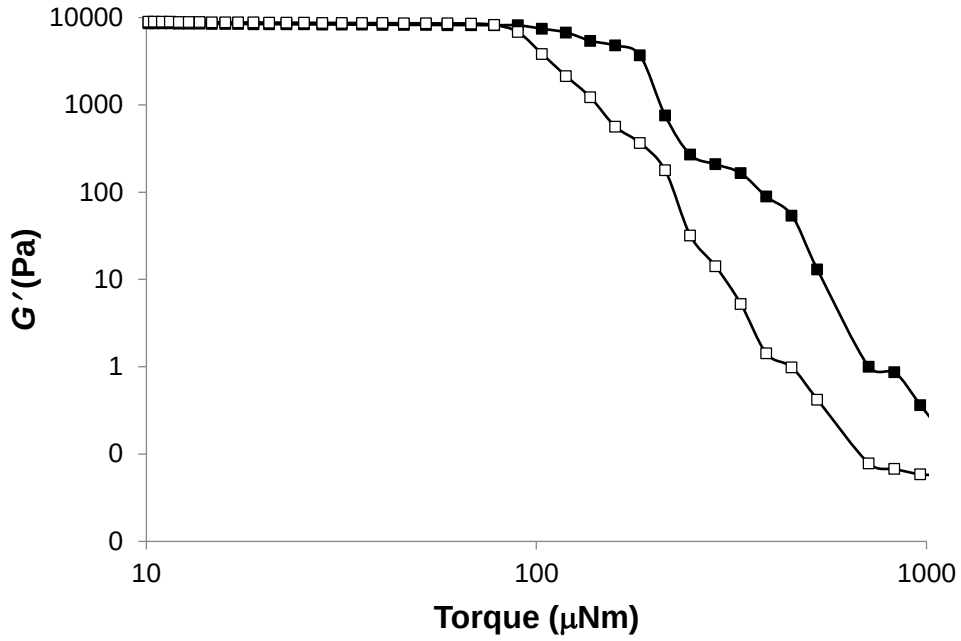

Figure 3.21. Results of the stress sweep rheology experiment for the gel prepared using both an *in situ* and *ex situ* synthesised sample of $\mathbf{R_7}$ at a concentration of 25 mM. Storage modulus *G′* for *in situ* (■) and *ex situ* (□) synthesised samples (Pa) (y-axis) plotted against torque (μNm) shown as a log scale (x-axis).

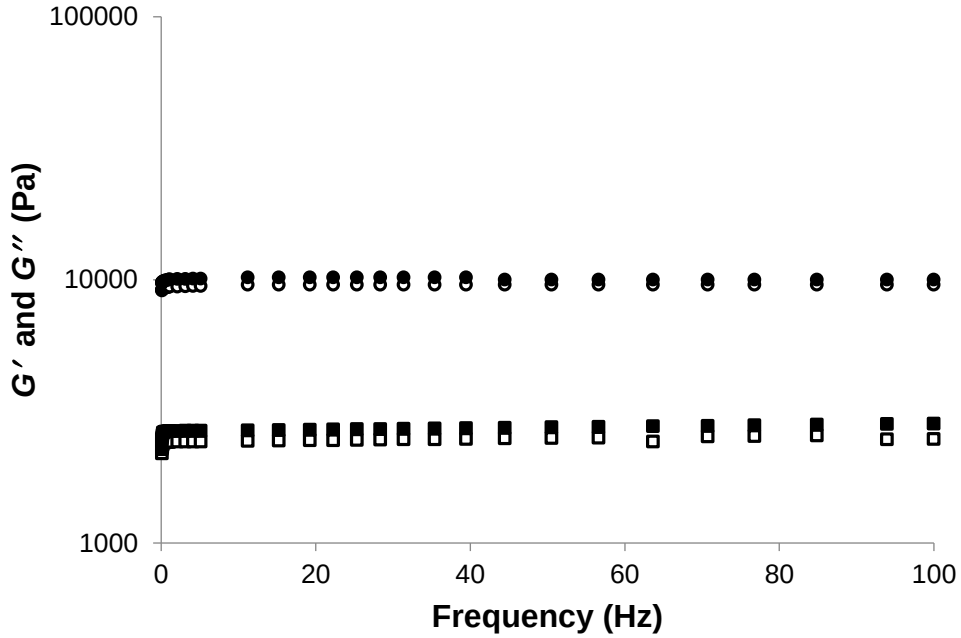

Figure 3.22. Results of the frequency sweep rheology experiment for the gel prepared using both an *in situ* and *ex situ* synthesised sample of $\mathbf{R_8}$ at a concentration of 25 mM. The storage modulus *G′*(Pa) *in situ* (●) and *ex situ* (○) as well as the loss modulus *G″*(Pa) *in situ* (■) and *ex situ* (□) are shown as a log scale (y-axis) against the frequency (Hz) (x-axis).

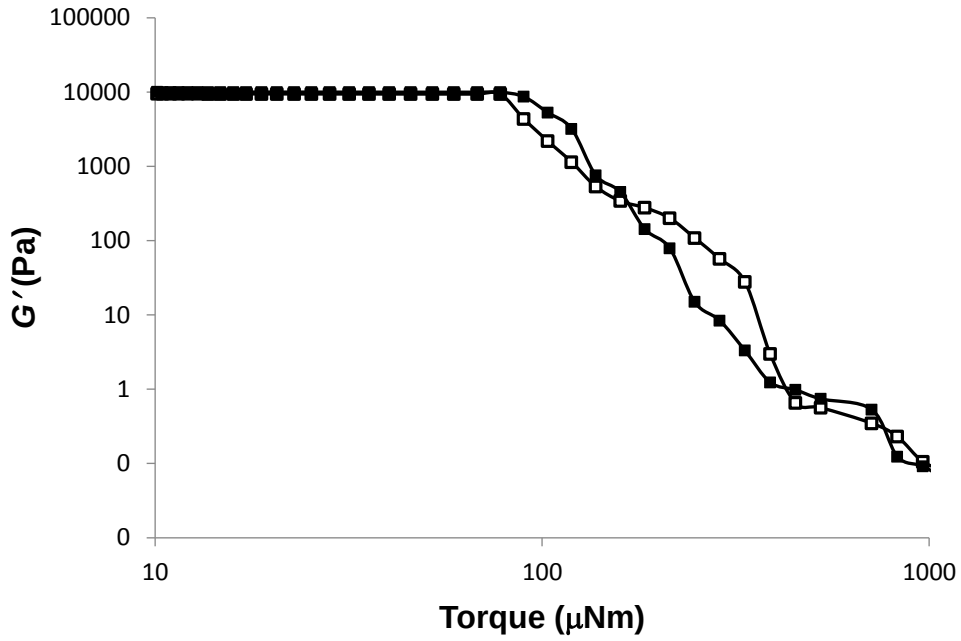

Figure 3.23. Results of the stress sweep rheology experiment for the gel prepared using both an *in situ* and *ex situ* synthesised sample of $\mathbf{R_8}$ at a concentration of 25 mM. Storage modulus *G′* for *in situ* (■) and *ex situ* (□) synthesised samples (Pa) (y-axis) plotted against torque (μNm) shown as a log scale (x-axis).

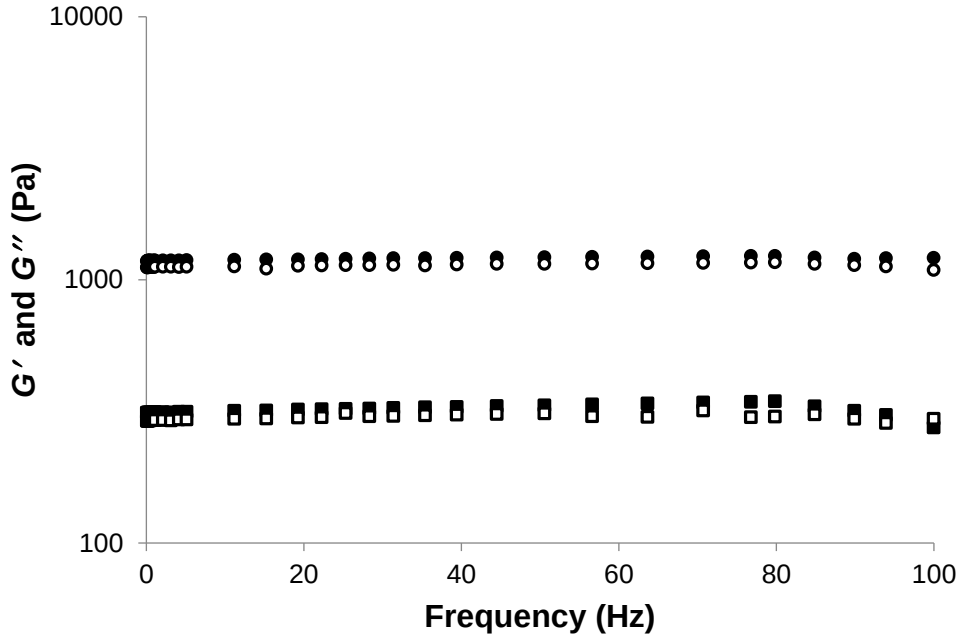

Figure 3.24. Results of the frequency sweep rheology experiment for the gel prepared using both an *in situ* and *ex situ* synthesised sample of $\mathbf{R_9}$ at a concentration of 25 mM. The storage modulus *G′*(Pa) *in situ* (●) and *ex situ* (○) as well as the loss modulus *G″*(Pa) *in situ* (■) and *ex situ* (□) are shown as a log scale (y-axis) against the frequency (Hz) (x-axis).

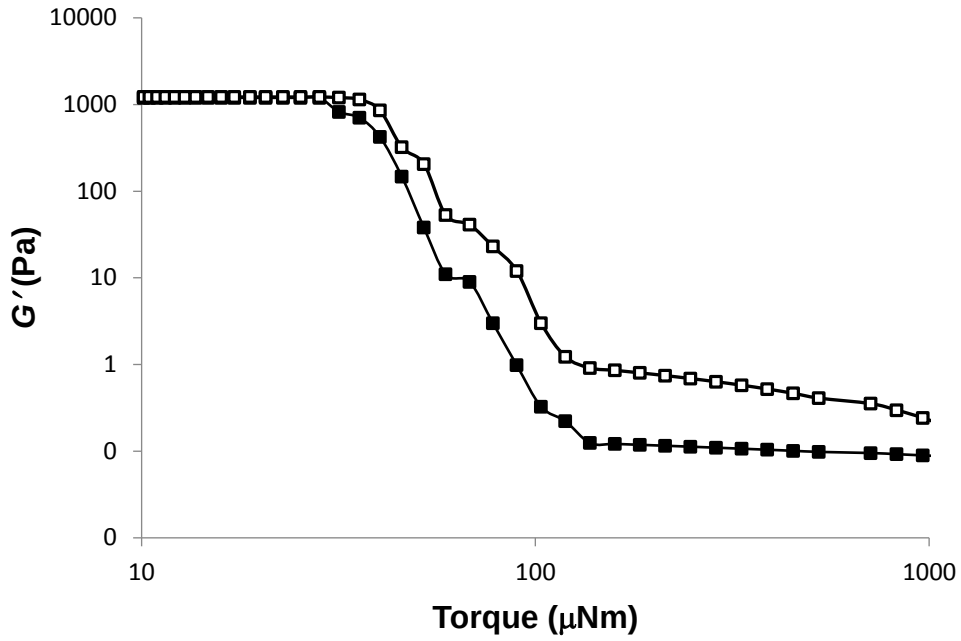

Figure 3.25. Results of the stress sweep rheology experiment for the gel prepared using both an *in situ* and *ex situ* synthesised sample of **R₈** at a concentration of 25 mM. Storage modulus *G′* for *in situ* (■) and *ex situ* (□) synthesised samples (Pa) (y-axis) plotted against torque (μNm) shown as a log scale (x-axis).

Table 3.2 highlights the similar nature of the relation between the three measured rheological properties of *G′*, *G″* and yield stress. The fact that in all cases the *G′* for the gels exceeded that of *G″* demonstrate the gelatinous nature of the materials. These frequency sweep results confirm the gels are behaving as truly viscoelastic materials. The stronger gels, based on the *G′*, are loosely similar to the trends seen in the yield stress and CGC.

Table 3.2. Summary of rheological properties for gels R_1 to R_9.

Gel	*G′*(Pa)	*G″*	Yield stress (μNm)	CGC (wt%)
R₁	9000	2300	140	0.3
R₂	12700	3300	80	0.2
R₃	10200	2100	140	0.5
R₄	9300	2100	40	0.4
R₅	10800	3100	80	0.4
R₆	15400	2600	250	0.1
R₇	8800	2100	90	0.5
R₈	9600	2500	70	0.5
R₉	1200	300	20	0.9

3.8 Relation between hydrophobicity and rheology

The reason for the difference in the *G′* between members of the LMWG family is not necessarily apparent. All examples would appear to rely on face-to-face π-π interactions to drive the propagation of the high aspect ratio fibres needed for the entangled network for gelation to occur. Despite this the relationship between the physical properties of the individual gelator molecules and the physical properties of the macroscopic gel assembly was sought. By far the gel with the highest *G′* was gel **R6**, which was composed of molecular building blocks that featured a trifluoromethyl group on each of its three benzoic acid units. The trifluoromethyl group has long been associated with increasing the hydrophobicity of molecules that are functionalised with it.[25] The hydrophobicity of a molecule can be quantified through calculation of that molecules theoretical *c*logP value calculated using Chemdraw (see appendix A section 6.2.10). Briefly put, a *c*logP value for a molecule refers to the logarithm of its partition coefficient between n-octanol and water, $\log(c_{octanol}/c_{water})$. While this value can be determined experimentally, most reference to *c*logP values in the modern literature refer to a calculated theoretical value.[26] With this in mind, the *c*logP values for gelators **R1** – **R9** was calculated in both their protonated, i.e. gelating form, and deprotonated solubilised form.[27,28] Once calculated a plot of *G′* against *c*logP could be produced in order to ascertain whether there was any realistic correlation between the two quantities. Figure 3.26 highlights this relationship between *c*logP and *G′*, which would appear to be linear in nature.

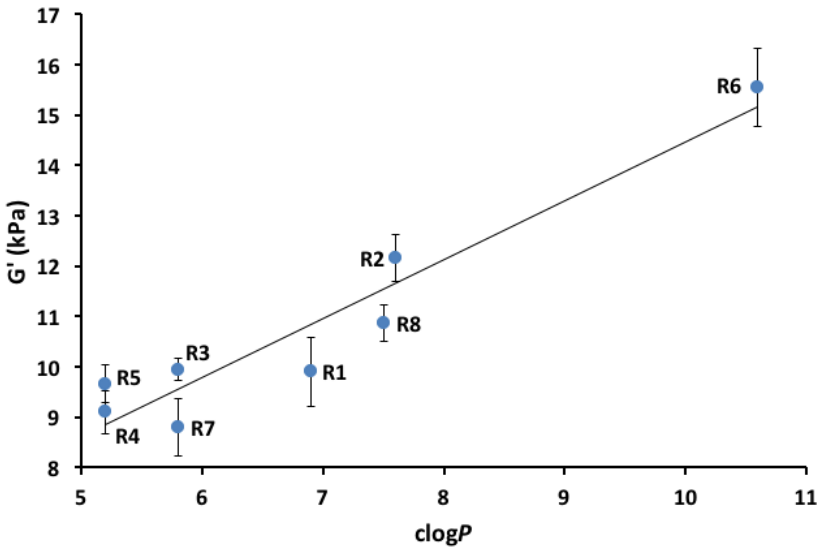

Figure 3.26. Plot showing linear relationship between the *c*logP value of the gelating (protonated) for of molecules **R1** – **R8** (molecule **R9** omitted owing to it being impossible to set a homogenous sample of a gel composed of it using the same method used for gels **R1** – **R8**) and the *G′* (in kPa) for the corresponding gels. All gels setting using nine equivalents of GdL with *ex situ* synthesised gelator.

The gel featuring the highest G' value is composed of the molecule with the highest *c*logP value, the trifluoromethyl appended **R6**. Two of molecules with the lowest *c*logP values, **R4** and **R5**, also result in gels with some of the lowest G' values amongst the family. Overall the fit of the line is remarkable when considering the errors that are associate with frequency sweep experiments used to determine the G' value and the fact that the *c*logP values are calculated rather than determined experimentally.[16,29–33]

Another interesting plot that can be produced is that seen in Figure 3.27. Figure 3.27 represents three different data sets involving the *c*logP values for molecules **R1** – **R9**, in both their charge neutral and trianionic forms (where the three negative charges are assumed to be the result of deprotonation of the carboxylic acid groups), the calculated pK_a values for each of the molecules, along with the experimentally determined pK_a values for each. As expected, deprotonation does result in a large decrease in the *c*logP values of the molecules, which explains why the molecules go from highly insoluble in their neutral form, to highly soluble in their trianionic state. When considering only the protonated molecules, it is clear there is a difference between the points plotted using the calculated pK_a (triangles) and the experimentally determined pK_a (circles). While the difference is significant between the calculated and experiment pK_a values, the difference is consistent across all molecules.

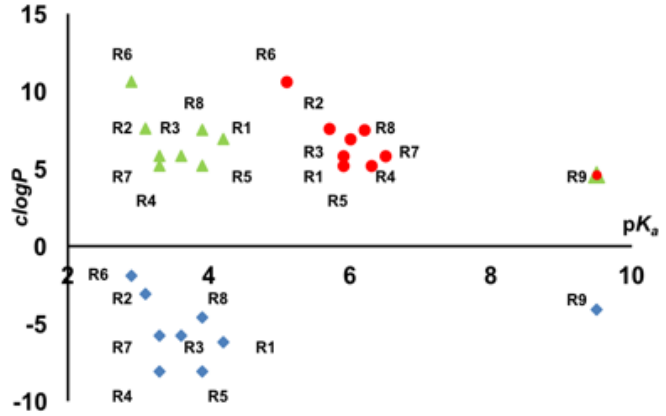

Figure 3.27. Graph showing the calculated values for the pK_a and clogP of gelators R1 to R9. *C*logP vs calculated pK_a (green Δ) neutral species, *c*log*P* vs calculated pK_a (blue ◊) trianionic species, and *c*log*P* vs measurement pK_a (red ○).

The exception is **R9**, which shows an excellent correlation between the experimental and theoretical pK_a values. Calculated pK_a and in particular *c*logP values have proven useful in understanding the behaviour of this system, particularly with

regards to difference in G' between family members. A summary of this data can be seen in Table 3.3. The analysis here indicates that increasing the hydrophobic character is this family of gels without significantly decreasing the pK_a of carboxylic acid can result in a higher apparent pK_a for gelation and a rheologically stronger gel. The rheology may simply be related to the higher hydrophobic character through stabilising smaller fibres, resulting in greater numbers of fibres and cross-links, consistent with the cellular solid description of gelation.

Table 3.3. Data used to plot Figure 3.27, calculated *c*logP values for molecules **R₁ – R₈** with the G' for gels corresponding to each of these molecules. G' value corresponds that recorded during the frequency sweep experiments at 50 Hz for 2 wt% gels.

Gelator	*c*logP value	G' (kPa)
R₁	6.9	9.9
R₂	7.6	12.2
R₃	5.8	9.9
R₄	5.2	9.1
R₅	5.2	9.5
R₆	10.6	15.6
R₇	5.8	8.8
R₈	7.5	10.8

3.9 PXRD analysis of dried gel samples

Obtaining the absolute atomically resolution structural that forms the three-dimensional network within the gel structure is difficult.[34–38] This is because, despite the gel featuring definite long range order, the structure is far from crystalline. Despite this lack of crystallinity analysis of the PXRD patterns of dried samples of the gels can provide useful information into structure of the three-dimensional network. PXRD patterns were collected on dried gel samples that had not been processed in anyway i.e. grinding, which is generally considered common practice with the technique. Figures 3.28 and 3.29 show the PXRD patterns obtained for each of the dried gel samples and allow for comparison to be made between samples. All patterns, perhaps unsurprisingly, are similar in profile. That said, all patterns feature a significant reflection at a 2θ value equal to 26 °, which corresponds to a *d*-spacing value of approximately 3.4 Å. This *d*-spacing is likely to be the result of the face-to-face separation distance between the molecules within the gel fibres.

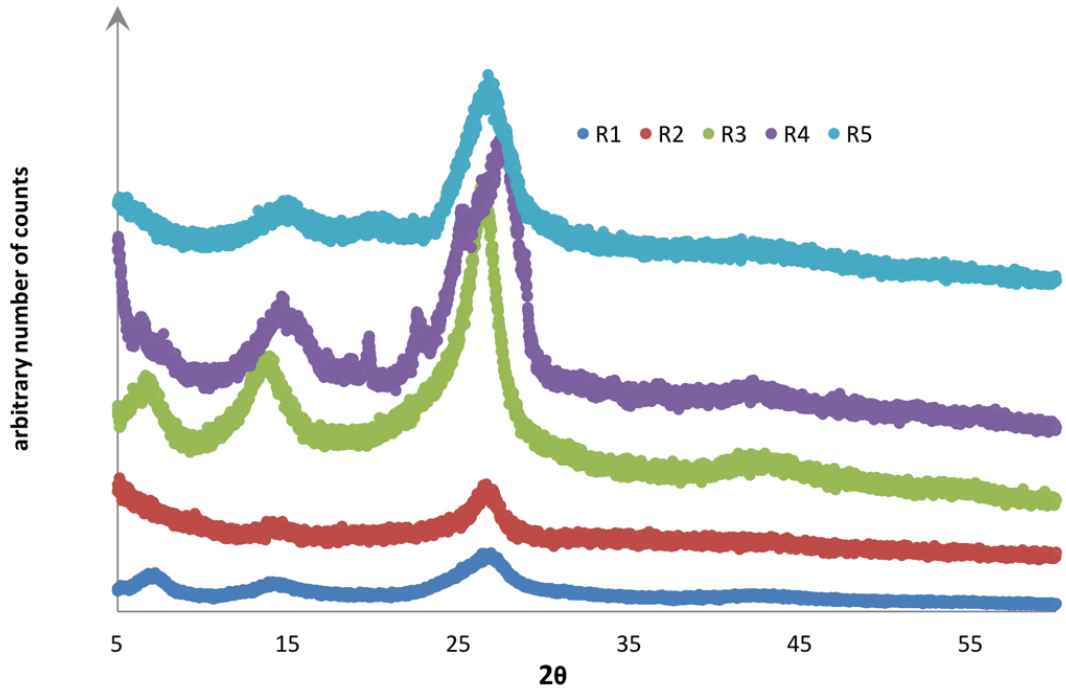

Figure 3.28. PXRD patterns for samples produced from dried gels **R_1, R_2, R_3, R_4 and R_5** recorded between 5 – 60 ° over a time 30 minutes. An arbitrary scale is used for count intensity for the sake of comparisons. Data presented in this manner allows for direct comparison between samples.

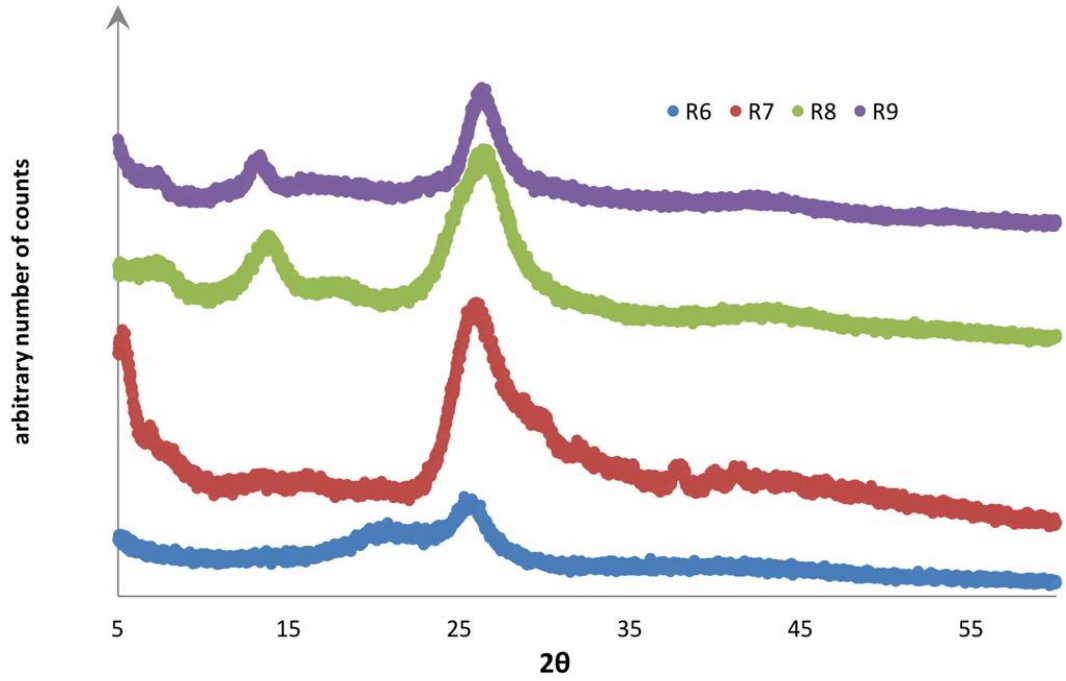

Figure 3.29. PXRD patterns for samples produced from dried gels **R_6**, **R_7**, **R_8** and **R_9** recorded between 5 – 60 ° over a time 30 minutes. An arbitrary scale is used for count intensity for the sake of comparisons. Data presented in this manner allows for direct comparison between samples.

When examining the chemical structure of compounds **R**$_1$ – **R**$_9$, it is apparent there is no clear directional intermolecular interactions to be formed, e.g. no clear hydrogen bonds such as amides. The molecules are, however, very planar and feature areas of π character. The intramolecular hydrogen bonding contributes to this planarity. This molecular geometry and the *d*-spacing of approximately 3.4 Å are both highly suggestive of face-to-face π-π interactions. This π-π stacking corresponds well with self-assembly in water and matches well with the self-assembly of the hydrazone chemistries, even though there are no clear amide-type hydrogen bonding patterns.[39–41]

The non-gelating compound **R**$_{10}$ yielded a suspension, the solid component of which could be collected using vacuum filtration and analysed using PXRD. Figure 3.30 shows the powder pattern obtained from this sample. What is immediately noticeable is the significant increase in the number of clear and sharp reflections when comparing it to the patterns obtained for compounds **R**$_1$ – **R**$_9$. This number of reflections shows that the precipitation of **R**$_{10}$ from a basic solution GdL results in a crystalline material.

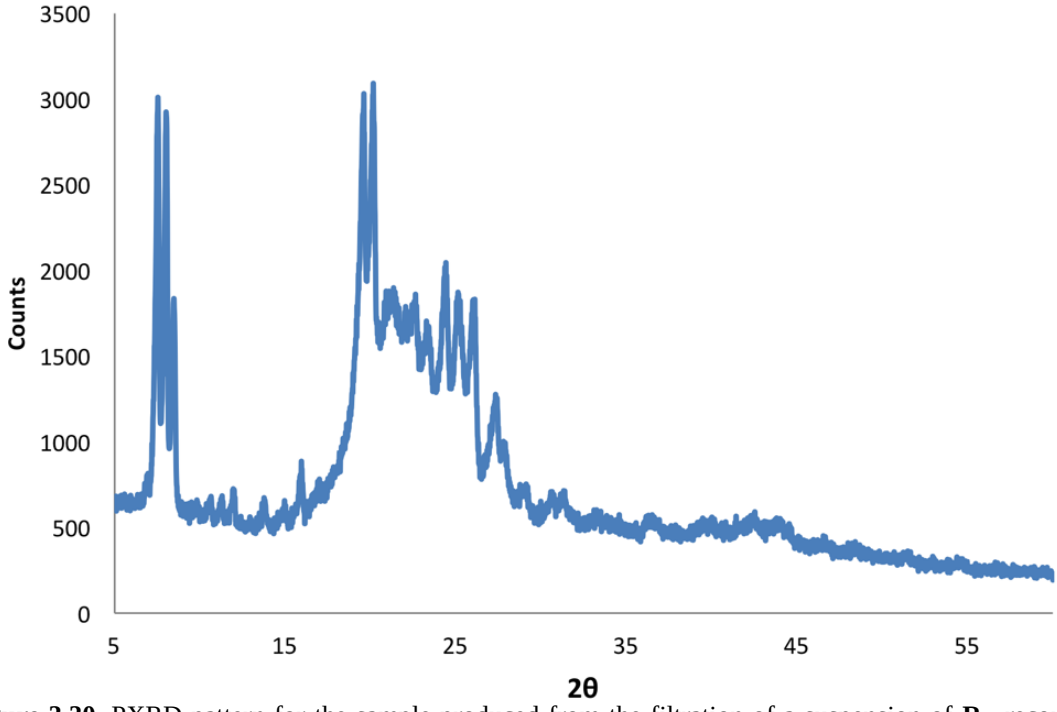

Figure 3.30. PXRD pattern for the sample produced from the filtration of a suspension of **R**$_{10}$ recorded between 5 – 60 º over a time 30 minutes.

As well as having significantly more reflections than its gelating relatives, **R**$_{10}$ does not appear to feature the broad reflection centred on 2θ = 26 ° observed in compounds **R**$_1$ – **R**$_9$. This would imply that the replacement of the phenyl arm units with the alkyl chain has had a dramatic effect on the way the molecules organise themselves

with respect to one another. The alkyl chain is unlikely to interact in the same way, or as strongly as the phenyl group, resulting in a different means of intermolecular interactions, this would in turn influence the supramolecular assembly.

The PXRD analysis presented in the section suggest that a face-to-face stacking arrangement driven by π-π interactions results in the formation of the fibres that go on to produce the gel network. It is also interesting to consider the pattern of **R_{10}** which highlights how a related but chemical different compound can have a dramatically different supramolecular arrangement. So much so that gelation is switched off entirely. The structural information that has been obtained through this PXRD analysis demonstrates the similarities between the gels, this raised the prospect of producing gels containing more than one gelator.

3.10 Mixed systems

Multi-gelator gelation systems are increasing emerging as effective ways to cooperatively influence the gelation process of the LMWG components, with a view to obtaining a gel that benefits from desirable traits from all of the present LMWGs.[3,37,42,43] Summed up, the concept is that in some cases the whole is greater than the sum of the parts.

When pursuing a multi-gelator system careful consideration has to be given to the needs of all the LMWGs, as well as the manner in which they interact with each other. The method of triggering gelation has to be compatible in all cases and the assembly of one gelator cannot overly influence the assembly of another. For example, if there was a two gelator system where one species gelled rapidly upon triggering while the second gel set much more slowly, the properties of the gel might not be cooperative as the nucleation of each of the LWMGs is separated.

The family of LMWGs presented in this chapter represent an ideal set of candidates to explore mixed LMWG systems. All examples rely on a pH trigger to induce gelation. They all appear to be chemically robust with similar chemical structures. They all also appear to assemble in the same manner to produce supramolecular gels with a fibrous morphology. There are nine gelators presented here which give significant potential to attempt to create a vast number of mixed gel systems. With this in mind, a rational had to be developed when considering which species to mix, with the question being what is the goal when creating a multi-gelator gel. Two gelator gels presented the greatest opportunity to create gels were at least some predictions could be made on

physical properties of the gels. Because it was control over the physicals properties of the gels that was being targeted, it was necessary to look at the properties that could be easily quantified. That is mechanical robustness in terms of the gels *G′* value and opaqueness.

Gel **R6** has so far demonstrated both an outstanding response to an externally applied mechanical stress with the highest recorded *G′* value of all the presented gels, as well as being transparent. This meant that the LMWG **R6** was selected for the mixing experiments. As all the other gelators are similar both in terms of opaqueness and *G′* values, an arbitrary selection of **R1** was made to be mixed with **R6**.

Initial experiments would focus on using *ex situ* synthesised samples of the LMWGs **R1** and **R6**. These compounds would be mixed in different ratios while maintaining the same overall molar concentration of the resulting gels. It is worth noting that when dealing with multi-gelator gels it is important to work the absolute concentration of gelator present rather than wt%, owing to the difference in molar weights between the gelators used. The hypothesis was that as the molar ratio moved from **R1**, being the dominant gelator, to **R6**, the resulting mixed gels would become stronger. It was also hoped that the gels would become more transparent as the number of molecules of **R6** exceeded that of **R1**. Mixed gels of both **R1** and **R6** were produced using *ex situ* synthesised samples of **R1** and **R6** in a variety of ratios.

After weighing out the necessary masses of **R1** and **R6**, the difference in properties between the two LMWG gelators became apparent immediately upon addition of the required volume of water. As discussed in previous sections, there is a significant difference in the *c*logP values between molecules of **R1** and **R6**, with **R6** having a much larger calculated *c*logP value than **R1**, 10.6 vs. 6.9, respectively. This would suggest that **R6** represents a significantly more hydrophobic molecule than **R1**, indeed this would appear to be confirmed by Figure 3.31. Figure 3.31 is a photograph of the various ratios of **R1** and **R6** with increasing concentrations of **R6** when moving from left to right cross the photograph. The photograph was taken before the addition of any sodium hydroxide, but immediately after twenty minutes of the suspensions being sonicated to ensure complete mixing between the **R1** and **R6** components. The striking difference between the components is very easily noticed. Despite attempts to create a homogenous LMWG suspension through sonication, a very obvious separation between the **R1** and **R6** components occurred. The higher relative hydrophobic character of **R6** makes mixing on any level with water virtually impossible. This is highlighted in vial **F** of Figure 3.31 (LMWG content is 100% **R6**) where the entire mass of **F** in the vial is lying on top of the

water at the air/water interface, something that is typical of highly hydrophobic compounds.

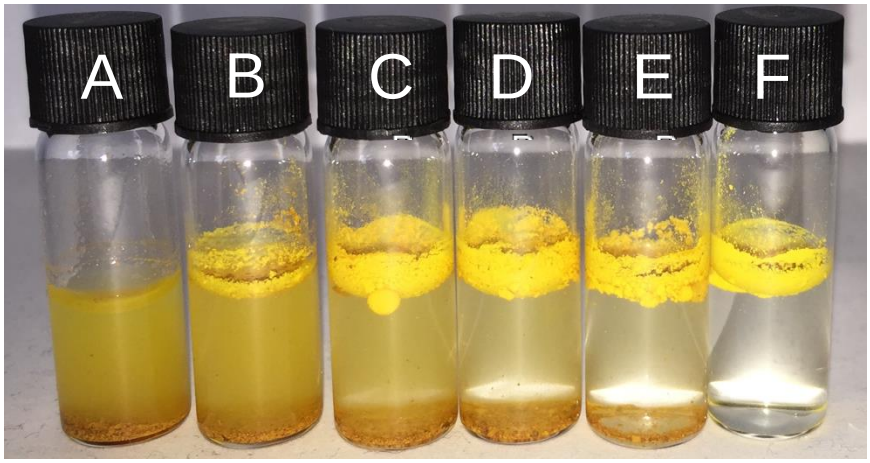

Figure 3.31. Photograph of *ex situ* synthesised mixtures LMWGs **R$_1$** and **R$_6$** suspended in water after 20 minutes of sonication. From left to right vials contain (in terms of LMWGs) **A** = 100% **R$_1$**, **B** = 80% **R$_1$** 20% **R$_6$**, **C** = 60% **R$_1$** 40% **R$_6$**, **D** = 40% **R$_1$** 60% **R$_6$**, **E** = 20% **R$_1$** 80% **R$_6$**, and **F** = 100%.

By contrast vial, where the content is 100% **R$_1$** show sedimentation on the bottom of the vials, along with a fine suspension throughout the liquid phase. The lower apparent hydrophobicity of **R$_1$** allows these particles, while not dissolved, to remain suspended in solution. Vials **B** – **E** highlight the contrast between gelators **R$_1$** and **R$_6$**, with the **R$_6$** solid at the air/water and **R$_1$** dispersed or at the bottom of the vial as a sediment, thus showing the gelators behave as completely separate entities. Addition of sodium hydroxide to these vials resulted in the gelators rapidly dissolving. Once fully dissolved, and the pH adjusted to 8, the vials were again sonicated to ensure mixing of the components was thorough. Once sonicated a clear yellow homogenous solution was present in all six vials, with no noticeable difference in colour to give an indication of which vial was which. After this sonication process nine molar equivalents of GdL could be added to each vial, after 15 minutes, gelation had occurred in all six vials as shown in Figure 3.32. As can be seen in Figure 3.32 the colour of the gels remains similar regardless of the composition, however, what does change remarkably is the transparency. Vial **A** holds the opaque gel **R$_1$** with vial **F** containing the highly transparent gel **R$_6$**. Vials **B** – **E** hold gels that demonstrate a transition from opaque to transparent gels, depending on the ratio of the two gelators. Although there is a clear and gradual transition the steps do not appear to be equal. When inspecting these vials with the naked, as seen in Figure 3.32, there is a slight but noticeable increase in transparency when going from vials **C** to **D**. However, the increase in

transparency is most striking when going from vial **D** to vial **E,** with these vials representing the transition into a truly transparent gel. Visually the contents of vials **E** and **F** look similar. With this in mind it would appear this mixed gelation system does present the means with which the physical property of transparency can be tuned. The system requires a high percentage of the LMWG that produces transparent gels, $\mathbf{R_6}$ some 60 – 80 %. Transparency is requirement of some gel materials for their use in some technologies, such as cell or tissue growth.

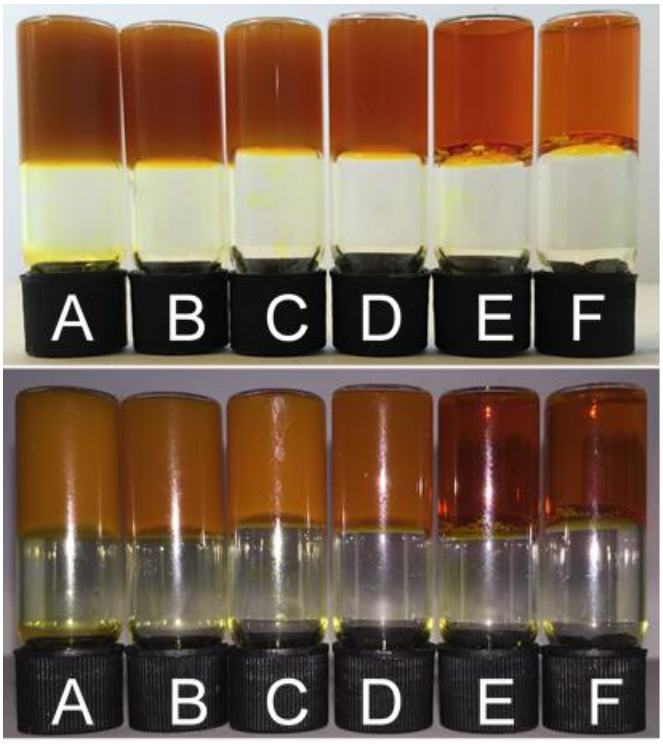

Figure 3.32. Photograph of gels composed of *ex situ* synthesised samples LMWGs $\mathbf{R_1}$ and $\mathbf{R_6}$ in various ratios. Gels set from suspensions shown in Figure 3.31 through the addition of sodium hydroxide up to a pH of 8, before the addition of 9 equivalents of GdL. From left to right vials contain (in terms of LMWGs) **A** = 100% $\mathbf{R_1}$, **B** = 80% $\mathbf{R_1}$ 20% $\mathbf{R_6}$, **C** = 60% $\mathbf{R_1}$ 40% $\mathbf{R_6}$, **D** = 40% $\mathbf{R_1}$ 60% $\mathbf{R_6}$, **E** = 20% $\mathbf{R_1}$ 80% $\mathbf{R_6}$, **F** = 100%.

With this mixed gelator system giving the ability to tune transparency of the gel, it was necessary to quantify these optical properties.[44,45] These could be done through preforming a series of transmission UV-Vis experiments on gels composed of the various ratios of $\mathbf{R_1}$ and $\mathbf{R_6}$ discussed in Figures 3.31 and 3.32. The transmission experiments were performed on gels set with a lower overall combined molar concentration of gelator, rather than the examples shown in Figure 3.32 (10 mM vs. 28 mM), with the transmission of light through the gel measured over a wavelength range of 400 – 900 nm (Figure 3.33).

It is clear there is not a linear relationship between concentration of **R6** with transparency from these experiments.

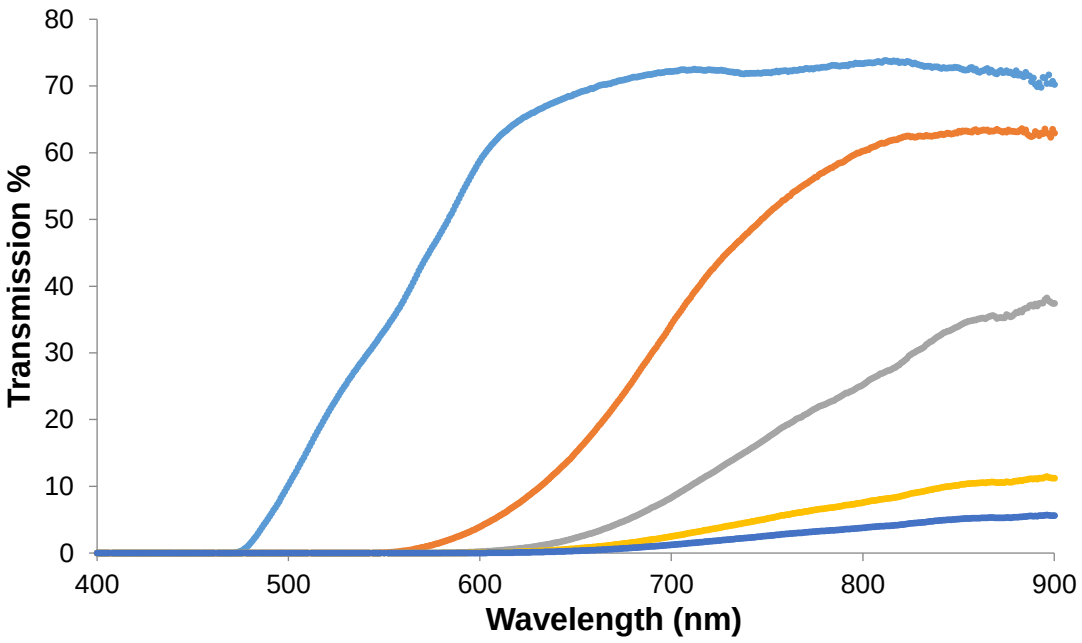

Figure 3.33. Combined spectra for the transmission experiments conducted on 100% **R1** at 10 mM (●), 75% **R1** : 25% **R6** (●), 50% **R1** : 50% **R6** (●), 25% **R1** : 75% **R6** (●),100% **R6** (●).

With this demonstration of control over the optical properties now dome, it was now necessary to investigate the mechanical response of these multi-component gels. This was done using rheology, which would focus primarily on the results of the frequency sweep experiments. The frequency sweep experiments revealed that by increasing the amount of **R6** with respect to **R1** strengthened of resulting gels, at least in terms of the gels *G′* value. This relationship between the mixed component gels **R6** content and its *G′* is non-linear in nature as well.

With characterisation in terms of the two studied physical properties, transparency and mechanical response, giving an insight into how these properties can be controlled within mixed gelator system, the next objective was to characterise the supramolecular three-dimensional network of the gels to ascertain if co-assembly or self-sorting had occurred. This level of characterisation is challenging for single LMWG gels and even more so for multi-component LMWG systems[37] with diffraction techniques (be it small angle x-ray or neutron scattering) being widely acknowledged as the best way to proceed in the characterisation.[46] Of course, it is not the only technique that can be used with fluorescence and circular dichroism[47] also being possible. However, even with the

plethora of techniques available, the characterisation of multi-component supramolecular gels still heavily relies on the comparisons between the data collected for gels set from each of the individual components, to that of the data collected for the mixed gelator system.

Analysis of the mixed systems presented in this chapter initially involved PXRD analysis on the dried powders of each of the mixed component gels. When considering the supramolecular assembly of these systems, there may be self-sorting into two distinct types of fibres. This could be manifested in two peaks appearing in the PXRD as opposed to the one peak seen in the one component gels. Even if two discrete peaks are not observed, there could be a clear broadening of the single reflection indicating self-sorting.

Figure 3.34 represents a collection of PXRD patterns for dried samples of **R$_1$** and **R$_6$** along with three examples gels that were set containing both **R$_1$** and **R$_6$** (25% **R$_1$** and 75% **R$_6$**, 50% **R$_1$** and 50% **R$_6$**, 75% **R$_1$**, 25% **R$_6$**). When looking at these patterns it is again clear that the most striking features are the reflections at a 2θ value of approximately 26 °, corresponding to a *d*-spacing of ~ 3.4 Å, which represents the intermolecular face-to-face separation distance between the gelator molecules within the fibres.[33]

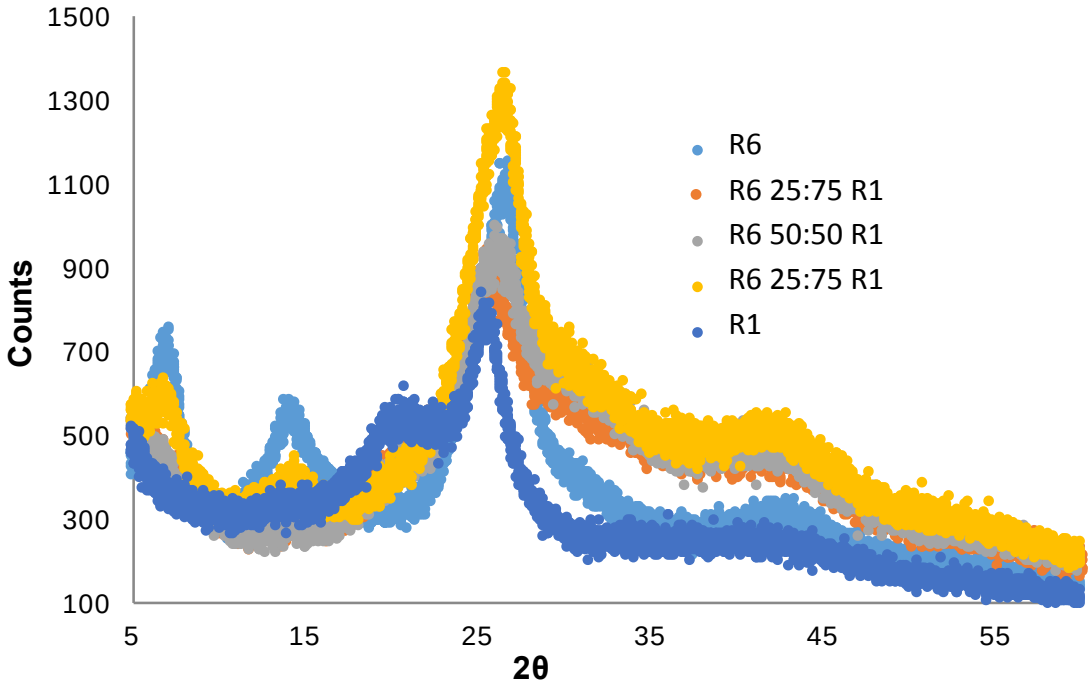

Figure 3.34. PXRD patterns collection for dried samples of gels **R$_1$** and **R$_6$**, as well as three dried gel samples of gels composed of both **R$_1$** and **R$_6$** in the ratios defined in the Figure.

With these patterns there is no obvious difference between them, at least when comparing the width of the main reflection. There does, however, appear to be a shift to a larger 2θ value as the concentration of **R₁** increases relative to **R₆**. In order to better appreciate this shift, an expansion of the patterns for the 2θ values 22 – 29 º was created (Figure 3.35). The patterns for each of the gel systems was the ordered from smallest 2θ to largest. This demonstrates correlation between the contents of the gel and the 2θ value of the main reflection in the PXRD patterns. These 2θ values and the corresponding calculated *d*- spacing data is summarised in Table 3.4.

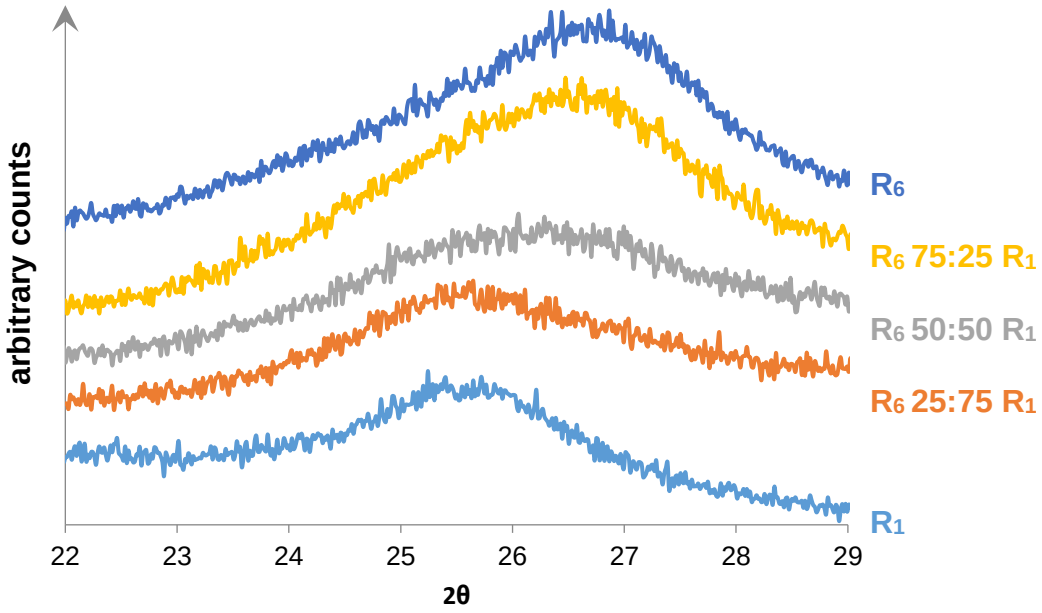

Figure 3.35. PXRD patterns collection for dried samples of gels **R₁** and **R₆** as well as three dried gel samples of gels composed of both **R₁** and **R₆** in the ratios defined in the Figure.

Table 3.4. Data on 2θ and corresponding *d*-spacing obtained from the PXRD patterns for the mixed **R₁**/**R₆** systems presents in Figures 3.34 and 3.35.

Gel composition	2θ (º)	*d*-spacing (Å)
100% R₁	25.42	3.53
75% R₁ 25% R₆	25.61	3.47
50% R₁ 50% R₆	26.05	3.42
25% R₁ 75% R₆	26.47	3.36
100% R6	26.87	3.32

This demonstrates how as the percentage fraction of **R₆** increases, with no change in overall gel concentration, the 2θ also increases, meaning the *d*-spacing between the molecules also decreases. This gradual change in the *d*-spacing from sample to sample would imply that the gel network is composed of fibres containing both molecule types,

meaning the fibre structure is gradually altered in terms of the spacing between the molecules. The alternative model would be the existence of two discrete types of fibres, one composed of **R_1** and one of **R_6**, each with their own *d*-spacing. But as discussed this would result in two peaks or a set of broadened peaks.

While examination of the diffraction data obtained for the mixed systems does seem to imply a co-assembly process leading to a homogenous gel structure in terms of the individual gelator components, this theory is dependent on the gels maintaining the fibrous morphology they demonstrated in their single LMWG sets. Morphology could again be determined using SEM for the **R_1**/**R_6** mixed systems discussed in the previous diffraction section. The results of this SEM analysis are shown in Figure 3.36.

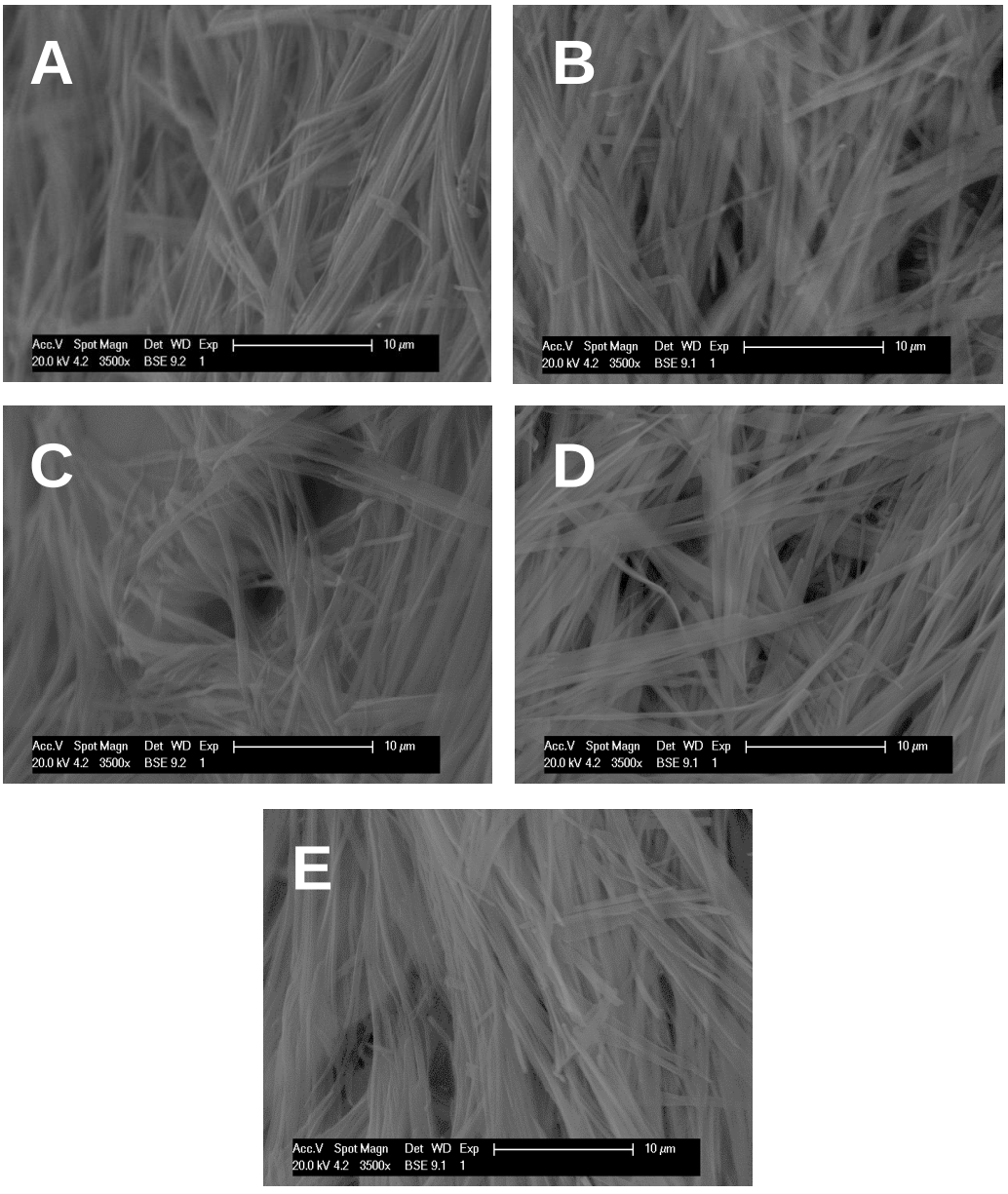

Figure 3.36. SEM analysis showing the consistency of morphology for gels set using various molar ratios of R_1 and R_6. a) R_1 100 : 0 R_6. b) R_1 75 : 25 R_6. c) R_1 50 : 50 R_6. d) R_1 25 : 75 R_6. e) R_1 0 : 100 R_6.

These images crucially show the fibrous morphology observed in the single gelator gels is maintained throughout these multi-gelator systems. Despite the composition changing from 100% **R**$_1$ to 100% **R**$_6$, when going from images **A** to **E** in Figure 3.36, there is no obvious change in the morphology of the dried network in terms of fibre width or length. However, it is also worth noting that the images that show the network of the mixed systems do show a very homogenous network structure, implying the existence of one type of fibre rather than two distinct (self-sorted) varieties.

In order to further investigate this co-assembly assembly process, the apparent *p*K$_a$ of solutions containing mixtures of **R**$_1$ and **R**$_6$ in a number of ratios were determined. The fact that the apparent *p*K$_a$ determination for the mixed **R**$_1$/**R**$_6$ systems shows an altering of the overall *p*K$_a$ of the system, demonstrated by the single plateau region, rather than the existence two separate plateaus, is a strong indication that the gel forms through a co-assembly process (Figure 3.37). The co-assembly of the two gelators is down to the fact the protonation event of the molecules, which transitions them from a soluble to insoluble form, happens at the same pH for both molecules simultaneously.

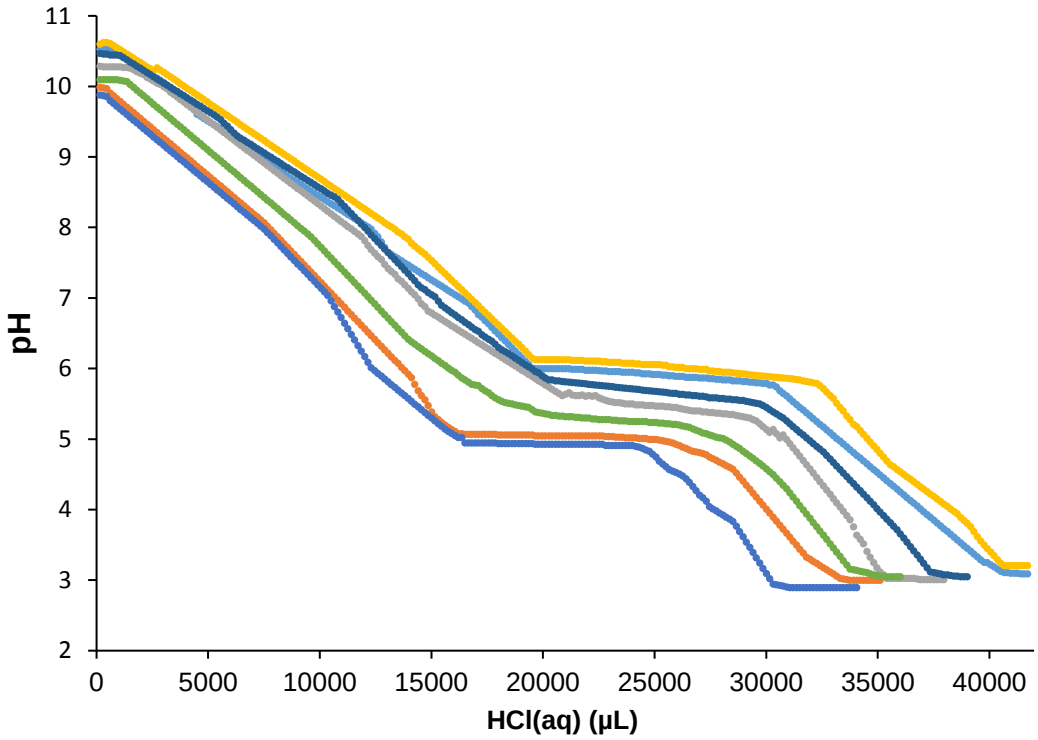

Figure 3.37. Apparent *p*K$_a$ determination for **R**$_1$/**R**$_6$ mixed systems using a series of solutions of pH 10 – 10.5 containing a total of gelator concentration of 10 mM. Aliquots of HCl (0.1 M) were added to these solutions and the resulting pH recorded. Continuous stirring was used to stop a gel forming and the resultant convection problems associated with gelation. **R**$_1$ (●), **R**$_1$:**R**$_6$, 80:20 (●), **R**$_1$:**R**$_6$, 60:40 (●), **R**$_1$:**R**$_6$, 50:50 (●), **R**$_1$:**R**$_6$, 40:60 (●), **R**$_1$:**R**$_6$, 20:80 (●), **R**$_1$ (●).

When discussing this pH change it would be correct to discuss it along with ideas of self-sorting and co-assembly within the supramolecular structure. As can be seen in Figure 3.37, a single plateau "pK_a" region is observed. As the assembly process is controlling gelation, all molecules can move into the solid-phase as the pH reaches this one critical point, this produces a gel with a co-assembled fibrous structure.

In order to demonstrate this sol to gel transition happening at the same time for gelators **R1** and **R6**, solution based ^{1}H NMR experiments were run. When in solution, both gelators are NMR visible. However, as the gel begins to set the individual gelator molecules move from the NMR visible solution phase to the NMR invisible solid-phase. This results in a decrease in the integration values of the gelators in the corresponding spectra.[48–51] A 50/50 mixture of **R1** and **R6** at a total concentration of 10 mM was dissolved in D_2O with the addition of sodium hydroxide. GdL was then added to this solution and a spectra was recorded every five minutes for a total of two hours over a range of 6 – 9 ppm. Examination of the integrations of peaks that relate to the aromatic protons of both **R1** and **R6** allowed the plot shown in Figure 3.38 to be produced. The initial measurement at time zero (before the addition of GdL) was used as the reference with which to normalise the data. Figure 3.38 elegantly demonstrates the sol to gel transition for this system. The plot shows that both **R1** and **R6** make the transition from sol to gel at the same and in the same proportions.

The mixing for **R1** and **R6** proved remarkably successful and resulted in a gelation system where a wide variety of mechanical strengths could be targeted. Of course, the minimum strength that could be reached with this system is the inherent *G′* value of **R1**. This left the question of would it be possible to adjust the *G′* value the other way and instead of reinforcing a "gel of **R1**" could it instead be weakened? Owing to the similarities between the *G′* values of all the other gels, it was decided to utilise the non-gelator **R10** for this weakening experiments. This "targeted" weakening arises from the occurrence of self-sorting within the two component system due to the fact **R10** does not gel, but rather crystallises. This self-sorting or orthogonal assembly process acts as a way of modulating the mechanical strength of the gel.

In the same manner as the **R1** and **R6** mixed systems, different ratios of **R1** and **R10** were mixed, dissolved with the addition of sodium hydroxide, before the addition of GdL in order to attempt to set the gel. This gel weakening system exhibited the desired characteristics, with an increasing non-gelator (**R10**) concentration relative to the total concentration of both **R1** and **R10**, there was a drop in the gel *G′* values measured. This

weakening of the gel is highlighted in Figure 3.39, where a reduction in the *G′* value can be seen with increasing **R**$_{10}$ concentration.

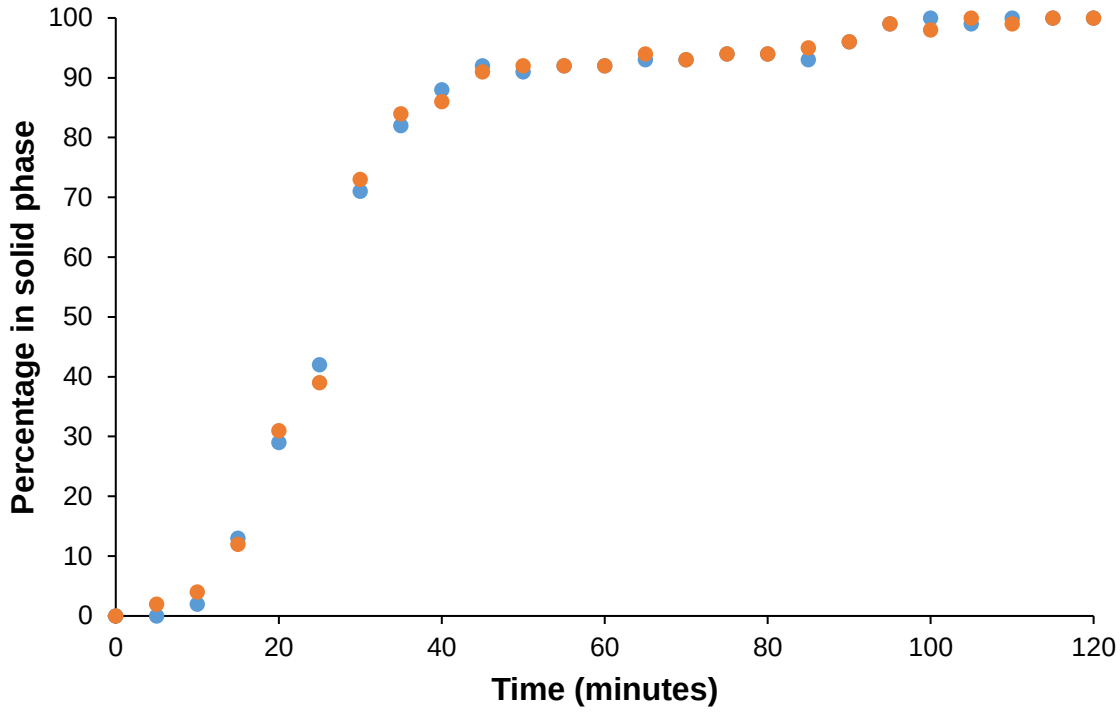

Figure 3.38. Plot of the evolution of the percentage of gelators in the solid-phase over time. Percentage calculated from the integration of distinct peaks for each of the gelators in the ^{1}H NMR spectra for a sample contain a mixture of 50% **R**$_{1}$ (●) and 50% **R**$_{6}$ (●).

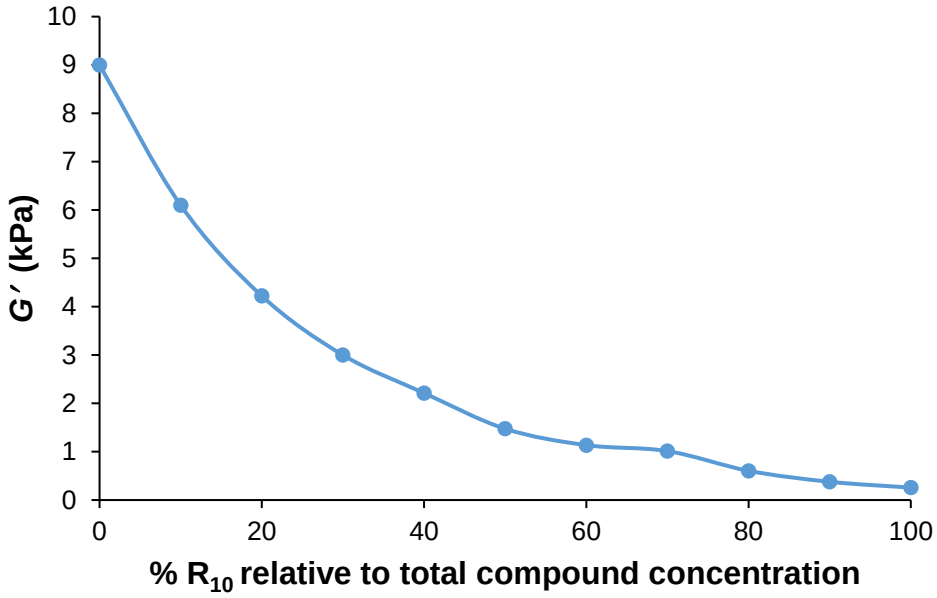

Figure 3.39. Plot demonstrating the effects of increasing **R**$_{10}$ concentration (relative to the total concentration of both compounds) on *G′*.

Structural information that infers a reason for this reduction in the elastic modulus can be gleaned from PXRD analysis of both dried samples of **R**$_1$ and **R**$_{10}$. When examining the dried compound collected from a gel set using a mixture of **R**$_1$ and **R**$_{10}$ several significant well-defined reflections can be observed (Figure 3.40). This suggests there is long range order present in the system that is not there when compared to the PXRD patterns of the pure dried gel (**R**$_1$ – **R**$_9$) samples.

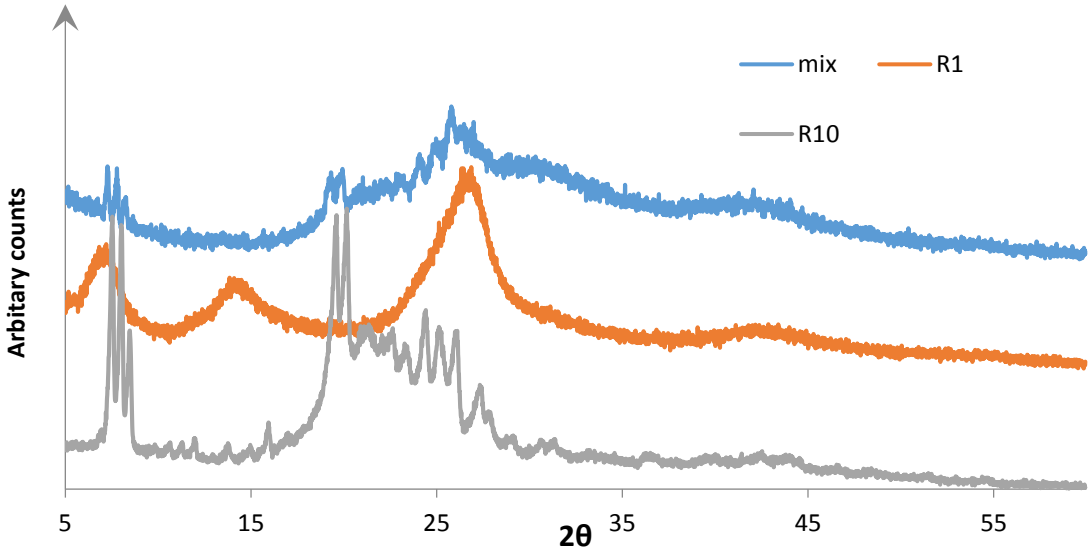

Figure 3.40. PXRD patterns comparing the patterns for pure sample of gel **R**$_6$, a sample of **R**$_{10}$ precipitated from water with GdL and the 50:50 mixed **R**$_6$ and **R**$_{10}$ Gel.

Figure 3.40 serves to highlight the assembly nature of an **R**$_1$ + **R**$_{10}$ gel. The PXRD pattern for the mixed system shows reflections that correspond to reflections in the individual patterns of both pure **R**$_1$ and **R**$_{10}$ patterns. This is in contrast with what was found for the **R**$_1$ and **R**$_6$ combination PXRD patterns, where a gradual transformation from one pattern to the other is observed. This combination of mixed samples is suggestive that this mixed system is self-sorting, rather than co-assembling.

As was previously demonstrated in Figure 3.37, the apparent pK_a can be determined for mixed systems. With the **R**$_1$ + **R**$_6$ mixed system, the apparent pK_a gradually and consistently decreases from the value recorded for **R**$_1$ to the value for **R**$_6$, as more **R**$_6$ is added, relative to the total gelator concentration. This is different to what is observed with the **R**$_1$ + **R**$_{10}$ system. This difference is highlighted in Figure 3.41. What is demonstrated in this Figure is an apparent pK_a determination for a 50:50 **R**$_1$:**R**$_{10}$ mixed system with the key event highlighted. This event is a step-change in the apparent pK_a of

the mixed system. This step change is again suggestive of a self-sorting system as the apparent pK_a of the mixed system is a combination of the two individual pK_as, rather than an "average".

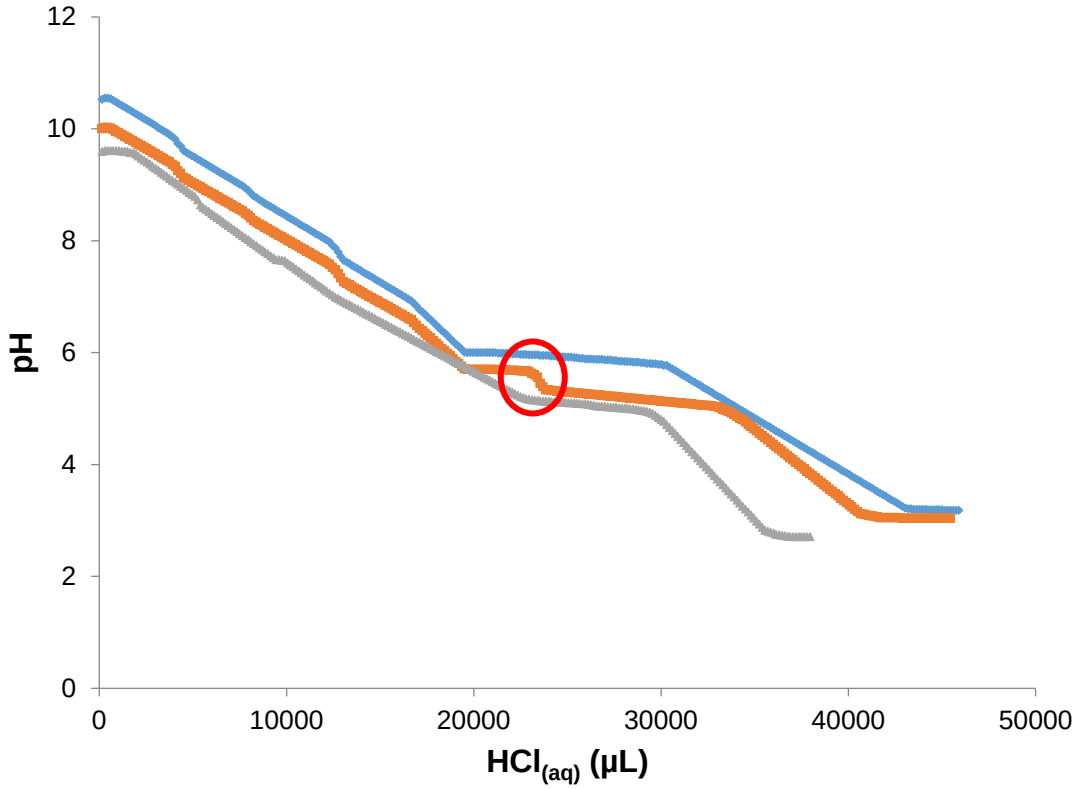

Figure 3.41. Apparent pK_a determination for **R₁** (●), **R₁₀** (●), and a 50:50, **R₁**:**R₁₀** mixed solution (●). The red circle highlights the step change in apparent pK_a, demonstrating the self-sorting nature of the system.

The final part of the analysis on the **R₁**:**R₁₀** system consists of a ^{1}H NMR study on the mixed solution, focusing on when the compounds move from the solution phase to the solid-phase. The results of this experiment are presented in Figure 3.42, and differ significantly from the results in Figure 3.38, where the **R₁**:**R₆** system is displayed. As can be seen in Figure 3.42, the time at which **R₁₀** begins to move out of solution occurs before **R₁** does.[52,53] Time is related to the rate of GdL hydrolysis, at a particular temperature, and is therefore a good measure of the change in pH, although the pH is not being measured directly. This disparity in time means that the **R₁₀** molecules begin their crystallisation process, i.e. higher pH value, before the gelation involving **R₁**, lower pH value. This is a key factor in the self-sorting that is exemplified in this particular system.

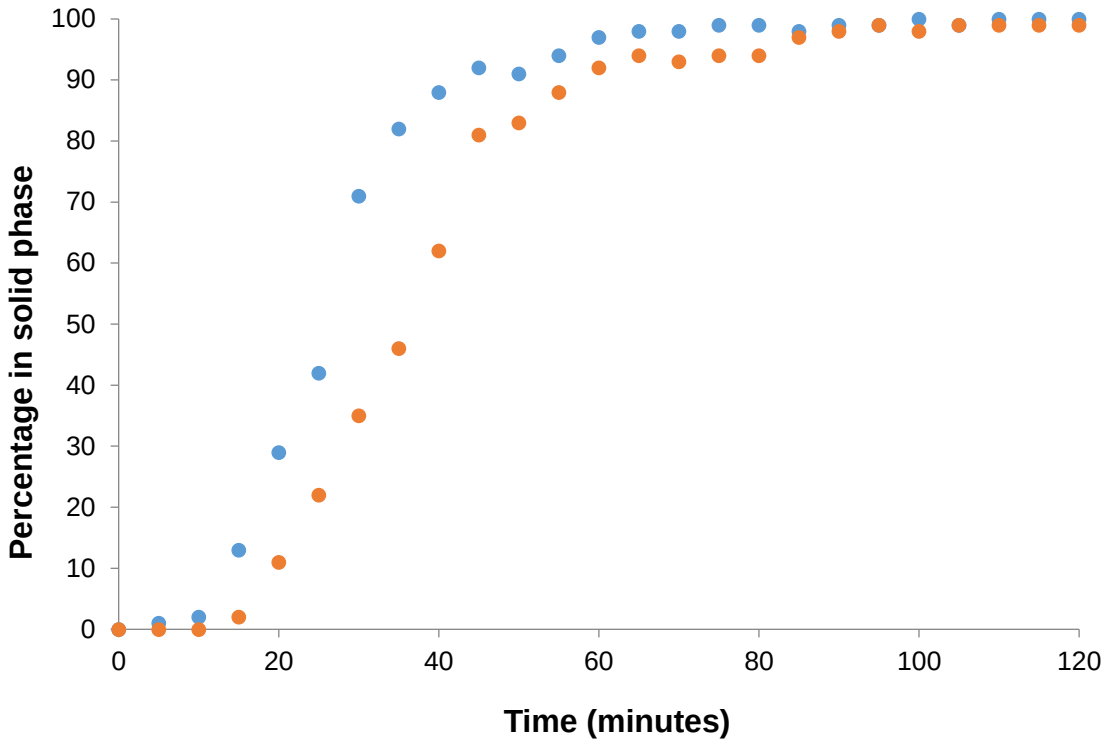

Figure 3.42. Plot of the evolution of the percentage of gelators in the solid-phase over time. Percentage calculated from the integration of distinct peaks for each of the gelators in the ^{1}H NMR spectra for a sample containing a mixture of 50% **R$_1$** (●) and 50% **R$_{10}$** (●).

The use of mixed gelator systems has produced two different effects on the mechanical properties of the resultant gels through both self-sorting and co-assembly. Gels can be relatively strengthened or weakened depending on the composition of the mixtures. When considering the presented family of gels, **R$_1$** – **R$_9$**, one of the gels with a lower *G′* value is **R$_1$**. The addition of **R$_6$**, the strongest gelator, to **R$_1$**, while keeping the total gelator concentration the same, serves to strengthen the gel that consists primary of **R$_1$**. Increasing amounts of **R$_6$** within the gel strengthens the material, peaking when the composition is 100 % **R$_6$** (Figure 3.43). However, the relationship of the increase in *G′* with **R$_6$** is not linear. Such a system was found to be co-assembling, with the supramolecular fibres containing both **R$_1$** and **R$_6$**. Conversely by taking the **R$_1$** and adding the non-gelator **R$_{10}$**, the strength of the gel could be controllably dialled down (Figure 3.43). This arose from a supramolecular self-sorting process, whereby **R$_1$** was continuing to form fibres, while the **R$_{10}$** species crystallised out, effectively reducing the number of molecules that could take part in the gelation process.

So far these mixed systems have utilised *ex situ* synthesised gelators. The distinction between self-sorting and co-assembling of the two gelator systems is at the

supramolecular physical interactions level. The solubility of the reaction components allows similar investigations to be conducted at the chemical level.

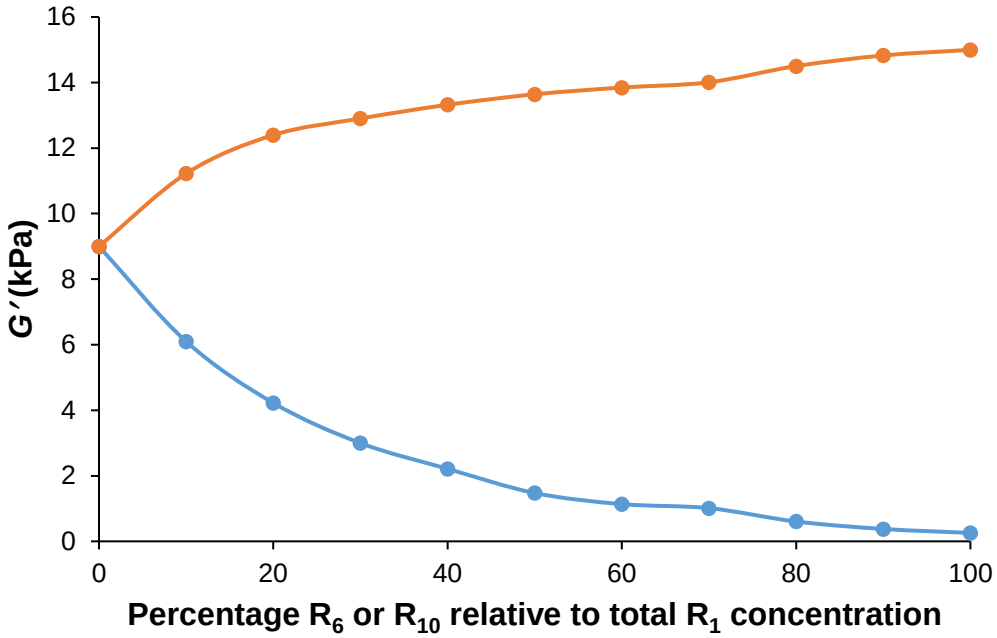

Figure 3.43. Demonstrates the variation in *G′* of an **R₁** gel with increasing percentages of **R₆** (orange) and **R₁₀** (blue) relative to the total compound concentration.

3.11 Using in situ reaction for mixed gelator systems

One important aspect of this gelator family is the ability to form the gelator molecules *in situ*. This *in situ* synthetic approach has allowed the exploration of systems chemistry, something that will be discussed in this section.

In the previous section, two mixed systems were discussed, gels containing **R₁** and **R₆** or gels containing **R₁** and the non-gelator **R₁₀**. In all cases these ligands were synthesised *ex situ* and represented very pure products of the reactions that synthesised them. This section will explore using the amine starting materials from which these gels derive their nomenclature (Figure 3.44).

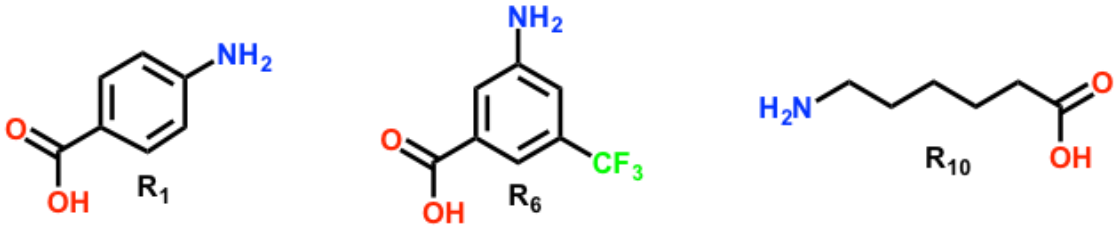

Figure 3.44. Amines that will feature in the discussions in this section regarding the *in situ* formation of LMWGs when combining these amines with the trialdehyde core unit ***II***.

The *in situ* experiments would focus on two different experiments, the combination of **R₁** + **R₆** + ***II***, and a separate set of experiments examining **R₁** + **R₁₀** + ***II***. Investigations into any resulting gel would look at the gels mechanical properties, as well as the chemical composition of the individual gelator molecules. The *in situ* synthesis nature of these molecules does raise an interesting issue regarding the statistical distribution of the products. Figures 3.45 and 3.46 demonstrate all possible products that could arise from the two separate reactions. Both reactions present the opportunity to produce molecules that have already been characterised, **R₁**, **R₆** and **R₁₀**. However, because with each reaction there are two amines present throughout the reaction process, there is the potential for molecules to emerge featuring mixed amine components, i.e. the arm units can be chemically different from one another. In the case of **R₁** + **R₆** + ***II*** in addition to the production of the compounds **R₁** and **R₆** two new products could also emerge, namely **R₁²,₆¹** and **R₁¹,₆²** (Figure 3.45).

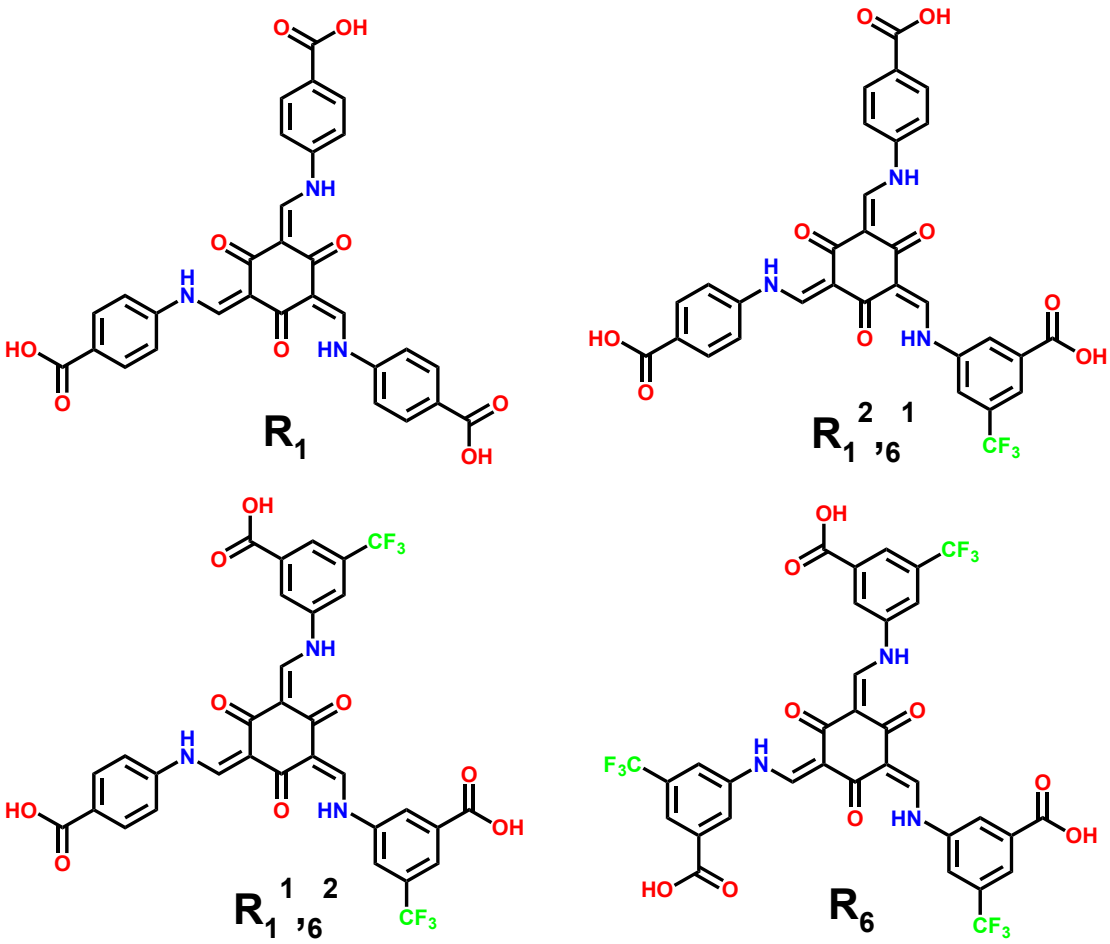

Figure 3.45. All possible reaction products for the *in situ* **R₁** + **R₆** + ***II***, including the gelators **R₁**, **R₆**, and products composed of mixed amines **R₁²,₆¹** and **R₁¹,₆²**.

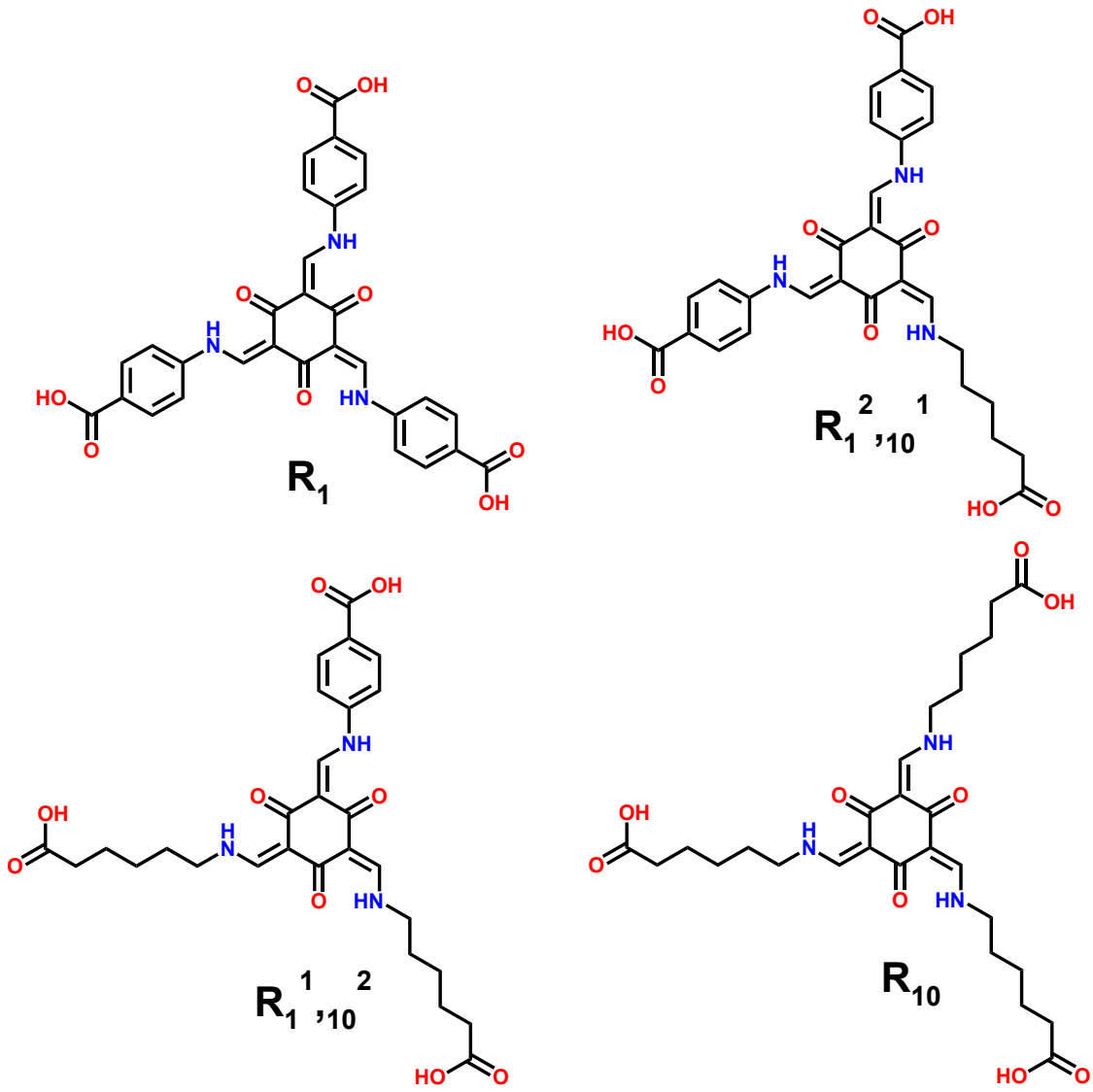

Figure 3.46. All possible reaction products for the *in situ* $\mathbf{R_1}$ + $\mathbf{R_{10}}$ + ***II***, including the known molecules $\mathbf{R_1}$ and $\mathbf{R_{10}}$, and products composed of mixed amines $\mathbf{R_1^{2},_{10}^{1}}$ and $\mathbf{R_1^{1},_{10}^{2}}$.

These mixed amine molecules feature arm units derived from two molecules of the amine $\mathbf{R_1}$ with one of the amine molecule $\mathbf{R_6}$ or one molecule of the amine $\mathbf{R_1}$ with two of the amine molecule $\mathbf{R_6}$, respectively. With the reaction system $\mathbf{R_1}$ + $\mathbf{R_{10}}$ + ***II***, in addition to "pure" $\mathbf{R_1}$ and $\mathbf{R_{10}}$ reaction products, there is the potential for two "mixed products; $\mathbf{R_1^{2},_{10}^{1}}$ with its two arms derived from the $\mathbf{R_1}$ and one from $\mathbf{R_{10}}$; and $\mathbf{R_1^{1},_{10}^{2}}$ with one arm derived from the amine $\mathbf{R_1}$ and two from the amine $\mathbf{R_{10}}$. With both these *in situ* reaction systems there is no way to theoretically determine the final composition of the reaction mixture accurately. The composition of the reaction mixture will depend on the thermodynamic and kinetic factors at play within the reaction system.

Testing initially conducted on the $\mathbf{R_1}$ + $\mathbf{R_6}$ + ***II*** involved dissolving all three components in water with the addition of sodium hydroxide. These components were then

mixed and allowed to react for four hours in a similar manner to the single amine reaction systems. The total quantity of amine required for the reaction is three molar equivalents with respect to the number of moles of ***II***.

In order to analysis the chemical composition of the gel, in terms of the number of products present and related to those outlined in Figure 3.45, HPLC analysis was used. Of the four products that are presented in Figure 3.45, pure samples of $\mathbf{R_1}$ and $\mathbf{R_6}$ existed through the *ex situ* synthetic procedures for these molecules. These pure samples can therefore be used as HPLC standards in order to help determine the composition of the *in situ* reaction mixture. Figures 3.47 and 3.48 show the HPLC traces for compounds $\mathbf{R_1}$ and $\mathbf{R_6}$. These figures show the retention time for $\mathbf{R_1}$ to be 323 seconds, and for $\mathbf{R_6}$ 391 seconds. It is fortunate there is a significant difference in the retention time, as it will make distinguishing between these two products, should they be present in the *in situ* reaction mixture, easy. HPLC analysis of the *in situ* reaction mixture was performed on a reaction mixture that had been allowed to react for 16 hours in order to insure complete conversion into the product(s). The pH of the reaction mixture was measured to nine which was sufficient to keep the reaction products in solution. This reaction solution could then be injected directly into the instrument, with methanol being used as the mobile phase. The results of this HPLC experiment can be seen in Figure 3.49.

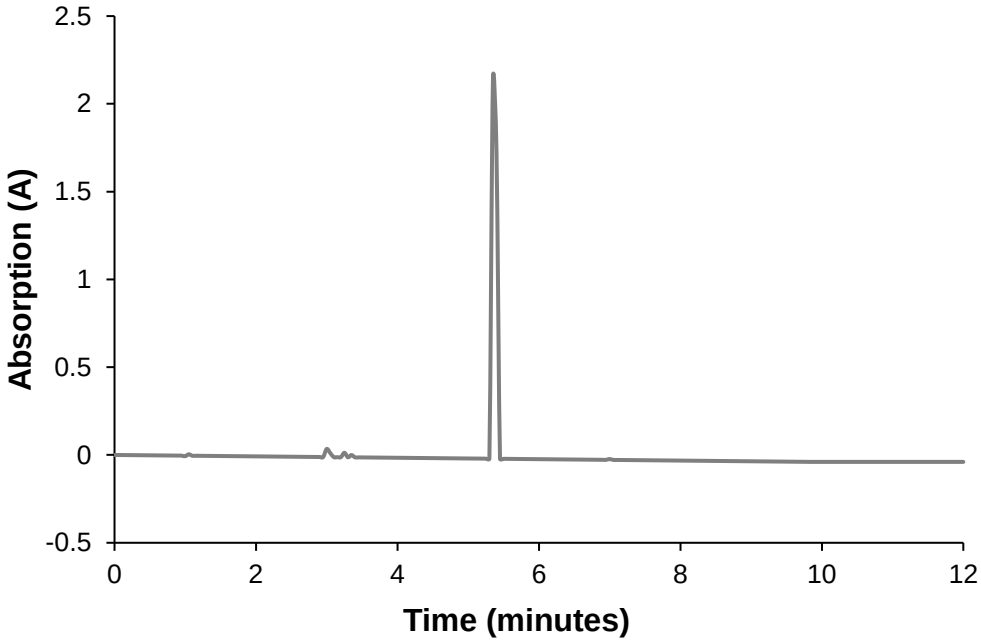

Figure 3.47. HPLC trace for *ex situ* synthesised compound $\mathbf{R_1}$, with a retention time of 323 seconds recorded.

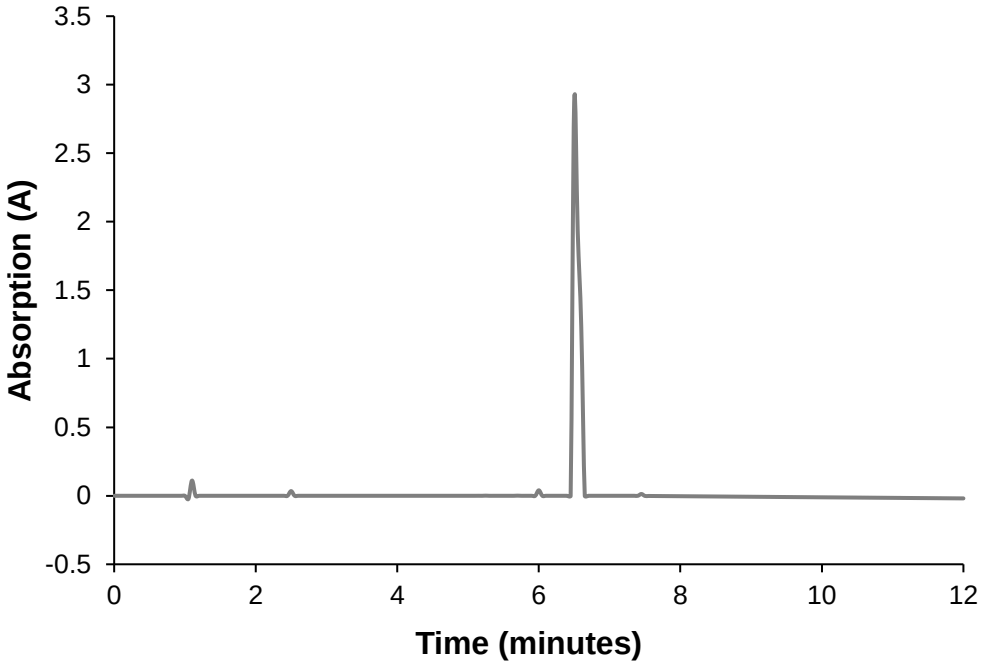

Figure 3.48. HPLC trace for *ex situ* synthesised compound $\mathbf{R_6}$, with a retention time of 391 seconds recorded.

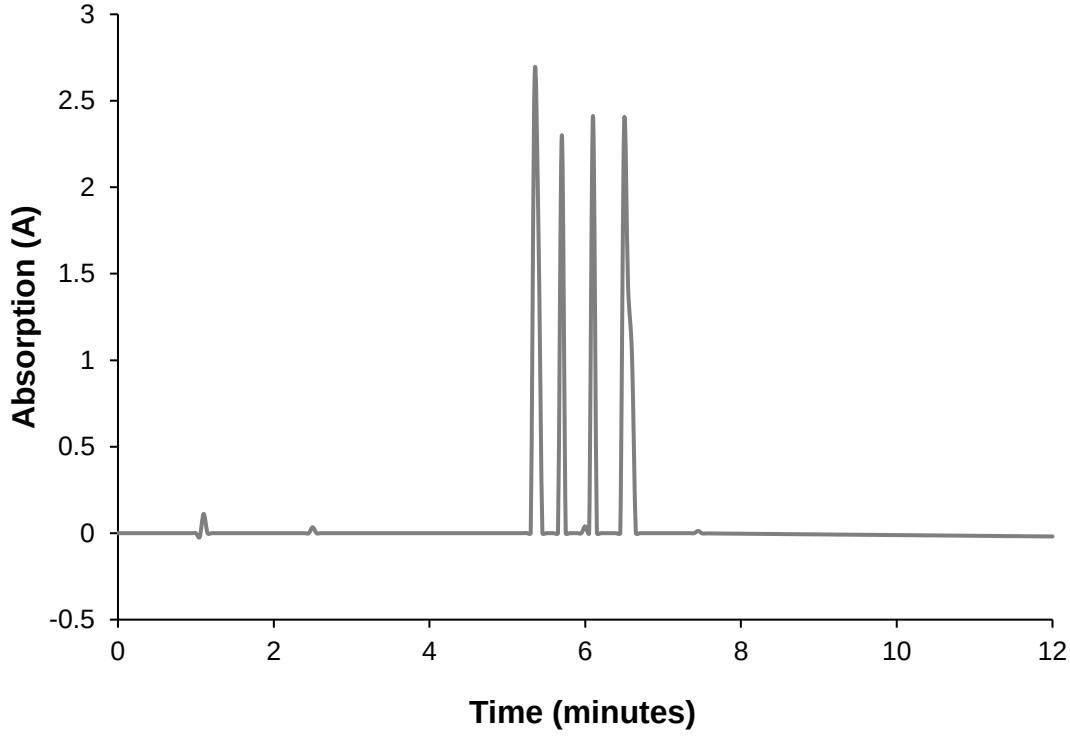

Figure 3.49. HPLC trace for *in situ* reaction mixture containing $\mathbf{R_1}$ amine, $\mathbf{R_6}$ amine and ***II***. All components were dissolved in water at pH 8, with the HPLC analysis performed after 16 hours.

The presence of four peaks can be clearly seen. Through comparison with retention time data obtained for $\mathbf{R_1}$ and $\mathbf{R_6}$ it was possible to identify two absorption peaks

which corresponded to these reaction products. This left two unidentified absorption peaks at retention times 356 and 374 seconds. These peaks likely correspond to the two mixed reaction products that were highlighted in Figure 3.45, $\mathbf{R_1^2,R_6^1}$ and $\mathbf{R_1^1,R_6^2}$. Through use of the Beer-lambert law it was possible to calculate the concentrations of the previously synthesised pure products $\mathbf{R_1}$ and $\mathbf{R_6}$. The calculated concentration of $\mathbf{R_1}$ and $\mathbf{R_6}$ where shown to account for 28% and 24% of the total concentration of this *in situ* reaction mixture. This would suggest the reaction mixture consists of a statistical mixture of all four the possible reaction products.

The reaction between the amines $\mathbf{R_1}$ and $\mathbf{R_{10}}$ was conducted in a similar fashion. Although it was only possible to do limited analysis on this system due to the time constraints associated with the project, initial results proved interesting. Mass spectroscopy experiments indicted that chemical self-sorting was occurring. This self-sorting process manifested itself in the formation of pure $\mathbf{R_1}$ and $\mathbf{R_{10}}$ ligands being obtained from the reaction mixture. There was no detectable presence of the mixed amine systems, $\mathbf{R_1^2,_{10}^1}$ and $\mathbf{R_1^1,_{10}^2}$, in the reaction mixture. This would imply that chemical selectivity and self-sorting is occurring, this is likely driven by a kinetic effect. This would arise from the aliphatic amine, $\mathbf{R_{10}}$, being more reactive than the aromatic species $\mathbf{R_1}$. Further work is currently on going to complete our understanding of these observations of chemical mixing and chemical self-sorting. This work is utilising computational calculations (preformed by Andrew Prentice working in the group of Prof. Martin Paterson, Heriot-Watt University) to determine stability of the products and potential reaction kinetics. Initial results indicate that the alkyl amines have lower barriers to the imine formation, therefore kinetically reacting faster than the aromatic amines. This effect tis well known for these two types of amines. Once reacted, the alkyl amines are also more stable thermodynamically. This would also bias the chemistry towards a self-sorted system. In the case of the two aromatic amines, little difference has been found in their reactivity and product stabilities. The computational work is not complete yet as the effects of the tautomerisation on the reaction has not fully be accounted for.

3.12 Conclusion

The development of a closely related family of LMWGs, where the chemical synthesis of the individual gelator molecules could be performed *in situ* or *ex situ*, allowed for interesting systems chemistry research to be done. Despite all the LMWGs in the family

being chemically very similar, they demonstrated differences in terms of the physical characteristics of the gels that they could go on to form, despite undeniable similarities in the morphology of their three-dimensional networks. Visually the nine presented gels were all different, with a variety of colours from yellow to brown, and a variety of transparencies from opaque to transparent. These differences in transparency also matched the more quantifiable rheological data. Characterisation highlighted the range of mechanical robustness of the gels, which seems to be intrinsically linked to the hydrophobicity of the individual LMWG molecules, with an increase in hydrophobicity seeming to result in an increase in the gels mechanical robustness (Figures 3.26 and 3.27).

Due to the chemical and conformational similarities between the LMWG molecules, the novel gel family represented an ideal candidate to explore multi-component LMWG systems, where two gelators, or a gelator and a non-gelator, could be mixed and the physical properties of the resulting material explored. The mixing experiments involving a gelator at the lower end of the mechanical strength spectrum (**R_1**) with the gel featuring the highest mechanical strength (**R_6**) or a related species (**R_{10}**) that has demonstrated no gelation abilities. What was observed was the ability to accurately and reproducibly tune the strength of the gels. By increasing the overall percentage of the mechanically superior gel, the resultant gel could be strengthened, while mixing in an increasing percentage of the non-gelator would result in an increasingly weak gel until a critical value was reached at which gelation was switched off. In addition to its superior mechanical performance, the mechanically most robust gel was also the most transparent. This physical property was also reflected in the mixed gels, resulting in increasingly transpareny with the addition of the transparent gelator. All these relationships between the physical properties and chemical identities were non-linear in nature.

The fact that this mechanical tuning occurred was attributed to the supramolecular organisation within the three-dimensional structure of the solid-phase of the gel. The increasing strong gel mix featured a co-assembly mechanism where the gel fibres would consist of a random mixture of both the gelator molecules. This matches a gradual increase in hydrophobic character of the mixed gel fibres, thus an increase in the rheological strength. On the other hand, the gel system that demonstrated a weakening through mixing, relied on a self-sorting mechanism where the non-gelating species crystallised out of solution before the gel formed resulting in a reduction in the theoretical wt% of the gel.

The ability to synthesis the molecules used for these mixing experiments also allowed exploration of self-sorting or co-reacting at the molecular level. The amine that

gave rise to the non-gelator would self-sort from the other, gelating, amines. The solution of the two gelating amines produced a product mixture that consisted of all possible product combinations being observed. This systems chemistry concept was further investigated through a theoretical study which elucidated the mechanisms through which chemical self-sorting and mixing occurred.

3.13 References

1 A. R. Hirst and D. K. Smith, *Chem. Eur. J.*, 2005, **11**, 5496–5508.

2 D. J. Cornwell, O. J. Daubney and D. K. Smith, *J. Am. Chem. Soc.*, 2015, **137**, 15486–15492.

3 E. R. Draper, E. G. B. Eden, T. O. McDonald and D. J. Adams, *Nature Chem.*, 2015, **7**, 848–852.

4 J. A. Foster, R. M. Edkins, G. J. Cameron, N. Colgin, K. Fucke, S. Ridgeway, A. G. Crawford, T. B. Marder, A. Beeby, S. L. Cobb and J. W. Steed, *Chem. Eur. J.*, 2014, **20**, 279–291.

5 D. J. Cornwell, B. O. Okesola and D. K. Smith, *Angew. Chem. Int. Ed.*, 2014, **126**, 12669–12673.

6 D. J. Cornwell, B. O. Okesola and D. K. Smith, *Soft Matter*, 2013, **9**, 8730.

7 L. E. Buerkle and S. J. Rowan, *Chem. Soc. Rev.*, 2012, **41**, 6089–6102.

8 C. Colquhoun, E. R. Draper, E. G. B. Eden, B. N. Cattoz, K. L. Morris, L. Chen, T. O. McDonald, A. E. Terry, P. C. Griffiths, L. C. Serpell and D. J. Adams, *Nanoscale*, 2014, **6**, 13719–13725.

9 M. M. Smith, W. Edwards and D. K. Smith, *Chem. Sci.*, 2013, **4**, 671–676.

10 R. Afrasiabi and H.-B. Kraatz, *Chemistry*, 2013, **19**, 15862–15871.

11 K. L. Morris, L. Chen, J. Raeburn, O. R. Sellick, P. Cotanda, A. Paul, P. C. Griffiths, S. M. King, R. K. O'Reilly, L. C. Serpell and D. J. Adams, *Nat. Commun*, 2013, **4**, 1480.

12 Y. Zhang, P. Xue, B. Yao and J. Sun, *New J. Chem.*, 2014, **38**, 5747–5753.

13 J. H. Chong, M. Sauer, B. O. Patrick and M. J. MacLachlan, *Org. Lett.*, 2003, **5**, 3823–3826.

14 C. V Yelamaggad, A. S. Achalkumar, D. S. Shankar Rao and S. K. Prasad, *J. Am. Chem. Soc.*, 2004, **126**, 6506–6507.

15 J. A. Riddle, S. P. Lathrop, J. C. Bollinger and D. Lee, *J. Am. Chem. Soc.*, 2006, **128**, 10986–10987.

16 L. Chen, S. Revel, K. Morris, L. C Serpell and D. J. Adams, *Langmuir*, 2010, **26**, 13466–13471.

17 H. Wang, Z. Yang and D. J. Adams, *Mater. Today*, 2012, **15**, 500–507.

18 S. Shinkai and K. Murata, *J. Mater. Chem.*, 1998, **8**, 485–495.

19 J. H. van Esch and B. L. Feringa, *Angew. Chem. Int. Ed.*, 2000, **39**, 2263–2266.

20 N. M. Sangeetha and U. Maitra, *Chem. Soc. Rev.*, 2005, **34**, 821–836.

21 M. George and R. G. Weiss, *Acc. Chem. Res.*, 2006, **39**, 489–497.

22 P. Terech and R. G. Weiss, *Chem. Rev.*, 1997, **97**, 3133–3160.

23 H. Kobayashi, A. Friggeri, K. Koumoto, M. Amaike, S. Shinkai and D. N. Reinhoudt, *Org. Lett.*, 2002, **4**, 1423–1426.

24 F. Ono, H. Watanabe and S. Shinkai, *RSC Adv.*, 2014, **4**, 25940–25947.

25 F. R. Leroux, B. Manteau, J.-P. Vors and S. Pazenok, *Beilstein J. Org. Chem.*, 2008, **4**, 13.

26 A. K. Ghose, and V. N. Viswanadhan and J. J. Wendoloski, *J. Phys. Chem. A*, 1998, **102**, 3762–3772.

27 J. J. Panda, A. Mishra, A. Basu and V. S. Chauhan, *Biomacromolecules*, 2008, **9**, 2244–2250.

28 L. Chen, T. O. McDonald and D. J. Adams, *RSC Adv.*, 2013, **3**, 8714–8720.

29 C. Tang, R. V. Ulijn and A. Saiani, *Langmuir*, 2011, **27**, 14438–14449.

30 D. J. Adams, L. M. Mullen, M. Berta, L. Chen and W. J. Frith, *Soft Matter*, 2010, **6**, 1971–1980.

31 C. Tang, A. M. Smith, R. F. Collins, R. V Ulijn and A. Saiani, *Langmuir*, 2009, **25**, 9447–9453.

32 K. A. Houton, K. L. Morris, L. Chen, M. Schmidtmann, J. T. A. Jones, L. C. Serpell, G. O. Lloyd and D. J. Adams, *Langmuir*, 2012, **28**, 9797–9806.

33 R. C. T. Howe, A. P. Smalley, A. P. M. Guttenplan, M. W. R. Doggett, M. D. Eddleston, J. C. Tan and G. O. Lloyd, *Chem. Commun.*, 2013, **49**, 4268–4270.

34 G. Yu, X. Yan, C. Han and F. Huang, *Chem. Soc. Rev.*, 2013, **42**, 6697–722.

35 F. M. Menger and K. L. Caran, *J. Am. Chem. Soc.*, 2000, **122**, 11679–11691.

36 P. Dastidar, *Chem. Soc. Rev.*, 2008, **37**, 2699–2715.

37 J. Raeburn and D. J. Adams, *Chem. Commun.*, 2015, **51**, 5170–5180.

38 E. Ostuni, P. Kamaras and R. G. Weiss, *Angew. Chem. Int. Ed.*, 1996, **35**, 1324–1326.

39 C. R. Martinez and B. L. Iverson, *Chem. Sci.*, 2012, **3**, 2191–2120.

40 S. E. Wheeler and K. N. Houk, *J. Am. Chem. Soc.*, 2008, **130**, 10854–10855.

41 S. E. Wheeler, *J. Am. Chem. Soc.*, 2011, **133**, 10262–10274.

42 K. Sugiyasu, S. Kawano, N. Fujita and S. Shinkai, *Chem. Mater.*, 2008, **20**, 2863–2865.

43 M. Zhou, A. M. Smith, A. K. Das, N. W. Hodson, R. F. Collins, R. V. Ulijn and J. E. Gough, *Biomaterials*, 2009, **30**, 2523–2530.

44 R. Winter, D. W. Hua, X. Song, W. Mantulin and J. Jonas, *J. Phys. Chem.*, 1990, **94**, 2706–2713.

45 V. F. Felicetta, A. E. Markham, Q. P. Peniston and J. L. McCarthy, *J. Am. Chem. Soc.*, 1949, **71**, 2879–2885.

46 J.-B. Guilbaud and A. Saiani, *Chem. Soc. Rev.*, 2011, **40**, 1200–1210.

47 R. K. Das, R. Kandanelli, J. Linnanto, K. Bose and U. Maitra, *Langmuir*, 2010, **26**, 16141–16149.

48 H. C. Geiger, M. Lamson and D. J. Galka, *Langmuir*, 2014, **30**, 13979–13986.

49 W. Edwards and D. K. Smith, *J. Am. Chem. Soc.*, 2014, **136**, 1116–1124.

50 W. Edwards and D. K. Smith, *J. Am. Chem. Soc.*, 2013, **135**, 5911–5920.

51 A. R. Hirst, I. A. Coates, T. R. Boucheteau, J. F. Miravet, B. Escuder, V. Castelletto, I. W. Hamley and D. K. Smith, *J. Am. Chem. Soc.*, 2008, **130**, 9113–9121.

52 Dean C. Duncan and D. G. Whitten, *Langmuir*, 2000, **16**, 6445–6452.

53 B. Escuder, M. LLusar and J. F. Miravet, *J. Org. Chem.*, 2006, **71**, 7747–7752.

Chapter 4 - Autocatalytic synthesis of an *in situ* formed hydrogelator

4.1 Introduction

Self-replication and autocatalysis are terms that are often used interchangeably to describe a concept that is deeply rooted in almost every aspect of life. The idea of an entity that through some mechanism can produce more and more copies of itself from a fuel source is undeniably very intriguing concept. Of course one might immediately think of life as we know it as a self-replicating system. Indeed, it is widely accepted that autocatalytic chemical reactions must have played a central role during the emergence of life, with the RNA world concept a key example of a scenario where autocatalysis is central to the origins of life.[1]

When citing autocatalysis within an artificial chemical system, what is being referred to is the ability of one of the reaction products to catalysis its own formation (Figure 4.1). The simplest example of a synthetic autocatalytic system, presented in Figure 4.1, represents an excellent handle with which an understanding of more complex autocatalytic systems, such as mutually cross-catalytic cycles and hyper-cycles, can be developed.[2,3] The development of such an autocatalytic systems, one that is synthetic in nature, requires a multidisciplinary approach and results in a blurring of the lines between chemistry and biology.[4]

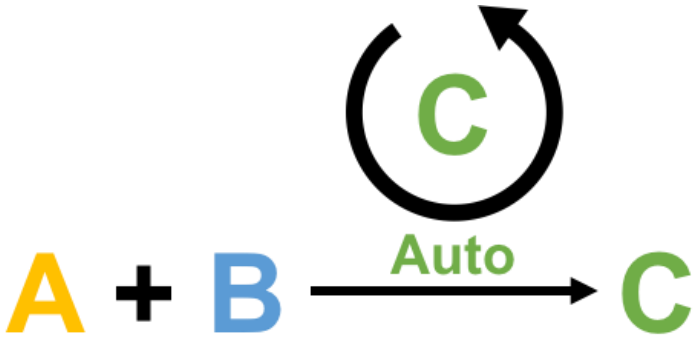

Figure 4.1. Example of the simplest possible manifestation of an autocatalytic reaction where A + B goes to C, with C then acting as a catalyst, resulting in an exponential increase in the concentration of C occurring as time progresses until the supply of A and B are exhausted.

This chapter discusses a system which is chemically similar to those that were discussed in the previous chapter. The difference being that this system takes considerably longer for the tripodal imine to form, and ultimately the enol to keto tautomerisation process to occur. Due to this extended reaction time the kinetics of this particular reaction could be easily studied in detail. Through analysis of these reaction kinetics this system was shown be autocatalytic. The autocatalytic nature of this reaction arose due to the face-to-face intermolecular associations that give rise to a templating affect. The fact that the molecules can act as an *in situ* synthesised LMWG offered the existing prospect to control the mechanical robustness of the gel through influencing the autocatalytic mechanical reaction. The reaction kinetics of the autocatalytic reaction have been characterised in detail, as well as a means to link the elasticity of the supramolecular gel to the reaction that produces the gelator molecules.

4.2 LMWG design

Attempts to expand the gel library discussed in the previous chapter looked at utilising amino acids in place of the aminobenzoic acids that have been successfully used so far. Natural amino acids were tested. This screening process involved mixing three equivalents of phenylalanine, leucine, tryptophan or tyrosine (see Figure 4.2.) individually with the trialdehyde core (***II***) in water at a pH of 8. After allowing the mixtures to react at room temperature for 72 hours, upon acidification, no gelation was observed. The experiment was repeated with the mixtures heated to 60 ^{o}C for 72 hours, and again upon acidification no gelation was observed. Acidification of these solutions did however result in a pale yellow precipitate coming out of solution. The precipitate was isolated and thoroughly dried before ^{1}H NMR showed it to be consist of the two unreacted starting materials. This lack of reaction between the starting materials was deemed to be a trait of the $-NH_2$ functionality within the amino acid group of these natural amino acids. The zwitterionic nature of the amino acids means the nucleophilic character of the amine is lost.

With the lack of reactivity observed with natural amino acids resulting in no gel being produced, a search for an alternative, albeit unnatural, amino was conducted. A modified version of phenylalanine was selected for investigation were an additional amine group had been added to the phenyl ring para to the amino acid group, 4-amino-L-phenylalanine (***$_4$F***) (Figure 4.2.). As with the previous amino acid examples, ***$_4$F*** was dissolved with ***II*** in water at pH 8 and allowed to react for a total of 72 hours. After this

reaction time had elapsed and with the addition of GdL,[5–7] a hydrogel did indeed form. As with all *in situ* formed supramolecular hydrogelators, it was essential to conduct chemical analysis on the solid-phase of the material to determine what the gelator species actual was.

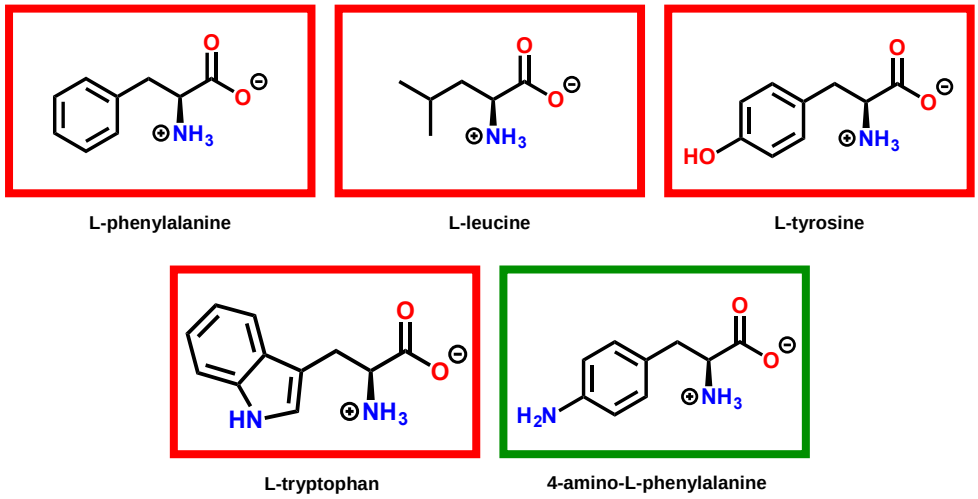

Figure 4.2. Amino acids; phenylalanine, leucine, tyrosine and tryptophan were used in gel screening with the trialdehyde core unit ***II***. Amino acids highlighted in red to not produce a gel upon acidification, the unnatural amino acid 4-aminophenylalanine (***4F***), highlighted in green, does form a gel upon acidification.

The use of ***4F*** had the potential to add additional complications into the formation of the LMWG. Because there are two amine groups, the aromatic and amino acid, there was the potential for two products to form or even a complex mixture of the four possible products that could arise from the reaction. These four products are; all aldehyde groups reacted at the aromatic amine, all aldehyde groups reacted at amino acid amine, two aldehyde groups reacting at aromatic amine and one at amino acid amine, two aldehyde groups reacting at amino acid and one at the aromatic amine (see Figure 4.3). Analysis of the ^{1}H and ^{13}C NMR experiments showed that the product had a relatively high degree of symmetry when compared to the simulated spectra of the more asymmetric of the four possible reaction products. By looking at the structures presented in Figure 4.3 and visualising a rotation axis through the central core perpendicular to the plane of the page, a symmetry element of the molecules can be understood. This rotation exhibits C_3 symmetry for the two molecules were the reaction occurs fully at the aromatic amine or at the amino acid amine. With the molecules where the reaction occurred at two aromatic amines and one amino acid amine or vice versa the system around this axis drops to C_1. This reduction in symmetry would result in an increase in the number of peaks observed in the ^{1}H and ^{13}C NMR experiments. For example, when considering the results of the

^{13}C NMR experiments, the C_3 symmetric molecules would ideally be expected to exhibit 10 distinct carbon environments, while the C_1 symmetric molecules would feature twenty.

This meant the product of this *in situ* type was either the result of complete reaction between the aldehydes groups and the amino acid amine or, more likely, reaction with the aromatic amine. In order to determine which of these hypothesis was correct, comparison NMR and FTIR experiments were conducted.

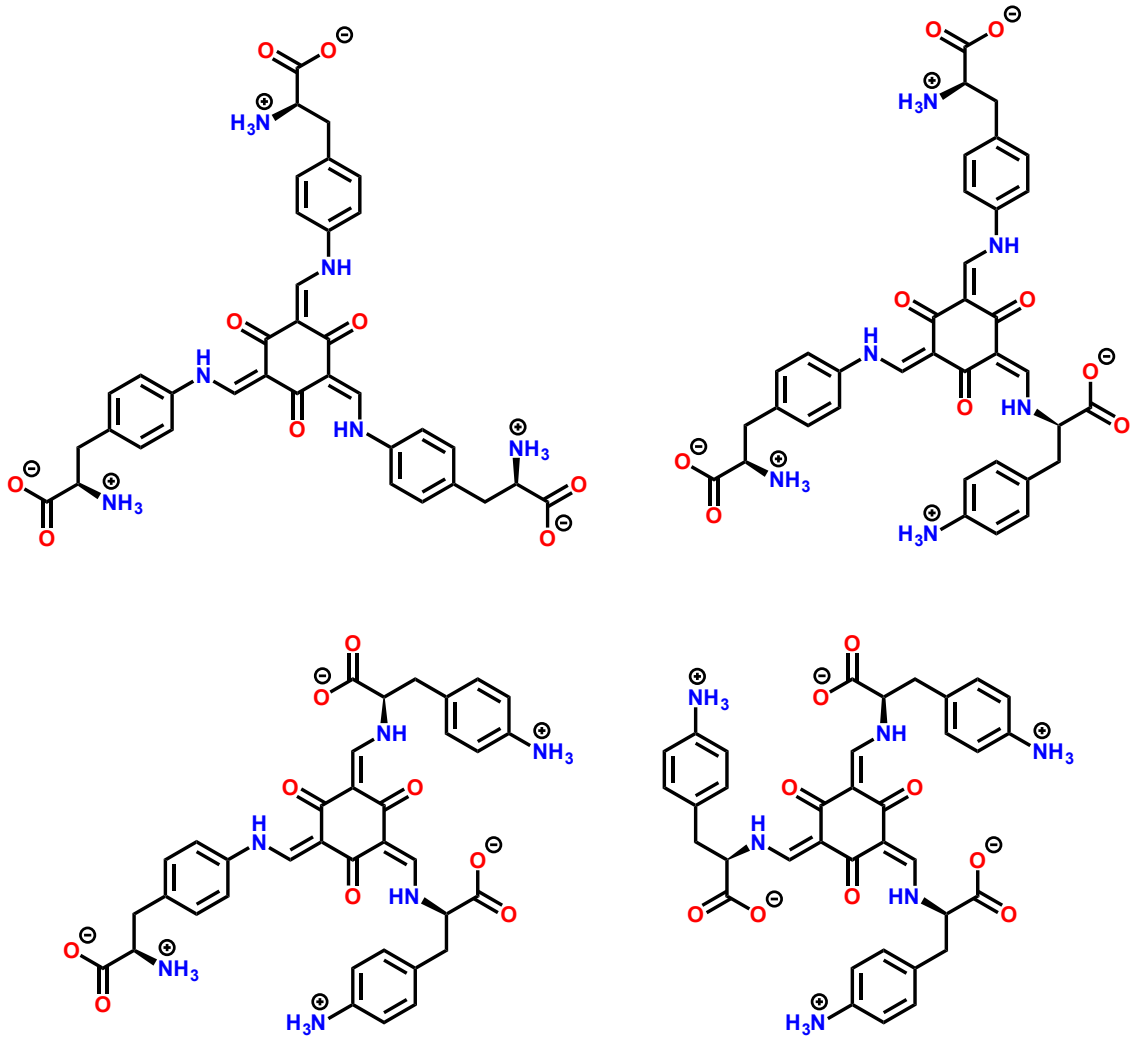

Figure 4.3. Diagrams showing all possible proposed reaction products for the reaction between ***II*** and ***$_4$F***. From top left and going clockwise reaction occurs at all three aromatic amines, two aromatic amines and one amino acid amine, one aromatic amine and two amino acid amines and all three amino acid amines.

Figure 4.4 shows four transmittance FTIR spectra and allows important comparisons to be made. When regular phenylalanine, **a**, is compared to the spectra for 4-aminobenzoic acid, **b**, it can be observed that there are twin peaks (~ 3400 cm^{-1}) apparent in **b** but not in **a**. When this is compared to the spectra for ***$_4$F*** (spectra **c**) it is clear that this twin peak feature, something expected for a primary amine group, relates

to the aromatic amine $-NH_2$ group. This peak feature is not present in any form in the spectra **d**, which is the FTIR spectra for compound ***Z***. This is suggestive that the reaction occurs at this aromatic amine position and the resulting chemical change from Ar-NH_2 to Ar-NH- means the twin amine peak that would otherwise be associated with the aromatic amine is not apparent in the spectra.

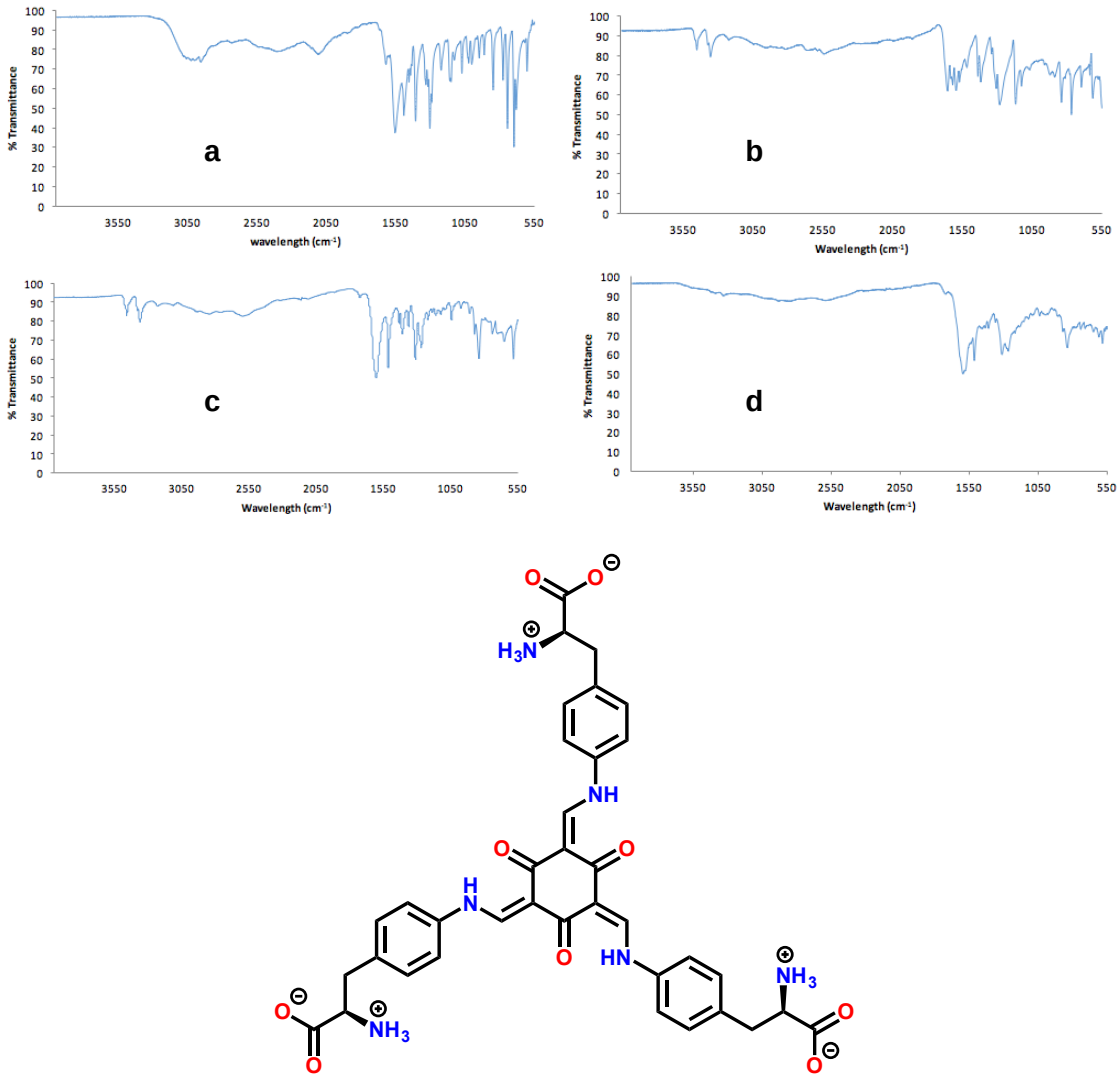

Figure 4.4. IR spectra presented with wavelength (cm^{-1}) on the x-axis and percentage transmission on the y-axis. These spectra show L-phenylalanine (**a**), 4-aminobenzoic acid (**b**), 4-amino-L-phenylalanine (**c**), compound ***Z*** (shown chemical structure) (**d**).

In addition to the FTIR spectroscopy it was also possible to determine the reaction product by careful analysis of the shifts in the ^{13}C NMR spectra of ***Z*** and comparing them with the spectra that was obtained for unreacted ***$_4$F***. The spectra for ***$_4$F*** shows a peak at 144.4 ppm which corresponds to the aromatic carbon that is functionalised with the amine group. When this is compared to the ^{13}C NMR of ***Z*** it can be seen that this peak under

goes a substantial and repeatable 2.5 ppm upfield shift to 141.9 ppm (Figure 4.5). Crucially, however, all other peaks do not undergo any significant change in their chemical shifts, and perhaps most noteworthy is the lack of change in the shift value for the carbon adjacent to the amino acid $–NH_2$ group. This shift is consistent and highly reproducible, and when considered along with the FTIR spectroscopic evidence confirms reaction at the aromatic $–NH_2$ group to give ***Z*** as the sole reaction product.

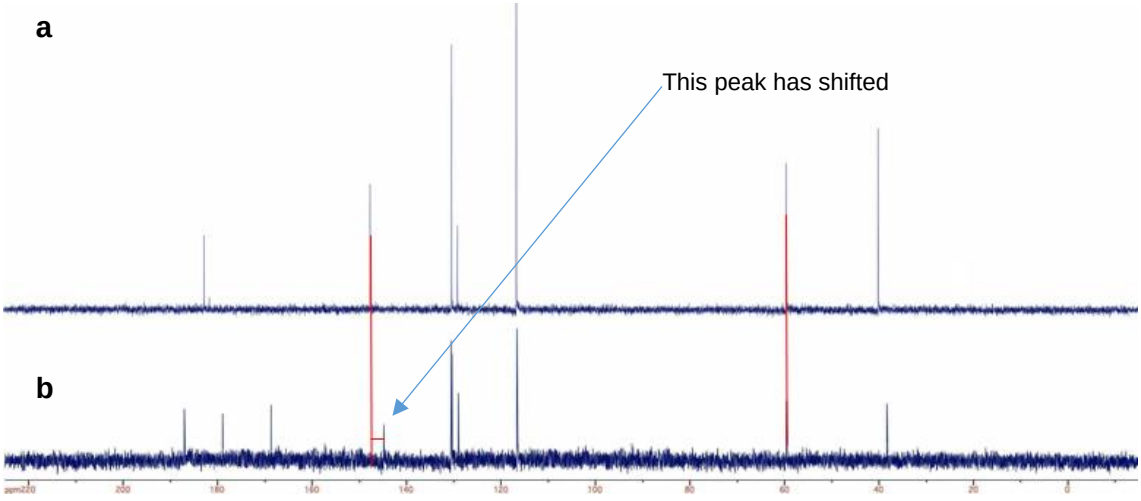

Figure 4.5. The ^{13}C NMR spectra obtained for ***4F*** dissolved in D_2O at pD 9 (**a**) and for ***Z*** recorded under the same solvent conditions (**b**). Arrow highlights peak that has moved, with red lines added to guide the eye as to the size of the shift 144.4 to 141.9 ppm, and to demonstrate the lack of a shift in the other peaks. The peaks 59.8 ppm are used to exemplify this.

4.3 Ex Situ preparation method

As with the *in situ* formed gelator family discussed in the previous chapter, the *in situ* formed system that is the focus of this chapter can also be formed in an *ex situ* manner, as outlined in Figure 4.6.

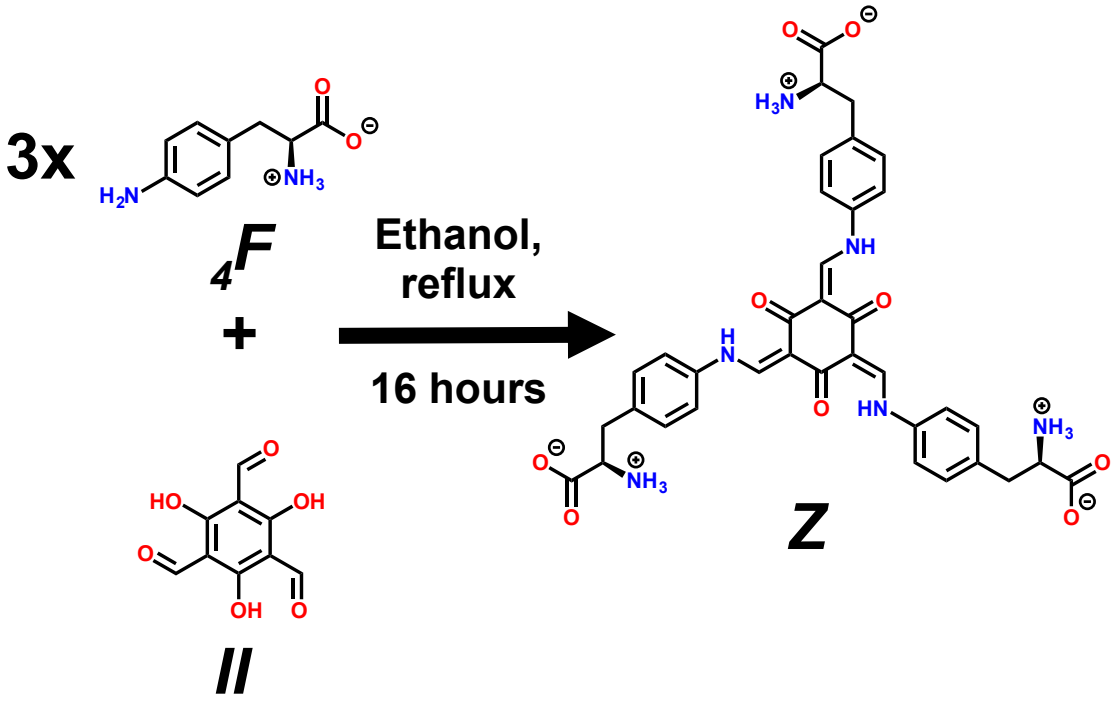

Figure 4.6. The *ex situ* reaction between three equivalents of ***4F*** and one equivalent of ***II*** in ethanol. Reaction is performed at reflux for 16 hours, with the product being the tripodal LMWG ***Z***.

The *ex situ* method of producing ***Z*** yielded a high purity product that was readily collected through filtration. After drying the filtrate and removal of residual ethanol, ***Z***, in the form of a dark orange solid chemical, was collected. Through chemical analysis of this *ex situ* synthesised product, including ^{1}H and ^{13}C NMR, it was confirmed that the product of the *ex situ* reaction was identical to that of *in situ* reaction. ***Z*** could be added to water and would readily dissolved once the pH or the suspension/solution had been adjusted to pH 8. This resulted in a yellow-orange solution that when acidified with the addition of GdL produced a yellow-brown supramolecular gel. Using this *ex situ* prepared sample of ***Z***, the CGC for the system could be determined. This was done using the inverted vial method, which showed the CGC for this particular system to be 0.5 wt% (7.2 mM), which is comparable to the similar systems in the previous chapter. *Ex situ* prepared ***Z*** was also used to quantitatively characterise the rheology of the gels at a concentration of 2.0 wt% and set using nine equivalents of GdL.

The three standard experiments of time, frequency and stress sweeps were all preformed. The time sweep gave rise to a standard profile for gels set using this method, with the *G′* value seen to plateau at 1000 Pa after 17 minutes, before reaching its maximum of 2400 Pa after 90 minutes (Figure 4.7).

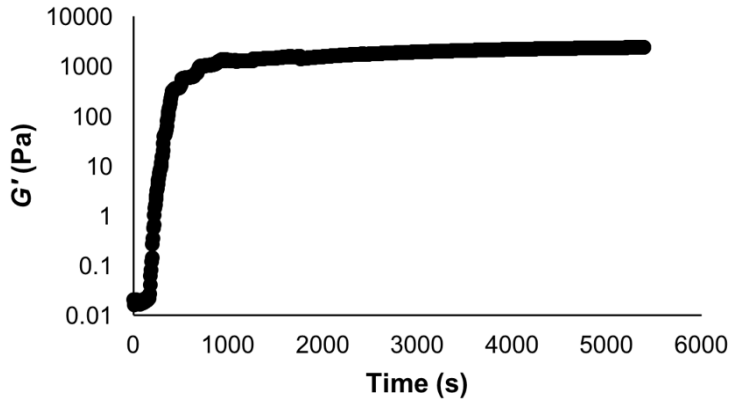

Figure 4.7. Results of the time sweep rheology experiment for the gel prepared using an *ex situ* synthesised sample of ***Z*** to produce a gel at 2 wt%. Storage modulus *G′*(●) (Pa) (y-axis) plotted (log scale) against time (s) (x-axis).

Immediately after preforming the time sweep experiment the frequency sweep was started and performed at frequencies from 0.1 – 100 Hz. The linear profile of the frequency sweep plot for the *G′* and *G″* values proved the material was indeed viscoelastic and a supramolecular gel (Figure 4.8). At an oscillating frequency of 50 Hz *G″* was found to be 470 Pa and, while not an order of magnitude larger, the value of *G′* was significantly greater at 2300 Pa. The final stress sweep experiment tested the gels mechanical robustness. The gels structural integrity was preserved up to an applied force of 90 μNm, after which point it began to yield. The value of *G″* began exceeding *G′* after 184 μNm, this is the point at which the dominant solid-like characteristics of the gel give way to the liquid-like characteristics of the water, which contains the broken gel network after sheering (Figure 4.9).

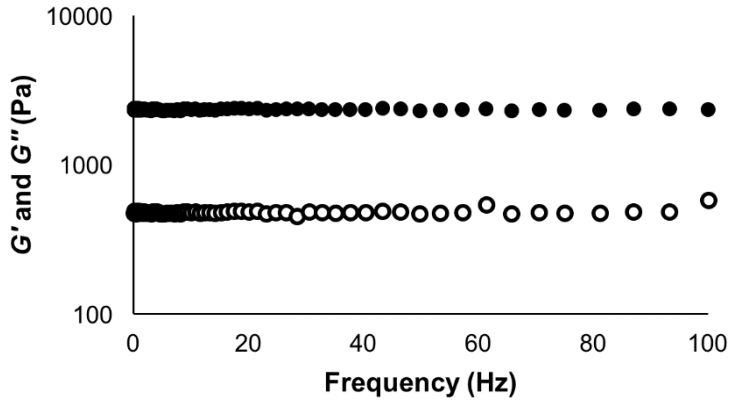

Figure 4.8. Results of the frequency sweep rheology experiment for the gel prepared using an *ex situ* synthesised sample of ***Z*** to produce a gel at 2 wt%. The storage modulus *G′*(Pa) (●) and the loss modulus *G″*(Pa) (○) are shown as a log scale (y-axis) against the frequency (Hz) (x-axis).

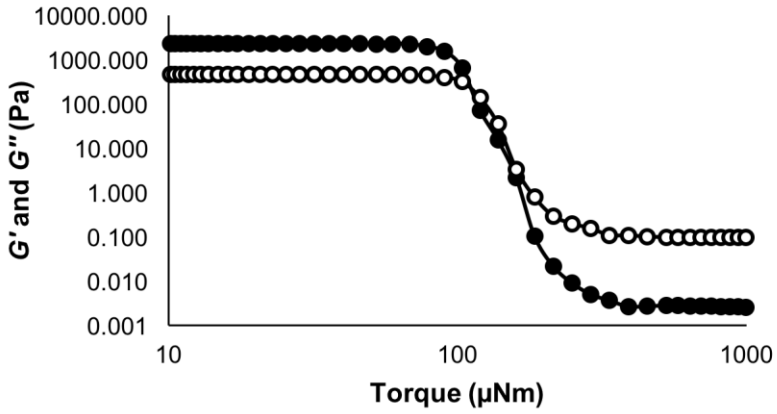

Figure 4.9. Results of the stress sweep rheology experiment for the gel prepared using an *ex situ* synthesised sample of ***Z*** to produce a gel at 2 wt%. The storage modulus *G′*(Pa) (●) and the loss modulus *G″*(Pa) (○) are shown as a log scale (y-axis) plotted against torque (μNm) (x-axis) shown in a log scale. A line between data points added to guide the eye.

The data obtained during the time sweep experiment can be used to calculate the Avrami constant for the system.[8–10] As discussed previously, the Avrami constant describes the fractal growth nature of the supramolecular polymers. The Avrami coefficient (n) could be determined by plotting ln(-ln(1-X)), where $X = (G'_t - G'_0)/ (G'_\infty - G'_0)$ (G'_t = G′ at time t, G'_0 = G′ at time = 0, G'_∞ = G′ average of last 5 data points), against $\ln(t - t_0)$. The Avrami constant is determined from the first part of the slope where the nucleation process begins. As demonstrated in Figure 4.10, the Avrami constant

determined for the gel set using *ex situ* synthesised ***Z*** at 2.0 wt% is n = 2.4. This value is an excellent fit for a supramolecular gel and is highly suggestive of a fractal growth mode for the fibre formation leading to a well-connected gel network.

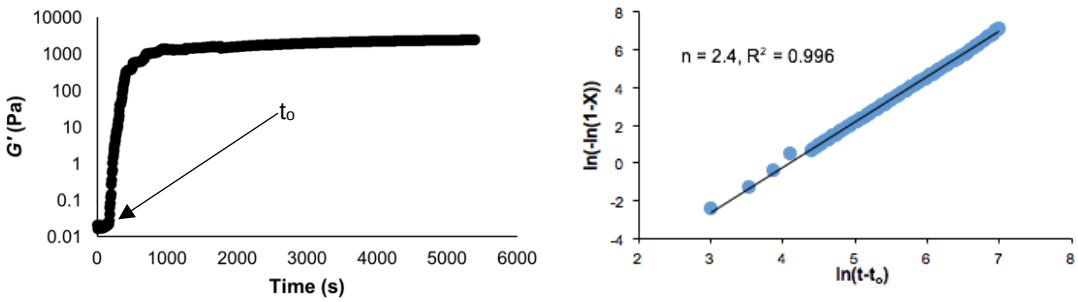

Figure 4.10. Time sweep rheology experiment (left) and the derived Avrami plot (right) of the gel prepared using *ex situ* synthesized ***Z***. t_0 marks the point at which the onset of gelation begins and the region with which the Avrami constant is calculated.

The use of *ex situ* synthesised ***Z*** in a concentration study experiment also allowed inferences to be made on the fibrous networks growth using the cellular solid model.[11–13] Frequency sweep experiments were performed on gels set using ***Z*** at various concentrations, ranging from 0.7 wt% to 10 wt%, and the *G′* value was recorded at 50 Hz for each of samples. The log of these *G′* values was then plotted against the log of concentration, this yielded a straight line. From the gradient of this straight line, a value of 1.9 was determined, which gives a good agreement with the cellular solid model[12] (Figure 4.11). The rheological measurements also allow comparisons of the mechanical properties to be made between the gels set using *in situ* and *ex situ* prepared samples of ***Z***. As can be seen in Figure 4.12, the plots are identical, within error.

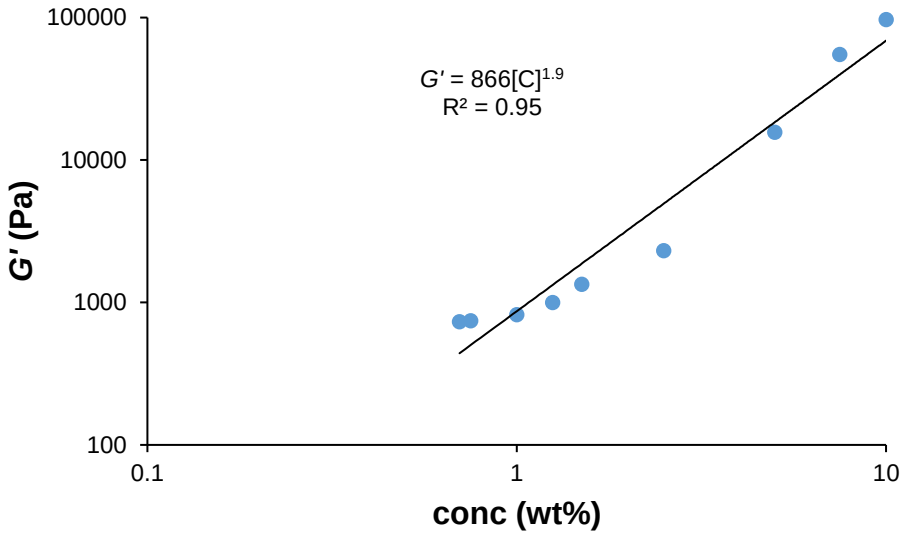

Figure 4.11. Concentration study of the gel produced using *ex situ* synthesised ***Z*** used to determine the cellular solid model for the system presented in this chapter.

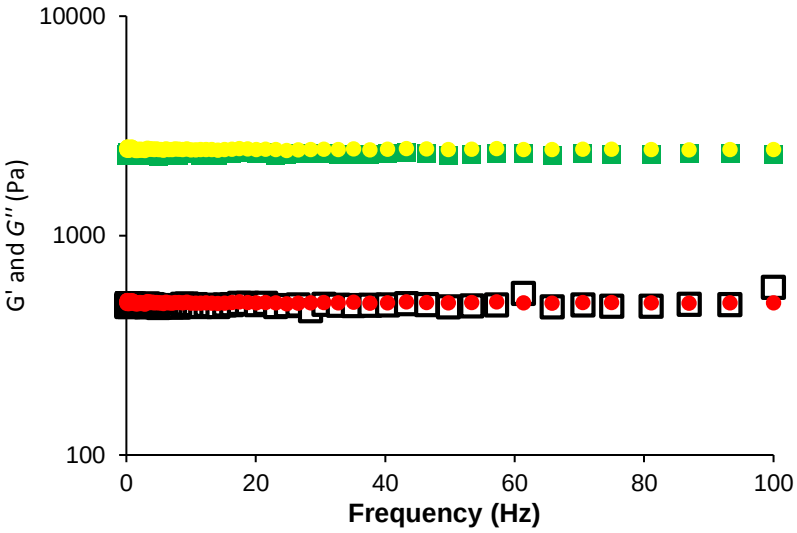

Figure 4.12. Results of the frequency sweep rheology experiment for the gel prepared using an *ex situ* synthesised sample of ***Z*** to produce a gel at 2 wt%, as well as a sample of the *in situ* prepared gel at 2 wt%. The storage modulus *G′*(Pa) for the *in situ* formed gel (●) and *ex situ* formed gel (■), as well as the loss modulus *G″*(Pa) for the *in situ* form gel (●) and *ex situ* formed gel (□), are shown as a log scale (Pa) (y-axis) against the frequency (Hz) (x-axis).

What is clear as that there is essential no difference in the *G′*and *G″*values where the gel is prepared *in situ* or *ex situ*. This means that despite there being differences in the way the ligand is synthesised, the final material properties are identical.

Useful structural information can also be gained from looking at the PXRD pattern of dried samples of the gel. It will also give an insight into whether or not the method used to form the individual LMWG molecules (i.e. *in situ* or *ex situ*) leaves any impression on the structure of the supramolecular gel network. PXRD patterns of powders obtained from gels set using both the *ex situ* and *in situ* method are shown in Figure 4.13. When these patterns are compared, there is no obvious difference between them, suggesting the supramolecular arrangement in both materials are very similar. There are also significantly more reflections for these patterns than can be observed in the patterns of the imine-type gels discussed previously. An increase in the number of reflections shows that these processed gels have more long range order than the processed imine-like gels presented in the previous chapters. This could, and most likely does, result from a phase transition that occurs during the removal of the bulk water phase.

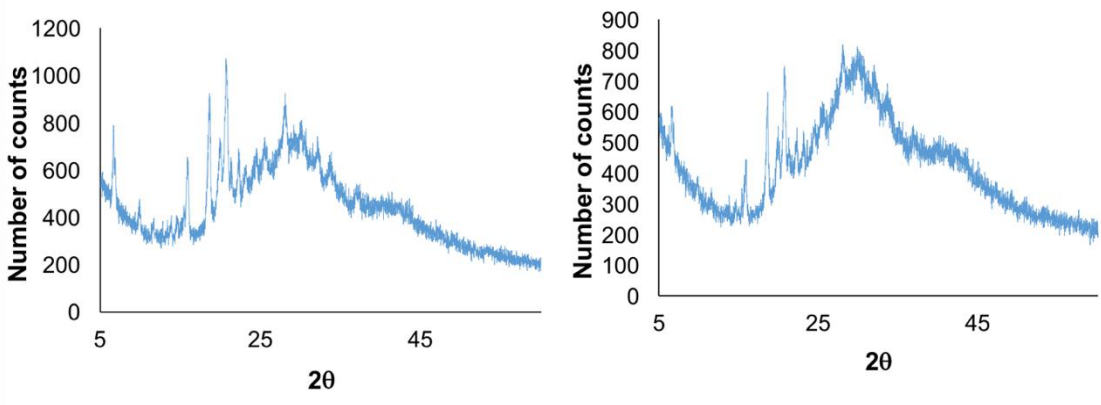

Figure 4.13. PXRD patterns obtained from dried samples of gels prepared using the *ex situ* method (left) and the *in situ* method (right).

4.4 Mechanism of Gelation

The use of an unnatural amino acid derived from phenylalanine means care has to be taken when discussing the nature of the species that forms the gel. With some LMWGs that are set using a pH switch the mechanism for gelation is very clear. A group, often a carboxylic acid group, is deprotonated through raising the pH of the solution. This results in the molecule becoming charged and causes dissolution of the molecule. When the pH is lowered to a value below the apparent pK_a of the LMWG, the groups that had been deprotonated are reprotonated removing the charge from the molecule, reducing its solubility which in turn causes gelation. This whole process is a simplistic view of the complex equilibria between all the neutral and charged species in solution and the solid

state materials. However, when dealing with amino acids, although the molecule may be charge neutral, it will still exhibit regions of discreet charge due to the zwitterionic nature of amino acids. Indeed, it is even possible that lowering the pH too far could result in amino acid-based LMWGs exhibiting an overall positive charge as the carboxylate and amine groups become protonated. While gels formed using LMWGs derived or consisting from amino acids are relatively common place, there is little discussion regarding the zwitterionic nature of the gelator molecules.[14] In the case of the gelator discussed here, ***Z***, it will be zwitterionic in nature, therefore, it is unclear what the trigger for gelation is. So, the "apparent pK_a" was determined for the point of gelation and found to be 6.5. This value corresponds closely to the p*I* value of most zwitterionic amino acids. The p*I* value is the point at which that amino acid is at its most charge neutral form. Therefore, the hypothesis here is that the acidification of a basic solution of ***Z*** results in the formation of the zwitterion from the majority negatively charged solubilised species at this "apparent pK_a" value. This results in self-assembly of the gel and the remove of ***Z*** from solution. Therefore it may be more appropriate to refer to this point of assembly as the "apparent p*I*", rather than the "apparent pK_a".

4.5 Temporal dependence on gels mechanical properties

The reaction time of 72 hours that was employed for the initial *in situ* synthesis of ***Z*** was to ensure complete conversion from starting materials to products. This did, however, seem like an excessive length of time when compared to the other similar imine-based gel examples. A reaction optimisation was conducted in order to determine the ideal reaction time for the reaction to go to completion.

HPLC proved an effective method of monitoring the progress of the reaction[15–17] and revealed some interesting traits with respect to this particular system. As with the hydrazine-based gelation system discussed in chapter 2, it could be expected that the system moves through a mono-, di- then tri- reacted states before the enol-keto tautomerisation occurs, as would be expected for an imine/enamine system (see Figure 4.14). HPLC analysis of the reaction solution showed the presence of only a maximum of two peaks in the resulting trace, when monitoring UV-vis absorption at any wavelength at any given time (Figure 4.15). It could be observed that the intensity of the peak that appeared at a time of 3 minutes and 20 seconds (peak A) decreases as the *in situ* reaction was allowed to progress. This was strongly suggestive that this peak relates to one of the

starting materials. The peak at 5 minutes and 15 seconds (peak B) increased in intensity as the reaction progressed, suggested that this was the known product ***Z***.

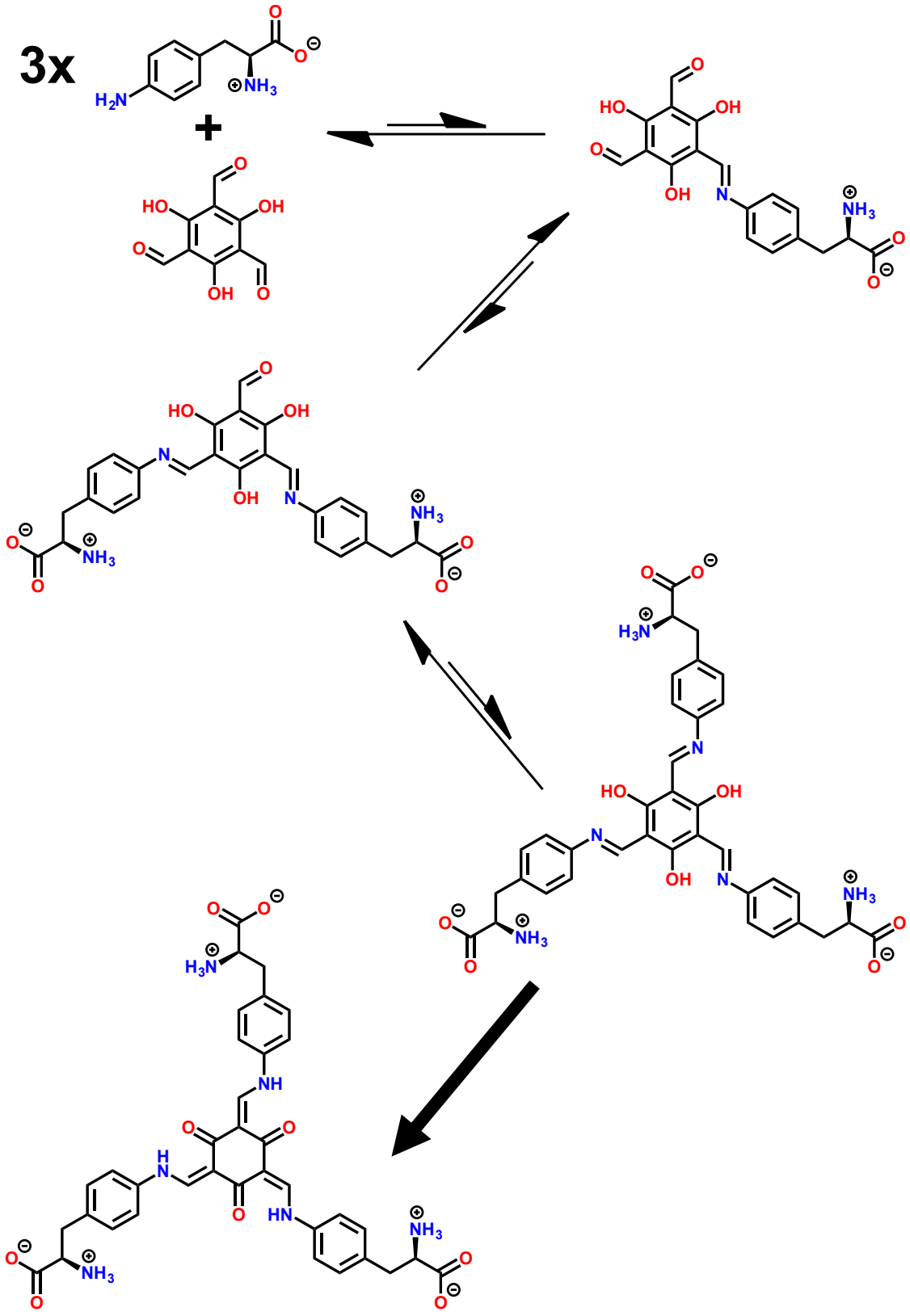

Figure 4.14. Reaction scheme for the formation of ***Z*** for ***4F*** and ***II*** with mono-, di- and tri- (enol and keto forms) reaction products shown as the proposed reaction pathway. Arrows indicate relative equilibriums, that arise because of the lack of stability of the imine species in water, between the species before the energetically irreversible enol to keto tautomerisation step.

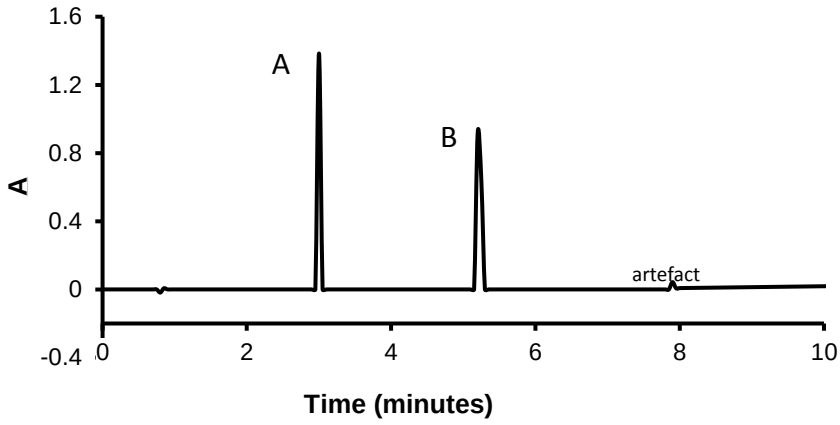

Figure 4.15. HPLC trace for the *in situ* reaction to form ***Z***. Peak A (retention time 3 minutes and 20 seconds) is associated with ***II*** and peak B (retention time 5 minutes and 15 seconds) is associated with the reaction product ***Z***.

In order to identify the chemical entity which is responsible for the A and B peaks, HPLC analysis was performed on both starting materials and an *ex situ* prepared sample of ***Z***. It was found that ***II*** had a retention time that corresponded to peak A, while ***Z*** had a retention time that corresponded to peak B. It is worth reiterating that these are the only two peaks observed in the HPLC trace despite there being the possibility for a number of products that result from incomplete reaction with regards to the trialdehyde core. This can be tentatively explained through the equilibriums that will exist between these partially reacted intermediates. Due the systems initial reliance on DC_vC chemistry in the form of imine chemistry, the first three products in the pathway to ***Z*** rely on a reversible reaction between two compounds (Figure 4.14). However, as none of these imine products are observed, the equilibrium must lie predominately in favour of the starting materials. This is a result of the imine hydrolysis driving the equilibrium towards the starting material and explains why the mono- and di- reacted imines are not observed.[18,19] This is also true of the tri- imine species, however, in the case of the tri- imine species, there is also the chance for the enol-imine to keto-emamine tautomerisation process to occur. This tautomerisation would yield the product, ***Z***, which lies in a significant energy well on the systems energy landscape. This effectively makes this tautomerisation process irreversible, trapping out ***Z***. This makes ***Z*** the only observable product, with none of the other possible reaction intermediates that have been discussed being observed.

With identification of the peaks in the HPLC trace being possible, the reaction progress can now be quantified. In order to do this, the molar extinction coefficient had to be determined for both ***II*** and ***Z*** in methanol, as this was the eluent used for the HPLC

analysis of the reaction. Solutions of both ***II*** and ***Z*** at a range of concentration were made up and the UV-vis spectra for each of these solutions were recorded. The results of these experiments for ***II*** and ***Z*** are shown in Figures 4.16 and 4.17, respectively. By using the Beer-Lambert law it was possible to determine the molar extinction coefficient for both species at a wavelength of 290 nm. With the molar extinction coefficient determined for ***II*** and ***Z*** it made it possible to quantify the concentrations of each at any given time in an *in situ* reaction mixture using HPLC and monitoring the absorbance at 290 nm.

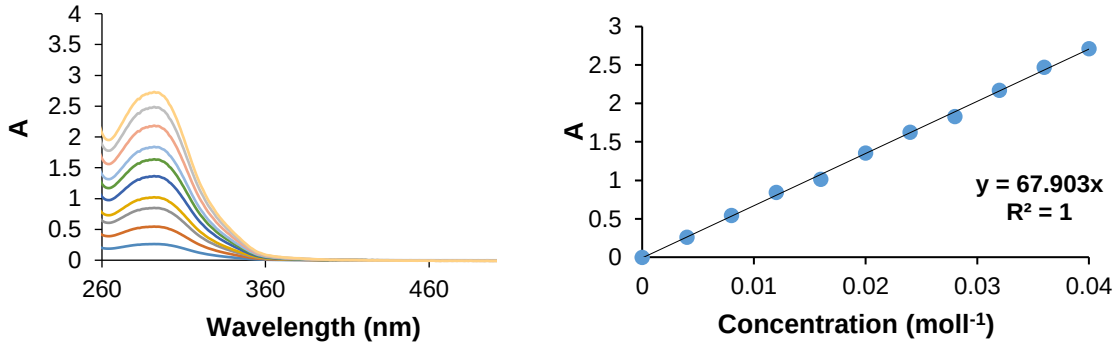

Figure 4.16. Concentration UV-vis absorption experiment for ***II*** using concentrations of: 4.0, 8.0, 12.0, 16.0, 20.0, 24.0, 28.0, 32.0, 36.0 and 40.0 mmol (left). Determination of molar absorptivity (ε) for ***II*** at 290 nm by plotting the absorption (AU) at 290 nm against each concentration. ε is defined as the slope of the straight line (67.9) (right).

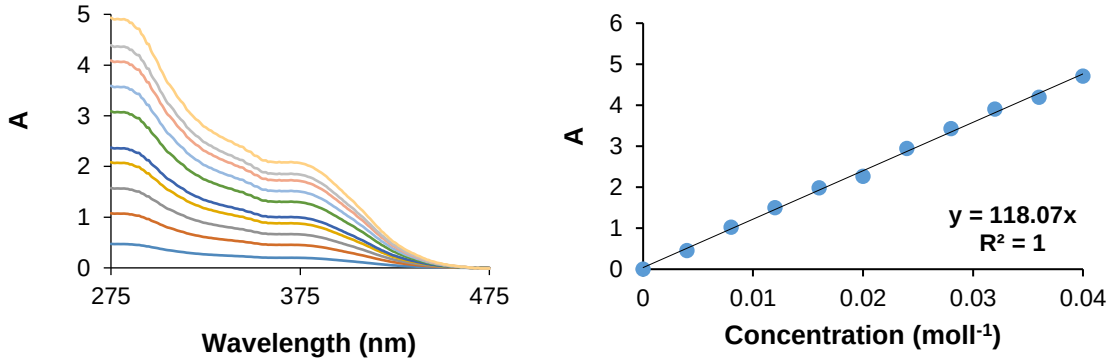

Figure 4.17. Concentration UV-vis absorption experiment for ***Z*** using concentrations of: 4.0, 8.0, 12.0, 16.0, 20.0, 24.0, 28.0, 32.0, 36.0 and 40.0 mmol of an *ex situ* prepared sample of ***Z*** (left). Determination of molar absorptivity (ε) for ***Z*** at 290 nm by plotting the absorption (AU) at 290 nm against each concentration. ε is defined as the slope of the straight line (118) (right).

4.6 Reaction Kinetics for standard conditions

For the purposes of this section, standard conditions are defined as the reaction occuring at 20 °C in a sealed vial that is kept completely stationary, i.e. with no form of external agitation. Through the use of HPLC and the determined molar extinction coefficients, it was possible to determine the actual concentrations of starting material and product in the reaction mixture at a number of different time intervals. In addition, through knowledge of the concentrations determined by HPLC, complementary techniques such as NMR, UV-Vis spectroscopy and rheology could be used to determine the reactions kinetics.

The concentration of ***Z*** at 30 minutes is approximately equal to the CGC of the gel set with ***Z*** when using an *ex situ* prepared sample of ***Z***. With this in mind the *in situ* reaction mixture was acidified after a reaction time of only 30 minutes. Despite the short reaction time, acidification (with GdL) did result in gelation. This low reaction time gel could be characterised from a rheological point of view. Through the frequency sweep experiment (Figure 4.18) the gelatinous nature of the material was confirmed. Despite having a very low *G′* of approximately 750 Pa the independent response of the material to the varying frequency showed the material to be a gel.

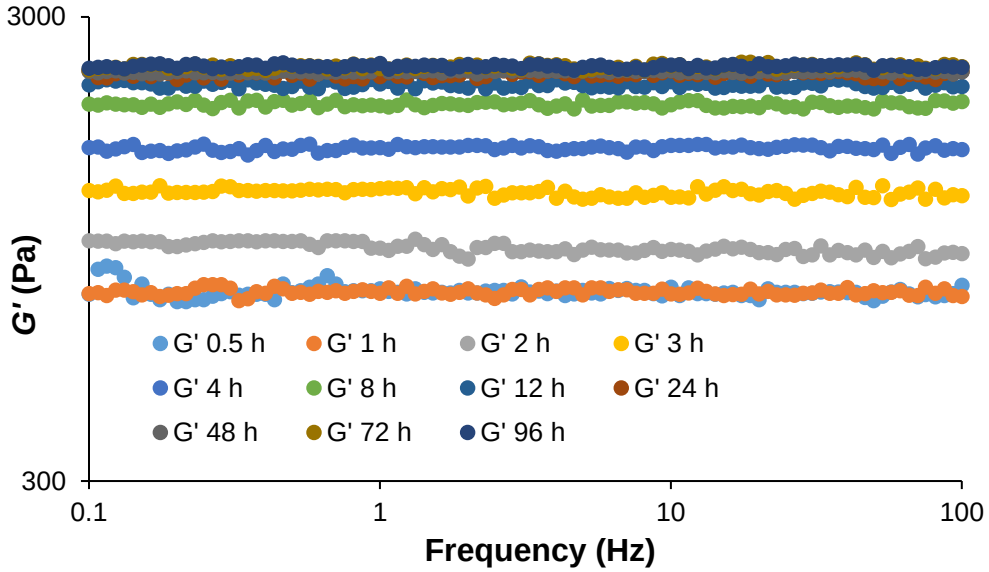

Figure 4.18. Frequency sweep experiments (G′ shown) for the gels resulting from the set using a 2 ml portion of a 25 ml stock solution with a potential maximum **Z** of 28.2 mmoll^{-1}.

With this experiment proving successful, portions of a stock *in situ* reaction mixture were acidified at a number of time intervals that mirrored those used for the HPLC analysis kinetic experiments. In all cases gelation of the sample was possible

through the addition of GdL, with rheology confirm the presence of a viscoelastic gel material with varying values of *G′*. As can be seen in Figure 4.18, there is a strong correlation between the *in situ* reaction time and the *G′* value of the resulting gels. After an initial incubation period, where there is no detectable increase in the *G′* value (at times less than 2 hours), there is a period of relatively rapid increase in the *G′* value for gels set at these corresponding times. This increase in *G′* continues until a time of 12 hours after the start of the *in situ* reaction process, at which point there is dramatic decrease in the rate that *G′* increases, effectively reaching a plateau after 24 hours at a value of approximately 2300 Pa.

Figure 4.19 demonstrates how *G′* varies as time progress, clearly showing the incubation period at the start of the sigmoidal plot profile. After this incubation period, the induction period begins were the rate of increase in *G′* reaches its maximum. Finally, the plateau region with no obvious change in the *G′* value is reached. The sigmoidal shape of this plot is a feature that is actually of significant importance. A sigmodal plot of concentration against time is strongly indicative of an autocatalytic process, which generally all feature periods of incubation, induction and plateau, when the starting materials have been completely consumed.

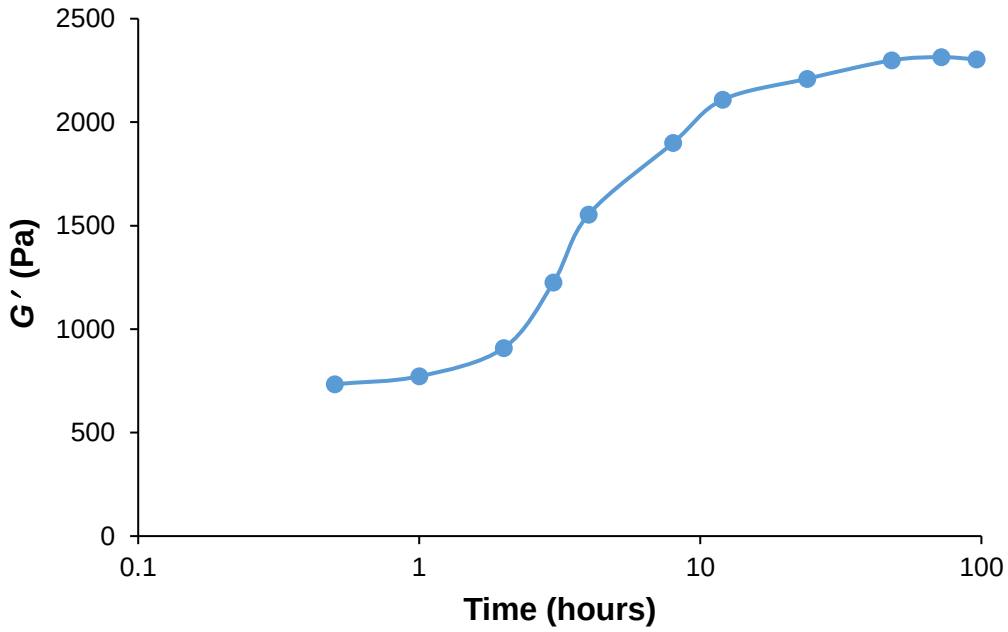

Figure 4.19. Graph showing the evolution of *G′* with time for gels set using portions of a stock *in situ* reaction mixture at times of 0.5, 1, 2, 3, 4, 8, 12, 24, 48, 72, 96 hours. Time on the x-axis is plotted using a log scale in order to highlight the sigmodal nature of the plot profile.

Of course, the G' value of a gel does not truly represent the concentration of its constituent LMWG. As the LMWGs concentration increases, then G' will also increase and the two values can be connected through the cellular solid model discussed previously. The cellular solid model predicts that $G' \propto [\text{gelator}]^n$ where G' is the elastic modulus of the gel and n can lie between 1 and 2. By looking at the concentration study performed previously and examining the gels responses to an applied oscillatory stress across a range of frequencies, the relationship $G' = 866[\boldsymbol{Z}]^{1.9}$ was obtained. This is clearly in good agreement with the model and will therefore allow the concentration of the gelator molecules to be calculated from the G' values recorded for the corresponding bulk gel materials. From the frequency sweep data obtained from gels set at different times from a single *in situ* reaction mixture, and the relationship $G' = 866[\boldsymbol{Z}]^{1.9}$, the plot that can be seen in Figure 4.20 could be obtained.

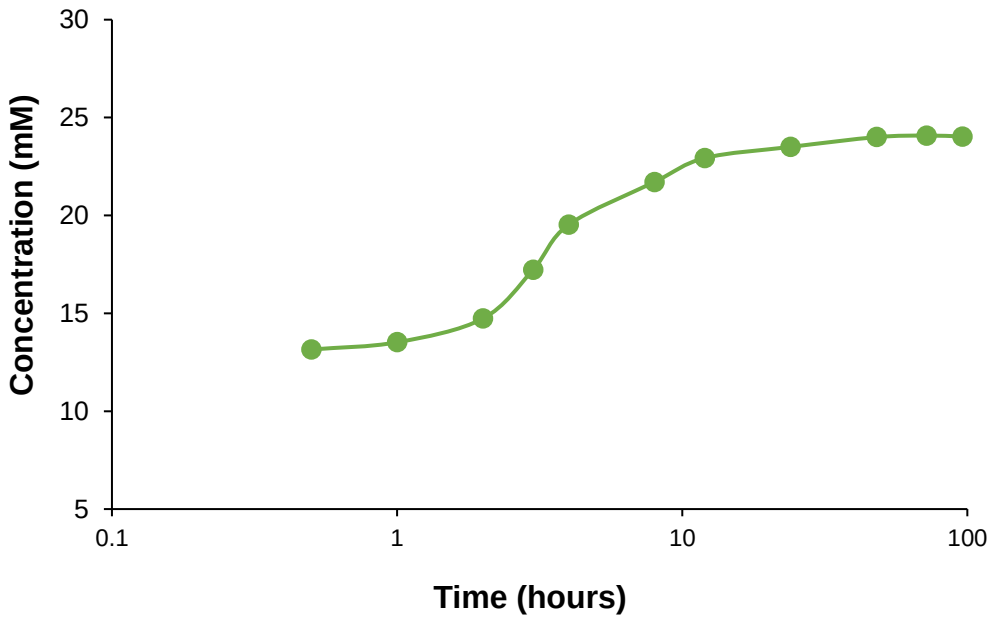

Figure 4.20. Concentration (in mM) of reaction product, ***Z***, monitored over time by rheology for the reaction **A** + $_4$**F** = ***Z***. calculated using the rheology data. Concentration (●) plotted against time (hours, log scale) with a line added between data points to guide the eye.

Crucially Figure 4.20, which shows how the concentration of ***Z*** evolves over time, clearly demonstrates the sigmodal profile for this type of plot. This *in situ* reaction is demonstrating the characteristics of a reaction that proceeds with an autocatalytic process, where ***Z*** acts as the replicator species. As well as the sigmodal profile for

product/replicator concentration over time, it also possible to get an idea of autocatalysis through examination of how the rate of reaction changes over time. As an autocatalytic reaction proceeds there should be an acceleration in the rate of reaction until the reaction starting materials reach a critical concentration. Once this concentration is reached the reaction rate will continuously decrease until all the starting materials are exhausted. This should give rise to a bell-shaped plot. Using the concentration values for each given time measurement as displayed in Figure 4.20, it was possible to calculate the rate of reaction over time, with Figure 4.21 providing a plot of this calculated reaction rate data.

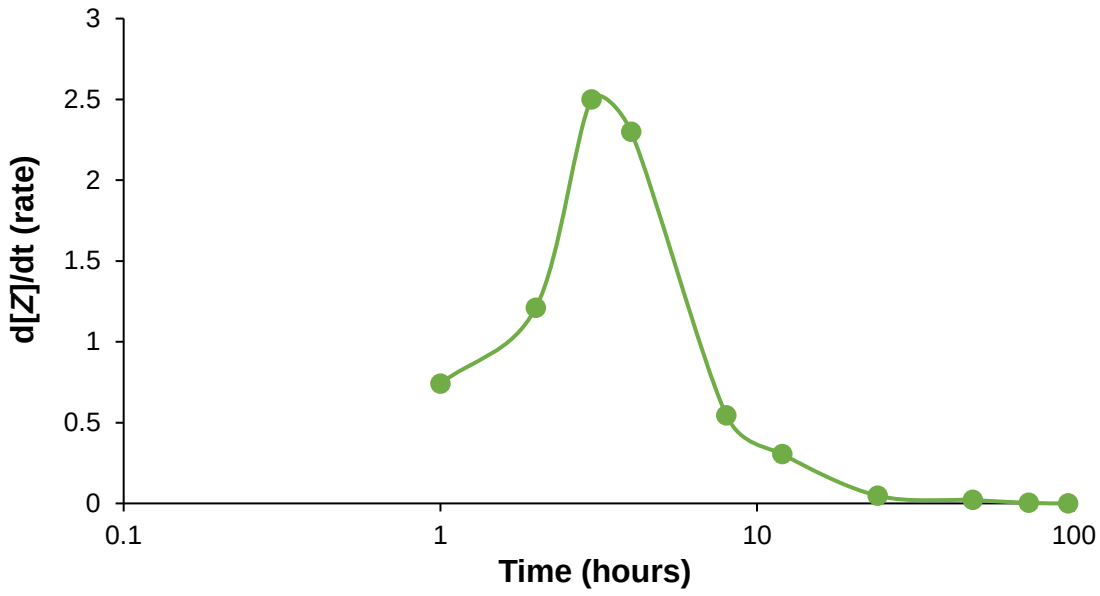

Figure 4.21. The rate of reaction of **A** + $_4$**F** = ***Z*** calculated using the previously determined concentration from the by rheology against time (hours, log scale) with a line added between data points to guide the eye.

Figure 4.21 does indeed clearly show the bell shape plot profile for reaction rate (d[***Z***]/dt) against time that would be expected for an autocatalytic process. From this plot it can be seen that the reaction rate peaks between three and four hours, before rapidly decreasing from four to 24 hours, with reaction rate effectively 0 after 24 hours. This relationship between the mechanical properties of a supramolecular material and the chemical reactivity involved in the *in situ* formation of the individual supramolecular building blocks is an interesting unique calculation of this system. The following results help to convey how accurate this methodology of linking rheology to concentration through the cellular model is.

As discussed in the previous section 4.5, HPLC has proven a valuable technique in the characterisation of this system. It has revealed that there are no "intermediate" mono- and di- reacted species or any enol reaction products. The calculated concentrations could be plotted in a similar manner to those that were calculated from the rheological data. Again the sigmoidal plot profile could be observed (Figure 4.22) and with HPLC being a more established technique for monitoring the progress of autocatalytic/self-replicating systems,[20,21] it provided confirmation of the autocatalytic properties of the molecules of ***Z***.

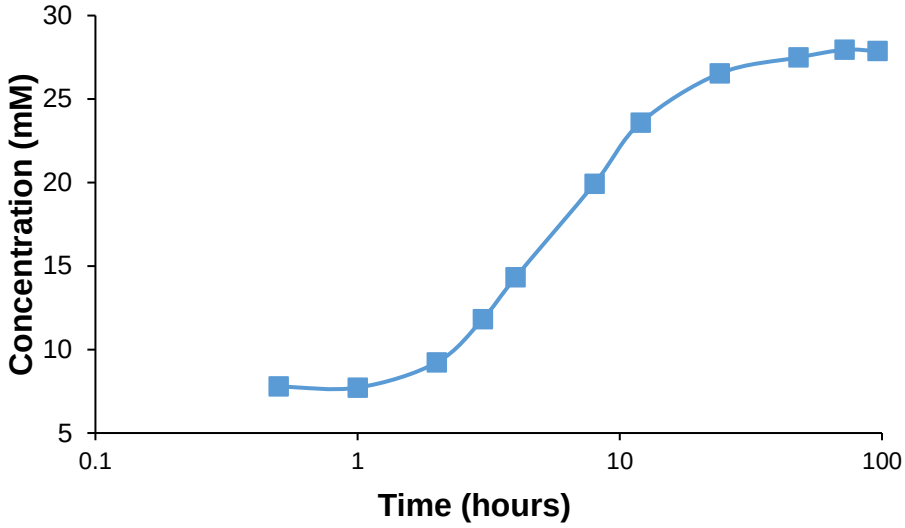

Figure 4.22. Concentration (in mM) of reaction product, ***Z***, monitored over time by HPLC for the reaction **A** + $_4$**F** = ***Z***. calculated using the previously determined molar absorption coefficients against time (hours, log scale) with a line added between data points to guide the eye.

There are several key features to note in the differences between the HPLC and rheology data. Noticeably when comparing the concentrations recorded in Figures 4.20 and 4.22, we can see that there are a number of differences in the plots. While the data obtained using HPLC reports a final concentration of 28 mM, a value that matches the theoretical maximum concentration of ***Z*** achievable based on the starting concentration of ***II***, the rheology is limited at 25 mM. It should be noted that the cellular solid model, while offering a good fit to the data, does not offer a perfect match between the theory and the experimental data, due to the CGC limit and the addition of the GdL. GdL provides acid conditions, and this is known to catalyse imine formation. This provides a systematic error to the rheology data that is not easily accounted for accurately. In addition, the cellular solid model normally only applies over a small range of

concentrations, rather than the full range that could be utilised with this system. Saying this, the close relationship between the rheology determined concentrations and standard analytical data is of interest.

4.7 Reaction Kinetics for mechanical agitation

An interesting observation of the *in situ* reaction solution was that there was a very obvious thickening of the reaction solution from the start to the end of the reaction. This increase in viscosity was not something that was necessarily expected, although it was possible to suggest reasons for it occurring.

It can be argued that supramolecular hydrogels are closely related to another type of supramolecular assembly, namely, supramolecular polymers. Supramolecular polymers are polymers in which the individual monomer building blocks are connected through physical interactions[22–24] (hydrogen bonding, π-π stacking or any other supramolecular interaction) as opposed to traditional polymers, where the monomer units are chemical bonded to one another. Supramolecular polymerisation often occurs in solution, with many examples occurring in an aqueous environment.[25,22] The formation of supramolecular polymers in solution is often accompanied by an increase in viscosity, something that can be correlated to the concentration of the monomer units and the resulting polymers.[26] This concept, could be thought of as the reason for the apparent increase in viscosity over time for the *in situ* reaction solution for the system discussed in this chapter.

In order to quantify the viscosity of the solution, various solutions were made up using *ex situ* synthesised samples of ***Z*** at different concentrations. The *ex situ* ***Z*** was dissolved with the addition of NaOH, once ***Z*** had fully dissolved, additional NaOH was added in order to keep the pH consistent with that of the *in situ* reaction mixture. The viscosity of these samples was then measured across a range of temperatures, from 5 – 50 ^{o}C. The results of these experiments can be seen in Figure 4.23. In addition to the solubilised samples of ***Z***, the viscosity of water was also measured so it could be used as a means of comparison. It is clear to see that dissolving ***Z*** in water results in an increase in the viscosity of the solution. The most crucial demonstration of this is the example were ***Z*** was dissolved at a concentration below its CGC. This sub-CGC concentration of 0.25 wt%, 3.59 mmolL^{-1} demonstrates that despite the concentration of the LMWG being insufficient to produce a fibrous network with a density sufficient to completely immobilise the solvent, it can still have a measurable impact on the physical properties

of the reaction solution. Once the concentration of ***Z*** reaches, and exceeds the CGC, there is a clear change in the nature of the solutions viscosity when compared to that of water and the solution below the CGC value. From temperatures of 5 to approximately 30 ^{o}C the viscosity of these solutions above the CGC remains very constant, with temperature appearing to have little or no effect on the viscosity. However, once the temperature exceeds 30 ^{o}C there is a rapid and dramatic decrease in the viscosity of the solutions.

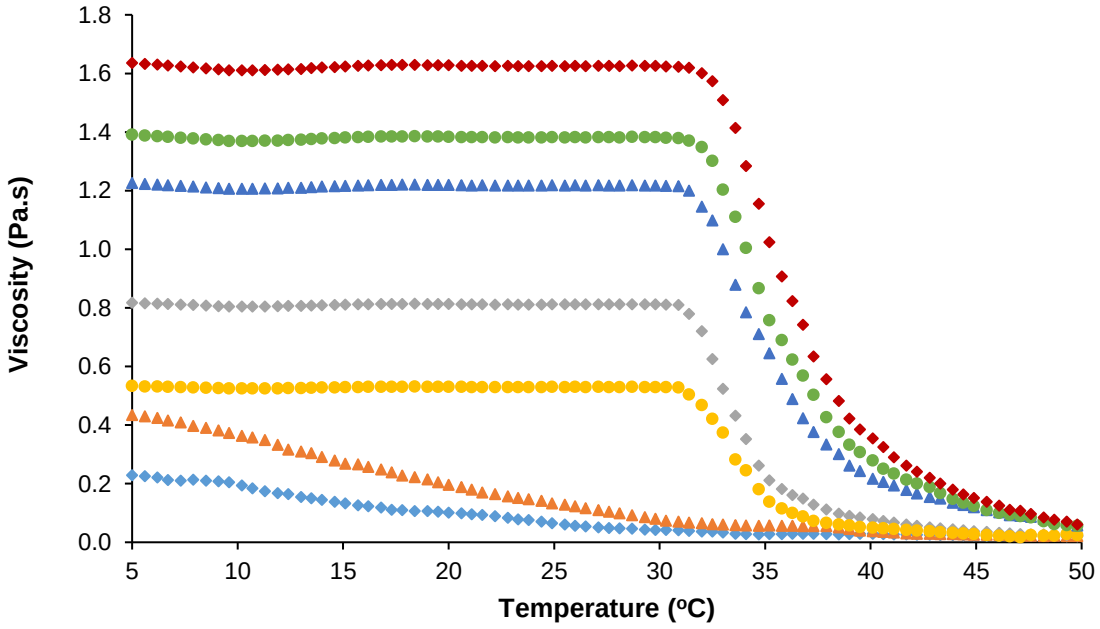

Figure 4.23. Measurements of the viscosity of various concentrations of solubilised samples of ***Z*** at pH 8.5 with increasing temperature: water (light blue ◆), 0.25 wt%, 3.59 mmol, below CGC (orange ▲), 0.5 wt%, 7.18 mmol at CGC (yellow ●), 1 wt% 14.36 mmol (grey ◆), 2 wt%, 28.72 mmol (dark blue ▲), 3 wt%, 43.08 mmol (green ●), 4 wt% 57.44 mmol (red ◆).

The idea that the viscosity of water can be enhanced by increasing the concentrations of ***Z*** and the fact that this new relatively high viscosity can be drastically reduced through heating the solution can be explained through the presence of supramolecular polymers. At low temperatures, i.e. under 30 ^{o}C, the deprotonated molecules of ***Z*** can form supramolecular polymers through face-to-face stacking driven by π-π interactions and hydrophobic effects (Figure 4.24). This aggregation is similar to what results in the fibre formation observed in the gel state, however, because these molecules are sufficiently charged, due to the basic conditions, they stay dispersed in solution in the form of supramolecular polymers.

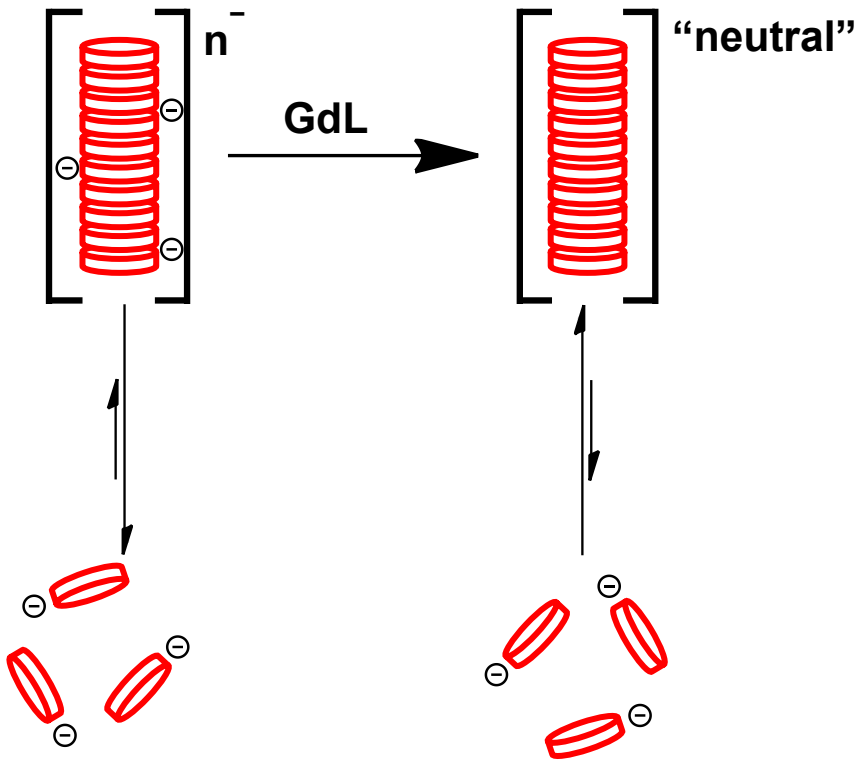

Figure 4.24. Pictorial representation of the dynamics that exist between the supramolecular polymer, the gel network and the free molecules. Protonation of the supramolecular polymers balances the charge resulting in a reduction in solubility and gelation.

Heating the solution while measuring the viscosity results in degradation of the supramolecular polymers structure. This occurs through the effects of increasing Brownian motion within the solution perturbing the larger polymer[27] but also and more importantly, the heating providing the energy required to overcome the supramolecular interactions between molecules of ***Z***. This results in dissociation of the polymer, changing the polymer into much smaller units with the potential for isolated, and therefore the formation of individual molecules of ***Z*** in solution. These viscosity experiments give an insight into the behaviour of ***Z*** in solution and the tendency of the molecules to aggregate even when fully solubilised. The presence of supramolecular polymers before the gel sets is a key aspect of the autocatalytic cycle, and therefore it is something that was subjected to further investigations.

The field of supramolecular polymers has received much attention in recent years with a number of exciting, chemically diverse systems with interesting potential applications.[28,29,23] Investigations into systems that not only self-replicate but also exhibit some form of supramolecular assembly have been previously presented. Crucially they have demonstrated how the structure and length of self-synthesising supramolecular

polymers can be controlled through two process, one being nucleated growth and the other being disassembly.[20] This involves controlling the length of the supramolecular polymers, where the monomer units may be self-replicating, through chemical or mechanical means. This concept of mechanical control of polymer growth and self-replication was highlight in a previous paper where the Otto group demonstrated exponential self-replication through a fibre elongation and breaking mechanism.[30] Here they subjected a reaction mixture that contained a self-replicator that had a tendency to form supramolecular polymers to mild agitation. This mechanical agitation resulted in a breaking of the polymer fibres, this liberated more chain ends, the active sight for the template driven autocatalytic process (see Figure 4.25). Due to the increase in the number of catalytic sites, the rate of reaction increases demonstrating an exponential increase in replicator concentration.

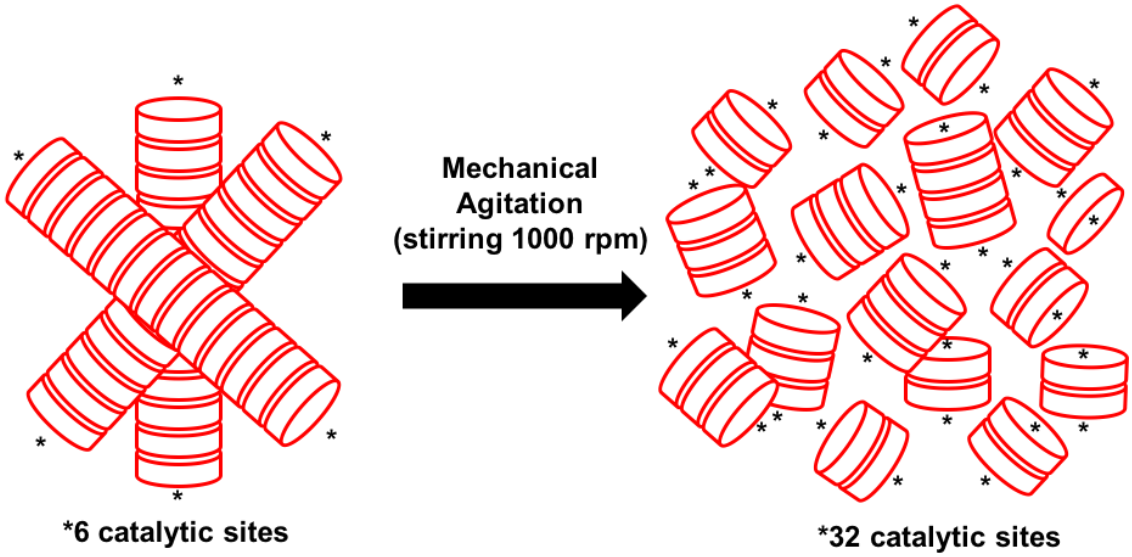

Figure 4.25. Pictorial representation of the effects of mechanical agitation on the supramolecular fibres formed in aqueous conditions (20 °C without mechanical agitation) by the anionic species $\mathbf{C^{n-}}$ and the subsequent increase in the number of catalytic sites.

This concept of applying an external mechanical agitation to the reaction solution in which the autocatalytic process is occurring, albeit potentially inhibited by the formation of supramolecular polymers, is an idea that could be applied to the *in situ* synthesis of ***Z***.[31,32] With this in mind, a reaction was performed of the *in situ* synthesis of ***Z*** was setup with the standard conditions outlined previously. The difference being on this occasion a stirrer bar was added to the reaction solution with stirring being performed at 1000 rpm for the duration of the reaction. The reaction was deemed to have reached

completion upon arrival at the plateau region of the concentration vs time plot, where hopefully a concentration of ***Z*** close to the theoretical maximum had been achieved. The concentration of ***Z*** could be determined as previously discussed using rheology and the cellular solid model, HPLC, UV-Vis and ^{1}H NMR.[33,34] The rheology part of this analysis can be seen in Figure 4.26. It is very apparent that while the gel reaches a comparable *G′* it does so in a much shorter time scale. With *G′* reaching approximately 2400 Pa at a time between 8 and 12 hours when compared to the same reaction without stirring (*G′* approximately 2400 Pa between 24 and 48 hours). This represents a significant decrease in the time required for the maximum *G′*, which as outlined previously, should represent a decrease in the amount of time taken for the maximum theoretical concentration of ***Z*** to be reached. Again through use of the rheology data (Figure 4.26) and the cellular solid model, a plot of ***Z*** concentration over time could be produced (Figure 4.27).

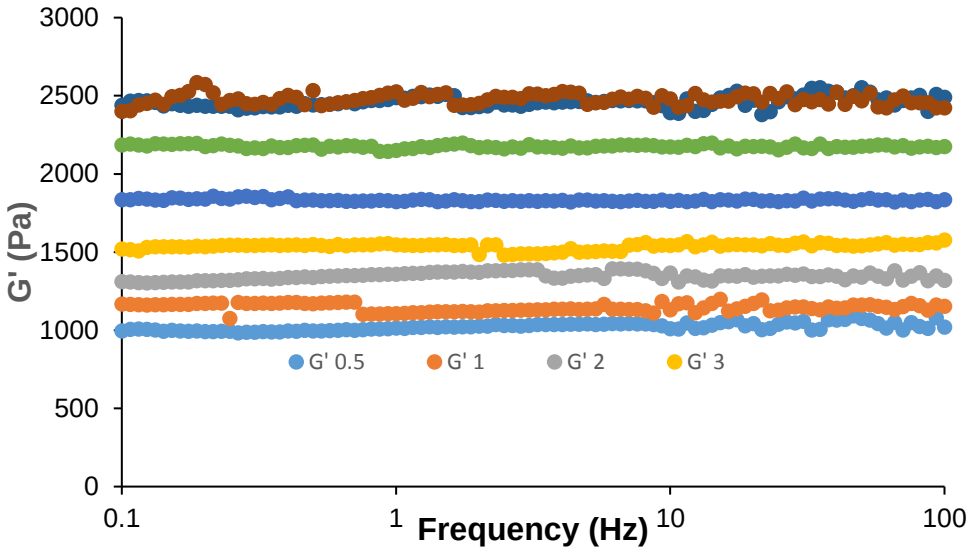

Figure 4.26. Frequency sweep experiments (G′ shown) for the gels resulting from the set using a 2 ml portion of a 25 ml stock solution with a potential maximum **C** of 28.2 mmoll^{-1} which was subjected to continuous mechanical agitation in the form of magnetic stirring at 1000 rpm.

When examining the concentration of ***Z*** in the *in situ* reaction, performed with the addition of mechanical agitation, the rheological method outlined previously could be used. When this data is plotted in the same manner as in Figure 4.20, a sigmodal shape associated with autocatalysis of the plot for concentration against time can be observed. The gradient of the curve is less pronounced but it is still clear that the system exhibits a period of incubation, induction and plateau, as shown in Figure 4.27. Of course, these concentrations of ***Z*** can then be used to calculated the rate at which it forms, with a plot

of reaction rate for the formation of ***Z*** again demonstrating a typical autocatalytic bell-shaped plot profile (Figure 4.28).

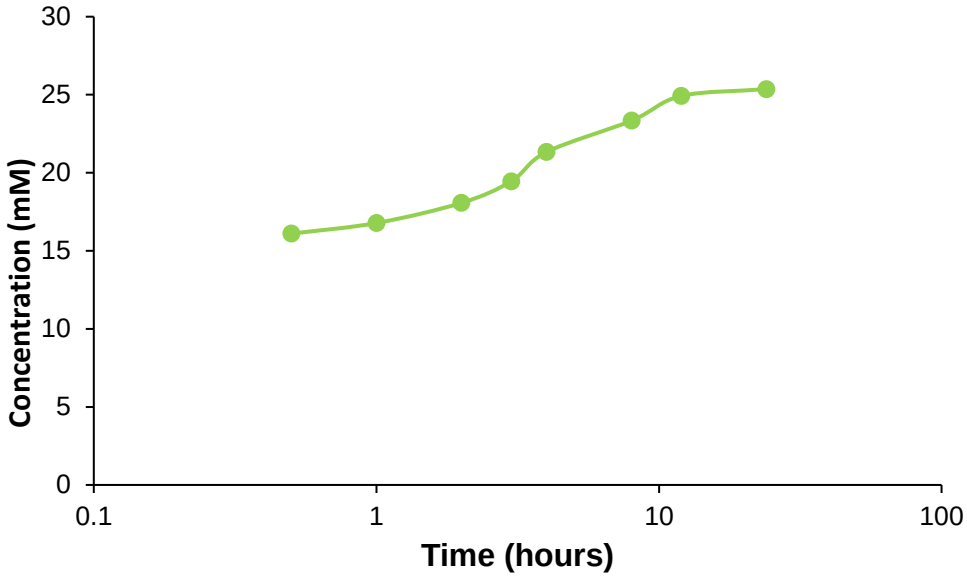

Figure 4.27. Concentration (in mM) of reaction product ***Z*** formed under standard conditions with the addition of magnetic stirring at 1000 rpm, monitored by using frequency sweep rheological experiments and calculated using the cellular solid model. Concentration plotted against time (hours, log scale) with a line added between data points to guide the eye.

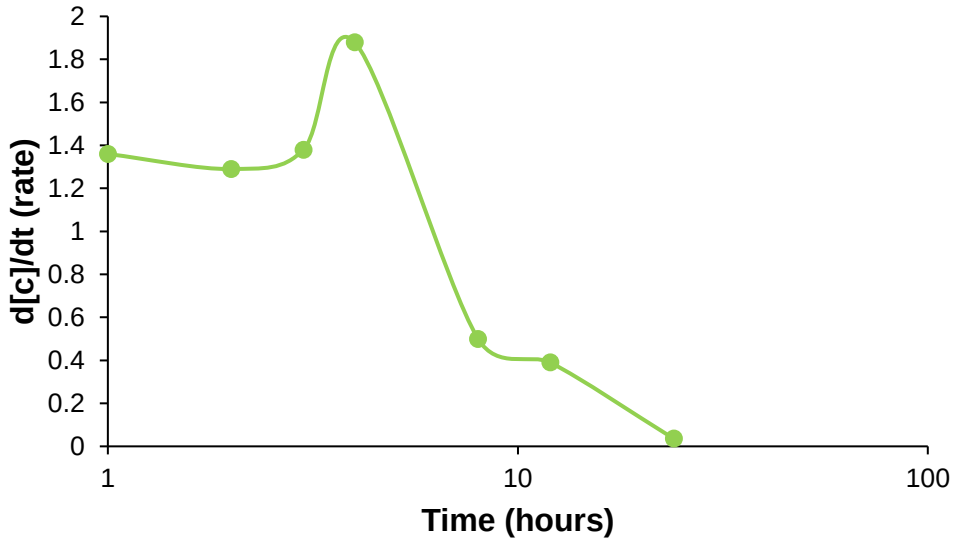

Figure 4.28. The rate of reaction for the formation of ***Z*** calculated using the previously determined concentration from the rheology (green ●), against time (hours, log scale), with a line added between data points to guide the eye.

While the plot of concentration against time showed a sigmodal plot and the plot of reaction rate against time gives a bell shaped plot, it would be difficult to claim with any integrity that either of these shapes are ideal. Of course, this approach of using rheology to determine the concentration of ***Z*** has the disadvantage of having to go through the cellular solid model and as a result means the concentration of ***Z*** is not directly observed. Also, and perhaps more crucially, the acidification of the *in situ* reaction solution through the addition of GdL has the potential to drastically alter the rate at which ***Z*** is formed due to the fact imine formation can be acid catalysed.[35] Both these factors have the potential to play a significant role in reaction rate. While the kinetic data obtained from the rheological measurements of the resulting gel is a significant point of interest, it must be consider along with additional studies of reaction kinetics preformed with different techniques. Like the previously presented example that does not feature any mechanical agitation, the concentration of ***Z*** could be determined by HPLC and ^{1}H NMR. The concentration data for ***Z*** determined by these techniques can be seen in Figure 4.29. The data in Figure 4.29 has a number of noteworthy features. There is a strong correlation between the data produced from the HPLC and ^{1}H NMR data. It shows an excellent agreement in terms of the concentration at any given time.

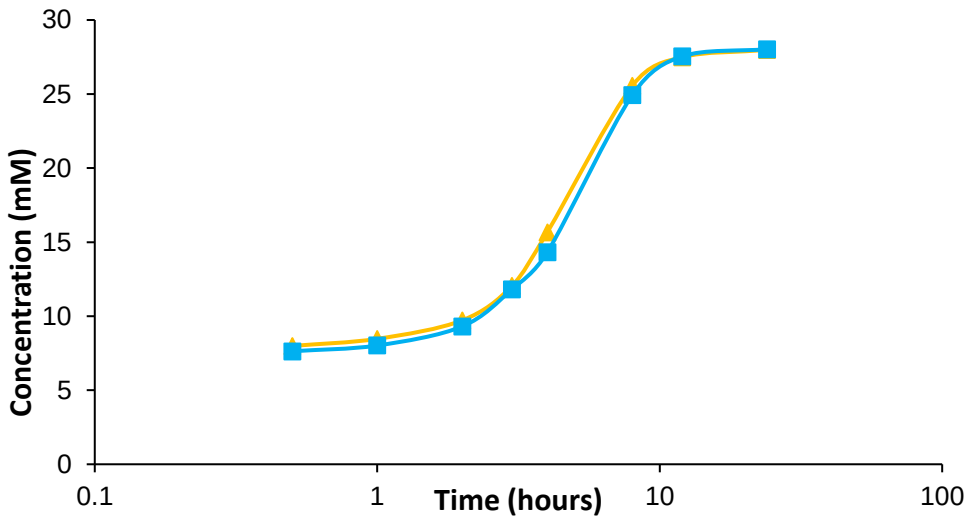

Figure 4.29. Concentration (in mM) of reaction product Z formed under standard conditions with the addition of magnetic stirring at 1000 rpm,. monitored over time by 1H NMR (yellow ▲) and HPLC (blue ■) against time (hours, log scale), with a line added between data points to guide the eye.

Both data sets show the beginning of the induction period beginning almost immediately (with very little incubation time), significantly quicker than the 1 – 2 hours

it takes for the induction period to begin when the *in situ* reaction is performed without the mechanical agitation. This effective removal of the incubation time results in the maximum concentration of ***Z*** being reached quicker. With mechanical agitation the ***Z*** concentrations reaches its maximum (28 $mmolL^{-1}$) and plateaus in 8 – 12 hours, compared to the 24 – 48 hour timescale without agitation. When the temporal concentration data obtained using HPLC and ^{1}H NMR is compared to that of the data determined through rheology, it is easy to see the difference in the values (Figure 4.30). The initial concentration of ***Z*** determined using the rheology method is significantly higher than the value determined by HPLC and ^{1}H NMR. This can be explained by previously discussed acid catalysed imine formation and that a CGC must be achieved to observe any formation of gel.

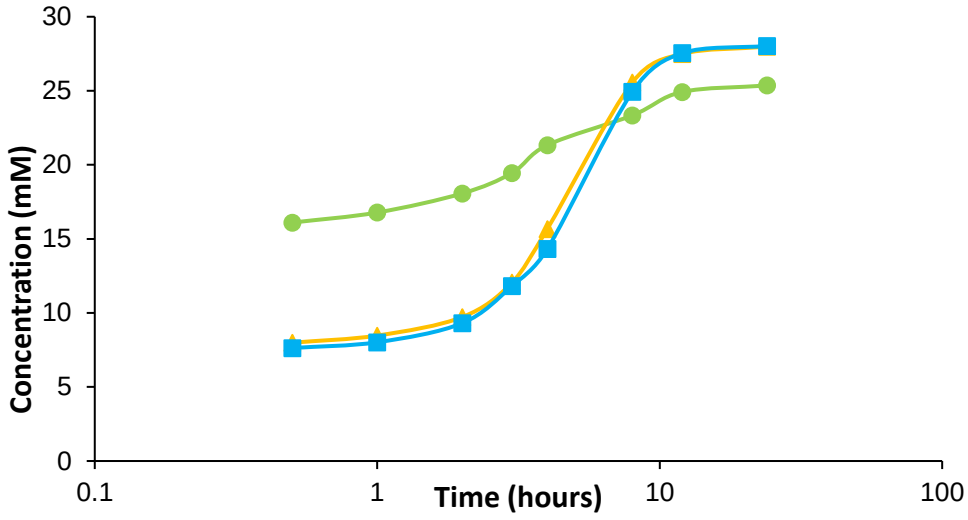

Figure 4.30. Concentration (in mM) of reaction product ***Z*** formed under standard conditions with the addition of magnetic stirring at 1000 rpm. Monitored over time by rheology (green ●), ^{1}H NMR (yellow ▲) and HPLC (blue ■) against time (hours, log scale) with a line added between data points to guide the eye.

The formation of supramolecular polymers during the *in situ* formation of ***Z***, while not expected always expected, was not entirely surprising when the nature of the deprotonated form of ***Z*** is considered. It has solubilising charged groups at the very ends of the arm units with the core remaining relatively hydrophobic, this charge distribution is likely to drive the face-to-face stacking that results in the formation of the supramolecular polymers. The presence of the polymer fibres can be demonstrated through the increase in the viscosity of the solution depending on the quantity of ***Z*** that

has be dissolved. With increasing ***Z*** concentrations clearly demonstrating an increase in the measured viscosity of the solution. By measuring the viscosity over a temperature range it is clear to see the point at which the polymers begin to break up and dissociate into smaller, lower order structures or monomer (individual ***Z***) units. The existence of supramolecular polymers inspired the use of continuous mechanical agitation of the reaction solution. This was theorised to break up the polymer fibres, increase the number of templating catalytic sites, which would in turn increase the rate of reaction for the formation of the self-replicator ***Z***. This theory proved accurate and with mechanical agitation the time taken for the maximum concentration of ***Z*** to be reached decreased dramatically. This resulted in the ability to set a gel with the highest possible *G´* value, for a given concentration of ***Z***, quicker using the *in situ* reaction methodology.

With this data for the evolution of the concentration of ***Z*** over time it was possible to calculate the rates of ***Z*** formation when the *in situ* reaction mixture is subjected to mechanical agitation. This rate data was calculated for the concentrations determined using HPLC and ^{1}H NMR, and compared to the previously calculated rates from the rheology data (Figure 4.31).

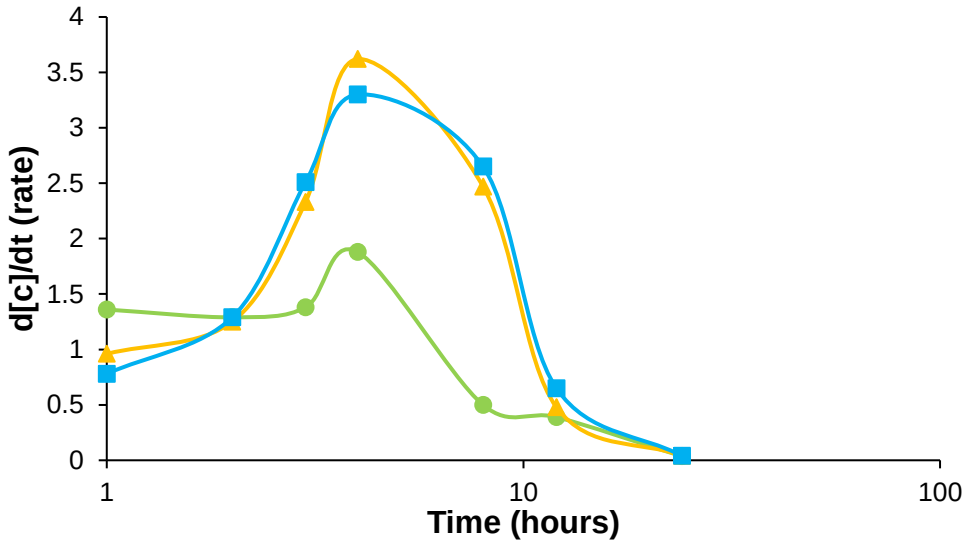

Figure 4.31. The rate of reaction for the formation of ***Z***$^{-}$ calculated using the previously determined concentration from rheology (green ●), ^{1}H NMR (yellow ▲) and HPLC (blue ■) against time (hours, log scale), with a line added between data points to guide the eye.

The data presented in Figure 4.31 shows the bell shape that is indicative of an autocatalytic process. The plots obtained using HPLC and ^{1}H NMR are very similar in shape with the peak rate being achieved at around 4 hours. This 4 hour time scale to reach the highest reaction rate is actually very similar to the time taken to reach the maximum

reaction rate when the reaction is allowed to proceed under standard conditions without mechanical agitation. The difference between the two experiments is that, without mechanical agitation, the maximum calculated reaction rate is 2.6 - 2.7 $mmolh^{-1}$. This value is significantly lower than the rate calculated at the same time for the *in situ* reaction that is subjected to mechanical agitation 3.3 – 3.6 $mmolh^{-1}$. This higher rate of reaction allows the maximum concentration of ***Z*** to be reached much quicker with mechanical agitation than without. This rate results in a concentration of ***Z*** of 28.0 mM (which matches the maximum theoretical concentration determined by the initial concentration of ***II***) being achieved after 12 hours. This shows that despite the aggregation, the autocatalysis is not switched off or inhibited, i.e. even without stirring there is dynamics within the polymer.

It is also very clear that the rates calculated from the rheology data are significantly lower than those determined with HPLC or ^{1}H NMR. This is not surprising considering that the final concentration of ***Z*** determined by the rheology experiments is only 25 mM and this concentration was determined after 24 hours. This discrepancy does further highlight the limitations of the rheological method of concentration determination. Despite these limitations and apparent inaccuracies in the results, it is still interesting to see that chemical kinetic data can be obtained from the material properties of a supramolecular gel. While this technique does offer a means of conveniently extracting chemical kinetic data from a set gel, the fit of the data is not perfect. It would be desirable to develop a concentration:rheology relationship model, other than that used to describe cellular solids, in an effort to produce a better fitting data set. Using rheological data and such a model to extract chemical kinetic data does come with a number of caveats. As far as analytical techniques go, rheology data has relatively large errors associated with it. Also there may be examples of gels where concentration is not always directed linked to elasticity. This could be the result of kinetic vs thermodynamic gel products and the different supramolecular assemblies associated with them.

4.8 Seeding of the *in situ* reaction

The data obtained so far for the formation of ***Z*** using the *in situ* reaction method confirms the reaction is autocatalytic regardless of whether mechanical agitation of the reaction solution is employed or not. The mechanism that induces the self-replication of ***Z*** is likely to involve templating between either of the faces of the individual ***Z*** molecule and the starting materials. For the purpose of this work autocatalysis can be divided into two

types; ideal (exponential growth in replicator concentration) and non-ideal (parabolic growth in replicator concentration).[36] Exponential growth in replicator concentration with a template driven system arises from the system operating at peak efficiency. The failure of a newly formed replicator molecule to dissociate from the molecule that resulted in its formation. This effectively poisons the catalyst and reduces the efficiency of the system. If this is the case, the system will exhibit parabolic growth in replicator concentration.

In systems such as this where there is no replicator destruction, in this case due to the enol to keto tautomerisation, the rate law for self-replication can be written as:

$$\frac{d[\boldsymbol{Z}]}{dt} = k_{\boldsymbol{Z}}[\boldsymbol{II}]^f[\boldsymbol{Z}]^p \quad \textbf{[equation 4.1]}$$

The order of the replicator, *p*, can be determined by considering equation 4.1 re-written in a different form, this re-written form equation 4.2 highlights a number of key considerations and approximations that can be made when dealing with an autocatalytic system of this nature.

$$log\frac{d[\boldsymbol{Z}]}{dt} = logk_{\boldsymbol{z}} + f\ log[\boldsymbol{II}] + p\ log[\boldsymbol{Z}] \quad \textbf{[equation 4.2]}$$

During the initial stages of the replicator production, the concentrations of the starting materials, ***II*** can be considered as being constant. This means that the term $logk_{\boldsymbol{Z}} + f\ log[\boldsymbol{II}]$ is a constant. It is worth noting here that the concentration of $_4\boldsymbol{F}$ used is so relatively large as to induce pseudo first-order conditions When developing a method to determine the order of the replicator, *r*, the work of von Kiedrowski proved very insightful. His work determined the order of replication, in this case *p*, could be determined from the slope of a plot of the initial rate of replication ($\log \mathrm{d}[\boldsymbol{Z}]/\mathrm{dt}$) against $\log[\boldsymbol{Z}]$.[37,38] Such a plot could be created through performing a series of seeding experiments where the replicator, ***Z***, is added to *in situ* reaction mixture at the start of the reaction at a variety of concentrations.

In order to investigated the effects of seeding a number of reactions were performed with a Varity of seed concentrations. A high purity *ex situ* synthesis sample of ***Z*** was used in the seeding of the *in situ* reactions.

Five seeded experiments were performed with various concentrations of the *ex situ* synthesised ***Z*** (0.5, 1.0, 1.5, 2.0, 2.5 mM) (Figure 4.32) added at the initial mixing of the starting materials. The concentration of ***II*** was adjusted so that the final concentration

of ***Z*** at the end of the reaction time was equal to 28.0 mM (this value includes concentration of the seed ***Z*** i.e. 26.0 mM of ***II*** and 2.0 mM of ***Z***).

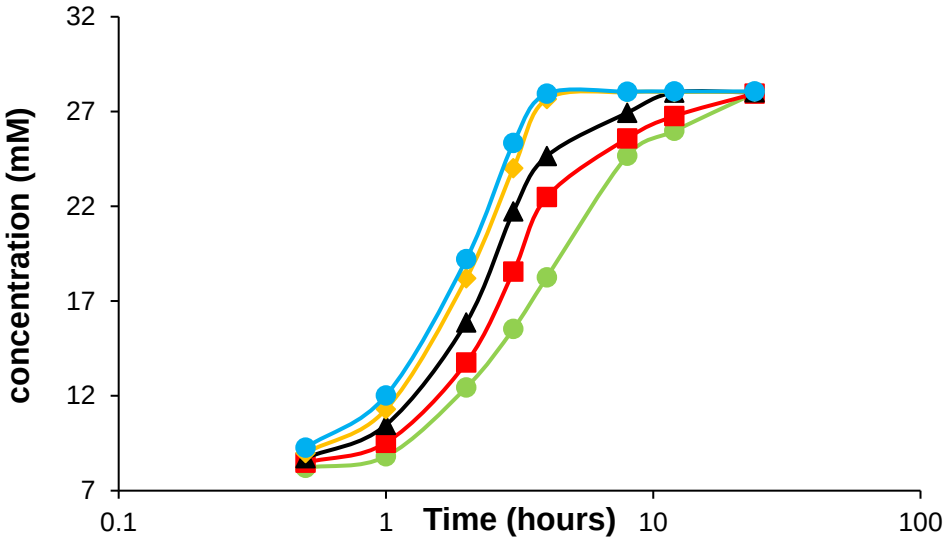

Figure 4.32. Total concentration of ***Z*** formed over time with different quantities of $\mathbf{C}^{n-}$ added as a seed at time 0 h. $\mathbf{C}_{catalyst}$ = 0.5 mM (green ●), $\mathbf{C}_{catalyst}$ = 1.0 mM (red ■), $\mathbf{C}_{catalyst}$ = 1.5 mM (black ▲), $\mathbf{C}_{catalyst}$ = 2.0 mM (yellow ◆) and $\mathbf{C}_{catalyst}$ = 2.5 mM (blue ●).

$$\%\ conversion = \frac{((conc_{time1.0h} - conc_{time0.5h}) - conc_{.seed})}{theoretical\ maximum\ conc.} \times 100 \quad \textbf{[equation 4.3]}$$

This adjustment was made so that comparisons could be made, particular in terms of the rheological measurements of any gels that were set could be made between the *in situ* reactions done at standard conditions, standard conditions with mechanical agitation and standard conditions with the addition of seed molecules. Figure 4.32 demonstrates the significance of adding seed molecules, at the highest concentration of seed ***Z*** used, 2.5 mM, the reaction reaches the plateau after only 4 hours which represents the maximum concentration of ***Z*** being achieved. The system does follow the expected trend of increased seed concentration resulting in a decrease in the reaction time. The effects of the addition of seed molecules becomes apparent even in the initial stages with measurements between 0.5 and 1 hour showing a 7.7 times percentage increase in ***Z*** concentration when comparing seed concentrations at 0.5 mM (green ●) and 2.5 mM (blue ●). This value takes into account the additional ***Z*** added at the start of the reaction was calculated using equation 4.3. The most noticeable difference in the measurements for the 0.5 and 2.5 mM seed concentrations occur at 4 hours with the ***Z*** concentration in the experiment performed with the 2.5 mM seed concentration 35.0 % higher when compared with experiment performed with a seed concentration of 0.5 mM.

As with the previous experiments, the rate of formation of ***Z*** could be calculated from the concentration data determined by HPLC. By comparing the variation rates of formation of ***Z*** for the different concentrations of seed, it is possible to gain an understanding of the evolution of the reaction over time. The reaction rates determined for the seed concentration 2.5 mM and 2.0 mM follow a similar plot profile with the maximum rate of reaction occurring between 2 and 3 hours. As can be seen in Figure 4.33 The 2.0 mM (yellow ◆) seed experiment shows an expected higher reaction rate going from 4 to 8 hours. The experiment with the lowest seed concentration (0.5 mM) exhibited a much more linear plot profile with the bell shaped plot profile being significantly less pronounced than with more heavily seeded experiments or indeed the mechanical agitated example.

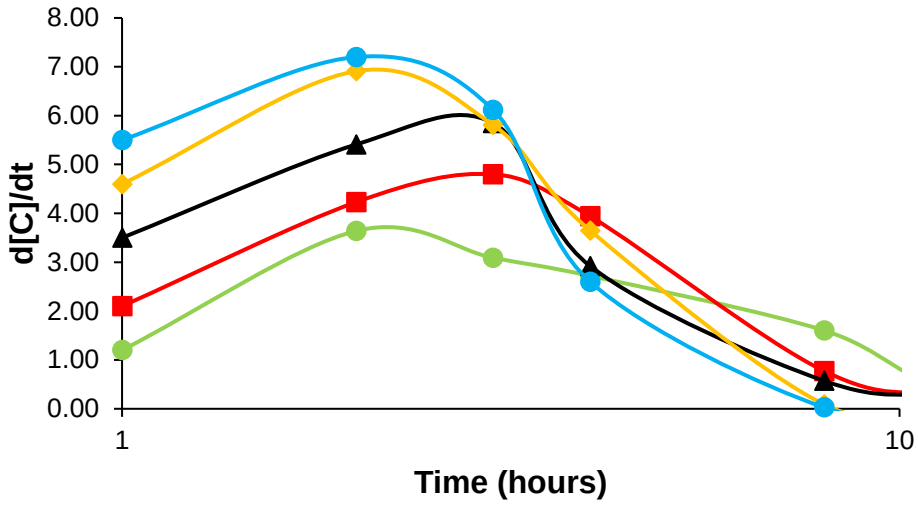

Figure 4.33. Rate (d[***Z***]/dt) for the formation of ***Z*** with varying concentration of $\boldsymbol{Z}_{catalyst}$ added to the reaction mixture at time = 0 h. $\boldsymbol{Z}_{catalyst}$ = 0.5 mM (green ●), $\boldsymbol{Z}_{catalyst}$ = 1.0 mM (red ■), $\boldsymbol{Z}_{catalyst}$ = 1.5 mM (black ▲), $\boldsymbol{Z}_{catalyst}$ = 2.0 mM (yellow ◆) and $\boldsymbol{Z}_{catalyst}$ = 2.5 mM (blue ●).

This more constant reaction rate results in a significantly higher rate of reaction being recorded at times greater than 4 hours with the concentration of 28.0 mM being reached after 24 hours. This series of experiments could then be used to determine the order of the autocatalytic reaction as outlined previously with equation 4.4 as shown in Figure 4.34.

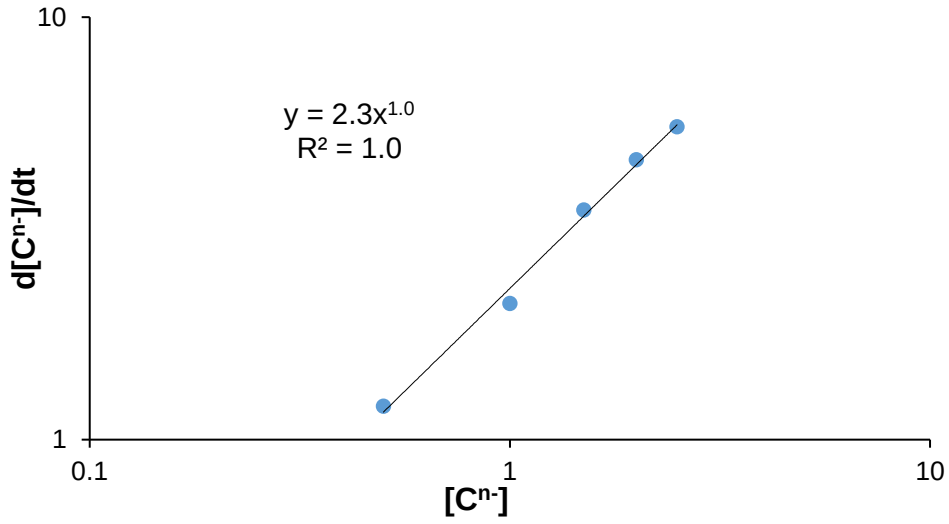

Figure 4.34. Determination of the reaction order for $\boldsymbol{II} + {}_4\boldsymbol{F} \rightarrow \boldsymbol{Z}^{n-}$ where y = mx^p with *p* being equal to the order of the reaction (concentrations of seed $\mathbf{C}^{n-}$ marked on graph).

$$log\frac{d[\boldsymbol{C}^{\boldsymbol{n}-}]}{dt} = plog[\boldsymbol{C}^{\boldsymbol{n}-}] + log2.3 \textbf{ [equation 4.4]}$$

With the order of the reaction, *p*, shown to be equal to 1, this autocatalytic process can be said to result in the exponential increase in the replicator. The fact the concentration of ***Z*** increases exponentially means the catalytic process is operating a high level of efficiency despite the ability of the replicator to form supramolecular polymers.

4.9 Conclusion

This chapter has presented a chemical system were the reaction between an aldehyde and an aromatic amine produces a self-replicating species giving rise to an autocatalytic chemical reaction. The reaction is not especially quick to reach completion, which in many ways is advantageous because it allows careful monitoring of the reaction's process through a variety of techniques and ultimately a detailed study of the systems reaction kinetics to be carried out. It is these kinetics that provide proof of the autocatalytic nature of the reaction and give an insight into the mechanisms that allow it occur.[39–41] The product of the autocatalytic reaction, ***F***, is an effective LMWG. Is ability to form supramolecular hydrogels arises from the fact it can form high aspect ratio fibres that form the solid-phase necessary for gelation. Formation of these fibres and ultimately gelation is triggered by acidification of the reaction solution, however, the supramolecular assembly process begins before this acidification step takes place. Analysis of the reactions solution viscosity shows the existence of supramolecular physical polymers

existing in solution. This physical polymer formation demonstrates the mechanism through which the autocatalytic process operates. The face-to-face interaction of molecules of ***F*** offer a templating route for the formation of additional ***F*** molecules. Should that be the only construction method at play then the fibres would go on increasing in the length until all the starting material had been consumed with no observable increase in the rate of reaction due to the number of catalytic sites not increasing Crucially, because of the physical nature of the bonds between the "monomers" in the supramolecular polymer dissociation of the polymers chain can occur. This dissociation is like to become a key factor in controlling not just the length of the polymers in solution but also the number of catalytic sites, resulting in an incubation time before the exponential autocatalytic process takes hold. After the incubation period and the supramolecular polymers have reached a critical the break mechanism results in an overall increase in the number of the catalytic site which, in turn increases the rate of reaction and the formation of even more fibres. This feedback loop can be affected by a number of factors, including increasing the temperature of the reaction solution which will increase the rate of dissociation resulting in a decrease in polymer length. It is also possible to break the polymers up through mechanically agitation of solution which corresponds to an increase in the reaction rate because more, smaller polymers or oligomers result in a higher number of catalytic sites.

Through using of *ex situ* synthesised ***Z*** it was possible to seed the *in situ* reaction with the catalytic species as soon as the two starting materials are mixed. This seeding experiment reduced the incubation time and displayed the expected correlation between rate of reaction and concentration of the seed. Use of various seed concentrations also allowed the order of the reaction to be determined. With a reaction order equal to one the system is said to exhibit exponential growth with respect to the concentration of the product/replicator. This exponential growth is an important and very interesting feature of the system. As proposed by von Kiedrowski exponential replication is required is a prerequisite for natural selection making this system and systems like it useful tools for studying natural selection processes. Indeed, as this particular branch of science advances and the distinction between synthetic, chemical models of life and biology becomes less and less clear it should be fully expected for a greater of the origins and definitions of life. This is as well examining the source of biological homochirality (as described by the Frank model[42]) and even looking at the possibility of discovering life beyond planet Earth.

4.10 References

1 M. P. Robertson and G. F. Joyce, *Cold Spring Harb. Perspect. Biol.*, 2012, **4**, a003608–a003608.

2 J. Chmielewski, S. Yao, I. Ghosh and R. Zutshi, *Nature*, 1998, **396**, 447–450.

3 M. Eigen, C. K. Biebricher, M. Gebinoga and W. C. Gardiner, *Biochemistry*, 2002, **30**, 11005–11018.

4 P. L. Luisi and P. Stano, *Nature. Chem.*, 2011, **3**, 755–756.

5 D. J. Adams, M. F. Butler, W. J. Frith, M. Kirkland, L. Mullen and P. Sanderson, *Soft Matter*, 2009, **5**, 1856–1862.

6 E. R. Draper, L. L. E. Mears, A. M. Castilla, S. M. King, T. O. McDonald, R. Akhtar and D. J. Adams, *RSC Adv.*, 2015, **5**, 95369–95378.

7 A. Z. Cardoso, A. E. Alvarez Alvarez, B. N. Cattoz, P. C. Griffiths, S. M. King, W. J. Frith and D. J. Adams, *Faraday Discuss.*, 2013, **166**, 101–116.

8 M. Avrami, *J. Chem. Phys.*, 1939, **7**, 1103–1112.

9 M. Avrami, *J. Chem. Phys.*, 1940, **8**, 212.

10 X. Huang, P. Terech, S. R. Raghavan and R. G. Weiss, *J. Am. Chem. Soc.*, 2005, **127**, 4336–4344.

11 M. Avalle, G. Belingardi and A. Ibba, *Int. J. Impact Eng.*, 2007, **34**, 23–27.

12 G. A. Buxton and N. Clarke, *Phys. Rev. Lett.*, 2007, **98**, 238103–238107.

13 G. O. Lloyd and J. W. Steed, *Soft Matter*, 2011, **7**, 75–84.

14 M. Suzuki, M. Kondo and K. Hanabusa, *Macromol. Symp.*, 2015, **358**, 112–119.

15 L. Xu, A. K. Horváth, Y. Hu, C. Ji, Y. Zhao and Q. Gao, *J. Phys. Chem. A*, 2011, **115**, 1853–1860.

16 K. J. Vastenhout, R. H. Tornberg, A. L. Johnson, M. W. Amolins and J. R. Mays, *Anal. Biochem.*, 2014, **465**, 105–113.

17 Ž. D. Bugarčić, T. Soldatović, R. Jelić, B. Algueró and A. Grandas, *Dalt. Trans.*, 2004, **99**, 3869–3877.

18 A. C. Dash, B. Dash and S. Praharaj, *J. Chem. Soc. Dalt. Trans.*, 1981, 2063–2069.

19 S. O. Krabbenborg, C. Nicosia, P. Chen and J. Huskens, *Nat. Commun.*, 2013, **4**, 1667.

20 A. Pal, M. Malakoutikhah, G. Leonetti, M. Tezcan, M. Colomb-Delsuc, V. D. Nguyen, J. van der Gucht and S. Otto, *Angew. Chem. Int. Ed.*, 2015, **54**, 7852–7856.

21 J. Li, I. Cvrtila, M. Colomb-Delsuc, E. Otten and S. Otto, *Chem. - A Eur. J.*, 2014,

20, 15709–15714.

22 E. Krieg, M. M. C. Bastings, P. Besenius and B. Rybtchinski, *Chem. Rev.*, 2016, **116**, 2414–2477.

23 L. Yang, X. Tan, Z. Wang and X. Zhang, *Chem. Rev.*, 2015, **115**, 7196–7239.

24 Y. Liu, T. Wang and M. Liu, *Chem. - A Eur. J.*, 2012, **18**, 14650–14659.

25 M. B. Baker, L. Albertazzi, I. K. Voets, C. M. A. Leenders, A. R. A. Palmans, G. M. Pavan and E. W. Meijer, *Nat. Commun.*, 2015, **6**, 6234.

26 S. M. Munzert, G. Schwarz and D. G. Kurth, *RSC Adv.*, 2016, **6**, 15441–15450.

27 J. van der Gucht, N. A. M. Besseling, W. Knoben, L. Bouteiller and M. A. Cohen Stuart, *Phys. Rev. E*, 2003, **67**, 51106–51113.

28 R. P. Sijbesma, F. H. Beijer, L. Brunsveld, B. J. Folmer, J. H. Hirschberg, R. F. Lange, J. K. Lowe and E. W. Meijer, *Science*, 1997, **278**, 1601–1604.

29 C. Wang, H. Wu, Z. Chen, M. T. McDowell, Y. Cui and Z. Bao, *Nature Chem.*, 2013, **5**, 1042–1048.

30 M. Colomb-Delsuc, E. Mattia, J. W. Sadownik and S. Otto, *Nature Commun.*, 2015, **6**, 7427.

31 D. Frascari, M. Zuccaro, A. Paglianti and D. Pinelli, *Ind. Eng. Chem. Res.*, 2009, **48**, 7540–7549.

32 J. W. Chen and W. M. Kalback, *Ind. Eng. Chem. Fundam.*, 1967, **6**, 175–178.

33 Y. J. Kim, T. E. Glass, G. D. Lyle and J. E. McGrath, *Macromolecules*, 1993, **26**, 1344–1358.

34 F. Susanne, D. S. Smith and A. Codina, *Org. Process Res. Dev.*, 2012, **16**, 61–64.

35 P. Crisalli and E. T. Kool, *Org. Lett.*, 2013, **15**, 1646–1649.

36 Z. Dadon, N. Wagner and G. Ashkenasy, *Angew. Chem Int. Ed.*, 2008, **47**, 6128–6136.

37 G. von Kiedrowski, *Angew. Chem Int. Ed.*, 1986, **25**, 932–935.

38 G. von Kiedrowski, Springer Berlin Heidelberg, 1993, 113–146.

39 Y. Deng, H. Wang, L. Xu, Y. Wu, C. Zhong and W. Hu, *RSC Adv.*, 2013, **3**, 4666–4672.

40 A. Saghatelian, Y. Yokobayashi, K. Soltani and M. R. Ghadiri, *Nature*, 2001, **409**, 797–801.

41 D. Sievers and G. von Kiedrowski, *Nature*, 1994, **369**, 221–224.

42 F. C. Frank, *Biochim. Biophys. Acta*, 1953, **11**, 459–463.

Chapter 5 - Conclusions and future work

The development of *in situ* formed LMWGs has allowed the incorporation and utilisation of a number of chemical concepts into the gelation process. Concepts such as pathway complexity, systems chemistry and auto-catalysis have been shown to be involved in the initial stages of the hierarchal assembly process that results in gelation. The combination of a water-soluble aldehyde with a variety of hydrazide and amine species has given rise to a number of gelators based on the formation of hydrazone and imine functionalities. Control over the physicals properties of these gels can be exerted through the use of the afore mentioned chemical concepts, as well as using multiple gelator systems. All of these ideas have been explored in detail in a bid to fully understand the gelation systems presented.

The chemical incorporation of a hydrazide functionalised drug molecule into the gel network through the use of dynamic covalent chemistry demonstrates the potential for such a system to be used as a means of drug delivery. The fact the reaction proceeded through a stepwise reaction sequence, as well as the inherent potential of the resultant gelator molecules to undergo a reversible tautomerisation process, allowed multiple gels to be arrived at from a single chemical starting point. The different gels were the result of the time before the *in situ* reaction mixture was set and whether gelation triggered by either raising or lowering the pH of the solution. Due to the multiple dependency factors these gels products were a result of the pathway complexity that exists within the system.

This system has made it clear the value that should be placed on understanding a gelation system's energy landscape in terms of the *in situ* chemical reaction that produces the LMWGs.[1,2] It also highlights the link between chemical reactivity, stability and the final supramolecular assembly of the gel. An understanding of the chemical reaction's energy landscape would be essential if its use as a drug delivery system was to be realised.

By swapping the hydrazide component for various aminobenzoic acid derivatives, a family of imine based gelators was created. They demonstrated a wide range of physical properties that were the result of subtle changes to the chemical functionalisation of the aminobenzoic acid derivatives. While not displaying the reversible tautomerisation of the hydrazone gelator, the fact a family of gelators could be studied, as opposed to a single

gelation system, presented the opportunity to investigate the properties of gels containing two different gelators. By virtue of the *in situ* method of synthesis for the preparation of these gelators the systems chemistry within the family could be explored through simultaneously mixing two different amines with the aldehyde. This resulted in gels where the assembled network showed physical differences depending on which amines and in what ratios they were used. These differences manifested themselves in one system where self-sorting of both the chemical and assembled entities was observed. This was accompanied by another system where the network resulted from a chemical co-assembly within the ligand products as well as the supramolecular structure. In terms of self-sorting at the chemical reaction level certain amine combinations giving rise to the two product minimum while others resulted in the four product maximum reaction mixture being observed.

This work demonstrated how chemical reactivity at one end of the hierarchal assembly process can influence the physical properties of the resultant supramolecular gel at the other.[3] With the introduction of a new gelator family that clearly has much potential for expansion, there is no doubt a vast wealth of unrealised new gelation systems can be formed. These systems may be based on single or multiple LMWG compositions. It is the ability to tune the physical characteristics of mixed gelator systems that is exciting when considering potential applications. The ability to produce as transparent a gel as possible while alsi being able to tune its rheological properties would be of particular benefit in the development of cell growth mediums.[4]

It is safe to say that one of the ultimate goals of any chemist that works with supramolecular gels is to fully understand the gelation phenomena and arrive at a set of rules for the rational design of new LMWGs. Attempts to forge a link between the properties of the individual molecular building blocks such as hydrophobicity and the physical shape of the molecule have shown promise. With the amount of research looking into supramolecular gels it is easy to envisage a time, perhaps in the not too distant future, when the rational, premediated design of LMWGs is possible.[5,6]

Even if it were possible to predict with certainty which molecules will go on to form gels the ability to predict and target desired physical properties represents an even greater challenge.[7] Fortunately, advances in understanding multi component supramolecular gels has presented a bridge to the time when LMWGs with specific qualities can be developed *ab initio*. The work presented in this thesis demonstrates this concept of targeted mechanical properties through mixing two gelators with different properties, be it mechanical strength or visual appearance.

The *in situ* nature of the reactions used to produce the gelators discussed in this work allowed a detailed study into the kinetics of the chemical reaction that results in the formation of the gelator molecules. One such system's kinetics were found to show autocatalytic behaviour. This results in a correlation between reaction time and mechanical strength of the final gel being demonstrated. Furthermore, use of theoretical models allowed the link between the elastic modulus of gel and concentration of the LMWG to be used, linking the chemical reactivity to the physical properties of the gel to be realised.[8,9]

What has been presented here represents a small percentage of what may be possible with an aldehyde/imine based *in situ* gelation system. There is massive scope to expand the existing family of gelators, particular the aminobenzoic acid derived family. While this would satisfy academic curiosity there is the potential to focus future research on the pursuit of applications for these gelators.

As previously mentioned due to the dynamic nature of hydrazone and imine bonds it is possible to envisage the use of these systems for the controlled release of amine or hydrazide functionalised drugs. The initial investigations into such a system should focus on quantitative analysis the dynamics of these bonds. These studies would also benefit from a theoretical element that focuses on developing an in-depth understanding of the keto-enol tautomerisation process. Such a study would shed light on why the tautomerisation process is reversible with the hydrazide derived and irreversible when amines are used. This knowledge could then potentially elucidate a means of accessing the so far unobserved enol tautomer for the imine based systems.

The systems chemistry of these *in situ* gelation systems and the co-assembly or self-sorting within the resulting gel is an obvious avenue for future research based on the work of this thesis. By utilising the systems discussed in this work as well incorporating any new discoveries the systems chemistry that will exist because of the far from equilibrium potential of *in situ* synthesised gelators can be explored.[10]

The autocatalytic formation of one of the gelators during its *in situ* synthesis offered an unprecedented way of controlling the mechanical robustness of the set gel. The understanding of the autocatalytic reaction was the result of a detailed study of the systems reaction kinetics. This study was possible because of the relatively slow reaction time of the system in question. A similar study should be extended to all *in situ* synthesised gelators developed in the future. It stands to reason that because of the inherent supramolecular interactions that exist between the individual gelator molecules there is the potential for autocatalytic dominated reaction kinetics to be observed in *in*

situ synthesised systems. Such autocatalytic systems would be interesting for the more traditional reasons of understanding the evolutions of biological systems but in the case of gelating species control over the physicals properties could be exercised in a similar manner to those outlined in this thesis.

The work of this thesis has highlighted how careful control of the chemical reaction process that forms the LMWGs can be used to control the physical properties of the gels. This fine control was also shown to be achievable through setting gels consisting of two different LMWGs. Because of the *in situ* synthesis of the gelators described in this thesis and the plethora of unexplored reaction components, not just on the amine and hydrazide front, but also the potential to investigate alternative aldehyde units, there is potential for this work to be advanced further in the future.

References

1 E. Mattia and S. Otto, *Nat. Nanotechnol.*, 2015, **10**, 111–119.

2 D. van der Zwaag, P. A. Pieters, P. A. Korevaar, A. J. Markvoort, A. J. H. Spiering, T. F. A. de Greef and E. W. Meijer, *J. Am. Chem. Soc.*, 2015, **137**, 12677–12688.

3 J. Raeburn, A. Zamith Cardoso and D. J. Adams, *Chem. Soc. Rev.*, 2013, **42**, 5143–5156.

4 M. W. Tibbitt and K. S. Anseth, *Biotechnol. Bioeng.*, 2009, **103**, 655–663.

5 J. H. van Esch, *Langmuir*, 2009, **25**, 8392–8394.

6 A. R. Hirst, I. A. Coates, T. R. Boucheteau, J. F. Miravet, B. Escuder, V. Castelletto, I. W. Hamley and D. K. Smith, *J. Am. Chem. Soc.*, 2008, **130**, 9113–9121.

7 P. Dastidar, *Chem. Soc. Rev.*, 2008, **37**, 2699–2715.

8 R. G. Weiss, *J. Am. Chem. Soc.*, 2014, **136**, 7519–7530.

9 M. De Loos, B. L. Feringa and J. H. Van Esch, *Eur. J. Org. Chem.*, 2005, **2005**, 3615–3631.

10 H. Bunzen and E. Kolehmainen, *Molecules*, 2013, **18**, 3745–3759.

Appendix A: Experimental.

6.1 Chemical list

All chemical compounds were either purchased from commercial sources (see chemical list) or prepared as described in subsequent sections of this chapter. Full characterisation of all synthesised compounds can also be seen below. Deionised water was used throughout and all chemicals were used as received.

6.1.1 Chemicals used throughout thesis

Trifluoroacetic acid – Fluorochem.
Hexamethylenetetramine – Alfa Aesar.
Phloroglucinol – Aldrich.
Glucono delta-lactone (GdL) – Alfa Aesar.
Sodium hydroxide (NaOH) – Fisher Chemicals.
Hydrochloric acid (HCl) – Fisher Chemicals.
All solvents – Fisher Chemical.
All deuterated solvents – Cambridge isotope laboratories.

6.1.2 Chemicals used in Chapter 2 The Hydra

II: Isonicotinc acid hydrazide – Alfa Aesar

6.1.3 Chemicals used in Chapter Imine

R_1: 4-aminobenzoic acid – Sigma Aldrich
R_2: 5-amino-2-chlorobenzoic acid – Alfa Aesar
R_3: 4-amino-2-methoxybenzoic acid – Alfa Aesar
R_4 4-amino-3-hydroxybenzoic acid – Alfa Aesar
R_5 3-amino-4-hydroxybenzoic acid – Sigma Aldrich
R_6: 3-amino-5-(trifluoromethyl)benzoic acid – Apollo Scientific
R_7: 3-amino-2-methoxybenzoic acid – Sigma Aldrich
R_8: 4-amino-2-methylbenzoic acid – Alfa Aesar
R_9: 4-aminophenol – Sigma Aldrich

R_{10} 6-aminohexanoic acid – Sigma Aldrich

6.1.4 Auto-catalysis chapter

4-amino-L-phenylalanine – Alfa Aesar

6.2 Analytical techniques

The analytical techniques used throughout this work, both in terms of chemical characterisation of synthesised compounds, and the characterisation of the physical properties of any resulting gels are described in this section.

6.2.1 Scanning electron microscopy

SEM images were produced using a Philips XL30 LaB6 ESEM equipped with an Oxford Instrument X-max 80 EDX detector at 3 kV. Wet gel samples were placed on carbon sticky tabs mounted on aluminium SEM stubs. Once mounted samples were dried under vacuum in a desiccator for 48 hours. These dried samples were then gold coated for two minutes at 12 μA using a sputter coater.

6.2.2 Tunnelling electron microscopy

TEM images were produced using a JEOL JEM-1400 microscope with an acceleration voltage of 120 kV. The samples were prepared on a copper grid with carbon film and dried for 24 hours before imaging. The images were produced using the Gatan Micrograph software.

6.2.4 High performance liquid chromatography (HPLC)

Chromatography carried out at UV detection at 290 nm using a Shimadzu HPLC with a Thermo Scientific Accucore C18 column (100 x 4.6 mm, particle size of μ 2.6). Flow rate 0.8 mL/min using 100 % methanol.

6.2.5 Rheology measurements

Rheological experiments were performed on a Bohlin nano II rheometer. A 40 mm aluminium plate was used with an operating gap of 300 μm gap and a solvent trap. For all gels 5 ml of the gelator solution and the desired was prepared and added to the plate with a syringe in the operating gap so the gel could form in contact with the cone.

6.2.5.1 Time sweeps

Time sweep experiments were commenced immediately upon addition of the gelator solution to the rheometer. Sample was added to the rheometer once GdL had fully dissolved. All samples were recorded over 15 h at 20 °C with a torque of 10 μNm and a frequency of 10 Hz, data was taken every 30 s for a sample time of 3 s.

6.2.5.2 Frequency sweeps

Frequency sweep experiments were performed immediately after the time sweep at 20 °C over a frequency range of 0.1 – 100 Hz. A constant applied stress of 20 Pa was used for the measurements which were conducted over the viscoelastic region for the gels.

6.2.5.3 Stress sweeps

Stress sweep experiments were recorded after frequency sweep experiments. All samples were recorded at 20 °C and at a frequency of 5 Hz. G' and G'' where measured over the entire stress strange which started at 0.1 Pa. The critical stress or "yield point" was determined to be the point at which G' and G'' crossed over signifying a breakdown in the gels structure.

6.2.6 Mass spectrometery

Mass spectrometry data were recorded using electrospray ionization (ESI) in negative mode using a Bruker microTOF instrument. High resolution mass spectrometry was used to confirm purity of the compounds produced. Samples were run at the University of Edinburgh by Dr A. T. Taylor.

6.2.7 Infrared spectroscopy

IR spectra were recorded on a Nicolet is5 instrument using 24 scans at a resolution of 1 cm^{-1} and data spacing of 0.964 cm^{-1} with all samples loaded directly onto the instrument.

6.2.8 X-ray diffraction techniques

6.2.8.1 Powder x-ray diffraction (PXRD)

PXRD patterns were collected at room temperature using a Bruker D8 Advance powder diffractometer in reflectance mode. Lynxeye super speed detector was used with the radiation being monochromated Cu Kα1, with a characteristic wavelength of 1.541 Å. 30 minute scans over the range $5° \leq 2\theta \leq 60°$ (stepsize = 0.014481°/counting time = 0.5 s/steps).

6.2.8.2 Single crystal x-ray diffraction (SCXRD)

Single-crystal X-ray data was collected on a Bruker X8 APEX-II CCD diffractometer with a graphite monochromator, using Mo-Kα radiation from a sealed source at 100 K. Data was collected using APEX-II software, integrated using SAINT and corrected for absorption using SADABS. All the structures were solved using Olex2, with ShelXS direct methods and refined using least squared refinement with ShelXL. Images where created in Xseed using pov-ray.

6.2.9 pH measurements

All pH measurements were conducted using a Mettler Toledo FiveEasy. The pH meter was calibrated each morning using a two-point calibration method. The stated accuracy of the pH meter is ± 0.1. During pH measurements the solution was stirred continuously.

6.2.10 Chemdraw calculations

Calculations to determine *c*logP and pK_a were done using the PerkinElmer program Chemdraw. *c*logP was calculated using the biobyte algorithm. pK_a was calculated using the MOPAC developed MP6 method.

6.3 Synthetic procedures

This section describes the synthesis of all synthesised compounds discussed in this thesis.

6.3.1 Synthesis of *II*

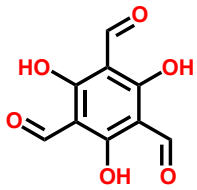

Figure 6.1. 1,3,5-triformylphloroglucinol, (***II***), F.W. = 210.14 $gmol^{-1}$.

To a mixture of hexamethylenetetramine (22.2 g, 157.5 mmol, 2.2 equiv.) and phloroglucinol (9 g, 71.4 mmol, 1 equiv) trifluoroacetic acid (135 ml) was added, the solution was then heated to 100 °C and stirred under nitrogen for 2.5 h. To the reaction mixture 3 M HCl (300 ml) was slowly added with continued heating at 100 °C and stirred for 1 h. After being allowed to cool to room temperature the reaction mixture was filtered and the filtrate obtained was extracted with dichloromethane (5 × 100 ml) before being dried with $MgSO_4$. Once dry the dichloromethane was removed by rotary evaporation yielding an orange solid. This solid was washed with hot ethanol (3 × 100 ml) to yield a pale yellow free flowing powder. This powder was dried in the oven overnight to yield the final product I_e. The synthesis is a scaled up version of the synthesis presented by Chong *et .al*.[1]

Yield: 19%, 2.96 g.

^{1}H NMR (d_6-DMSO, J/Hz, δ/ppm): 14.15 (S, 3H, Ar-OH), 10.82 (s, 3H, CHO).

^{13}C NMR ($CDCl_3$, δ/ppm): 189.07 (-CHO), 178.43 (C-OH), 105.23 (C-aldehyde).

Elemental analysis: Calculated %C = 51.44, %H = 2.88 Found %C = 51.17, %H = 2.92.

Melting point: 198-199 °C (literature mp: 198 – 200 °C).

6.3.1 Chapter 2 - The Hydra

Synthesis of all compounds relating to the chapter 2 including *ex situ* synthesised gelators.

6.3.1.1 Synthesis of C_e

To a mixture of 1,3,5-triformylphloroglucinol (***II***) (0.25 g, 1.19 mmol, 1 equiv.) and isonicotinc acid hydrazide (II) (0.50 g 3.69 mmol, 3.1 equiv.) ethanol (50 ml) was added. The resulting suspension was brought to reflux and the reaction was allowed to proceed for 4 hours to produce a bright yellow suspension. This was then allowed to cool to room temperature before being filtered to yield a yellow solid. This solid was then washed with water (4 × 50 ml) before being collected and dried in an oven overnight (80 °C) to yield the final product $\boldsymbol{C_e}$.

6.3.1.2 Synthesis of C_{eB}

To a mixture of 1,3,5-triformylphloroglucinol (0.25 g, 1.19 mmol, 1 equiv.) and benzhydrazide (0.50 g 3.69 mmol, 3.1 equiv.) ethanol (50 ml) was added. The resulting suspension was brought to reflux and the reaction was allowed to proceed for 4 hours to produce a bright yellow suspension. This was then allowed to cool to room temperature before being filtered to yield a yellow solid. This solid was then washed with water (4 × 50 ml) before being collected and dried in an oven overnight (80 °C) to yield the final product.

6.3.2 Chapter 3, Targetable mechanical properties with *in-situ* formed tripodal ketoenamine supramolecular

Synthesis of all compounds relating to the chapter 3 including *ex situ* synthesised gelators.

6.3.2.1 General *ex situ* synthesis of gelators **R$_1$ – R$_9$**

To a suspension of A (.250 mg, 1.19 mmol) in ethanol (50 ml) the appropriate amine was added (3.69 mmol, 3.1 molar equivalents) and the resultant suspension was refluxed for 16 hours. Once complete the reflux was cooled to room temperature then cooled to 0 ^{o}C, before the reaction mixture was filtered to obtain a yellow precipitate. The precipitate was washed with hot ethanol (5 × 50 ml) then dried overnight at 80 ^{o}C this produced the desired product at good yields and purity.

Table S1. Details for the synthesis of Gelators **R$_1$** – **R$_9$**.

Gelator	Amine	Mass of amine (mg)	yield (mg)	% yield	Molecular weight of gelator (gmol^{-1})
R$_1$	4-aminobenzoic acid	506	561	83	567.50
R$_2$	5-amino-2-chlorobenzoic acid	633	679	85	670.84
R$_3$	4-amino-2-methoxybenzoic acid	617	618	79	657.58
R$_4$	4-amino-3-hydroxybenzoic acid	565	659	90	615.50
R$_5$	3-amino-4-hydroxybenzoic acid	565	645	88	615.50
R$_6$	3-amino-5-(trifluoromethyl)benzoic acid	757	725	79	771.50
R$_7$	3-amino-2-methoxybenzoic acid	617	571	73	657.58
R$_8$	4-amino-2-methylbenzoic acid	558	638	88	609.58
R$_9$	4-aminophenol	403	512	89	483.47

6.3.2.2 *Ex situ* synthesis of compound **R$_{10}$**

To a suspension of A (.250 mg, 1.19 mmol) in ethanol (50 ml) 6-aminohexanoic acid was added (3.69 mmol, 3.1 molar equivalents) and the resulting solution was refluxed for 16 hours. Once complete the reflux was cooled to room temperature and rotary evaporation was used to remove all the ethanol resulting in a dark orange oil. After a week at 5 ^{o}C the oil had solidified to give a dark orange solid. The solid ground to a fine powder and washed with hot ethanol (5 × 50 ml) then dried overnight at 80 ^{o}C this produced the desired product at good yields (71 %) and purity.

6.4 Chemical characterisations

6.4.1 Hydra chapter

6.4.1.1 *Ce* characterisation

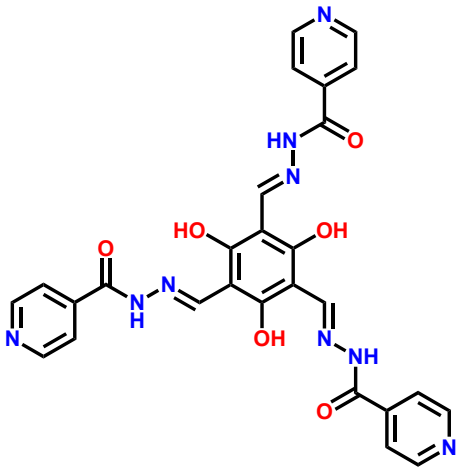

Figure 6.2. *N*',*N*''',*N*''''-((1*E*,1'*E*,1''*E*)-(2,4,6-trihydroxybenzene-1,3,5-triyl)tris(methanylylidene))tri(isonicotinohydrazide) (***Ce***) F.W = 567.16 gmol$^{-1|}$.

Yield: 93 %, 0.63 g (M.W. 567.51 gmol^{-1}).

^{1}H NMR (d$_6$-DMSO, J/Hz, δ/ppm): 13.79 (broad s, 3H, Ar-OH), 12.47 (broad s, 3H, -NH-), 8.94 (s, 3H, - CHN), 8.79 (d, J = 5.03, 3H, Ar-H), 7.84 (d, J = 5.43, 3H, Ar-H)

^{1}H NMR D$_2$O (d$_2$-D$_2$O, J/Hz, δ/ppm): 8.58 (d, J = 5.77, 6H, Ar-H), 8.48 (s, 3H, -CHN), 7.82 (d, J = 5.27, 6H, Ar-H)

^{13}C NMR (d$_6$-DMSO, δ/ppm): 161.99 (3 × Ar-OH), 160.06 (3 × -NHCO-), 150.42 (6 × Ar-H), 146.16 (3 × - N=C-), 139.86 (3 × C, pyridyl), 121.38 (6 × Ar-H), 98.94 (3 × C, core)

IR (cm^{-1}): 2820, 1676, 1632, 1588, 1454, 1410, 1371, 1324, 1280, 1219, 1186, 1155, 1091, 1064, 997, 945, 892, 837, 781, 746, 682, 633, 557

HRMS (ESI$^-$): calculated for [M-H]$^-$ 566.1542, $C_{21}H_{16}N_6O_6$ found: 566.1562

Melting point: Decomposes upon heating (>300 °C)

6.4.1.2 C_{eB} characterisation

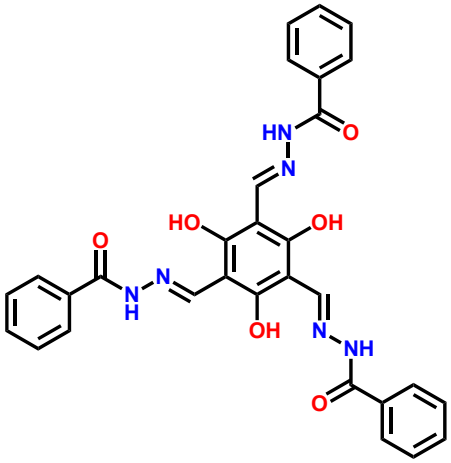

Figure 6.3 *N*',*N*''',*N*''''-((1*E*,1'*E*,1''*E*)-(2,4,6-trihydroxybenzene-1,3,5-triyl)tris(methanylylidene))tri(benzohydrazide) (***C_{eB}***) F.W = 563.15 gmol^{-1}.

Yield: 89 %, 0.62 g (M.W. 564.18 gmol^{-1}).

^{1}H NMR (d$_6$-DMSO, J/Hz, δ/ppm): 13.95 (s, 3H, Ar-OH), 12.29 (s, 3H, -NH-), 8.97 (s, 3H, -CHN), 7.97 (d, J = 7.10, 6H, Ar-H), 7.61 (m, 9H, Ar-H).

^{13}C NMR (d$_6$-DMSO, δ/ppm): 162.88 (3 × Ar-OH), 162.20 (3 × -NHCO-), 145.57 (3 x N=CH-), 132.87 (3 x Ar-H), 132.56 (3 x Ar), 129.09 (6 x Ar-H), 128.01 (6 x Ar-H), 99.57 (3 x Ar).

IR (cm^{-1}): 3227, 3057, 1645, 1601, 1580, 1529, 1489, 1455, 1398, 1371, 1328, 1277, 1185, 1155, 1100, 1027, 1001, 958, 928, 900, 883, 815, 795, 776, 705, 686, 678, 620, 606, 595, 583, 571, 559.

HRMS (ESI$^-$): calculated for [M-H]$^-$ 563.1452, $C_{30}H_{23}N_6O_6$ found: 563.1443.

Melting point: Decomposes upon heating (>300 ^{o}C).

6.4.2 Chapter 3 Targetable mechanical properties with *in-situ* formed tripodal ketoenamine supramolecular

6.4.2.1 **R₁** chemical characterisation

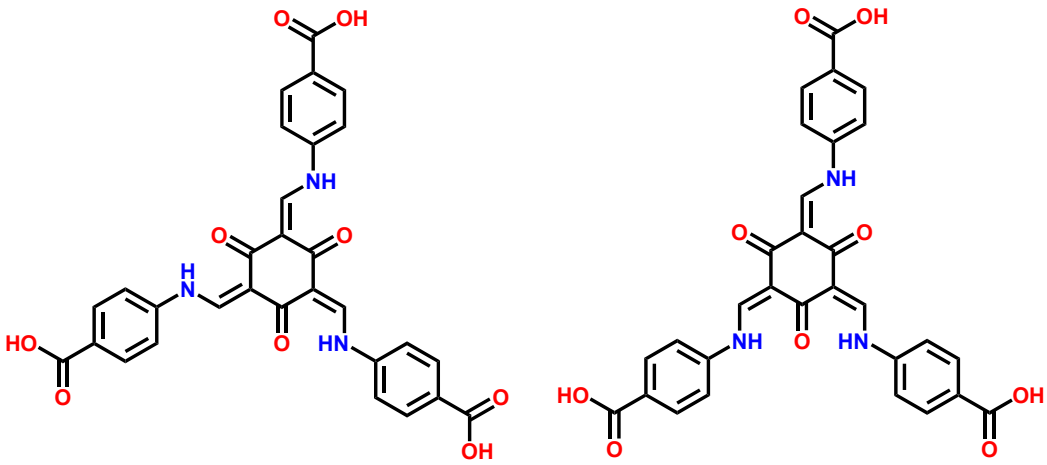

Figure 6.4. 4,4',4"-(((1*E*,1'*E*,1"*E*)-(2,4,6-trioxocyclohexane-1,3,5-triylidene)tris(methanylylidene))tris(azanediyl))tribenzoic acid (**R₁**) F.W = 566.12 gmol^{-1}. Both detected geometric isomers shown (C_3 on the left and C_s on the right).

1H NMR (d$_6$-DMSO, J/Hz, δ/ppm): 13.33 (d, J = 12.70, =CNH), 12.86 (dd, J = 11.47, 8.83, =CNH), 8.74 (d, J = 12.76, 3H, HC-N), 7.99 (d, J = 2.41, 6H, Ar-H), 7.58 (dd, J= 16.88, 8.16, 6H, Ar-H).

^{13}C NMR (D_2O, δ/ppm): 187.94, 187.58, 186.93, 175.75, 171.97, 149.75, 130.88, 130.58, 126.21, 116.75, 115.10, 112.05, 111.87, 107.32.

IR (cm^{-1}): 3065, 1712, 1623, 1595, 1570, 1455, 1427, 1304, 1229, 1175, 1100, 1034, 995, 847, 764, 686, 649, 635, 578.

HRMS (ESI$^-$): Calculated for $[M-H]^-$ 566.1205, $C_{30}H_{20}N_3O_9$ found 566.1191.

Melting point: Compound decomposes upon heating (.>300 °C).

6.4.2.2 **R2** chemical characterisation

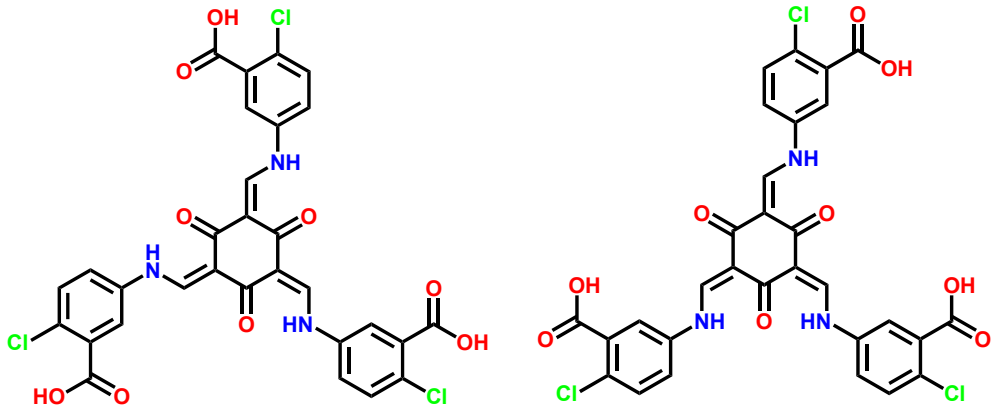

Figure 6.5. 5,5',5''-(((1*E*,1'*E*,1''*E*)-(2,4,6-trioxocyclohexane-1,3,5-triylidene)tris(methanylylidene))tris(azanediyl))tris(2-chlorobenzoic acid) (**R2**) F.W = 668.00 $gmol^{-1}$. Both detected geometric isomers shown (C_3 on the left and C_s on the right).

^{1}H NMR (d_2-D_2O, J/Hz, δ/ppm): 9.51 (s, 3H, HC-N), 7.29 (s, 6H, Ar-H), 7.02 (s, 3H, Ar-H).

^{13}C NMR (D_2O, δ/ppm): 187.93, 187.42, 186.94, 175.88, 173.73, 147.88, 145.00, 139.76, 139.45, 138.06, 135.85, 131.22, 130.16, 126.68, 118.47, 117.35, 116.17, 114.87, 112.08, 106.01.

IR (cm^{-1}): 2987, 2589, 1725, 1605, 1568, 1548, 1444, 1409, 1340, 1294, 1270, 1228, 1121, 1037, 985, 890, 816, 763, 695, 665.

HRMS (ESI^-): Calculated for $[M-H]^-$ 668.0036, $C_{30}H_{17}Cl_3N_3O_9$ found 668.1007.

Melting point: Compound decomposes upon heating (.>300 ºC).

6.4.2.3 **R3** chemical characterisation

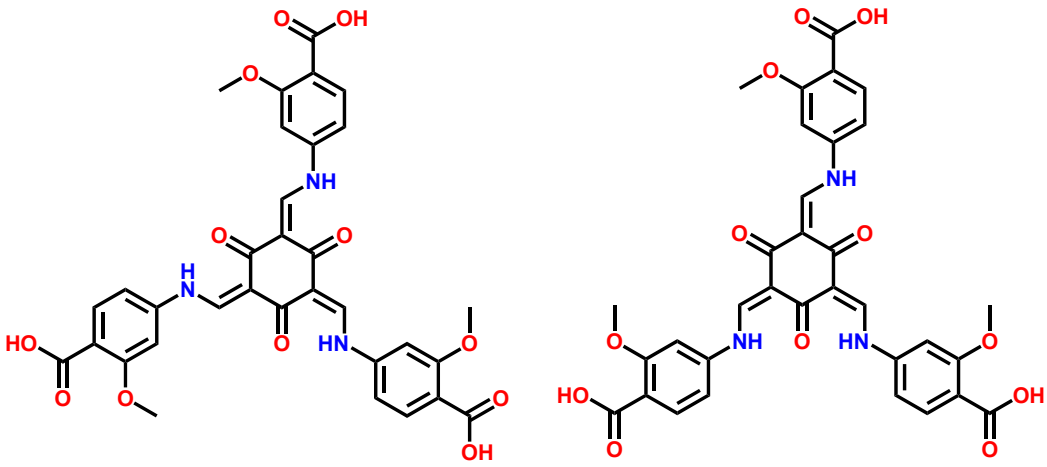

Figure 6.6. 4,4',4''-(((1*E*,1'*E*,1''*E*)-(2,4,6-trioxocyclohexane-1,3,5-triylidene)tris(methanylylidene))tris(azanediyl))tris(2-methoxybenzoic acid) (**R3**) F.W = 656.15 $gmol^{-1}$. Both detected geometric isomers shown (C_3 on the left and C_s on the right).

^{1}H NMR (d_6-DMSO, J/Hz, δ/ppm): 13.92 (d, J = 13.00, =CNH), 13.29 (dd, J = 24.67,13.41, CNH), 8.80 (m, 3H, HC-N), (td, J = 7.71,3.75, 3H, Ar-H), 7.22 (m, 6H, Ar-H), 3.90 (d, J = 3.63, 9H, OCH_3).

^{13}C NMR (D_2O, δ/ppm): 187.44, 187.0, 175.87, 158.56, 149.82, 131.56, 117.71, 112.12, 107.33, 99.50, 55.22.

IR (cm^{-1}): 3010, 1725, 1627, 1565, 1468, 1446, 1296, 1216, 1153, 1075, 1024, 948, 871, 796, 763, 645, 560.

HRMS (ESI^-): Calculated for $[M-H]^-$ 656.1522, $C_{33}H_{26}N_3O_{12}$ found 668.1581.

Melting point: Compound decomposes upon heating (.>300 ºC).

6.4.2.4 **R₄** chemical characterisation

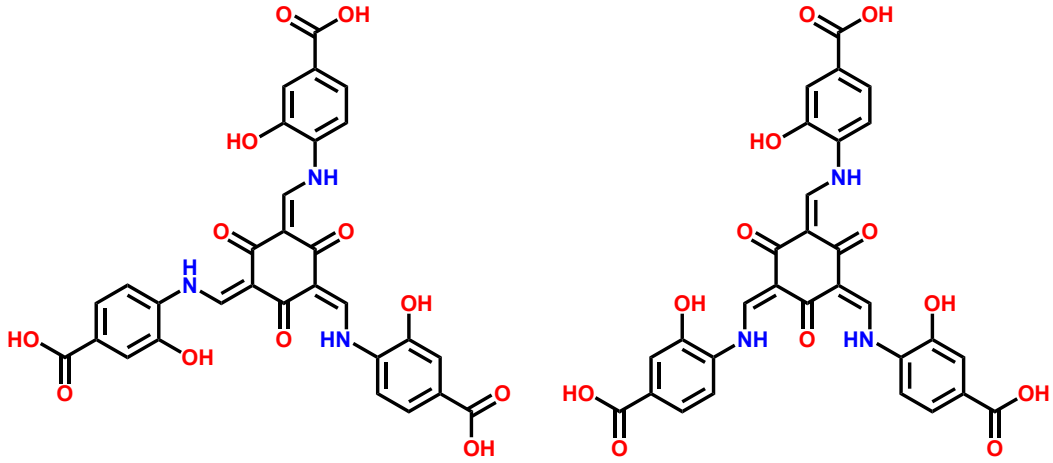

Figure 6.7. 4,4',4''-(((1*E*,1'*E*,1''*E*)-(2,4,6-trioxocyclohexane-1,3,5-triylidene)tris(methanylylidene))tris(azanediyl))tris(3-hydroxybenzoic acid) (**R₄**). F.W = 614.11 gmol^{-1}. Both detected geometric isomers shown (C_3 on the left and C_s on the right).

^{1}H NMR (d_6-DMSO, J/Hz, δ/ppm): 13.99 (d, J = 13.29, =CNH), 13.50 (dd, J = 28.00, 13.31, =CNH), 12.81 (s, 3H-OH), 8.78 (m, 3H, HC-N), 7.74 (dt, J = 8.57,4.52, 3H, Ar-H), 7.48 (t, J = 7.49, 6H, Ar-H)

^{13}C NMR (D_2O, δ/ppm): 188.04, 187.4, 187.13, 176.63, 176.02, 156.77, 154.26, 147.19, 140.64, 133.65, 132.50, 127.79, 119.50, 117.67, 116.45, 115.46, 114.70, 113.79, 111.96, 106.41.

IR (cm^{-1}): 3394, 3263, 1662, 1575, 1530, 1429, 1353, 1277, 1196, 1142, 1092, 988, 949, 884, 841, 816, 758, 721, 672, 635, 570.

HRMS (ESI$^-$): Calculated for [M-H]$^-$ 614.1052, $C_{30}H_{20}N_3O_{12}$ found 614.1233.

Melting point: Compound decomposes upon heating (.>300 ºC).

6.4.2.5 **R**$_5$ chemical characterisation

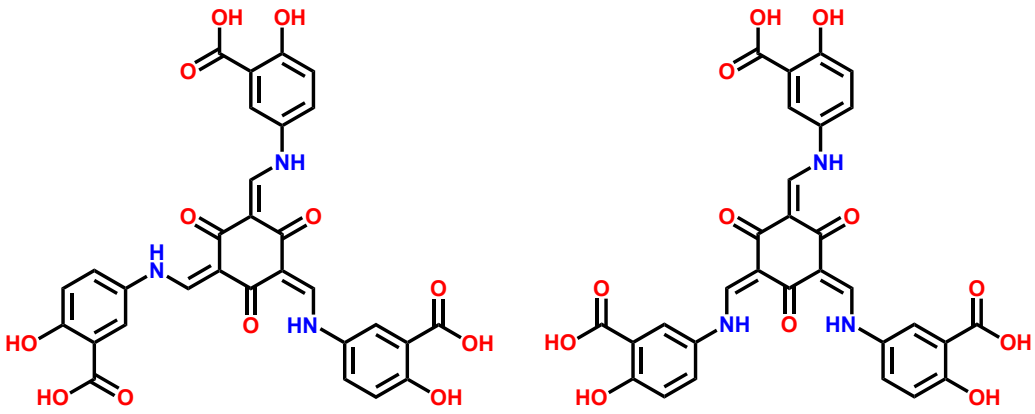

Figure 6.8. 5,5',5''-(((1*E*,1'*E*,1''*E*)-(2,4,6-trioxocyclohexane-1,3,5-triylidene)tris(methanylylidene))tris(azanediyl))tris(2-hydroxybenzoic acid) (**R**$_5$). F.W = 614.11 gmol^{-1}. Both detected geometric isomers shown (C_3 on the left and C_s on the right).

^{1}H NMR (d_6-DMSO, J/Hz, δ/ppm): 13.29 (dd, J = 18.92, 13.56, =CNH), 12.83 (dd, J = 13.59, 8.14, =CNH), 11.36 (s, 3H, –OH), 8.74 (dd, J = 13.37,2.88, 3H, HC-N), 8.01 (d, J = 16.78, 3H Ar-H), 7.69 (d, J = 8.36, 3H, Ar-H), 7.08 (m, 3H, Ar-H).

^{13}C NMR (D_2O, δ/ppm): 176.51, 175.81, 162.17, 148.35, 135.76, 129.25, 128.96, 128.61, 123.52, 121.28, 118.70, 117.29, 116.59, 105.97.

IR (cm^{-1}): 3076, 1693, 1580, 1450, 1320, 1250, 1121, 1093, 999, 941, 820, 761, 614, 562.

HRMS (ESI$^-$): Calculated for [M-H]$^-$ 614.1052, $C_{30}H_{20}N_3O_{12}$ found 614.1759.

Melting point: Compound decomposes upon heating (.>300 ºC).

6.4.2.6 $\mathbf{R_6}$ chemical characterisation

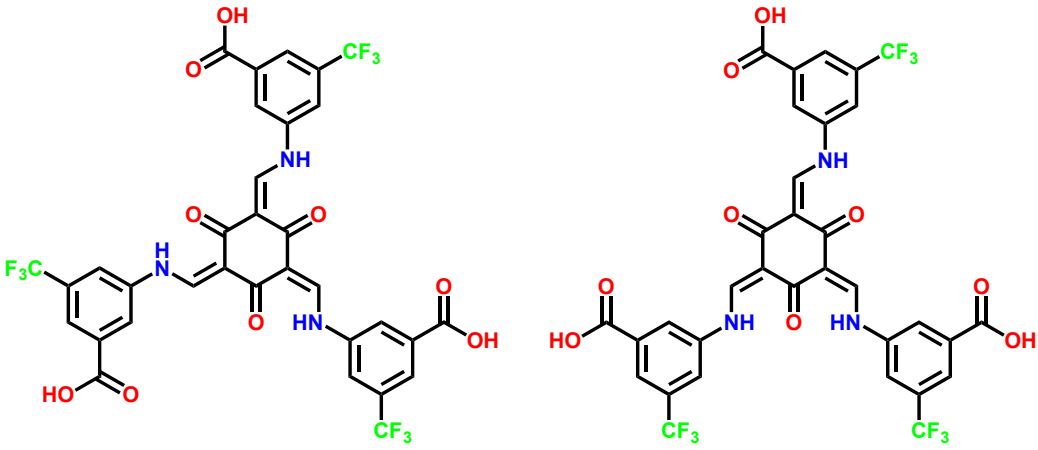

Figure 6.9. 5,5',5''-(((1*E*,1'*E*,1''*E*)-(2,4,6-trioxocyclohexane-1,3,5-triylidene)tris(methanylylidene))tris(azanediyl))tris(3-(trifluoromethyl)benzoic acid) (**R_6**) F.W = 770.09 gmol^{-1}. Both detected geometric isomers shown (C_3 on the left and C_s on the right).

^{1}H NMR (d_2-D_2O, J/Hz, δ/ppm): 9.45 (s, 3H, HC-N), 7.36 (s, 3H, Ar-H), 7.11 (s, 6H, Ar-H).

^{13}C NMR (D_2O, δ/ppm): 187.22, 173.94, 147.12, 138.25, 131.19, 130.81, 130.28, 129.93, 129.86, 129.35, 125.75, 122.13, 119.39, 115.69, 114.40, 111.99.

IR (cm^{-1}): 3079, 2577, 1715, 1621, 1586, 1471, 1355, 1274, 1172, 1124, 1042, 946, 870, 829, 768, 734, 675, 607, 571, 562.

HRMS (ESI$^-$): Calculated for [M-H]$^-$ 770.0827, $C_{33}H_{17}F_9N_3O_9$ found 770.0495.

Melting point: Compound decomposes upon heating (.>300 ºC).

6.4.2.7 $\mathbf{R_7}$ chemical characterisation

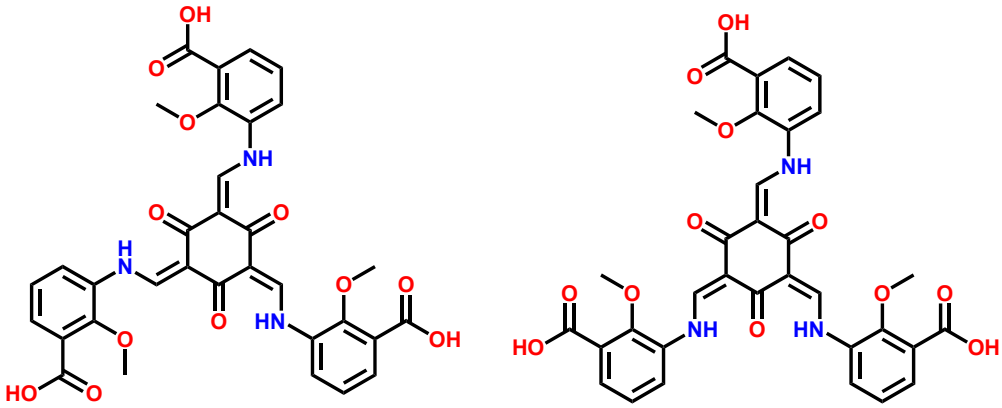

Figure 6.10. 3,3',3"-(((1*E*,1'*E*,1"*E*)-(2,4,6-trioxocyclohexane-1,3,5-triylidene)tris(methanylylidene))tris(azanediyl))tris(2-methoxybenzoic acid) (**R_7**). F.W = 668.11 gmol^{-1}. Both detected geometric isomers shown (C_3 on the left and C_s on the right).

^{1}H NMR (d_2-D_2O, J/Hz, δ/ppm): 9.57 (s, 3H, HC-N), 7.40 (s, 3H, Ar-H), 7.04 (s, 3H, Ar-H), 6.70 (s, 3H, Ar-H).

^{13}C NMR (D_2O, δ/ppm): 188.34, 187.91, 187.09, 178.68, 177.46, 148.41, 147.79, 147.01, 139.26, 138.45, 137.76, 137.24, 137.07, 135.84, 129.97, 129.26, 128.47, 118.91, 117.74, 114.10, 113.01, 111.83, 106.87, 106.18, 20.17, 19.82.

2.3.7.3 IR (cm^{-1}): 2973, 2613, 1698, 1623, 1563, 1448, 1344, 1284, 1217, 1143, 1039, 984, 821, 770, 751, 688, 648, 567.

HRMS (ESI$^-$): Calculated for [M-H]$^-$ 656.1522, $C_{33}H_{26}N_3O_{12}$ found 668.1085.

Melting point: Compound decomposes upon heating (.>300 ºC).

6.4.2.8 **R₈** chemical characterisation

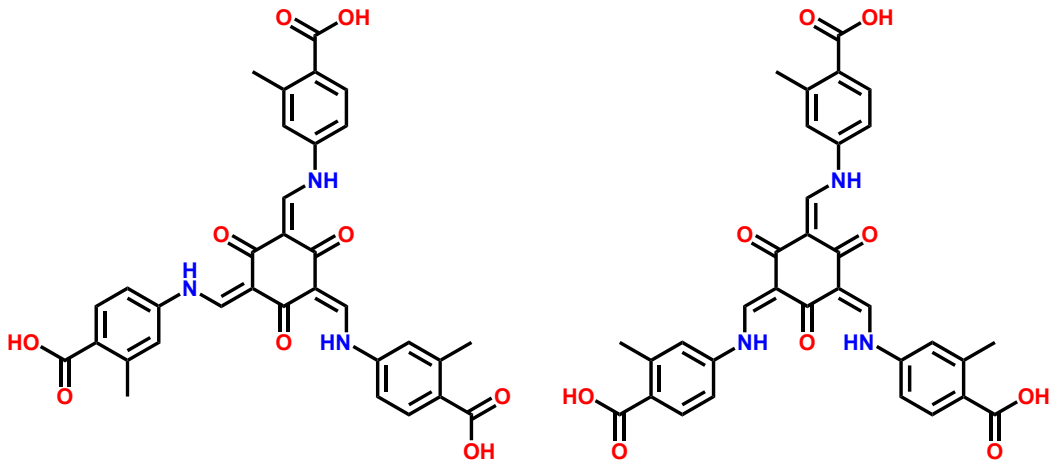

Figure 6.11. 4,4',4''-(((1*E*,1'*E*,1''*E*)-(2,4,6-trioxocyclohexane-1,3,5-triylidene)tris(methanylylidene))tris(azanediyl))tris(2-methylbenzoic acid) (**R₈**). F.W = 608.17 $gmol^{-1}$. Both detected geometric isomers shown (C_3 on the left and C_s on the right).

^{1}H NMR (d_2-D_2O, J/Hz, δ/ppm): 9.43 (d, J = 11.43, 3H, HC-N), 7.32 (s, 3H, Ar-H), 7.04 (s, 3H, Ar-H), 6.61 (s, 3H, Ar-H).

^{13}C NMR (D_2O, δ/ppm): 187.93, 187.47, 186.97, 176.47, 173.75, 146.46, 144.01, 139.06, 133.37, 131.45, 130.40, 126.09, 124.53, 124.23, 118.60, 117.84, 114.45, 112.02, 106.25, 61.81, 60.92.

IR (cm^{-1}): 3079, 1705, 1623, 1566, 1454, 1420, 1221, 1170, 1113, 1091, 1034, 985, 846, 764, 688, 634.

HRMS (ESI^-): Calculated for $[M-H]^-$ 608.1675, $C_{33}H_{26}N_3O_9$ found 608.1752.

Melting point: Compound decomposes upon heating (.>300 ºC).

6.4.2.9 **R₉** chemical characterisation

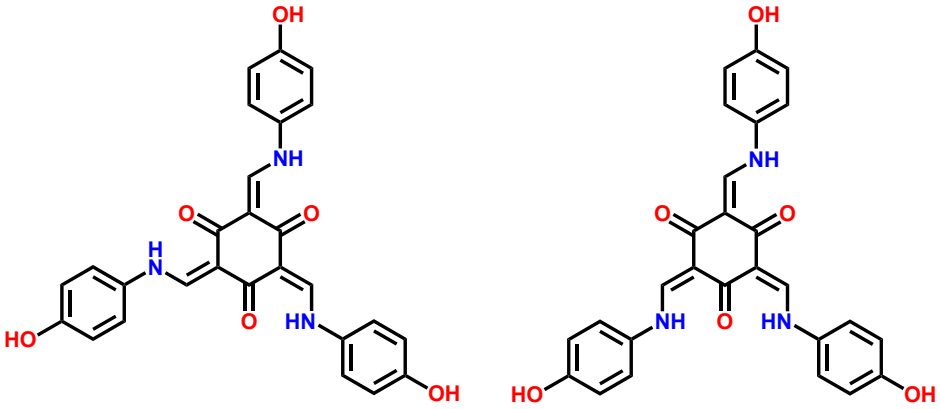

Figure 6.12. (2*E*,4*E*,6*E*)-2,4,6-tris(((4-hydroxyphenyl)amino)methylene)cyclohexane-1,3,5-trione (**R₉**). F.W = 482.17 gmol^{-1}. Both detected geometric isomers shown (C_3 on the left and C_s on the right).

^{1}H NMR (d_6-DMSO, J/Hz, δ/ppm): 13.36 (t, J = 13.11, =CNH), 12.77 (dd, J = 13.50, 4.15, =CNH), 9.61 (s, 3H, Ar-OH), 8.53 (m, 3H, HC-N), 7.28 (dd, J = 7.71, 5.45, 6H, Ar-H), 6.84 (d, J = 8.39, 6H, Ar-H).

^{13}C NMR (D_2O, δ/ppm): 187.78, 185.80, 184.00, 165.22, 159.52, 148.51, 147.89, 133.32, 126.51, 126.17, 119.36, 118.85, 111.92, 104.85.

IR (cm^{-1}): 3079, 1705, 1623, 1566, 1454, 1420, 1221, 1170, 1113, 1091, 1034, 985, 846, 764, 688, 634.

HRMS (ESI$^-$): Calculated for [M-H]$^-$ 482.1358, $C_{27}H_{20}N_3O_6$ found 482.1731.

Melting point: Compound decomposes upon heating (.>300 °C).

6.4.2.10 R_{10} chemical characterisation

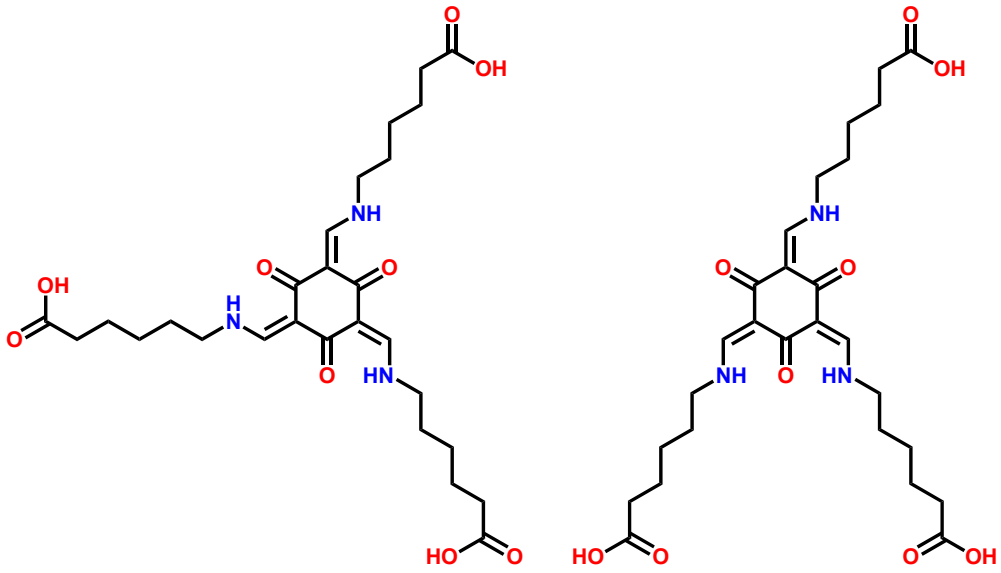

Figure 6.13. 6,6',6"-(((1*E*,1'*E*,1"*E*)-(2,4,6-trioxocyclohexane-1,3,5-triylidene)tris(methanylylidene))tris(azanediyl))trihexanoic acid. (**R_{10}**) F.W = 548.26 gmol^{-1}. Both detected geometric isomers shown (C_3 on the left and C_s on the right).

^{1}H NMR (d_6-DMSO, J/Hz, δ/ppm): 11.31 (m, =CNH), 10.87 (m, =CNH), 8.06 (m, 3H, HC-N), 3.40 (m, 6H, N-CH_2-), 2.18 (t, J = 6.96, 6H, -CH_2-), 1.52 (dt, J = 15.06, 7.47, 12H, -CH_2-), 1.30 (m, 6H, -CH_2-).

^{13}C NMR (d_6-DMSO, δ/ppm): 187.19, 184.26, 181.25, 175.20, 157.78, 157.31, 157.16, 156.55, 104.26, 104.07, 49.62, 49.42, 34.47, 30.49, 27.36, 26.07, 24.75.

2.5.3 IR (cm^{-1}): 2932, 2860, 1716, 1601, 1525, 1450, 1306, 1160, 1105, 1074, 1021, 832, 776, 732, 655.

HRMS (ESI$^-$): Calculated for [M-H]$^-$ 548.2608 $C_{27}H_{38}N_3O_9$ found 548.2588.

Melting point: 128 – 132 °C.

6.4.3 Chapter 4 - Autocatalytic synthesis of an *in situ* formed hydrogelator

6.4.3.1 ***Z*** chemical characterisation

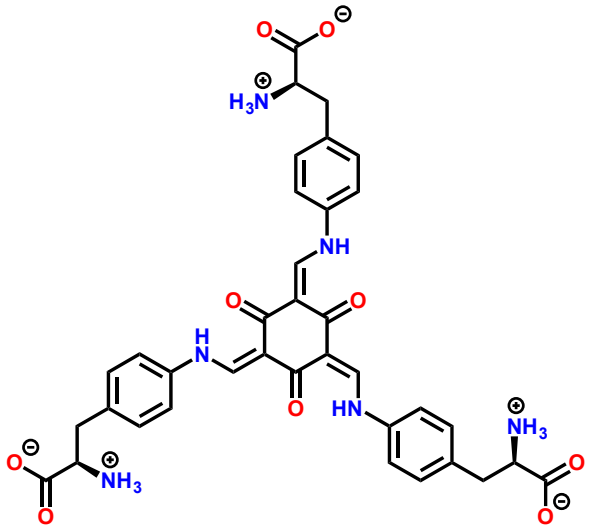

Figure 6.14. (2*R*,2'*R*,2"*R*)-3,3',3"-((((1*E*,1'*E*,1"*E*)-(2,4,6-trioxocyclohexane-1,3,5-triylidene)tris(methanylylidene))tris(azanediyl))tris(benzene-4,1-diyl))tris(2-ammoniopropanoate).

Yield: 91 %, 0.75 g, (M.W. = 696.25 $gmol^{-1}$)

^{1}H NMR (D_2O + NaOH J/Hz, δ/ppm): 7.51 (s, 3H, =CH-), 7.48 (dd, J = 7.21, 8.08, 12H, Ar-H), 3.92 (dd, J = 7.89, 5.3, 6H, -CH_2-), 3.15 (m, 3H, -CH-NH_2) *.

^{13}C NMR (D_2O + NaOH J/Hz, δ/ppm): 187.21 (10), 179.11 (1), 169.03 (8), 144.59 (7), 130.66 (5), 130.31 (9), 129.41 (4), 116.72 (6), 59.98 (2), 38.07 (3).

IR (cm^{-1}): 3334, 2859, 1598, 1515, 1411, 1361, 1314, 1269, 1041, 839, 742, 711, 651, 611, 584.

HRMS (ESI$^-$): calculated for $[M-H]^-$ 695.2507, $C_{36}H_{35}N_6O_9$ found: 695.2471.

Melting point: Decomposes upon heating (> 300 °C).

* The use of D_2O + NaOH as the NMR solvent due to the insolubility of the species all NH_x and OH ^{1}H signals are lost through deuterium exchange and deprotonation.

6.5 Gelation protocols

6.5.1 chapter 2 *in situ* gelation methods

In situ gelation methods for gels $\boldsymbol{C_e}$, $\boldsymbol{B_e}$ and $\boldsymbol{C_k}$.

6.5.1.1 $\boldsymbol{C_e}$ gelation protocol:

A typical example of setting gel C_e by method 2 at 1 wt% is described. ***II*** (33.6 mg, 0.16 mmol) was mixed with water (5 ml) to create a suspension. To this suspension NaOH (3 mg, 0.08 mmol) was added and the solution was well shaken until I_e had completely dissolved. To a separate portion of water (5 ml) ***I*** (65.83 mg, 0.48 mmol) was added and the mixture shaken until it had completely dissolved. These two solutions were then mixed together and shaken. This produced a dull yellow solution after 6 hours (ideally overnight to ensure complete formation of C_e). To this solution GdL (42.76 mg, 0.24 mmol) was added and allowed to dissolve, this resulted in the formation of a red gel after 2 hours. Gelation will occur over the optimum pH range 4-5. Apparent pK_a is 6.8 (+/- 0.1).

Critical gelation concentration 0.2 wt%.

6.5.1.2 $\boldsymbol{B_e}$ gelation protocol:

A typical example of setting gel $\boldsymbol{B_e}$ by method 3 at 1 wt% is described. ***II*** (33.6 mg, 0.16 mmol) was mixed with water (5 ml) to create a suspension. To this suspension NaOH (3 mg, 0.08 mmol) was added and the solution was well shaken until ***II*** had completely dissolved. To a separate portion of water (5 ml) ***I*** (43.89 mg, 0.32 mmol) was added and the mixture shaken until it had completely dissolved. These two solutions were then mixed together, shaken and immediately GdL (42.76 mg, 0.24 mmol) was added and allowed to dissolve, this resulted in the formation of an orange gel after 15 minutes. Gelation will occur over the optimum pH range 4-5. Apparent pK_a is 6.6 (+/- 0.1).

Critical gelation concentration 0.3 wt%.

6.5.1.3 C_k gelation protocol:

A typical example of setting gel C_k by method 1 at 2 wt% is described. I_e (67.2 mg, 0.32 mmol) was mixed with water (5 ml) to create a suspension. To this suspension NaOH (10 mg, 0.26 mmol) was added and the solution was well shaken until I_e had completely dissolved creating a solution at approximately pH 8. To a separate portion of water (5 ml) II (131.65 mg, 0.96 mmol) was added and then shaken until it had completely dissolved. These two solutions were then mixed together and shaken; the pH of the resulting solution was raised to between 9.5 and 12 with the addition of NaOH before being allowed to stand overnight producing a yellow gel. Gelation will occur over the optimum pH range 9.5-12.

Critical gelation concentration 0.5 wt%.

6.5.2 Hydra chapter *Ex situ* gelation methods

Ex situ gelation methods for gels $\boldsymbol{C_e}$, $\boldsymbol{B_e}$ and $\boldsymbol{C_k}$.

6.5.2.1 Gel $\boldsymbol{C_e}$ using *ex situ* prepared $\boldsymbol{C_e}$:

A typical example of setting gel $\boldsymbol{C_e}$ using ex situ prepared $\boldsymbol{C_e}$ at 1 wt% is described. 0.1 g (0.16 mmol) of $\boldsymbol{C_e}$ was mixed with water (10 ml) to create a suspension. To this suspension NaOH (12 mg, 0.32 mmol) was added and the solution was well shaken until $\boldsymbol{C_e}$ had completely dissolved. Once $\boldsymbol{C_e}$ dissolved, GdL (85.51 mg, 0.48 mmol) was added to the solution which was shaken until the GdL had completely dissolved at which point the vial was allowed to stand. After 2 hours a red gel had formed. Gelation will occur over the optimum pH range 4-5.

Critical gelation concentration 0.2 wt%

6.5.2.2 Gel $\boldsymbol{B_e}$ using *ex situ* prepared $\boldsymbol{B_e}$:

A typical example of setting gel $\boldsymbol{B_e}$ by method 5 at 1 wt% is described. A previously prepared sample of gel $\boldsymbol{B_e}$ prepared by method 6.5.1.2 had been dried by vacuum filtration and washed with water (5 × 100 ml) to produce a dull orange powder that was dried in

the oven over night at 80 °C. This powder (0.1 g, 0.22 mmol) was mixed with water (10 ml) to create a suspension. To this suspension NaOH was added (3 mg, 0.08 mmol) once the solid had completely dissolved, GdL (42.76 mg, 0.24 mmol) was added resulting in the formation of an orange gel after 1 hour. Gelation will occur over the optimum pH range 4-5.

Critical gelation concentration 0.3 wt%.

The dynamic character of the hydrazone bond does present some issues when using this methodology. Upon dissolving the compounds at pH 8 there is some rearrangement resulting in NMR and MS data showing the presence of small quantities of ***I***, ***II***, $\boldsymbol{A_e}$, $\boldsymbol{B_e}$ and $\boldsymbol{C_e}$ within the mixture. There is one dominant species in this mixture (> 90%), with the starting material being the significant majority species present in all cases studied. For example, if $\boldsymbol{B_e}$ is utilised then the majority of the species present is $\boldsymbol{B_e}$ and if $\boldsymbol{C_e}$ is the starting material then $\boldsymbol{C_e}$ is the significantly abundant species present.

6.5.2.3 Gel $\boldsymbol{C_k}$ using ex situ prepared $\boldsymbol{C_e}$:

A typical example of setting gel C_k using ex situ prepared C_e 1 at 2 wt% is described. 0.2 g (0.32 mmol) of C_e was mixed with water (10 ml) to create a suspension. To this suspension NaOH (25 mg, 0.65 mmol) was added and the solution was well shaken until C_e had completely dissolved. At this point a further portion of NaOH (25 mg, 0.65 mmol) was added. This resulted in the formation of a yellow gel after approximately 4 hours. Gelation will occur over the optimum pH range 9.5-12.

Critical gelation concentration 0.6 wt%

6.5.3 Targetable mechanical properties with *in-situ* formed tripodal ketoenamine supramolecular hydrogels

6.5.3.1 *In situ* gelation methods for gels $\mathbf{R_1}$ – $\mathbf{R_8}$:

This procedure describes the method used in a typical in situ setting of the hydrogels using a solution of 1,3,5-triformylglucinol and the appropriate aminobenzoic acid.

1,3,5-triformylglucinol (0.082g, 0.39 mmol) was suspended in water (5 ml), to this suspension sodium hydroxide (0.05 g, 1.25 mmol) was added and sonication and gentle heating was used to produce a clear pale yellow solution. To a separate portion of water (5 ml), the appropriate aminobenzoic acid was added (1.17 mmol), along with sodium hydroxide (0.016 g, 0.4 mmol) to ensure the complete dissolution of the aminobenzoic acid. These two aqueous solutions were then mixed together and vigorously shaken, before being allowed to react at room temperature for 4 hours. After this reaction period GDL (0.08 g, 0.45 mmol) was added and the solution was shaken until the GDL had completely dissolved, this resulted in the formation of the gel after approximately 2 hours.

6.5.3.2 *In situ* gelation methods for gel **R_9**:

This procedure describes the method used in a typical in situ setting of the hydrogel R_9 using a solution of 1,3,5-triformylglucinol and the 4-aminophenol.

1,3,5-triformylglucinol (0.082g, 0.39 mmol) was suspended in water (5 ml), to this suspension sodium hydroxide (0.05 g, 1.25 mmol) was added and sonication and gentle heating was used to produce a clear pale yellow solution. To a separate portion of water (5 ml) the 4-aminophenol was added (0.13 g, 1.17 mmol) along with sodium hydroxide (0.016 g, 0.4 mmol) to ensure the complete dissolution of the 4-aminophenol. These two aqueous solutions were then mixed together vigorously shaken before being allowed to react at room temperature for 4 hours. After this reaction period, conc. HCl (0.8 ml) was rapidly added to the solution instantly producing a bright orange gel.

6.5.3.3 *Ex situ* gelation methods for gels **R_1 – R_8**:

This procedure describes the method used in a typical setting of the hydrogel at 2 wt% using the previously prepared synthesised compound.

The gel ligand (0.1 g) was suspended in water, to this suspension sodium hydroxide was added (0.05 g, 1.25 mmol). Sonication and gentle heating was used to ensure the ligand had completely dissolved giving a solution with a pH of 9 – 10. To this solution glucono delta-lactone (GDL) (0.08 g, 0.45 mmol) was added and the solution was shaken until the GDL had completely dissolved, this resulted in the formation of the gel after approximately 2 hours.

6.5.3.4 *Ex situ* gelation methods for gel **R$_9$**:

This procedure describes the method used in a typical setting of the hydrogel R_9 at 2 wt% using the previously prepared synthesised compound R_9.

The synthesised compound **R$_9$** (0.1 g, 0.21 mmol) was suspended in water (5 ml), to this suspension sodium hydroxide was added (0.05 g, 1.25 mmol). Sonication and gentle heating was used to ensure the ligand had completely dissolved giving a solution with a pH of 9 – 10. To this solution conc. Hydrochloric acid (0.4 ml) was rapidly added instantly producing a bright orange gel.

6.5.4 Auto-catalysis chapter

In situ gelation methods for gel ***Z***:

Z (0.075 g, 0.108 mmol) was added to water (3 ml) to create a suspension. To this suspension solid NaOH was slowly added until C had completely dissolved and the solution had reached a pH of 8.5. To this solution GdL (0.170 g, 0.972 mmol, 9 equivalents relative to **C**) was added and the solution shaken until the GdL had fully dissolved. The solution was allowed to rest at room temperature resulting in the formation of a gel after 20 minutes.

CGC = 0.5 wt%, 7.18 mmol.

6.6 Additional techniques

6.6.1 Apparent pK_a determination

The apparent pK_a of the compounds ***B$_e$***, ***C$_e$*** and **R$_1$** – **R$_{10}$** could be determined in the following manner. The *ex situ* synthesised compound or *in situ* synthesised compound isolates for gel (250 mg) were mixed with 25 ml water to create a suspension. To this suspension solid NaOH was added with stirring will the pH was constantly monitored until a pH of 10.2 had been achieved. Once the pH had stabilized at 10.2 aliquots of 0.1 M HCl (150 μL) were added with stirring. The pH was recorded after every aliquot. Data was plotted as acid addition against pH and the apparent pK_a was taken to be a range over which the pH change plateaus.[2]

6.7 References

1 J. H. Chong, M. Sauer, B. O. Patrick and M. J. MacLachlan, *Org. Lett.*, 2003, **5**, 3823–6.

2 C. Colquhoun, E. R. Draper, E. G. B. Eden, B. N. Cattoz, K. L. Morris, L. Chen, T. O. McDonald, A. E. Terry, P. C. Griffiths, L. C. Serpell and D. J. Adams, *Nanoscale*, 2014, **6**, 13719–25.

Publications and other work

Publications

J. S. Foster, *et. al.,* "Gelation Landscape Engineering Using a Multi-Reaction Supramolecular Hydrogelator System" *J. Am. Chem. Soc.*, 2015, **137**, 14236–9.

J. S. Foster, *et. al.,* "Targetable rheological properties by switching between self-sorting and co-assembly with *in-situ* formed tripodal ketoenamine supramolecular hydrogels." *submitted*.

J. S. Foster, *et. al.,* "Template based in situ autocatalytic formation of a low molecular weight gelator through supramolecular polymer formation." *submitted.*

Additional work

Research done but not included in this thesis explored gelators designed around the benzene triamide (BTA) motif. This class of molecule was first reported by Curtius in 1915[1] and since then has been the focus of a huge volume of research.[2–4] A significant portion of this research as involved the development of supramolecular gels.[5,6] This research into LMWGs has yielded an extensive family of hydrogelators that utilise a pH trigger in order to initialise gelation.[6,7] Use of a GdL pH trigger introduces a time delay into the sol to gel transition[8] for the BTA gelators. This made them an ideal candidate for exploring the continuous manufacture of discrete gel particles, with the time delay being important to allow formation of the desired particle shape. In collaboration with Dr Karen Robertson and Pierre-Baptiste Flandrin of the University of Bath the continuous manufacture of discrete gel pieces was realized using a BTA gelator system. This work provide it was possible to manufacture small, discrete and highly reproducible pieces of gel formed using a LMWG. This manufacturing technique has the potential to be applied to crystallisations as well as the controlled release of drug molecules. A paper is in drafting stage.

Phenylalanine gelation has been a major focus of the Lloyd group for a number of years. I have been assisting in the project by doing a number of rheological or SEM measurements. I have helped supervise visitors from the University of East Anglia (Susana Ramalhete) and summer internships (Margaux Heinrich). There are four drafted papers for which I am a co-author.

1 T. Curtius, *J. für Prakt. Chemie*, 1915, **91**, 39–102.

2 Y. Matsunaga, N. Miyajima, Y. Nakayasu, S. Sakai and M. Yonenaga, *Bull. Chem. Soc. Jpn.*, 1988, **61**, 207–210.

3 A. R. A. Palmans, J. A. J. M. Vekemans, E. W. Meijer, A. R. A. Palmans, H. Kooijman and A. L. Spek, *Chem. Commun.*, 1997, **57**, 2247–2248.

4 J. van Herrikhuyzen, P. Jonkheijm, A. P. H. J. Schenning and E. W. Meijer, *Org. Biomol. Chem.*, 2006, **4**, 1539–1545.

5 D. K. Kumar, D. A. Jose, P. Dastidar and A. Das, *Chem. Mater.*, 2004, **16**, 2332–2335.

6 A. Bernet, R. Q. Albuquerque, M. Behr, S. T. Hoffmann and H.-W. Schmidt, *Soft Matter*, 2012, **8**, 66–69.

7 R. C. T. Howe, A. P. Smalley, A. P. M. Guttenplan, M. W. R. Doggett, M. D. Eddleston, J. C. Tan and G. O. Lloyd, *Chem. Commun.*, 2013, **49**, 4268–70.

8 D. J. Adams, M. F. Butler, W. J. Frith, M. Kirkland, L. Mullen and P. Sanderson, *Soft Matter*, 2009, **5**, 1856–1862.